UNIVERSITY OF SOUTHAMPTON

FACULTY OF ENGINEERING, SCIENCE & MATHEMATICS

School of Electronics and Computer Science

Optical properties of metal nanoparticles and their influence on silicon solar cells

by

Tristan Leigh Temple

A thesis for the degree of Doctor of Philosophy

June 2009

UNIVERSITY OF SOUTHAMPTON

ABSTRACT

FACULTY OF ENGINEERING, SCIENCE & MATHEMATICS
SCHOOL OF ELECTRONICS AND COMPUTER SCIENCE

Doctor of Philosophy

OPTICAL PROPERTIES OF METAL NANOPARTICLES AND THEIR INFLUENCE ON SILICON SOLAR CELLS

by Tristan Leigh Temple

The optical properties of metal nanoparticles have been investigated by simulation and experimental techniques. The aim of this investigation was to identify how to use metal nanoparticles to improve light-trapping in silicon solar cells. To do this we require nanoparticles that exhibit a high scattering efficiency and low absorption (i.e. high radiative efficiency) at near-infrared wavelengths. The simulation results identified Ag, Au, Cu and Al as potential candidates for use with silicon solar cells. The optical properties of Ag, Au and Cu nanoparticles are very similar above 700 nm. Below this wavelength Ag was found to be the preferred choice due to a decreased effect from interband transitions in comparison with Au and Cu. Al nanoparticles were found to exhibit markedly different optical properties to identical noble metal nanoparticles, with broader, weaker resonances that can be excited further into the UV. However, Al nanoparticles were found to exhibit higher absorption than noble metals in the NIR due to a weak interband region centred at around 825 nm.

Tuning of the resonance position into the NIR was demonstrated by many methods, and extinction peaks exceeding 1200 nm can be achieved by all of the metals studied. However, it is important that the method used to red-shift the extinction peak does not also decrease the radiative efficiency. Core-shell nanoparticles, triangular nanoparticles and platelet-type nanoparticles were found to be unsuitable for silicon solar cells applications due their low radiative efficiencies. Instead, we propose the use of large (> 150 nm) Ag spheroids with moderate aspect ratios. A maximum radiative efficiency of 0.98 was found for noble metal nanospheres when the diameter exceeded 150 nm.

The optical properties of Au and Al nanoparticles fabricated by electron-beam lithography were found to be in good agreement with simulations, provided that the substrate and local dielectric environment were accounted for by inclusion of an effective medium in the model. Cr adhesion layers were found to substantially weaken the extinction peaks of Au nanoparticles, and also result in a strong decrease of radiative efficiency. Adhesion layers were not required for Al nanoparticles. The morphological and optical properties of Ag island films were found to be highly dependent on the layer thickness, deposition speed and anneal temperature. Dense arrays containing average particle sizes ranging from 25 nm to 250 nm were achieved using anneal temperatures lower than 200^{o}C. The largest nanoparticles were found to exhibit high extinction from 400 nm to 800 nm.

Depositing Ag nanoparticles onto a-Si:H solar cells was found two have two effects on the spectral response. At short wavelengths the QE was decreased due to absorption by small particles or back-scattering by larger particles. At longer wavelengths large maxima and minima are present in the QE spectra. This latter effect is not due to excitation of surface plasmons, but is instead related to modification of interference effects in the thin-film layer stack.

Contents

Declaration of authorship

I, TRISTAN TEMPLE, declare the thesis entitled

OPTICAL PROPERTIES OF METAL NANOPARTICLES AND THEIR INFLUENCE ON SILICON SOLAR CELLS

and the work presented in the thesis are both my own, and have been generated by me as the result of my own original research. I confirm that:

- this work was done wholly or mainly while in candidature for a research degree at this University;

- where any part of this thesis has previously been submitted for a degree or any other qualification at this University or any other institution, this has been clearly started;

- where I have consulted the published work of others, this is always clearly attributed;

- where I have quoted from the work of others, the source is always given. With the exception of such quotations, the thesis is entirely my own work;

- I have acknowledged all main sources of help;

- where the thesis is based on work done by myself jointly with others, I have made clear exactly what was done by others and what I have contributed myself;

- parts of this work have been published as:

  1. T. L. Temple and D. M. Bagnall, "*Optimised efficiency enhancement of inorganic solar cells by highly-scattering metal nanoparticles*", Proc. 4th Photovoltaic Science Applications and Technology (PVSAT) Conference, Bath, U.K., April 2008.
  2. T. L. Temple and D. M. Bagnall, "*Plasmonic enhancement of silicon solar cells*", Technical Digest of the 17th International Photovoltaic Science and Engineering Conference (PVSEC), Fukuoka, Japan, December 2007.
  3. T. L. Temple and D. M. Bagnall, "*Metal nanoparticles for enhancement of silicon solar cells: optical properties, applications and fabrication techniques*", Proc. 3rd Photovoltaic Science Applications and Technology (PVSAT) Conference, Durham, U.K., April 2007.
  4. T. L. Temple and D. M. Bagnall, "*DDA simulation of gold nanoparticles, with applicability for enhanced absorption in silicon solar cells*", Proc. 21st European Photovoltaics Solar Energy Conference, Dresden, Germany, September 2006.

Signed: ………………………………………………………………….

Date: ………………………………………………………………….

Acknowledgements

First and foremost I would like to thank Mum and Dad. Throughout my lengthy education you have both been a continual source of motivation, inspiration and support. I dedicate all but one chapter of this thesis to you both, thank you for everything. (I withhold one chapter because in addition to inspiration, motivation and support you also gave me a ridiculously big nose!) I also wish to thank my brother Karsten for his continual support and for reminding me that there is a big, nice world outside of academia. Also he has been the only person consistently willing to listen to me drone on about my half-baked, crazy ideas both during my undergraduate degree and my PhD. (Of course only the non-crazy, fully-baked ideas ended up in this thesis. Honest!)

This PhD has been a difficult journey, beset by an unusual number of problems. Most notable of these occurred at the end of my first year, when a fire destroyed the building that housed my desk and paperwork, and also the state of the art cleanroom that was the reason I came to Southampton in the first place! However, thanks to the support of the University and the welcoming reception by our temporary hosts in the School of Engineering Sciences, we were soon able to resume work… albeit work of a substantially less experimental form (for a year or so anyway). To the cleanroom fire I dedicate the simulation work in Chapter 4.

I would like to thank my erstwhile and long-suffering supervisor Prof. Darren Bagnall; a student simply could not ask for a nicer supervisor. I am extremely grateful to my fellow Bagnollian PhD students Stuart Boden and Owain Clark for sharing this journey with me and providing help and support along the way. I am also grateful to many other past and present members of the Nano Group for making this a fun, friendly and interesting place to work. In particular, thank you to Becky Neal, Wen Zhang, Enrico Gilli, Graham Ensell, Claudia Cerrina, Chien Chau, Xiaoli Li, Kian Kiang, David Gonzalez, Chris Johnson and Mike Pollard. Big thanks to the cleanroom technicians Zondy Weber, Neil Sessions and Dave Sagar and the Nano Group secretaries Glenys Howe and Lucia Hewitt for their tireless and cheerful help over the years. Although it is sometimes difficult to remember that there is a life outside the lab, thanks to all of my other friends over the years for providing me with so many lovely distractions. And thanks, most importantly of all, to Judith Joseph for her continued support and delicious, delicious cooking.

I am extremely grateful to the Japanese Society for the Promotion of Science (JSPS) for funding a scholarship that enabled me to spend two months based in AIST, Tsukuba, Japan during the final year of my PhD. This was a wonderful trip, and allowed me to get a taste of life in Japan in addition to a large number of very useful experimental results. I am particularly grateful to Prof. M. Kondo for agreeing to let me visit his group, and to Dr. Hitoshi Sai for being such a welcoming and helpful host. I would also like to thank the other members of the group, including Yoscina, Mastui-san, Takeyama-san, Karasawa-san, Arno, Ivan and Vladimir for their kind welcome and frequent trips to the *izakaya*. ありがとうございました! An extra special thank-you must go to Karasawa-san for his soul-stirring rendition of Judas Priest's プアンキラ at my farewell karaoke night. The man is truly gifted.

And last, but by no means least, thanks to you, dearest Reader. Without you this would just be a stack of paper gathering dust in a library. Please don't tell me about any erorrs or typos you may find. (Yes, that one was intentional. In fact, they all are!)

[To be sung.]

The sun is a mass of incandescent gas
A gigantic nuclear furnace
Where Hydrogen is built into Helium
At a temperature of millions of degrees.

The sun is hot, the sun is not
A place where we could live
But here on Earth there'd be no life
Without the light it gives.

We need its light, we need its heat
The sun light that we seek
The sun light comes from our own sun's
Atomic energy.

TMBG

Chapter 1

Introduction

In optimum conditions the sun provides nearly 1 kW of power per square metre to the Earth's surface in the form of ultraviolet (UV), visible and infrared (IR) light. Even on cloudy days at non-optimal latitudes the energy density is still around 300 W per square metre. Photovoltaic devices can convert this abundant energy into electricity, and are readily integrated into buildings and other man-made structures. However, photovoltaics is still an immature technology, and modern solar cells are expensive to produce and inefficient at converting sunlight to electricity. To become competitive with other forms of renewable energy the cost of power generated by solar cells must be reduced. This can be achieved by increasing device efficiency and reducing fabrication costs.

1.1 The need for light-trapping in silicon solar cells

The photovoltaic process can be considered as two steps: first light is absorbed to create electron-hole pairs, and then these carriers are separated and transported to external contacts. For the first step we require a device that is thick enough to optimally absorb incident photons, while for the second step we require a carrier diffusion length that exceeds the device thickness. Therefore there is a relationship between the absorption coefficient and the electrical quality of the semiconductor material. A weakly absorbing material such as crystalline silicon (c-Si) requires thick layers and an extremely low defect and impurity density to ensure high carrier lifetimes. Therefore solar cell grade c-Si is expensive to produce as it must be very high quality, and a large amount of material is required in each cell to sufficiently absorb the solar spectrum. Commercial c-Si solar cells are currently fabricated on wafers around 200 µm thick. To reduce fabrication cost there is a trend towards ever thinner wafers, with the IMEC roadmap predicting 100 µm processes within the next five years, and less than 50 µm by 2020. In addition to reduced fabrication cost, thinner silicon layers have better electrical properties, as light is absorbed closer to the depletion region. However, extremely thin wafers present several production challenges (including stress-induced flexing and kerf losses), and less of the solar spectrum is absorbed by thinner layers, which leads to a decrease in device efficiency.

Light-trapping schemes can be used to alleviate this problem by increasing the effective optical path length within the device. Due to the high refractive index of silicon materials, once light is within the active layer it can be effectively trapped by total internal reflection, provided it does not impinge at normal incidence on the front surface. Therefore the effective optical path length can be increased by texturing the front and/or rear surfaces of a solar cell. Yablonovitch and Cody predicted a maximum path length enhancement factor of 50 for the case of a silicon slab with texturing on both surfaces *[1].* Figure 1.1a illustrates the absorption of the AM1.5 spectrum by a 100 µm crystalline silicon layer (assuming zero reflection). Increasing the path length by a factor of 10 leads to a 7.2% increase in power absorption (Fig. 1.1b). The increase is more significant for thinner layers, with a 13.1% increase in power absorption for a tenfold path length increase in a 25 µm layer. The path length factor can also be considered as a materials reduction factor. A light-trapping method that increases the path length by a factor of 10 also enables a factor of 10 reduction of silicon usage.

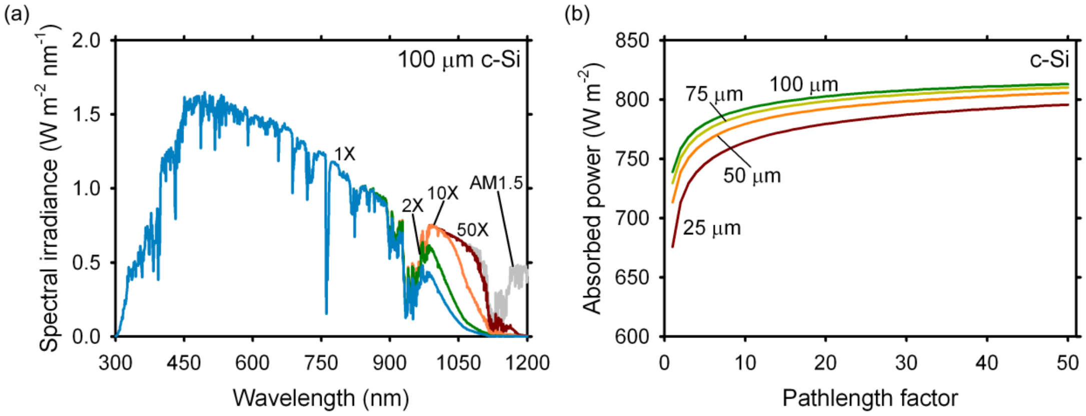

Figure 1.1: (a) Fraction of the AM1.5 spectrum absorbed by a 100 µm thick crystalline silicon layer assuming zero reflectance loss and ideal (lossless) light-trapping for path length factors of 1, 2, 10 and 50. (b) Corresponding absorbed power as a function of path length factor for four slab thicknesses.

The most common forms of anti-reflection and light-trapping texturing for wafer-based solar cells are achieved by unmasked acid etching (Fig. 1.2) *[2, 3]*. These are low-cost, large area techniques suitable for large-scale fabrication. For monocrystalline silicon an anisotropic wet etch is used to form a series of randomly sized pyramids, with height of the order of 3 to 5 µm. These pyramids serve to increase the number of front-surface interactions, thereby reducing reflection, and also couple light in at more oblique angles, thereby increasing light-trapping.

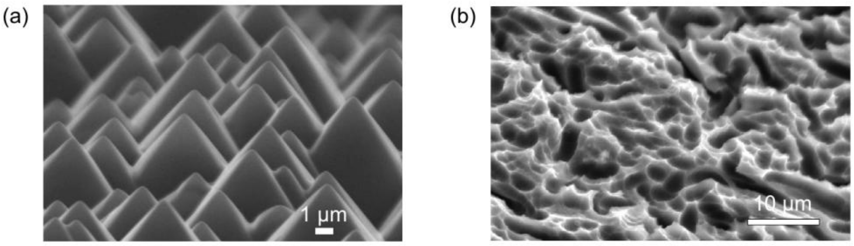

Figure 1.2: SEM images of (a) pyramid texturing on <100> silicon surface *[2]*, (b) surface of isotextured multicrystalline silicon *[3]*.

Silicon can also be deposited at low cost onto glass and other substrates in the form of hydrogenated amorphous silicon (a-Si:H). Due to the disordered atomic structure of a-Si:H it features markedly different optical and electrical properties to c-Si. Optically, a-Si:H is a quasi-direct bandgap material and so has a much larger absorption coefficient than c-Si. However, the carrier diffusion length in a-Si is far lower due to the high defect density. This limits the layer thickness of a-Si:H solar cells to 300 nm or less. A 300 nm layer has moderate optical and electrical properties. Decreasing the layer thickness will improve the electrical properties, but will also reduce the amount of light absorbed. Unlike c-Si, the motivation to reduce a-Si:H layer thickness is not related to lowering fabrication costs (except for an improved throughput arising from the shorter deposition time), but is instead due to the improved electrical properties of thinner films. As with c-Si solar cells, light-trapping schemes enable reduction of layer thickness while maintaining sufficient absorption. Figure 1.3b demonstrates that a factor of ten increase in optical path length gives rise to a 27.6% increase in absorbed power for a 300 nm a-Si:H layer, and a 54.6% increase for a 100 nm layer.

Note that even with light-trapping a-Si:H does not absorb as much of the solar spectrum as c-Si, as it has a higher energy bandgap (Fig. 1.3a). Other forms of thin-film silicon can be used to improve absorption of the solar spectrum, including microcrystalline silicon (µc-Si:H) and amorphous or microcrystalline silicon-germanium (µc-$Si_{1-x}Ge_x$:H). Therefore there is a need to develop efficient thin-film light trapping for photons with wavelength up to ~1200 nm.

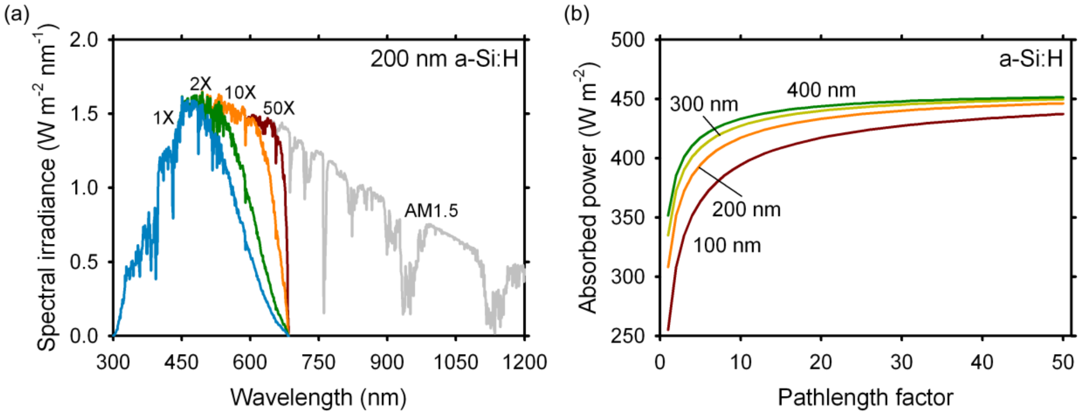

Figure 1.3: (a) Fraction of the AM1.5 spectrum absorbed by a 200 nm thick amorphous silicon layer assuming zero reflectance loss and ideal (lossless) light-trapping, for path length factors of 1, 2, 10 and 50. (b) Corresponding absorbed power as a function of path length factor for four slab thicknesses.

Texturing of thin-film devices can be achieved by depositing them onto a pre-textured substrate or superstrate. The film growth is conformal for thin layers, resulting in texturing of the front and rear surfaces. Most thin-film solar cells are deposited onto transparent conducting oxide (TCO) layers, which act as transparent top-contacts. TCOs can be textured during growth, or by plasma etching or wet chemical etching. The industry standard textured TCO is Type-U indium tin oxide (ITO) from Asahi (Fig 1.4a). However, although large improvements in cell efficiency are reported for devices fabricated onto textured substrates, the light-trapping achieved is far from optimum. One measure of the effectiveness of a textured substrate is haze. Haze is defined as the ratio of transmitted light to diffusely transmitted light, *i.e.* 100% haze implies that all transmitted light has been diffusely scattered. Fig. 1.4c shows the poor haze performance of Asahi Type-U, particularly in the NIR. Recently, Asahi developed a new version of textured ITO, Type-W, which offers considerably improved haze at longer wavelengths (Fig. 1.4b,c) *[4]*. This improvement is due to increased surface roughness. In general, the surface texture must be on the scale of the wavelength of the photon we wish to scatter, and so large features are required to scatter IR photons. However, this roughness degrades the electrical properties of the film, as it does not provide a good surface for the layer to nucleate, resulting in poor film growth. Therefore there is a trade-off between improved light-absorption due to surface texturing, and degraded electrical properties due to poor film growth.

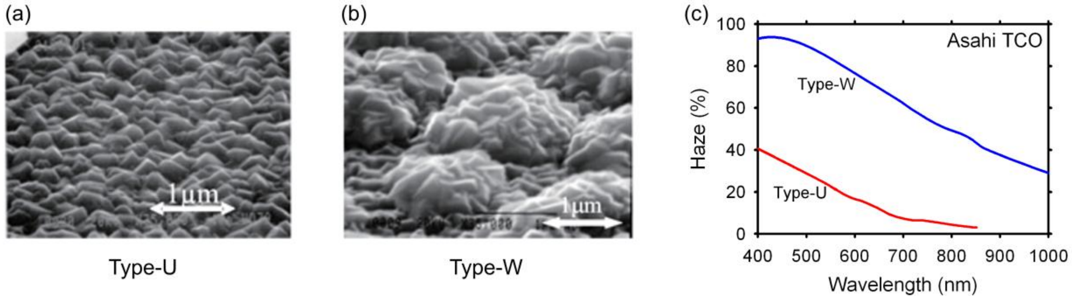

Figure 1.4: SEM images of (a) Type-U and (b) Type-W glass, with (c) the respective haze measurements *[4]*.

To reduce cost and improve the electrical properties of silicon films we require efficient light-trapping mechanisms that do not necessitate substantial roughening of the substrate. An answer to this may be found in the field of photonics. Photonics is an area of research concerned with study of the generation, detection and control of photons. Therefore, many technologies developed by the photonics community may be of use for improving light-trapping and reducing reflection of solar cells. However, photonic experiments are typically concerned with only the very narrow emission ranges provided by lasers, and are fabricated without consideration of process cost. Therefore the critical challenges of applying photonic strategies to solar cells are the requirements of interaction over a broad range of wavelengths and angles of incidence, and the limit of a low process cost. Numerous photonic structures have been proposed for use in photovoltaic applications, including 2D diffraction gratings, distributed Bragg reflectors (DBRs) and photonic crystals. However, each of these structures either adds considerable process cost (*e.g.* requires the use of photolithography or electron-beam lithography), does not function well over a range of wavelengths, or both.

Recently, there has been considerable interest in the applications of metal nanoparticles to silicon solar cells. Metal nanoparticles interact strongly with visible and/or IR light, due to the excitation of localized surface plasmons. This interaction can be tuned across the solar spectrum, and metal nanoparticles can be made using low-cost fabrication methods.

1.2 Plasmonics

Plasmonics is a subset of photonics, and concerns the interaction of light with metal films or metal nanostructures. In recent decades research into plasmonics has soared, driven by novel physics and applications such as single molecule bio-sensing, sub-wavelength waveguiding, data storage, lithography and optoelectronic device enhancement. Surface plasmons are oscillations of charge density that arise due to the interaction of light with the conduction electrons in some metals. Once coupled to a surface plasmon, incident photons can be confined to sub-wavelength volumes, and therefore exhibit giant local electric field enhancement.

Of particular interest are metal nanoparticles, which can exhibit an intense interaction with UV, visible and IR photons due to excitation of localized surface plasmons (LSPs). The wavelength range over which the interaction is strongest is highly tuneable by modification of the particle size, shape and chemical composition, or by changes in the local dielectric environment. In addition to the potential for giant electric-field enhancement, metal nanoparticles feature extremely large optical cross-sections, usually far exceeding the respective geometric cross-section. In fact, metal nanoparticles interact with light more strongly than any other chromophore. For example, the absorption cross-section of Au nanoparticles is 4-5 orders of magnitude higher than strongly absorbing dyes such as indocyanine green, rhodamine-6G and malachite green *[5]*. The fact that the optical cross-section can greatly exceed the particle's geometrical area leads to the surprising realization that even sub-monolayers (*i.e.* monolayers with incomplete surface coverage) can scatter and/or absorb *all* incident photons across a broad range of wavelengths.

Unlike most other photonic structures, many of the broad range of nanoparticle fabrication and synthesis methods are well-suited to covering large areas at low cost with minimal or moderate process complexity. The simplest approach is to moderately heat a thin continuous or semi-continuous film of metal, which results in the formation of a dense submonolayer of nanoparticles. The tools to achieve this are already in use as part of all standard a-Si:H and c-Si solar cell fabrication processes.

Investigation of metal nanoparticle enhancement of silicon solar cells is still at a very early stage, with just a small number of published experimental results *[6-14]*. Importantly, gains in photocurrent at certain wavelengths are often accompanied by losses at other wavelengths. The mechanisms responsible for metal nanoparticle mediated photocurrent enhancement and suppression are as yet incompletely understood.

The scattering cross-section of some metal nanoparticles is exceptionally high and, combined with the ability to tune the optical response across the solar spectrum, this suggests that metal nanoparticles can be used to improve light-trapping, despite having dimensions substantially smaller than the incident wavelength. Additionally, enhancement of the local electric-field intensity may also result in improved absorption in the active layer. Finally, if metal nanoparticles are able to inject excited carriers into the active layer, then absorption of photons by the nanoparticle is also of interest. However, as metal nanoparticles can also induce optical losses we must be careful to optimize their optical properties. These losses are a complex function of the nanoparticle size and shape, the chemical composition (*i.e.* the choice of metal), and the optical properties of the surrounding material.

Therefore the aim of this thesis is to investigate the optical properties of metal nanoparticles, with a particular aim of optimizing these properties to improve the absorption of light in thin silicon solar cells.

1.3 Thesis structure

This thesis consists of two literature reviews and four experimental chapters. Chapter 2 reviews the optical modelling, fabrication and characterisation of metal nanoparticles. Chapter 3 reviews recent developments in metal nanoparticle enhancement of inorganic solar cells. Chapter 4 investigates the optical properties of metal nanoparticles by means of simulations. Chapter 5 presents the results of optical experiments on arrays of particles fabricated by electron-beam lithography. These results are compared with simulation results, and optical trends in terms of particle size, shape and composition are investigated. Chapter 6 explores a lower cost fabrication method based on film islanding. The geometrical structure and optical properties of dense silver nanoparticle arrays are investigated, with the aim of optimising deposition parameters for solar cell applications. In Chapter 7 we investigate the effect of depositing silver island films onto the front surface of a-Si:H solar cells. Chapter 8 presents conclusions and suggestions for further work.

Chapter 2

Review of the fabrication and optical properties of metal nanoparticles

To investigate the interaction of metal nanoparticles with silicon solar cells we need to understand how to model their optical properties, how to fabricate them, and how to characterise them.

The intense optical properties of metal nanoparticles arise from the coupling of light to localized surface plasmons bound to the particle. The conditions required to excite these modes are highly dependent on the particle geometry and chemical composition. Therefore we require modelling methods to predict and explain the observed optical properties.

In this chapter we review the current understanding of these issues. We begin with the simulation of optical properties of metal nanoparticles, covering both analytical and numerical methods. Then we discuss three broad groups of techniques for fabricating metal nanoparticles: chemical synthesis, lithography and islanding. To conclude this section we review the optical properties of metal nanoparticles obtained by theory and experiment.

2.1 Simulation

2.1.1 Optical properties of metals

Most metals exhibit a high electrical conductivity and high specular reflectivity. Both of these properties are to due to the non-localized nature of electrons in metals. In the plasma model we consider the electrons within a metal as a negatively charged gas surrounding fixed ionic cores. This model ignores the variation of lattice potential experienced by electrons and also the interactions between electrons, but to a first approximation provides a good understanding of the optical properties of metals. The response of a plasma to an external field sets up a restoring force, leading to a resonance condition. In bulk metal the plasma resonance condition occurs at the volume (or bulk) plasmon frequency. Volume plasmons are longitudinal propagating modes, and therefore cannot be excited by the transverse electric field of photons. However the volume plasmon frequency marks an important boundary in the frequency-dependent optical response of metals. Photons with frequency below the plasmon frequency are effectively screened by induced motion of the plasma, and are therefore reflected. Photons with frequency above the bulk plasmon frequency have fields that oscillate more quickly than the plasma can respond, and so are transmitted. The bulk plasmon frequency, ω_p, is given by:

$$\omega_p^2 = \frac{n_c e^2}{\varepsilon_0 m_c} \tag{2.1}$$

Where ε_0 is the relative permittivity of free space, n_c is the number density of mobile charge carriers, e is the carrier charge, and m_c is the carrier mass. The wavelength-dependent optical properties of metals are usually discussed in terms of optical constants, $N = n + \mathrm{i}k$ (*i.e.* the refractive index and extinction coefficient), or the dielectric function, $\varepsilon_m = \varepsilon_1 + \mathrm{i}\varepsilon_2$. In both cases the real term is related to the polarizability of the metal, while the imaginary term is related to absorption. For free-electron metals the Drude model relates the bulk plasmon frequency to the frequency-dependent dielectric function as follows:

$$\varepsilon_{m,Drude}\,(\omega) = 1 - \frac{\omega_p^2}{\omega^2 + \mathrm{i}\gamma\omega} \tag{2.2}$$

Where ω is the frequency and γ is a constant related to the damping of the oscillation due to scattering events. We note that both γ and ω_p are frequency independent parameters of a given metal, and that the resulting values ε_1 and $\mathrm{i}\varepsilon_2$ are dimensionless constants.

In a free-electron metal the optical properties are entirely due to the conduction electrons (*i.e. intra*band transitions), and the Drude model is valid. However, for some metals transitions between lower band energies (*i.e. inter*band transitions) can become relevant at near UV and visible frequencies, resulting in dielectric functions that deviate strongly from the Drude model. The noble metals –gold (Au), silver (Ag) and copper (Cu) – only exhibit free-electron behaviour for a range of frequencies above the interband threshold. Beyond this threshold the optical properties deviate strongly from those predicted by the free-electron model due to the excitation of interband transitions by photons. Above the interband threshold the reflectivity of metals is dramatically reduced, which is the cause of the difference in colouration between pure Ag, Au and Cu layers. The interband threshold for Ag is in the UV and so it efficiently reflects all visible photons, but the threshold occurs in within the visible for Au (~520 nm) and Cu (~590 nm) leading to a range of wavelengths in the visible that are absorbed instead of reflected. The Drude model can be expanded by including Lorentzian terms to account for interband transitions. Therefore the dielectric function can be modelled as the sum of the Drude response (related to intraband transitions) and a series of Lorentzian oscillators (related to interband transitions):

$$\varepsilon_{m,LD}(\omega) = \varepsilon_{m,Drude}\,(\omega) + \sum_{j=1}^{k} \frac{f_j \omega_j^2}{\left(\omega_j^2 - \omega^2\right) - \mathrm{i}\gamma_j \omega} \tag{2.3}$$

Where k is the number of oscillators, each with resonant frequency ω_j, bandwidth γ_j, and strength f_j,. The parameters of the oscillators can be obtained by procedural fitting to experimental data *[15]*. Typically 3-5 Lorentzian terms (*i.e.* oscillators) are used to fit the dielectric functions of the noble metals in the visible and NIR. However, although much improved, the Lorentz-Drude model is not entirely able to accurately represent the rapid transition in optical properties at the interband transition region *[15]*. As such, it is common to use experimentally obtained dielectric function data directly where possible.

In addition to volume plasmons, the surface of a metal can also support bound oscillations of charge density known as propagating surface plasmons (PSPs). However, due to a momentum difference between free-space waves and the bound propagating mode, free-space waves cannot directly couple to PSPs, and by reciprocity PSPs cannot directly radiate into free space. The momentum gap can be bridged by prism couplers, grating couplers, or scattering from subwavelength elements. The resonance condition of a propagating surface plasmon is related to the dielectric function of the metal, the structure of the metal, and to the refractive index of the surrounding medium. PSPs present a rich diversity of physics and applications but, currently, their applicability to photovoltaic research is not clear. This is due to the difficulty in minimizing absorption losses of PSPs over a wide range of wavelengths, and the non-trivial problem of coupling broadband, unpolarized light from a wide range of angles into a propagating plasmon mode without severely complicating the device structure. For this reason and for sake of brevity we choose instead to focus only on the optical properties of metal nanoparticles. For more information of propagating surface plasmons we refer the interested reader to a range of comprehensive books *[16-19]* and review articles *[20-23]*.

So far we have discussed two types of plasmon excitation: volume and surface. Volume plasmons cannot be excited by incident light, but their resonance frequency marks a boundary in the optical properties of bulk metal. Propagating surface plasmons can be excited by incident light under certain conditions, and exist as bound surface modes at the boundary between a metal film and a dielectric. A third type of plasmon, a localized surface plasmon, exists where the geometry of the metal prohibits propagation. The most common observation of localized surface plasmons is in metal nanoparticles. The key advantage is that the plasmon is not propagating and so no momentum disparity need be overcome. Therefore, coupling of light to localized surface plasmons is implicit, and only dependent on the wavelength of the incident light and the resonance condition.

Note on nomenclature: we note that the term plasmon refers to the quantization of plasma oscillations (as photon refers to the quantization of light), with the plasma in question being the electron cloud. Therefore the correct terminology is surface plasmon-polariton, where polariton is used to denote the interaction of a photon with a plasmon. However, for brevity we use the term plasmon in place of plasmon-polariton throughout this thesis.

2.1.2 Optical properties of metal nanoparticles

The excitation of localized surface plasmons on metal nanoparticles can be qualitatively understood by considering the particle as a simple oscillator. An external electric field is able to displace the free electrons in a metal nanoparticle with respect to the fixed ionic core. This displacement sets up a restoring force, leading to coherent, resonant oscillations of charge density (Fig 2.1).

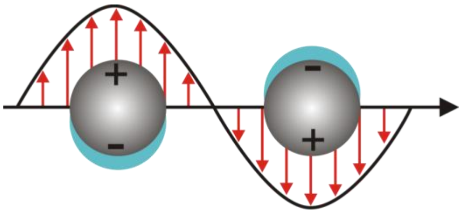

Figure 2.1: Representation of the interaction of an oscillating electric field with the electron cloud of a metal nanoparticle (after *[24]*).

Once excited, localized surface plasmons (LSPs) decay either radiatively or non-radiatively. Radiative decay results in re-emission of photons, *i.e.* scattering. Non-radiative decay processes are due to energetic relaxation, and result in absorption of incident photons and heating of the nanoparticle. Relaxation primarily occurs through creation of electron-hole pairs, either through interband or intraband methods *[18]*. Both radiative and non-radiative decay lead to damping of the oscillation. Damping results in a broadening and attenuation of the resonance.

Excitation of LSPs gives rise to intense scattering and/or absorption of light, which in turn results in a decrease in optical transmission (Fig. 2.2). This decrease is known as extinction, which is the sum of absorption and scattering. The strength of scattering and absorption of light by a particle varies strongly with wavelength. In the case of metal particles these effects are primarily due to excitation and relaxation of LSPs. The extinction peak correlates with the LSP peak, and is a strong function of the particle geometry, composition, and the surrounding dielectric environment. Essentially, altering these properties changes the resonant condition of oscillation, and hence the magnitude and spectral position of the LSP. Excitation of LSPs also results in strong confinement of incident photons, and corresponding giant enhancements of local field intensity, which are particularly related to particle shape.

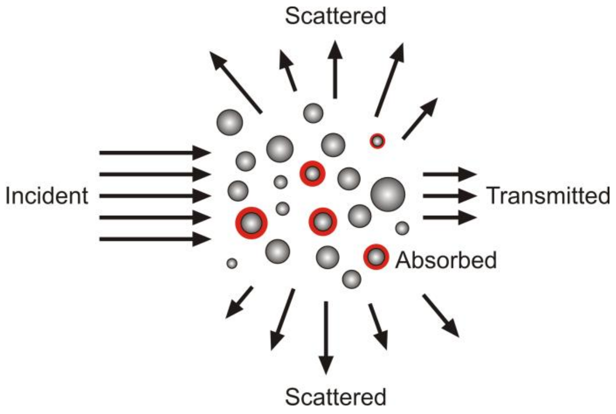

Figure 2.2: Representation of scattering and absorption of light by an ensemble of particles (after *[25]*).

The interaction of light with metal nanoparticles is a complex process and highly sensitive to a number of geometric and material considerations. To maximise the usefulness of metal nanoparticles we require analytical or numerical methods to predict their optical properties. In particular, we require information about near-field localization and the far-field scattering and absorption intensities for a given particle geometry and composition.

2.1.3 Dipole approximation

For metal nanoparticles much smaller than the wavelength of an incident electromagnetic wave, the phase of the wave will be nearly constant across the particle volume. Therefore the field can be treated as constant and homogenous, and the response of the particle to the field can be calculated using electrostatics. Using this assumption a spherical particle can be represented as an ideal dipole with polarizability, α, given by the electrostatic result *[25]*:

$$\boldsymbol{P} = {N_{med}}^2 \alpha \boldsymbol{E}_0 \tag{2.4}$$

$$\alpha = 4\pi r^3 \frac{N^2 - {N_{med}}^2}{N^2 + 2{N_{med}}^2} \tag{2.5}$$

Where r is the particle radius, $\boldsymbol{P}$ is the induced polarization, $\boldsymbol{E}_0$ is the incident electric field, and N and N_{med} are the complex optical constants of the particle and medium respectively. This is known as the quasistatic approximation, as the field is treated as static in phase but the time-dependence is retained. Scattering and absorption of light by a particle can be calculated by consideration of energy crossing the boundary of an imaginary sphere concentric with the particle. Provided the embedding medium is non-absorbing the choice of sphere size is arbitrary, enabling use of the far-field approximation. From this the rate of the scattered energy crossing the sphere, W_s, can be calculated. Absorption is related to a decrease in rate of all fields (incident and scattered) crossing the sphere, W_a. Scattering and absorption cross-sections C_{sca} and C_{abs} are defined as the ratio of W_a and W_s to the irradiance (power per unit area), I_i, of the source.

$$C_{sca} = \frac{W_s}{I_i} = \frac{k^4}{6\pi}|\alpha|^2 = \pi r^2 \frac{8}{3} x^4 \left| \frac{N^2 - N_{med}{}^2}{N^2 + 2N_{med}{}^2} \right|^2 \tag{2.6}$$

$$C_{abs} = \frac{W_a}{I_i} k \, Im\{\alpha\} = \pi r^2 4x \, Im \left\{ \frac{N^2 - N_{med}{}^2}{N^2 + 2N_{med}{}^2} \right\} \tag{2.7}$$

$$C_{ext} = C_{sca} + C_{abs} \tag{2.8}$$

$$Q_{ext} = \frac{C_{ext}}{\pi r^2} \quad ; \quad Q_{sca} = \frac{C_{sca}}{\pi r^2} \quad ; \quad Q_{abs} = \frac{C_{abs}}{\pi r^2} \tag{2.9}$$

$$k = \frac{2\pi N_{med}}{\lambda} \quad ; \quad x = kr \tag{2.10}$$

Where k is the wavevector and x is the size parameter. Note that $N^2 - N_{med}{}^2$ becomes zero for $N = N_{med}$, *i.e.* the optical response of a particle embedded in an identical medium is zero, as we would expect. An important result from the quasistatic approximation is the relationship of absorption and scattering to particle volume. As polarizability is proportional to the volume, then absorption is linearly dependent on volume, while scattering is dependent on the square of the volume. As such, extinction by large particles is predominantly due to scattering.

The extinction, scattering and absorption cross-sections C_{ext}, C_{sca} and C_{abs} represent the optical 'area' of a nanoparticle, and are typically given in units of µm^2. Dimensionless optical *efficiencies*, Q_{ext}, Q_{abs} and Q_{sca} are defined as the optical cross-section divided by the geometric cross-section. Optical efficiencies are effectively the normalized optical response of a particle, and enable comparison of optical interaction strength unbiased by particle size. This accounts for the ability to physically fit more small particles than large particles in a particular volume, which offsets the lower optical cross-sections of the smaller particles.

The quasistatic approximation is also valid for small ellipsoidal particles by addition of correction factors related to the three particle axes *[25]*. However, quasistatic approximations for spheres and ellipsoids are only valid for particles much smaller than the incident wavelength. Larger particles are subject to retardation effects that result in the excitation of higher order modes, which are not included in the quasistatic approximation.

2.1.4 Spherical particles: Mie theory

Mie theory is an exact solution to Maxwell's equations for the case of a sphere. For details of the historical development of Mie theory we direct the reader to a recent paper by Horvath *[26]*. Mie theory is valid for absorbing or non-absorbing (but electrically neutral) spheres embedded in a homogenous non-absorbing medium, illuminated by a plane wave. Given wavelength, particle radius, particle refractive index, and the refractive index of the embedding medium, Mie theory can be used to calculate the exact extinction, scattering and absorption cross-sections, and the internal and external field intensities.

Modern derivations are given by several authors *[25, 27, 28]*; here we present only the salient steps. First the incoming plane wave must be converted to spherical coordinates. This is achieved by expansion into an infinite series of vector spherical harmonics:

$$\boldsymbol{E}_i = \boldsymbol{E}_0 \sum_{n=1}^{\infty} \mathrm{i}^n \frac{2n+1}{n(n+1)} \left(\boldsymbol{M}_{oln}^{(1)} - \mathrm{i}\boldsymbol{N}_{eln}^{(1)}\right) \tag{2.11}$$

Where $\boldsymbol{E}_i$ is the incident electric field, $\boldsymbol{E}_0$ is a constant related to the amplitude of the electric field, and $\boldsymbol{M}_{oln}$ and $\boldsymbol{N}_{eln}$ are spherical vector harmonics. Internal and scattered fields are also considered in terms of spherical vector harmonics, and can be calculated by suitable selection of boundary conditions at the sphere surface, where the electron density is assumed to sharply drop to zero. Scattering functions a_n and b_n are introduced as unknowns during the calculation of the scattered field:

$$a_n = \frac{m\psi_n(mx)\psi_n'(x) - \psi_n(x)\psi_n'(mx)}{m\psi_n(mx)\xi_n'(x) - \xi_n(x)\psi_n'(mx)} \tag{2.12}$$

$$b_n = \frac{\psi_n(mx)\psi_n'(x) - m\psi_n(x)\psi_n'(mx)}{\psi_n(mx)\xi_n'(x) - m\xi_n(x)\psi_n'(mx)} \tag{2.13}$$

$$x = kr = \frac{2\pi N_{med}\, r}{\lambda}, \qquad m = \frac{N}{N_{med}} \tag{2.14}$$

Where $\psi_n(z)$ and $\xi_n(z)$ are the Riccati-Bessel cylindrical functions of order n, which can be solved by recurrence *[27]*. Primes represent differentiation with respect to the contents of the bracket. The magnetic susceptibility is taken to be unity and is therefore neglected in the above equations. The summation index n gives the order of the harmonic and therefore the order of the multipole excitation, with $n = 1$ corresponding to dipolar excitation, $n = 2$ corresponding to quadrupolar excitation *etc.* x is the size parameter, which includes the particle radius r, the medium refractive index N_{med}, and the wavelength λ. m is the relative refractive index, which defines the relationship between the particle refractive index N to the refractive index of the medium N_{med}. Refractive index values are usually obtained from experimentally derived values given in the literature, *e.g.* the compilations by Palik *[29, 30]*.

With relationships to determine the field at any point inside or outside the sphere it is now possible to calculate the optical cross-sections. This is achieved in a similar manner to the quasistatic results, where we consider the energy crossing an imaginary sphere concentric with the particle. Relations for extinction and scattering cross-sections are as follows:

$$C_{ext} = \frac{W_{ext}}{I_i} = \frac{2\pi}{k^2}\sum_{n=1}^{\infty}(2n+1)\mathrm{Re}\{a_n + b_n\} \tag{2.15}$$

$$C_{sca} = \frac{W_s}{I_i} = \frac{2\pi}{k^2}\sum_{n=1}^{\infty}(2n+1)(|a_n|^2 + |b_n|^2) \tag{2.16}$$

$$C_{abs} = C_{ext} - C_{sca} \tag{2.17}$$

Clearly in practice an infinite sum cannot be computed. However, the influence of higher order modes becomes increasingly negligible, and so the summation can be truncated once the value is suitably converged.

No restriction on particle size or wavelength is intrinsically present in Mie theory, but several factors limit the practical range of calculations. For small metal nanoparticles (< 10 nm diameter) surface scattering effects must be taken into consideration by modification of the dielectric function *[31]*. For very small metal nanoparticles (< 1 nm diameter) classical electrodynamics no longer apply due to quantum effects, and so Mie theory is not valid. For spheres with large size factors inaccurate values may be obtained during recurrence calculations because of accumulation of rounding errors. This is due to the need to represent a number with infinite digits by one with finite digits, as is done by all computers. This problem can be somewhat alleviated by increasing the precision of the data type used in the calculation. A commonly used implementation of Mie theory, BHMIE, is given by Bohren and Huffman, who also detail the reasons for their approach, including factors affecting the choice of recurrence method *[25]*.

Due to the phenomological method of introducing the material properties by use of experimentally derived dielectric functions, no physical insight is given by Mie theory into the underlying mechanisms within the material that give rise to the calculated optical spectra. It is for this reason that the concept of localised surface plasmons was not established until long after Mie's original publication *[32]*.

2.1.5 Extensions to Mie theory for coated spheres and spheroids

Extensions to Mie theory enable the analytical treatment of the optical properties of spheroids and coated spheres. A coated sphere is considered as spherical core with a concentric sphere defining a shell or coating. The core and shell have different dielectric functions. A spheroid is an ellipsoid with two identical axes. A prolate spheroid has two identical long axes (*i.e.* a cigar shape), and an oblate spheroid has two identical short axes (*i.e.* a disc shape).

Including an extra boundary condition to account for a coating on a sphere doubles the number of unknown coefficients. The resulting solutions for a_n and b_n are of similar form to that for an uncoated sphere, but depend only on the shell radius and refractive index, and include additional Ricatti-Bessel functions that are weighted by parameters A_n and B_n *[25]*. A_n and B_n take the form of a_n and b_n for an uncoated sphere and depend on the core radius and core refractive index. The solution collapses to the form of an uncoated sphere for cases where the inner and outer materials are identical, or if the core radius is either zero or equal to the shell radius. Multiple shells can be treated by further 'nesting' of weighted parameters to account for further boundary conditions *[31]*. The computational time scales considerably with each additional shell.

Mie theory solves Maxwell's equations in spherical coordinates, but solutions can also be found for other coordinate systems, for example infinite cylinders and spheroids. The solution is valid provided that the particle surface coincides with one of the coordinate surfaces, and so solutions to the wave equations must be found for a suitable coordinate system. This is known as the separation of variables method (SVM). The only other particle geometry currently treated by a SVM approach is the spheroid, both oblate and prolate. The solution to Maxwell's equations for a spheroid was first given by Asano and Yamamoto *[33]*, and an improved version was later given by Voshchinnikov and Farafonov *[34]*. The methodology is essentially the same as for Mie theory, but the fields are expanded in terms of spheroidal wavefunctions. Note that conversion of optical cross-sections to optical efficiencies is performed using the 'viewing' cross-sectional area (*i.e.* the shadow area) of the spheroid, and not that of an equivalent sphere *[35]*.

2.1.6 Particles with arbitrary geometry: the discrete dipole approximation

No analytical solutions exist for the case of absorption and scattering of light by particles of arbitrary shape. Instead, numerical methods must be employed, for example the discrete dipole approximation (DDA). The DDA approximates a solid particle (or particle distribution) as a 3D lattice of polarisable point dipoles *[36, 37]*. In the ideal limit each dipole represents a single atom of a given particle, but this is computationally impractical for all but the smallest particles and so a lower number of dipoles must be used. This is the only approximation made, as scattering and absorption properties of an array of dipoles can be calculated exactly. No implicit restriction on grid geometry is made by DDA, but significant speed gains can be achieved by use of a cubic lattice due to the use of a Fourier transform solver. Additionally, there is no restriction on which lattice sites do or do not contain a dipole, and therefore particle distributions can also be modelled.

We consider a lattice of D dipoles, each with position $\boldsymbol{r}_i$ and polarizability α_i, with $i = 1, 2, \dots, D$. Each dipole moment, $\boldsymbol{P}_i$, is determined by:

$$\boldsymbol{P}_i = \alpha_i \boldsymbol{E}_{loc,i} \tag{2.18}$$

Where $\boldsymbol{E}_{loc,i}$ is the local field at $\boldsymbol{r}_i$, *i.e.* at dipole i. This field is the sum of the incident field $\boldsymbol{E}_{inc,i}$ and the field resulting from moments of the other dipoles ($\boldsymbol{P}_j$) in the lattice, $\boldsymbol{E}_{other,i}$. The self-consistent solution for dipole moments $\boldsymbol{P}_j$ satisfy a system of $3*D$ linear equations, defined by the interaction matrix $\boldsymbol{A}_{ij}$. Therefore the field at dipole i is given by:

$$\boldsymbol{E}_{loc,i} = \boldsymbol{E}_{\mathrm{inc},i} + \boldsymbol{E}_{\mathrm{other},i} = \boldsymbol{E}_0 \exp(i\boldsymbol{k}\cdot\boldsymbol{r}_i - i\omega t) - \sum_{j\neq i} \boldsymbol{A}_{ij}\cdot\boldsymbol{P}_j \tag{2.19}$$

Where $\boldsymbol{k}$ is the wavevector and may be complex. Solutions to the interaction matrix are found by iteration, and are evaluated using a fast Fourier transform (FFT) technique in the case of a cubic lattice. The polarizability of each dipole, α_i, can be found by the Clausius-Mossotti relationship, but this is only strictly valid for an infinite lattice with interdipole spacing tending to zero. Instead, Draine and Goodman introduced the Lattice Dispersion Relationship (LDR) to calculate dipole polarizability *[38]*. In short, LDR equates the dispersion of an infinite lattice of polarisable dipoles to the dispersion of a continuum of material with properties defined by the bulk material dielectric function. Once the polarizabilities of each dipole are known the optical cross-sections can be calculated:

$$C_{abs} = \frac{4\pi k}{|\boldsymbol{E}_0|^2} \sum_{j=1}^{D} \left[\mathrm{Im}\{\boldsymbol{P}_j\left(\alpha_j{}^{-1}\right)^* \boldsymbol{P}_j^*\} - \frac{2}{3}k^3 \left|\boldsymbol{P}_j\right|^2 \right] \tag{2.20}$$

$$C_{ext} = \frac{4\pi k}{|\boldsymbol{E}_0|^2} \sum_{j=1}^{D} \mathrm{Im}\{\boldsymbol{E}_{inc,j}^* \cdot \boldsymbol{P}_j\} \tag{2.21}$$

$$C_{sca} = C_{ext} - C_{abs} \tag{2.22}$$

Although each lattice element is only capable of supporting dipolar excitation, the array of elements is capable of supporting higher order oscillations as retardation effects are included in the calculation.

Accuracy of cross-sections calculated by DDA is defined by the number of dipoles, D, and the corresponding interdipole spacing, d. However, computation time scales with D and so the number of dipoles cannot be arbitrarily large. In practice, results are accurate to within 10% provided the following condition is met:

$$|m|kd \leq 1 \tag{2.23}$$

Where m is the relative refractive index of the particle, k is the wavevector and d is the interparticle spacing. Additionally the interparticle spacing must be small enough to adequately describe the particle shape. This is of particular concern for curved geometries, which can only be approximated by a step variation of dipoles when a cubic lattice is used. In general, at least 10,000 dipoles must be used to suitably calculate the optical response of simple metallic particles to visible light. Definition of target geometry by an insufficient number of dipoles results in erroneous oscillations in the calculated spectra *[39]*.

The target geometry defined by the dipole array is constrained only by the cubic grid and the computational time. Complex targets consisting of multiple particles, inhomogeneous materials or complex shapes can be modelled equally well. Computational constraints currently limit the practical number of dipoles in a simulation to around 500,000, which roughly corresponds to a maximum simulation volume of 1 μm^3 for metal structures at visible wavelengths. The restriction of a cubic grid also results in a staircase approximation of the near-field values close to the particle surface, but the far-field properties can still be considered accurate *[24]*.

2.1.7 Other methods for particles with arbitrary geometry

Although we have focused on the DDA, a wide variety of other numerical electrodynamics modelling methods exist that can calculate the optical properties of arbitrarily-shaped metal nanoparticles. Solutions to Maxwell's equations can be found in the time domain or frequency domain, using either differential equations or integral equations. By discretizing either the boundaries between objects (*i.e.* surface discretization) or the entire target volume, approximate solutions to these equations can be found by iterative methods. Discretization of the sample geometry results in a trade-off between accuracy and computation time. Correct modelling of the intense and exponentially decaying fields around metal nanoparticles requires extremely fine grid size, and a correspondingly sizeable computational effort. Additionally each unit cell must be substantially smaller than the incident wavelength, and able to accurately describe the smallest geometry in the target. A wide variety of numerical methods suitable for electromagnetic simulations exist. Each approach has advantages and disadvantages in terms of solution time, total memory requirements, flexibility of geometry definition and accuracy. Brief reviews of the topic are given by Wriedt for the case of dielectric particles (although most of the discussed methods are also applicable to metallic particles) *[40]*, and by Veronis and Fan for the case of metallic particles (Chp. 12 in *[18]*). Here we present short descriptions of three considerably different approaches to modelling the electrodynamic behaviour of metal nanoparticles.

The generalized multipole technique (GMT) is a surface discretization method based in the frequency domain *[41]*. In Mie theory the internal and external fields are described by the expansion of spherical harmonics with their origin at the centre of the sphere. The GMT also describes fields by expansion of multipoles, but these need not be spherical and can have arbitrary (*i.e.* not concentric) origin. The total fields are found by calculating the superposition of all multipoles. As with Mie theory each expansion contains a series of unknown coefficients which must be calculated by application of boundary conditions. The boundary conditions contain information on the dielectric properties of the materials in the model. Therefore the multipoles effectively discretize the boundaries between different materials, enabling calculations of complex geometries. The GMT features a high degree of freedom in the choice of multipolar functions and their position, but this also adds substantial modelling complexity. In particular, optimum placement of multipoles is not an intuitive process. One popular implementation of the GMT is the multiple multipole method (MMP) *[42]*. To study metal nanoparticles using MMP, the target is defined using multipoles positioned outside the particle to describe the internal field, and multipoles positioned within the particle to describe the external fields. Good progress has been made in developing automated multipole positioning algorithms for 2D geometries *[42]*, but a sufficiently fast 3D implementation has not yet been developed.

The finite-element method (FEM) is a volume discretization approach that is usually based in the frequency domain (and hence sometimes referred to as the finite-element frequency-domain method) *[43]*. FEM is a method of solving partial differential equations (PDEs) for complex geometries, and is extensively used in mechanical engineering simulations. Recently interest has grown in using FEM for electromagnetic simulations. The principle advantage of FEM is in the flexibility of discretization, where the size and shape of the unit elements can be varied across the sample volume. Triangular or tetrahedral elements are most often used. Field values are then found at the nodes or edges of each element. In comparison with techniques constrained to cubic discretization, FEM models provide better definition of complex (*e.g.* curved) boundaries. Additionally, the calculation matrix produced during FEM analysis is sparsely populated due to the locality property of PDEs, resulting in lower memory requirements than many other volume discretization approaches such as those based on integral methods. However, the mesh cannot be infinitely large and so a method to truncate or close it is required. Essentially this requires a condition that enables far-field field radiation to leave the mesh with minimal alteration of near-field values. Exact mesh truncation schemes result in a completely filled calculation matrix, and so substantially increase memory requirements *[43]*. Instead, approximate truncation schemes based on absorbing boundary conditions (ABCs) are often used to limit reflection at the mesh extremities while maintaining a sparsely populated matrix. The overall calculation process in FEM is more complex than many other methods, but potentially more accurate due to improved geometry definition.

In the finite-difference time-domain (FDTD) method both volume and time are discretized *[44]*. In finite-difference methods the solution is found by approximating derivatives with finite differences that relate the value of the field at a specific node to its neighbouring nodes. In the FDTD technique, finite-difference approximations are used to evaluate both the spatial and the temporal derivatives. First the target geometry is discretized into Yee cells, which are cubes composed of equal numbers of E and H components, arranged such that each E or H component is surrounded by four corresponding H and E components. Each cell can have distinct material properties (*i.e.* inhomogeneous materials can be modelled), and no boundary conditions are required between cells. However, as with FEM, absorbing boundary regions are required at the extent of the simulation volume to limit spurious reflection of the wave *[45]*. Alternatively, periodic boundary conditions can be used to model infinite arrays of particles (Chp. 13 in *[44]*). Once the geometry has been discretized, the solution is found by time-stepping until convergence is reached. Time-stepping is achieved by a 'leapfrogging' process: in one time step the E components are calculated based on the previous step's H component values, and *vice versa*. In contrast to other techniques, the near-field region around a particle must also be discretized, leading to an increase in the computational domain size. Additionally, in frequency-domain techniques experimentally derived dielectric constants can be used directly, but in time-domain techniques an analytical model is required. Lorentz-Drude models give a good match to experimental data for many applications, but large deviations from experimental data occur near the interband regions of the noble metals *[15]*. However, no matrix calculation is required for FDTD as each element only interacts with neighbouring elements, and a complete set of frequency results can be found by deconvolving the response to a single impulse.

2.1.8 Methods for multiple particles

Most experiments consist of multiple particles, and so the electrodynamic coupling between particles must also be considered. We must consider both the intense near-field coupling between pairs of particles, and the complex multiple scattering events that occur in extremely large arrays of nanoparticles. Near-field coupling between small numbers of particles is well treated by most numerical techniques, such as those described in the previous section. However, modelling the optical response of a large array of nanoparticles is more challenging, and is most appropriately modelled by analytical methods.

Bruning and Lo presented an analytical solution to the problem of scattering by multiple spheres, which we refer to as the translational addition method *[46]*. In this method the scattered field of a group of particles is taken to be the superposition of the scattered field of each particle. Importantly, the scattered field of each particle is calculated including effects of the scattered fields of all other particles. In the case of spherical particles the scattered field of a given particle is calculated using the Mie theory approach of expansion of multipoles at the sphere centre, and the fields arising from all other spheres are included by transposing their multipolar expansions using translational addition theorem. This approach is commonly implemented within the framework of the T-matrix method *[47]*, and is often confusingly referred to directly as the T-matrix method *[48, 49]*.

The coupled dipole approximation (CDA) is a simplification of the translation addition approach where only dipolar excitation is considered. The polarizability of each dipole can be found by the quasistatic approximation, including modifications for large or ellipsoidal particles if required *[39]*. CDA calculations are much faster than the full T-matrix approach, but only strictly valid for small particles. The CDA can be used to model the optical properties of extremely large numbers of arbitrarily arranged particles. However, for large particles or small interparticle separations the CDA does not provide accurate results *[47]*.

The available computational domain in FEM or FDTD is restricted by memory requirements, and this currently limits simulations to a small number of particles. Large distributions can be modelled by imposing periodic boundary conditions on a sample area containing a single particle or a small number of discrete particles. However, large arrays of aperiodically arranged nanoparticles cannot be modelled using these approaches.

2.1.9 Simulation summary

While full Mie theory simulations were once considered computationally demanding, modern computers can usually process a single wavelength calculation in fractions of a millisecond. Therefore, approximations such as the quasistatic approximation are no longer required for quantitative studies of isolated particles, and should only be used to provide a qualitative description of the optical properties of small metal nanoparticles. Mie theory is capable of simulating the optical properties of metal particles with diameters ranging from a few nanometres to many micrometres. Extensions to Mie theory enable calculation of the optical properties of coated spheres and spheroids. In all cases, the particle material must be homogenous and the embedding medium non-absorbing.

Full analytical solutions do not exist for more complex particle geometries, and so numerical methods must be used in these cases. Numerical techniques are based on surface and volume discretization, and are considerably more computationally demanding than analytical methods due to the need for extremely fine mesh sizes to model the rapidly changing fields associated with metal nanoparticles. In addition to the theoretical differences between each approach, the quality and cost of available implementations must also be considered. Currently DDA offers the most direct and intuitive method for obtaining far-field optical properties of arbitrarily shaped metal nanoparticles, and a robust implementation is freely available. However, complex environments such as substrates and multiple particle interactions are difficult to model using DDA.

2.2 Fabrication of metal nanoparticles

Metal nanoparticles have been made since ancient history. One famous example is the fourth century Lycurgus cup, which features a curious optical property: in reflected light it appears green, but in transmitted light it appears red (Fig. 2.3a,b) *[50]*. Recent TEM studies revealed metal nanoparticles embedded in the glass are responsible for the colouring (Fig. 2.3c) *[51]*. The nanoparticle sizes range from 20 to 100 nm, and most are made of alloyed Au and Ag. Very few other dichroic Roman glasses exist, suggesting that the fabrication process was not well understood at the time. Although there are many other examples of Roman and medieval coloured glass, these are due to metal compounds or oxides and not metal nanoparticles. It is now understood that the nanoparticles in the Lycurgus cup were formed by precipitation from the glass melt, as evidenced by the relatively high non-particulate Ag content of the glass. The addition of Ag and Au to the glass mix may have been accidental, or part of a more traditional colouring method. The technique does not seem to have outlasted the fourth century, and was not again rediscovered until the seventeenth century with the invention of ruby glass. Unlike the Lycurgus cup process, the ruby glass process was well understood and widely used, particularly in Victorian times. Another form of metal nanoparticle, colloidal Au solutions were known from around the fourth or fifth century B.C. (as ‘potable gold’). Later uses included the colouring of ceramics and fabrics, for example the seventeenth century dye known as purple of Cassius. However, it was not until the nineteenth century that cause of the colour of ruby glass and purple of Cassius was attributed to the size of the gold particles.

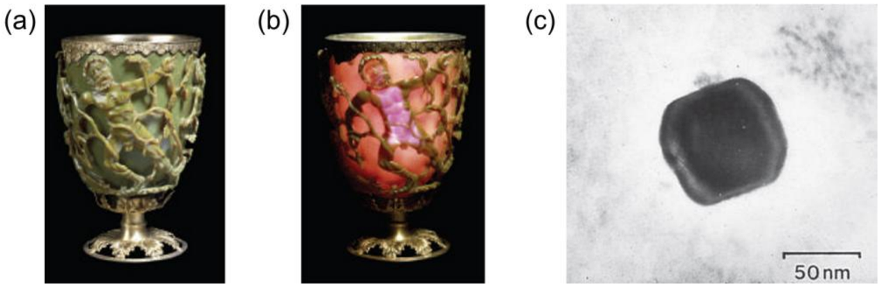

Figure 2.3: Photograph of Lycurgus cup (a) illuminated from the front (reflected light), and (b) from behind (transmitted light) *[50]*. (c) TEM image of Au-Ag nanoparticle embedded in glass from the Lycurgus cup *[51]*.

In recent decades research into metal nanoparticles has greatly intensified. This is largely due to the development of improved fabrication processes which enable precise control over nanoparticle size and shape, and therefore precise control over optical properties. Additionally, metal nanoparticles can now be made in large quantities at low cost, therefore expanding the range of possible applications. A full overview of modern metal nanoparticle fabrication processes is far beyond the scope of this thesis. A bewildering array of fabrication methods exist, ranging from the simple annealing of a thin film to exotic methods such as fungus-mediated synthesis *[52]*. Additionally, most methods receive frequent refinements and additions, making a detailed overview a daunting task. Instead, we aim to give a brief introduction and overview to the three principle families of metal nanoparticle fabrication processes: chemical synthesis, metal film islanding and lithography. In particular we focus on methods for producing submonolayers of metal nanoparticles on flat semiconductor and oxide substrates, as these are of principle interest for studies concerning silicon solar cells.

2.2.1 Chemical synthesis

Metal colloids, also known as sols, are metal nanoparticles suspended either in water (hydrosols) or organic solvents (organosols). Metal colloids are typically prepared from a metal solution by controlled precipitation (*i.e.* nucleation of metal crystals) and concurrent stabilization. Stabilization is necessary to prevent aggregation of the nanoparticles due to van der Waals attraction, and can be achieved using coatings that limit particle interaction through electrostatic or steric mechanisms (Fig. 2.4). In the classic Turkevich method metal nanoparticles are prepared by sodium citrate reduction of gold chloride (or silver nitrate) in solution, and stabilization is achieved by a self-forming negatively charged bilayer on the nanoparticle surface *[53]*. This layer is formed of citrate and chloride ions and provides a repulsive force between nanoparticles that limits aggregation. Nanoparticles prepared using the Turkevich method are typically 20 nm in diameter and exhibit low polydispersity. The more recent Brust-Schiffrin method makes used of steric stabilization by covalently bound thiol or other sulphur-containing monolayers, and offers several advantages such as improved stabilization and convenient routes to functionalization *[54]*. The method is more complex than the Turkevich method, involving a two-phase system and separate reduction in the presence of thiol ligands. The resulting nanoparticles are considerably smaller (1 – 3.5 nm) and have a narrower size distribution. Thiol-stabilized nanoparticles are air-stable and can be removed from one solvent and re-dispersed in another without any permanent chemical or structural change. In addition to thiol ligands, other steric stabilization methods based on polymers have also proved successful, such as polyvinyl pyridine (PVP) *[55]*. Extremely thick (60 – 70 nm) silica coatings were found to greatly improve the thermal stability of Au nanoparticles *[56]*.

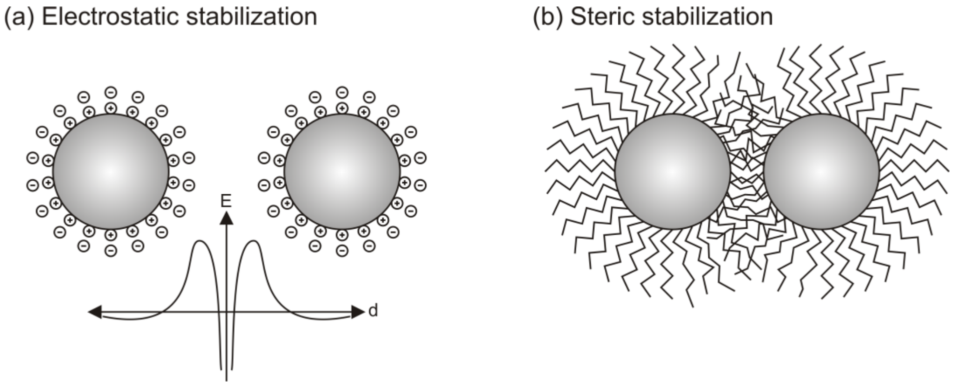

Figure 2.4: Schematic representation of (a) electrostatic stabilization, (b) steric stabilization (adapted from *[57]*).

Au and Ag are the most commonly studied metals for chemical synthesis, but nanoparticles of a wide range of other metals can also be synthesized, often using analogous methods. For example, Au, Ag, Cu and Pt nanoparticles can all be synthesized by the reduction of their corresponding metal salts by tetrakis(hydroxymethyl)phosphoniumchloride (THPC) *[58-60]*. Reduction by tetraalkylammonium hydrotriorganoborates provides a more general purpose synthesis route, and is applicable to a wide range of metals *[57]*.

The size of synthesized metal nanoparticles is determined by the relative rates of nucleation and particle growth, which are in turn determined by the temperature, pressure, reducing agent, solvent type, concentration and type of stabilizing agent, and the concentration and type of the metal-containing solution. Size-selective separation can be used to reduce polydispersity, and techniques include sieving *[61]*, centrifugation *[61]* and fractional crystallization *[62]*.

There is currently no accepted specific mechanism for the control of shape in chemically synthesized metal nanoparticles, but it is broadly due to selective growth of crystal facets *[63]*. The classical synthesis methods result in spheres or faceted-spheres, but a wide variety of other nanoparticle shapes have been produced by chemical synthesis. These include rods, platelets, cubes and multi-branched particles. Almost all methods are based on a process known as seed-mediated growth, where a colloid of small, uniform nanoparticles is first produced before a second growth process modifies these ‘seeds’. Two separate processes are needed because the conditions required for nucleation of nanocrystals are very different to those required for selective facet growth. Crystal nucleation is a fast process occurring in a supersaturated solution, while shape-controlled growth is typically much slower and performed using substantially milder reducing conditions to limit additional nucleation.

After the synthesis procedure(s) the end result is a suspension of metal nanoparticles, *i.e.* a colloid. The colloid is stable for periods ranging from days to years after synthesis, depending on the stabilization method employed. Many applications rely on removing the nanoparticles from solution, which can be achieved in a variety of ways. Often the particles are assembled into 2D or 3D structures. For example, small (1 - 3 nm) Au nanoparticles have been shown to form complex superlattice structures when slowly precipitated from solvent by evaporation *[64, 65]*. The superlattice structures exhibit remarkable three-dimensional periodicity and can have length-scales of tens of micrometres.

Applications such as biosensing require a submonolayer of particles assembled onto a planar substrate such as glass or silicon. For these applications simple drop-casting from solution is unsuitable due to the poor adhesion of particles to the substrate, and aggregation of particles during the drying process. As we will discuss later, aggregation of particles changes their optical properties and so must be avoided. Instead, a range of immobilization methods have been developed based on electrostatic attraction and covalent linkers. As previously discussed, some methods of synthesizing metal nanoparticles result in the particles having a negative electric charge. Therefore, by coating a substrate with a positively charged polymer the negatively charged nanoparticles can be immobilized on the surface by electrostatic attraction. The charge of the polymer must be carefully controlled –too strong and the particle charge will be entirely screened, resulting in aggregation; too weak and the nanoparticles will not be immobilized. Polymers such as polyvinyl pyridine (PVP)*[66]* and poly-l-lysine (PLL) *[67]* have successfully been used to electrostatically immobilize metal nanoparticles on glass and silicon substrates. These polymers can be applied by simple procedures such as spin-coating, with the charge strength controlled by the thickness of the layer. Electrostatic immobilization is relatively weak, and so other forms of immobilization based on covalent bonds are preferable for many applications. To achieve this we require a linker polymer that has functional head and tail groups with high affinity for the substrate and nanoparticle material, respectively. Certain types of organosilanes are well suited to this role, and a good overview on this topic is given by Grabar *et al. [68]*. Exposing a substrate coated in a self-assembled monolayer (SAM) of organosilane to a gold colloid results in the formation of a dense, self-limiting sub-monolayer of metal nanoparticles on the surface (Fig 2.5) *[69]*. The nanoparticles are firmly bound and remain adhered despite repeated rinsing and organic solvents. The density of the nanoparticle array is controlled by the duration of the exposure to the colloid. Saturation occurs at around 30% surface coverage due to repulsion of nanoparticles in the liquid by the charged particles already bound to the substrate, which also minimizes aggregation. Higher density arrays can be fabricated by partially screening the particle charge using organic adsorbates *[70]*.

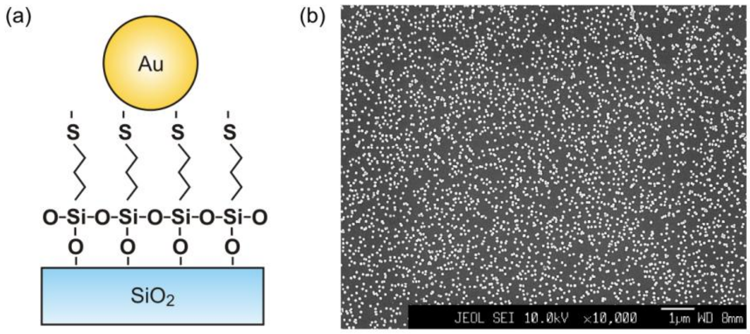

Figure 2.5: (a) Schematic representation of Au nanoparticles immobilized on a SiO_2 substrated by a 3-MPTS SAM, (b) SEM image of immobilized Au nanoparticles (adapted from *[71]*)

The organosilane adhesion approach is also applicable to many different structural types of oxides and metal, for example to bond planar layers of Au to silicon *[72, 73]* and to immobilize silica nanoparticles on planar Au layers *[71]*. In an interesting variation of this technique, Oldenburg *et al.* synthesized Au nanoshells on silica cores using a novel multistep process *[74]*. Silica cores are synthesized (*e.g.* by means of the Stöber process) and then coated with an organosilane layer. The functionalized cores are then introduced to a solution of 1-2 nm diameter Au nanoparticles, which covalently bind to the surface. Saturation of the surface occurs at around 30% coverage due to electrostatic repulsion in a similar manner to assembly of submonolayers on planar substrates. The bound Au nanoparticles then act as nucleation sites for the reduction of gold chloride, eventually coalescing to form a continuous layer (Fig. 2.6). The geometry is flexible: the core diameter is controlled by the silica sphere synthesis process, and the shell thickness is controlled by the reduction process. Ag nanoshells have also been synthesized by similar methods *[75]*.

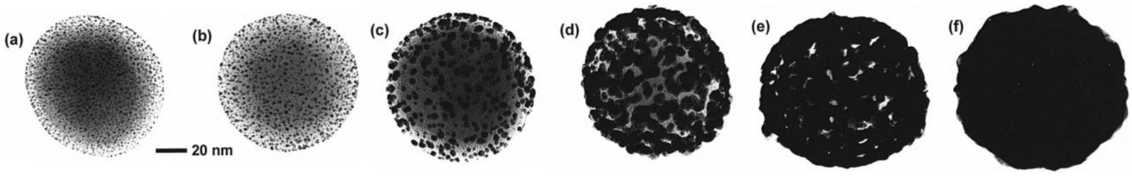

Figure 2.6: TEM analysis of core-shell formation (adapted from *[74]*).

2.2.2 Metal island films

Physical vapour deposition of metals leads to the formation of a continuous, planar layer of metal on a substrate. However, in the early stages of the deposition the film is not continuous. If the metal-metal binding energy is stronger than the metal-substrate binding energy then island (Volmer-Weber) growth occurs. Island growth continues until the percolation threshold is reached and the islands merge together, eventually forming a continuous film. Therefore metal nanoparticles can be formed by physical vapour deposition of very thin layers of metal. Such samples are often referred to as metal island films (MIFs). The thickness of an island layer is quantified by the "effective mass thickness", *i.e.* the thickness of a planar layer of metal with the same mass as the island layer. Metal island films can be fabricated using a variety of vapour deposition techniques including thermal or e-beam evaporation, and DC or RF sputtering. Large-area (200 mm wide, variable length substrate) metal island films have been fabricated by reel-to-reel sputtering onto a flexible substrate *[76, 77]*. The percolation threshold is determined by the metal used and a number of process parameters including deposition speed, substrate type, substrate temperature and chamber pressure.

Along with the percolation threshold, the average particle size, shape and surface coverage are also determined by process parameters *[78]*. Analysis of particle features can be achieved using automated software, for example using the open source program ImageJ program. Useful particle parameters include: area, equivalent diameter, circularity and aspect ratio. The equivalent diameter of a particle is the diameter of a circle with identical area. Circularity (also known as shape factor) is a measure of the 'compactness' of a shape, and is calculated using $C = (4\pi * \text{area}) / \text{perimeter}^2$. A circle has a circularity of unity, while a long thin shape has a circularity approaching zero. Aspect ratio is often taken as the ratio of the shortest diameter to the longest, resulting in values ranging from near zero to unity. Study of the statistical variations of particle parameters gives insight into the growth mechanisms and optical properties of a metal island film.

Metal island films are not thermally stable immediately after deposition, and morphological changes can be induced by thermal treatments *[79]*. Pronounced and often dramatic changes in average particle size, shape and surface coverage occur by atomic diffusion. The process is known as recrystallization for individual particles, and coalescence if multiple particles join together (Fig. 2.7). Although a minor decrease in melting temperature compared with bulk values is found for small (< 10 nm diameter) metal nanoparticles *[80]*, recrystallization and coalescence processes occur at temperatures far below the bulk melting temperature and so melting is not responsible for these processes. Indeed, HRTEM analysis of nanoparticles undergoing e-beam induced coalescence confirms that crystal structure is retained throughout the process *[81]*. Thermal-induced shape changes are therefore due to atomic diffusion along the particle surface and grain boundaries. Additionally, atoms can move across the surface through surface diffusion. Different sources of thermal energy can be applied, including furnace heating, laser irradiation and electron beam irradiation *[82, 83]*. Of these, furnace heating is most suitable for achieving large area coverage of metal nanoparticles. Laser irradiation is more often used to selectively pattern metal island layers, and electron beam irradiation is useful for TEM in-situ studies of morphological changes. Thermal stability is greatly improved for metal nanoparticles embedded in a solid matrix, *e.g.* for island films over-coated with a dielectric layer.

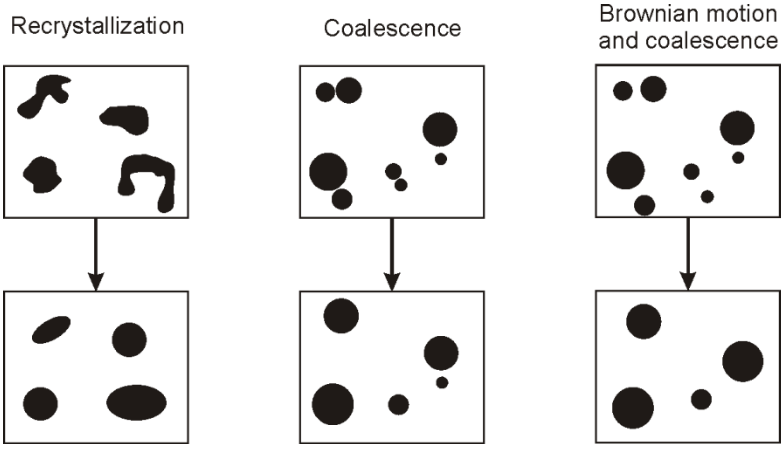

Figure 2.7: Representation of three possible reshaping processes (adapted from *[81]*).

Heilmann studied the effect of a 15 minute, 273^{o}C post-deposition vacuum anneal on Ag island films embedded in a polymer layer *[81]*. The Ag film mass thickness was varied for different samples and comparisons were made between TEM images of as-deposited and annealed films. In all cases thermal treatment resulted in a reduction of surface coverage, an increase of the mean particle diameter, and an increase of the mean circularity. The mean diameter increased with increasing mass thickness of the film, and values ranging from 16 nm to 46 nm were obtained. The largest change in circularity was observed for the thickest film, with a change from 0.52 as-deposited to 0.70 after annealing. Dalacu *et al.* observed similar trends for Au films on SiO_2, with a 5 hour 250^{o}C post-deposition anneal *[84]*. The obtained particle size increased with increase mass layer thickness, and the resulting nanoparticle distributions were found to have mean diameters ranging from 2.4 nm to 6.9 nm. Near unity values for mean circularity and aspect ratio were found for all samples. In both of these experiments variation in mass thickness was obtained using a relative gradient approach, and so exact values for mass thickness were not known. Suzuki *et al.* studied the effect of mass thickness and anneal temperature for Ag films on silicon substrates *[85]*. Although particle size and shape analysis was not performed, SEM images show a clear evolution of film morphology with increasing mass thickness (Fig. 2.8). As the layer mass thickness is increased the nanoparticles become large and more irregularly shaped. Percolation is achieved between 6 nm and 7 nm, after which the film shows a semi-continuous or porous structure. The films were annealed in a vacuum furnace for 1 hour at temperatures ranging from 100^{o}C to 300^{o}C. Surface coverage decreases and circularity appears to increase with increasing anneal temperature (Fig. 2.9).

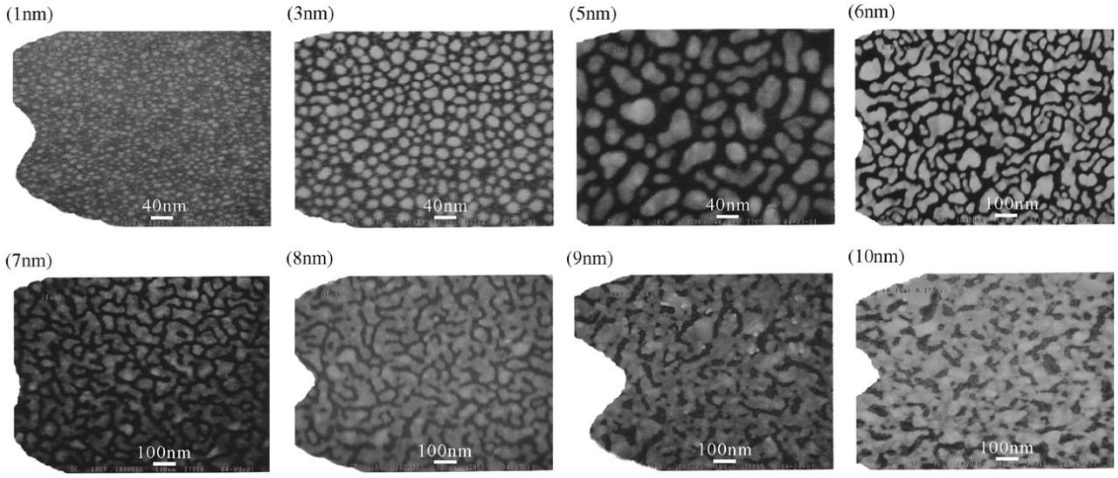

Figure 2.8: SEM images of as-deposited Ag films on Si substrate with increasing mass-thickness *[85]*.

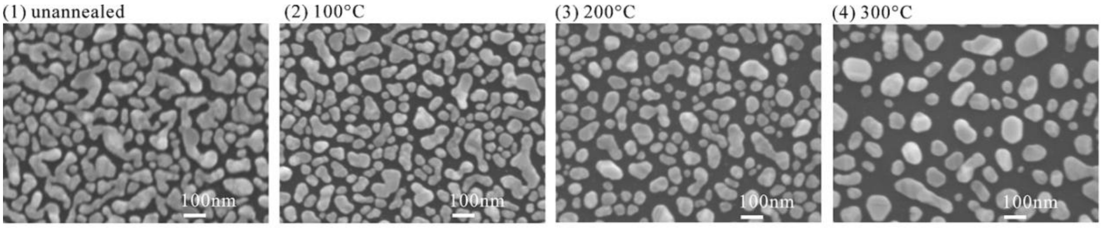

Figure 2.9: SEM images of 6 nm mass thickness Ag film, annealed for 1 hour at high vacuum *[85]*.

The substrate material also plays an important role in nanoparticle formation. Kalyuzhny *et al.* investigated the properties of Au island films on quartz and mica subtrates *[86]*. Au was evaporated on both substrate types simultaneously, ensuring that any differences were due to substrate effects only. A 250^{o}C anneal was performed for either four or twelve hours after deposition. The standard deviation of particle diameter was found to be consistently smaller for islands on the quartz substrates, and the average diameter was found to be larger compared with islands on mica. Often quartz and silicon are treated as identical substrates with respect to islanding processes, due to the thin native oxide present on silicon. However, while this may be true during deposition at ambient temperatures, clearly the different thermal properties of each substrate will affect any heating processes. Gupta *et al.* simultaneously produced Au island films on quartz and silicon substrates, and studied the particle geometries using AFM for quartz and SEM for silicon *[87]*. Differences in apparent particle size between the two methods were ascribed to AFM tip-broadening effects and not to substrate effects. However, this is erroneous, as in many images the nanoparticles on silicon (*i.e.* those imaged using SEM) appear larger than the corresponding nanoparticles on quartz (*i.e.* those imaged using AFM). Therefore, metal island films fabricated on quartz and silicon substrates cannot be assumed to be identical. Morphological differences have also been observed between films deposited simultaneously onto glass and Formvar *[88]*. To further investigate the role of the chemical properties of the substrate, Malynch and Chumanov varied the chemical affinity of ITO surfaces prior to deposition of an ultrathin Ag film. Substantial changes in morphology were observed, particularly for films below the percolation threshold *[89]*. Increasing the surface affinity by coating the substrate with PVP or thiol groups resulted in a denser array of smaller nanoparticles compared with the unmodified sample. This is most likely due to a decrease in surface diffusion due to the increase in surface affinity. Reducing the surface affinity by modifying with fluorocarbon also resulted in smaller nanoparticles, but the density was lower, suggesting that this sample had a lower mass thickness than the others. This could be due to the extremely low adhesion of Ag to fluorocarbon-modified surfaces. The authors also note that quartz microbalances used for in-situ determination of mass thickness may not be reliable for ultrathin films due to differences in surface adhesion between the substrate and the microbalance. Although alternative mass thickness measurement techniques can offer higher accuracy they are usually ex-situ and destructive *[90]*.

The texture of a substrate can also affect nanoparticle formation. Heilmann observed that island films formed on textured polymer layers exhibited a larger standard deviation in diameter than those formed on flat polymer layers *[81]*. In particular, it was noted that larger nanoparticles form on the 'hills' compared with the 'valleys'. This was ascribed to shadowing effects, resulting in less material being deposited in the valleys and therefore small nanoparticles. Oates *et al.* deposited an Ag island film on 'rippled' silicon substrates, with a texture period of around 35 nm and an average amplitude of 3 nm. For this geometry preferential growth occurs in the valleys; due the small peak height shadowing does not occur and growth is instead mediated by minimization of surface energy. Nanoparticles can also affect the morphology of the substrate during annealing. Karakouz *et al.* observed greatly improved adhesion of an Au island film to glass when annealed near the glass transition temperature *[91]*. The increased adhesion was found to be due to partial embedding of the nanoparticles in the glass. Acid removal of the nanoparticles revealed a series of depressions on the glass surface that was formed by the nanoparticles during annealing.

The role of deposition speed on nanoparticle formation is complex and not yet fully understood. Schelegel and Cotton studied the effect of varying deposition speed from 0.003 nms^{-1} to 0.5 nms^{-1} when evaporating a 5 nm Ag film *[92]*. TEM analysis revealed the slowest deposition speed resulted in isolated, well-defined nanoparticles, and increasing the deposition speed resulted in gradually less well-defined, more closely-spaced nanoparticles. The authors explained this effect in terms of atom migration time: for faster evaporation rates surface diffusion of atoms can be disrupted by arrival of additional atoms, resulting in shorter migration times. However, in a similar experiment Van Duyne *et al.* investigated deposition speeds from 0.05 nms^{-1} to 2.0 nms^{-1}, and found no strong difference in the resulting film morphology *[93]*. They attribute the differences to variation in equipment geometry, and the potential role of radiative heating during longer deposition runs. Results from an experiment by Semin and Rowlen to resolve this disparity resulted in similar qualitative results as Schelegel and Cotton *[94]*. The authors note that the most dramatic influence of deposition speed occurs for rates below 0.05 nms^{-1} (*i.e.* below that studied by Van Duyne *et al.*), and also that a small increase in substrate temperature during deposition can effect the resulting film properties. In a recent study Rakocevi *et al.* investigated the surface roughness of Ag films sputtered on glass as a function of deposition speed *[95]*. Film thicknesses ranging from 10 nm to 80 nm and deposition rates ranging from 0.0225 nms^{-1} to 2.6 nms^{-1} were investigated. Roughness measurements were made using a scanning tunnelling microscope (STM). For each thickness the roughness initially decreases with increasing deposition speed until a minimum occurs, after which the roughness increases with increasing deposition speed. Interestingly this leads to the case where pairs of deposition speeds either side of minimum result in the same surface roughness.

The three-dimensional structure of nanoparticles fabricated by metal film islanding has been studied by cross-sectional TEM and AFM. Studies report an oblate spheroid or spherical shape for annealed nanoparticles, as would be expected for minimization of surface energy *[81, 96]*. Kawasaki and Hori inferred nearly spherical shape from AFM images for all particle sizes after exposure to nanosecond laser irradiation *[97]*. Prior to laser irradiation the film comprised a dense array of oblate nanoparticles. The authors estimate that heating by the laser lead to instantaneous temperatures above the melting point of the metal, giving a possible explanation for the extremely well-formed spheres. Further increase of laser fluence lead to ablation of the film. Eurenius *et al.* also used laser irradiation to modify the morphology of an Au island film, but in their experiment the film was deposited on a Si_3N_4 membrane, and the resulting thermally-induced change in morphology exhibited a periodic pattern *[98]*. This was due to interference of the incident beam and a component of the beam scattered in the membrane, resulting in a periodic variation of beam intensity along the membrane.

Although Au is most widely studied material for island films, islands of many other metals have also been prepared. Stuart and Hall fabricated Au, Ag and Cu island films by evaporation and annealing *[14, 99]*. The annealing stage was substantially shortened for the Cu film, to limit oxidation. No microscopy studies were carried out to assess the size and shape of the nanoparticles, but transmission spectra showed clear resonant behaviour, demonstrating that isolated nanoparticles had been successfully fabricated in each case. Baba *et al.* fabricated alloyed Au/Ag metal island films using a two step deposition process and 300°C anneal *[100]*. Each metal was deposited separately, and the mixture ratio defined by the mass thickness of each layer. In a separate study the authors observed a change in particle morphology as the mixture ratio was changed *[101]*. For the same mass thickness, nanoparticles in an Au film were found to be more irregularly shaped than those in an Ag film.

Multilayered films can be fabricated by alternating deposition of metal and dielectric layers, resulting in metal island layer films (MILFs) *[102]*. Surface conformation decreases with intermediate layer thickness, and so a flat surface can be created for deposition of the next layer provided a thick enough dielectric spacer layer is deposited. More complex 3D distributions are also possible, for example Biswas *et al.* demonstrated that a fractal percolation network of Ag nanoparticles embedded in Teflon can be achieved by simultaneous evaporation of both materials *[103]*.

2.2.3 Electron-beam lithography

Electron-beam lithography (EBL) offers unrivalled control and repeatability of fabrication of sub-monolayers of metal nanoparticles on flat substrates. In brief, the lift-off process involves the following (Fig. 2.10). First, a thin layer of resist is spun-coat onto the substrate. An electron beam is raster- or vector-scanned across the substrate, selectively exposing areas of the resist. The pattern is defined using computer-aided design (CAD) software, which is then converted to beam control instructions. After development the resist is left patterned with holes of the desired size and shape, thereby selectively exposing the substrate. Physical vapour deposition, usually electron-beam evaporation, is used to deposit a planar layer of metal onto the patterned resist and substrate. A chemical etch is then used to selectively remove the resist layer. Provided the metal layer is thinner than the resist layer, the chemical etch can attack the resist underneath the metal layer through the sidewalls, thereby lifting-off the unwanted metal and leaving only the required pattern. Typical resists include PMMA, ZEP520 and UVIII. Sensitivity and etch-resistance are important considerations when choosing a resist. Sometimes a dual resist layer is used to achieve an ‘over-hang’ profile after patterning, which improves lift-off yield. However, intermixing between resist layers and a complex exposure process limit the usefulness of this technique. A thin layer of Cr or Ti is often deposited prior to Au or Ag deposition to improve adhesion to the substrate, which is particularly important during the lift-off process. Sharp edges in a pattern design are rounded due to electron-scattering. Scattering of electrons also results in low-dose exposure of resist outside of the scanned area, known as the proximity effect. This can lead to overexposure of adjacent features if the dose profile is not corrected. Lithographic techniques are capable of producing nanoparticles using a wide variety of metals, with precisely controlled size, shape and position. However, lithography is generally restricted to planar geometries.

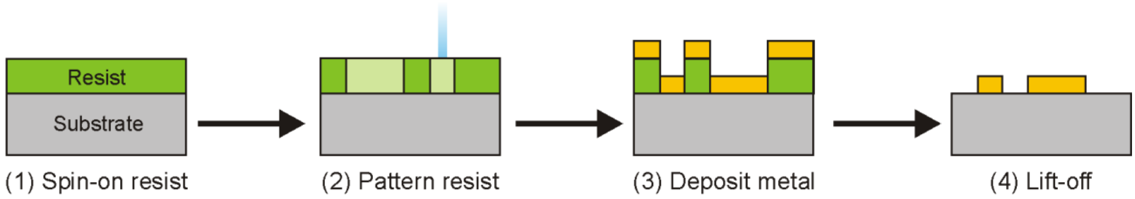

Figure 2.10: Schematic representaiton of EBL lift-off process.

EBL with conventional lift-off is restricted to the fabrication of prisms with a constant cross-section and constant height across all nanoparticles. The maximum height of the nanoparticle (*i.e.* the thickness of the metal layer) is limited to a fraction of the resist thickness, which is usually around 100 – 300 nm thick. Arrays of nanoparticles with circular, triangular and rectangular (rod-like) cross-sections fabricated by EBL are frequently reported *[104-107]*. To study the excitation of higher order modes, Krenn *et al.* used EBL to fabricate arrays of nanorods with aspect ratios ranging from 1:1 to nearly 13:1, for a constant rod width of 85 nm *[104]*. L-shape nanoparticles are of interest for their noncentrosymmetry, and have been fabricated and studied by Lamprecht *et al. [108]* and Canfield *et al. [109]*. The optical properties of subwavelength size split-ring resonators are of interest for biosensing and negative refractive index applications, and can be consistently fabricated by EBL *[110, 111]*. Heyderman *et al.* fabricated arrays of ferromagnetic nanorings (torii) but interestingly instead of a conventional raster scan, a vector scan was employed. The rings were exposed by tracing the beam around a single pixel wide loop, with the beam dose defining the ring thickness. EBL is also well suited for the study of interaction between two or more nanoparticles. Fromm *et al.* used EBL to study optical coupling between pairs of Au triangular prisms, with interparticle spacing down to 16 nm *[112]*. Recently, arrays of Au nanoparticles with gap sizes down to approximately 2 nm have been fabricated using standard lift-off techniques *[113, 114]*. Although there is no innate restriction to the structure of arrays produced by EBL, most experiments utilise square arrays, as these can be simply defined in CAD software as a single shape with a corresponding array period and size. Design of a pseudo-random array requires individual positioning of each nanoparticle.

EBL is a serial process and therefore inherently slow, limiting the size of fabricated arrays to the order of mm^2. Additionally, the required equipment is extremely expensive. This limits the use of EBL to research-based experiments. Other lithographic techniques have been developed to reduce the fabrication cost and time, although often at the expense of design flexibility.

2.2.4 Other lithographic techniques

Nanoimprint lithography (NIL) enables the replication of an EBL generated design *[115]*. In NSL, a mould patterned using EBL (or any other lithographic technique) is pressed into a thin layer of resist on the surface of a substrate. This imprint step leaves a pattern in the resist in the form of a thickness variation. RIE is then used to remove the thin areas of resist, and the layer can be used as a deposition mask, as with standard EBL-based lift-off. The resolution of pattern transfer is extremely high, and the mould can be reused repeatedly. Ordered arrays of metal nanoparticles have been fabricated by NIL *[116]*.

Many forms of low-cost lithography are based upon silica or latex nanospheres, which can be manufactured in large quantities with good monodispersity. Under the correct conditions, colloids of nanospheres spontaneously aggregate into highly ordered close-packed arrays. Assembly can be induced by drop-casting *[117]*, controlled evaporation, spin-coating and at a water/air interface *[118]*. Using this last technique Weekes *et al.* demonstrated assembly of arrays with defect-free areas over 1 cm^2 *[118]*. Hulteen *et al.*

showed that an array of assembled latex nanospheres can be used ask a deposition mask, to create a hexagonal array of nanotriangles, in a process known as nanosphere lithography (NSL) (Fig. 2.11) *[117]*. After metal deposition the nanospheres are removed by chemical etching or by simply using adhesive tape. NSL has been used to fabricate arrays of Au, Ag *[119]*, Cu *[120]* and Al *[121]* nanotriangles. The nanoparticle size and array period are defined by the nanosphere size, and so although some control is possible a choice of the full range of both parameters is not possible. Additionally, defects in the nanosphere array result in erroneous fabrication of large metal particles or stripes, which can swamp the overall optical properties of an array. In contrast with EBL, nanotriangles fabricated using NSL have exceptionally well-defined tips. Tan *et al.* showed that thermal annealing can be used to transform nanotriangles into nanospheres, with an intermediate stage of 'blunt-tipped' triangles *[122]*. Use of a double layer of spheres can also result in an array of circular nanodiscs *[123]*, although close-packed double layers are substantially more difficult to achieve over large areas than single layers. Microwave heating has been shown by Kosiorek *et al.* to increase the nanosphere size, leading to a reduction in the size of interstitial space and a corresponding reduction in the size of nanoparticles produced *[124]*. Tilting the substrate with respect to the physical vapour source results in formation of 'stretched' triangles and rod-like particles, depending on the tilt angle *[125]*. Murray *et al.* investigated the effect of isotropically etching the nanospheres prior to metal evaporation using O_2 reactive-ion etching *[126]*. Decreasing the nanosphere size resulted in an increase in nanotriangle size, which eventually resulted in merging of nanoparticles to form an array of circular holes in a continuous metal film.

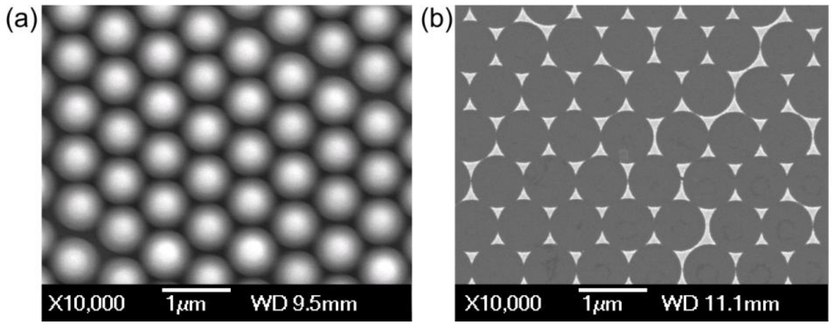

Figure 2.11: SEM images of assembled latex microsphere array: (a) before deposition of metal, (b) after deposition of 5nm Au layer and removal of spheres.

Many variations on NSL have been developed to produce a wider range of particle geometries and array structures. For example, the nanospheres can also be used as an etch mask when assembled onto a pre-deposited metal layer. The nanospheres are first isotropically etched in an O_2 plasma to reduce their size (and therefore increase the interparticle spacing) *[127]*, and then serve as an etch mask during anisotropic removal of the metal layer by ion-beam milling *[128]* or Ar reactive-ion etching *[129]*. In this way a periodic array of nanodiscs is formed, with the average nanodisc diameter determined by the duration of the O_2 etch. In an interesting variation of this technique, Aizpurua *et al.* demonstrated that etching a metal film deposited *after* deposition of nanospheres leads to re-deposition of metal around the sphere due to secondary sputtering, resulting in formation of nanorings *[130]*. A combination of angle-resolved metal deposition onto nanospheres and RIE etching can be used to create nanocrescents and nanorings. In this technique angled deposition leads to build-up of metal beneath the 'shadow' of the nanosphere, which is then masked by the nanosphere during ion-beam milling *[131]*. Interestingly, angle-resolved deposition also results in formation of discrete metal 'nanocap' particles on the sphere surface, which can be suspended in solution during dissolution of the nanospheres *[132]*.

The use of nanospheres as an etch mask rather than a deposition mask removes the need for the close-packed arrangement, and nanodiscs with random placement can be fabricated by means of sparse colloidal lithography (SCL) *[133]*. Fredriksson *et al.* further developed SCL into hole-mask colloidal lithography (HCL) by adding a layer of resist between the nanospheres *[134]*. The group demonstrated a wide variety of nanoparticle geometries by modifying various aspects of the fabrication process, including nanocones, nanoellipses and nanodisc binary pairs. Interestingly, as the nanodisc binary pairs are fabricated by a two stage angle-resolved deposition, the two particles can be made of different metals. As with all lithographic techniques, a wide range of metals can be used with HCL. Langhammer *et al.* used HCL to fabricate unordered arrays of Pt, Pd, Ag, Au and Al nanodiscs *[135, 136]*. However, the smallest nanodiscs were found to exhibit a high degree of polydispersity due to the non-uniform shape of nanospheres after long etch durations. Nanoparticles fabricated by lithography can also be made in a multi-layer fashion, for example the Au-SiO2-Au "nanosandwiches" fabricated by Dmitriev *et al.* using HCL *[137]*.

Large arrays (> 1cm^2) of metal nanoparticles can also be made by optical lithographic techniques such as extreme ultraviolet (EUV) interference lithography *[138]* and phase-shifting photolithography *[139]*. These techniques are relatively expensive and restricted to square arrays of nanodiscs, but offer the potential for large area coverage *[140]*.

Porous alumina membranes are made by electrochemical etching of aluminium, and contain a high density of similarly sized nanometer scale pores *[141, 142]*. The size and density of pores can be tailored by modifying the etch procedure, and both random and hexagonal array formations can be achieved *[143]*. Alumina membranes can serve as deposition masks, resulting in formation of nanodiscs or nanocones, depending on the pore size and deposited film thickness *[144, 145]*. Nanocones form due to shrinking of the pore size due to build-up of metal on the side-walls. Alumina membranes can also serve as growth templates during electrodeposition of metals, providing nanorods/nanowires with extremely high aspect ratios, both free-standing or in solution *[146]*. Tempalted electrodeposition is capable of producing far 'taller' structures than lithography, but requires a conductive substrate and full dissolution of the template. As with vapour-deposition, electrodeposition is not limited to a single metal type, and 'striped' nanorods with alternating layers of Au and Ag have been fabricated *[147, 148]*. Sander and Tan demonstrated the use of porous alumina templates as both lithographic masks and electrodeposition templates, achieving large area (> 1 cm^2), high density arrays of nanostructures with lateral dimensions ranging from 25 nm to 75 nm depending on etch and deposition conditions *[149]*.

Templating combined with lithography can also be achieved without membranes. Henzie *et al.* fabricated arrays of pyramidal nanoaprticles by evaporation into nanoscale pyramidal pits etched into silicon using the well-known KOH etch process *[139]*. The metal conformed to the silicon pit, resulting in well-defined pyramids with sharp tips. The same mask was used for etching and deposition, and the particles were released into solution by further etching of the silicon.

2.2.5 Fabrication summary

Metal island films are the least expensive and least complex methods for coating planar surfaces with dense arrays of metal nanoparticles. The average particle size can be varied over an extremely large range (nanometres to micrometres). However, the process requires a high vacuum and often high temperature annealing, limiting the range of substrates and metals that can be used. Additionally, a large distribution of nanoparticle size and shape is usually found, and the achievable shapes are limited to those ranging from the most thermodynamically favourable to highly irregular particles formed close to the percolation threshold.

In contrast, lithographic methods –particularly EBL– offer the most control over particle size, shape, composition and array structure. Lithographic methods are constrained by maximum array size and, in the case of EBL, the cost of the process. Large-area methods exist, but these offer substantially reduced geometry control. The minimum size of nanoparticles fabricated by lithography is limited to a few tens of nanometres, but maximum lateral size is unconstrained.

Chemical synthesis offers a good control of particle size and shape, does not require vacuum processing or high temperatures, and can be used to coat large areas. Growth mechanisms are still poorly understood for most processes and so bespoke nanoparticle design is not yet possible. Large nanoparticles are proving challenging to synthesise with high yields. However, unlike metal islanding and lithography, there appear to be no fundamental limitations to the improvement of chemical synthesis techniques.

2.3 Characterisation

2.3.1 Geometric measurements

The optical properties of metal nanoparticles are highly dependent on the particle size and shape, and the overall distribution of these attributes in a given sample. Metal nanoparticles can be often detected optically, but size and shape cannot be directly observed due to the diffraction limit. Instead, electron-beam or scanning-probe techniques can be used to quantitatively measure the size and shape of metal nanoparticles (Fig. 2.12). Although these systems are capable of myriad modes of operation, we limit our consideration to analysis of particle geometry.

Scanning electron microscopy (SEM) functions by raster-scanning an electron beam across the surface of a sample, and detecting the resulting emission of secondary electrons. An image is formed by creating an intensity map of secondary electrons at each point of the scan, resulting in a greyscale 2D image of the scanned area. The resolution of the image is related to the spot size and the interaction volume of the beam. High resolution SEM imaging can only be performed under high vacuum due to scattering of the electron beam by gas molecules. Therefore nanoparticles suspended in a colloid must be deposited onto a flat substrate and dried prior to imaging. Additionally, build up of charge on the sample surface results in deflection of the electron beam, and significant distortion of the acquired image. As such, nanoparticles must be situated on conductive substrates or coated with a thin and continuous conductive layer. SEM is capable of imaging with a wide field-of-view and very high depth-of-focus. The sample chamber of a typical SEM is capable of handling large samples, *e.g.* 150 mm silicon wafers. Additionally, samples can be tilted to gain additional topographic data. The height of nanoparticles can be measured by cross-sectional SEM, although samples are difficult to prepare for this as the nanoparticles must be situated very close to the edge of the sample to obtain a clear image.

In transmission electron microscopy (TEM) the electron beam is passed through the sample, and information is gained by detecting the transmitted beam. In bright-field imaging mode, nanoparticles absorb or block the electron-beam, and so appear as dark areas in the image. TEM is capable of providing higher resolution images than SEM due to reduced scattering of the electron beam. High-resolution TEM (HRTEM) makes use of phase information obtained by interference to achieve atomic resolution, and is often used to study crystallographic structure *[150]*. 3D data can be obtained using electron tomography, where the sample is rotated and imaged at each angle *[151]*. Sample preparation for TEM analysis is complicated by the need for a substrate that is near-transparent to the electron beam. Mechanical milling or ion-beam milling techniques are often used to suitably thin a sample. In the case of colloidal solutions sample preparation is simplified as nanoparticles can be deposited directly onto pre-prepared membrane or grid mounts.

Atomic force microscopy (AFM) uses a sharp tip that is scanned across the sample surface, and a topography map is generated by plotting the cantilever deflection (*i.e.* the force exerted on the tip). Extremely precise Z and X-Y tip movement is achieved using piezoelectric elements. Typically a laser spot is used to measure the deflection of the cantilever, and this is linked to a feedback mechanism to ensure a constant force on the probe tip. An AFM is capable of providing quantitative measurements of in-plane and out-of-plane topography, with potential for atomic resolution in scanning tunnelling (STM) mode. Unlike electron-beam microscopy, AFM is performed at ambient pressures and can image conductive or insulating samples equally well. However, the scan time is substantially longer than for SEM or TEM. Additionally, broadening of surface features in AFM images occurs due to finite tip size *[123, 152, 153]*.

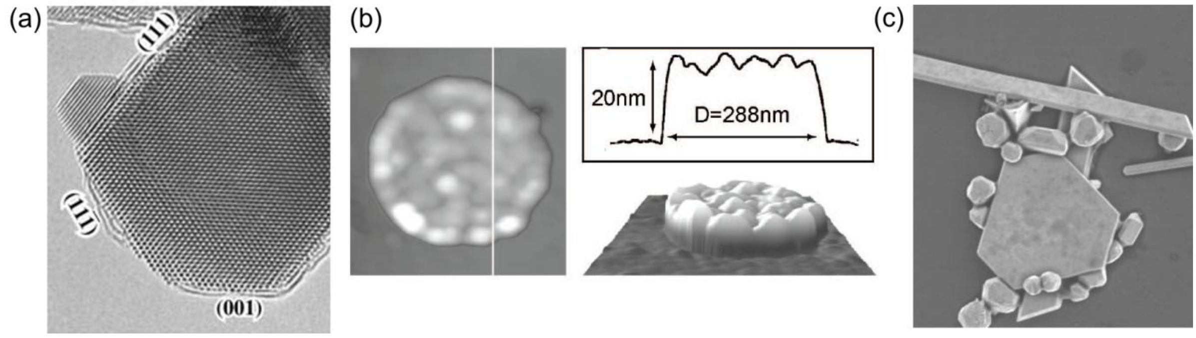

Figure 2.12: (a) HRTEM image of Au nanoparticle showing atomic lattice planes *[150]*, (b) AFM image of Al nanodisc *[136]*, (c) SEM image of Au nanoparticles *[154]*.

2.3.2 Measurement of extinction, absorption and scattering

Extinction can be measured by directing a collimated beam at a collinear detector, with the sample placed between the two. Light that is absorbed or scattered by the sample will not be detected, *i.e.* it will appear to be ‘extinguished’. Spectral information is obtained using a monochromatic light source and detector, or a white light source and spectrophotometer. The LSP resonance wavelength appears as an extinction maximum, *i.e.* a transmission minimum. More specific details of experimental extinction measurements are rarely given beyond this simple description. Clearly there are several important parameters: spot size at the sample, beam divergence (or degree of collimation), detector type and distance of detector and emitter from the sample. The rarely-mentioned caveat with this approach is that any photons scattered forwards at small angles may be detected and therefore not count towards extinction. Therefore the acceptance angle and distance of the detector are of crucial importance.

Extinction measurements are often cited in ‘arbitrary units’ or as percentages relative to a reference (*e.g.* an uncoated substrate). For sub monolayers of identical nanoparticles deposited on a transparent substrate, exact extinction cross-sections and efficiency factors can be calculated provided the surface or volume concentration is known *[155]*.

For many purposes it is useful to separate an extinction spectrum into its constituent parts: absorption and scattering. This can be achieved by using an integrating sphere (also known as an Ulbricht sphere), which consists of a large hollow sphere that has a diffusely reflecting interior (Fig. 2.13). Light incident on any point of the interior is uniformly distributed to all other points by multiple scattering events, *i.e.* an input beam is uniformly distributed across the sphere interior. Small ports in the sphere enable input and output of light. Mounting a detector in a small port samples part of the samples part of the uniform distribution, and therefore the detected signal is proportional to the amount of light collected over all angles. Evanoff and Chumanov measured the extinction, absorption and scattering of light by chemically synthesized Ag nanoparticles using an integrating sphere *[155]*. In their configuration the sample is placed in the centre of the sphere, and so only transmitted or scattered light is detected. This allows the calculation of absorption by subtracting the detected signal from the signal obtained from an empty sphere. The authors calibrated their measurements using the dyes $KMnO_4$ and methylene blue, and comparing the resulting spectra to those obtained from standard extinction measurements (in the absence of scattering, extinction = absorption). The sphere measurements were approximately 25% higher than the spectrometer measurements for all wavelengths, so this was used as a ‘correction factor’ for further measurements. Scattering spectra were obtained by subtracting the absorption spectrum from the corresponding extinction spectrum. In similar experiments Langhammer *et al.* measured the extinction, absorption and scattering of lithographically-defined metal nanodiscs *[156]*. Instead of a central mount, samples were mounted on the front and rear ports of the integrating sphere to measure forward scattering and diffuse reflectance (back-scattering) respectively. Subtracting the sum of these two measurements from 100% gives the absorption. Although this method involves two measurements compared to the single measurement required by the centre-mount technique, the ratio of forward- to backward-scattered light is also obtained. No absorption calibration samples were measured by Langhammer *et al.*, although a diffuse reference beam measurement was used to account for attenuation of the diffuse signal by the sample. This could be the cause of the 25% error encountered by Evanoff and Chumanov, as they did not use a diffuse reference.

Scattering has also been measured by off-axis detectors. Stuart and Hall measured the scattering of nanoparticles on a non-transparent substrate by sampling a cone of the scattering hemisphere that excluded the specularly reflected beam *[157]*. This method yields qualitative information on the wavelength-dependent scattering properties of the nanoparticles. However, due to differences in the angular dependence of scattering intensity for each excitation mode, the choice of detector position will considerably influence the relative intensity of the detected scattered signal. The angular dependence of scattering intensity can also be measured experimentally using a narrow field-of-view (FOV) detector mounted on a rotating arm. Such a system was used by Fragstein *et al.* to obtain scattering profiles of colloidal Au nanoparticles, which are in excellent agreement with Mie theory calculations *[31, 158]*.

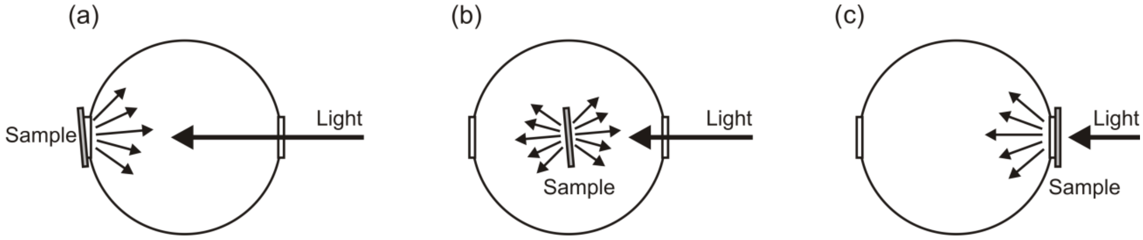

Figure 2.13: Cartoon representation of integrating sphere configuration for measuring (a) diffuse reflection, (b) absorption, (c) diffuse transmission.

Direct measurement of absorption can also be achieved using photothermal deflection spectroscopy *[159]*. Absorption of photons within a material leads to a slight increase in the temperature of the material. A layer of gas in contact with the material is also heated, leading to a decrease in its refractive index close to the surface of the material. The magnitude of the change in refractive index of the gas is proportional to the absorption within the material, and can be probed by measuring the deflection of a glancing-angle laser beam. Kreibig *et al.* used photothermal deflection spectroscopy and extinction spectroscopy to measure the optical properties of Ag nanoparticles embedded in gelatin *[160]*. The resulting spectra were in good qualitative agreement with Mie theory simulations, but did not provide quantitative data or a comparison of the contributions of absorption and scattering to extinction.

2.3.3 Far-field single particle spectroscopy

The characterisation methods outlined in the previous section probe the optical response of millions or even billions of nanoparticles simultaneously. Deviations in the average size or shape of the nanoparticles results in broadening of the acquired spectra due to averaging effects. To circumvent this problem, numerous methods have been developed to measure the optical spectra of individual metal nanoparticles.

Optical microscope-based methods are suitable provided that the surface coverage of nanoparticles is low, typically in the order of one nanoparticle per 1 µm^2, to ensure detection of only isolated nanoparticles. However, the signal from a single metal nanoparticle is very weak compared to the illumination volume, therefore requiring additional methods to improve the contrast of the nanoparticle signal to the background. Sönnichscen *et al.* developed a single particle spectroscopy system with a prism-based excitation source (Fig. 2.14a) *[161]*. In this configuration the nanoparticles are situated in the evanescent field region of light undergoing total-internal reflection within the prism.

The evanescent field can couple to radiative modes in the nanoparticles, which are detected by a spectrometer connected to a microscope. Only light that interacts with the nanoparticles is detected, with the remainder of the illumination signal reflected by the prism. A simplification of this method uses dark-field illumination, where the nanoparticles are excited by light emitted at an oblique angle. Only light scattered by the nanoparticles is detected due to the narrow acceptance cone of the detector objective, and so the nanoparticles appear as diffraction-limited spots on a dark background (Fig. 2.14b) *[162, 163]*. Spectral information is obtained in the same way as standard extinction measurements, *i.e.* either by monochromator or spectrometer *[164]*. Due to the weak signal strength cooled detectors are usually employed to limit thermal noise. Isolation of the scattering signal from a single nanoparticle is achieved using a pinhole or iris diaphragm for linear detectors, or a slit for CCD detectors.

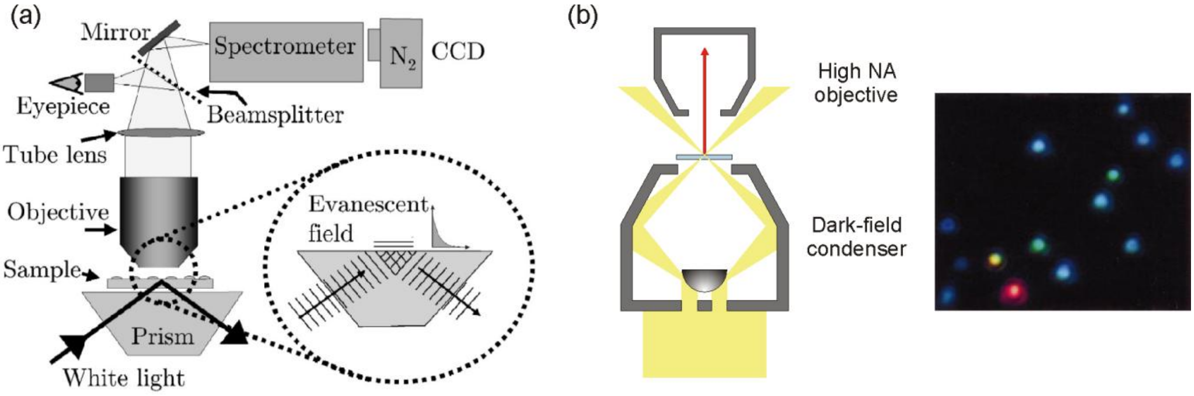

Figure 2.14: (a) Schematic of prism-coupled single particle spectroscopy system *[161]*, (b) schematic of dark-field illumination and example of acquired image *[163]*.

Scattering-based spectroscopy works well for particles with diameters of a few tens of nanometres or higher, but is not suitable for smaller particles whose optical properties are dominated by absorption. Arbouet *et al.* developed spatial modulation spectroscopy (SMS) as a means of detecting metal nanoparticles with extremely weak scattering cross-sections *[165]*. In SMS the sample is placed on a piezo-electric stage which modulates the sample position in one direction, and is then illuminated by a laser excitation source in a standard transmission configuration. The stage modulation results in a time-varying extinction signal, which can be detected by means of a lock-in amplifier. A further x-y piezoelectric stage enables scanning of the surface, providing 2D imaging of particle positions. Muskens *et al.* further developed this technique by including a super-continuum laser source to enable full spectral measurements to be taken of each particle (Fig 2.15) *[166]*.

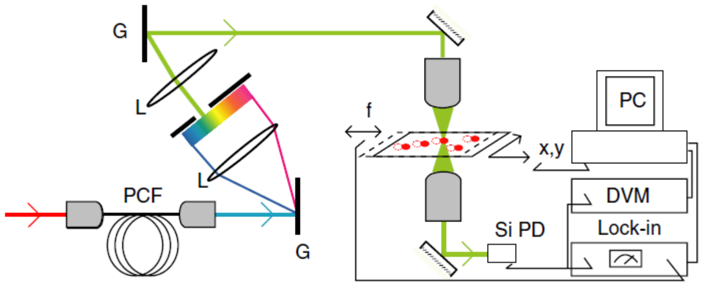

Figure 2.15: Schematic of spatial modulation spectroscopy system *[166]*.

Single particle spectroscopy has been used to investigate particle shape effects correlated with TEM images *[163]* and to study the influence of the local dielectric environment on individual nanoparticles *[164, 167]*. With the ability to detect and identify individual nanoparticles, functionalzied nanoparticles can be used as molecular labels *[162]*. Additionally, sensitivity to the local dielectric environment allows single nanoparticles to be used to probe very small scale interactions, for example to study protein-membrane interaction *[168]*. Eah *et al.* have used to this concept to develop a single particle probe, based on the collection of light scattered by a single metal nanoparticle attached to the tip of an optical fibre *[169]*.

2.3.4 Near-field single particle spectroscopy

Single particle spectroscopy can also be performed using scanning near-field optical microscopy (SNOM or NSOM). In SNOM systems a probe tip is positioned in the near-field region of a sample (*i.e.* closer than the wavelength of the excitation source), thereby overcoming limits on resolution imposed by far-field diffraction. The ultimate resolution of the system is defined by the size of the tip, which is typically in the range of 50-100 nm.

SNOMs can operate in various combinations of excitation and detection modes (Fig. 2.16), and make use of a variety of tip types. Apertured SNOM uses tapered hollow-tip probes for near-field excitation and/or detection, and can be used in conjunction with far-field excitation or detection. The tips are often metal-coated to increase the excited or detected field strength. In photon scanning tunnelling microscopy (PSTM) the sample is excited by evanescent field of a laser undergoing TIR, and perturbations to this field due to the sample are detected using a near-field probe *[170]*. Apertureless SNOM also uses prism-based excitation, but the probe does not collect light. Instead, both excitation and detection are in the far-field, and the tip is used to induce localized scattering of the evanescent field. A full discussion of SNOM configurations and tip types is beyond the scope of this report, and so we instead direct the interested reader to an overview by Kim and Song *[171]*.

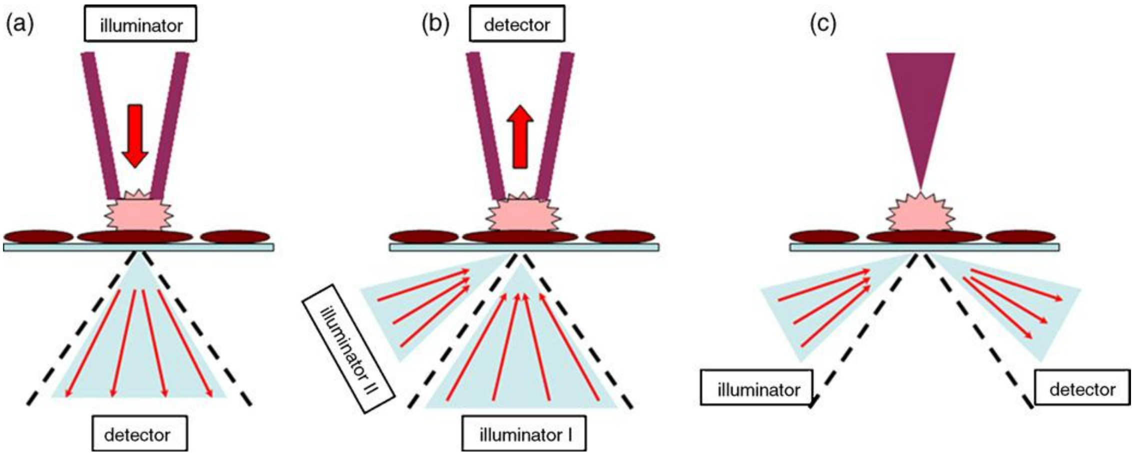

Figure 2.16: Modes of SNOM operation. (a) Illumination mode, (b) Illuminator I: collection mode; illuminator II: PSTM mode, (c) apertureless mode *[171]*.

SNOMs can simultaneously record topographic and spectral data, using the height feedback system and optical detectors respectively (Fig 2.17). The spatial resolution of topographic aperture SNOM data is often poor due to the large tip size compared with those used for AFM. Spectral data can be acquired by incorporating a tuneable or white-light excitation source in the system, which enables resonance positions and linewidths of single particles to be calculated. Klar *et al.* used near-field excitation and far-field detection to acquire scattering spectra of individual nanoparticles, which are in excellent qualitative agreement with Mie theory simulations *[172]*. Mikhailovsky *et al.* demonstrated that interference between the fields emitted by a fibre tip and re-radiated by a metal nanoparticle can be used to investigate phase dependence *[173]*. Destructive interference weakens the signal and constructive interference strengthens the signal, while the plasmon resonance occurs at the ‘zero extinction’ region at the transition between these two modes *[173]*.

Imaging the optical near field gains data on local electric field strength distribution and coupling between nanoparticles. However, the obtained data is often difficult to interpret due to tip-sample interactions, particularly when metal-coated apertures are used. Comparison with simulated intensity maps is usually used to interpret experimental data. The field around an isolated particle and a chain of particles was imaged by Krenn *et al.* using a PSTM *[174]*. In this approach the intensity distribution results from interference of the exciting field (*i.e.* the evanescent field) and the field scattered by the particle. Later work by the same group demonstrated coupling between resonantly excited nanoparticles and a non-resonantly excited nanowire *[175]*. Imura *et al.* used near-field excitation of two-photon-induced photoluminescence (TPI-PL) to image the field intensity of Au nanorods, and indentified discrete localization of field intensity along the rod length *[176, 177]*. Direct observation of dipolar and quadrupolar mode distributions have been reported by Esteban *et al.* for Ag nanodiscs (Fig. 2.18) *[178]*, and by Rang *et al.* for Ag (triangular) nanoprisms *[179]*. The study of areas of high electric field intensity in metal nanoparticle clusters is of great interest for optimizing SERS-active substrates. Markel *et al.* used a PSTM to identify electric field ‘hot spots’ in clusters of colloidal Ag, and to separate the individual contributions of nanoparticles to the overall optical response *[180]*. More recently, Shimada *et al.* correlated SEM spatial data with TPI-PL intensity maps to identify hot-spots in 2D arrays of Au nanoparticles (Fig 2.19) *[181]*.

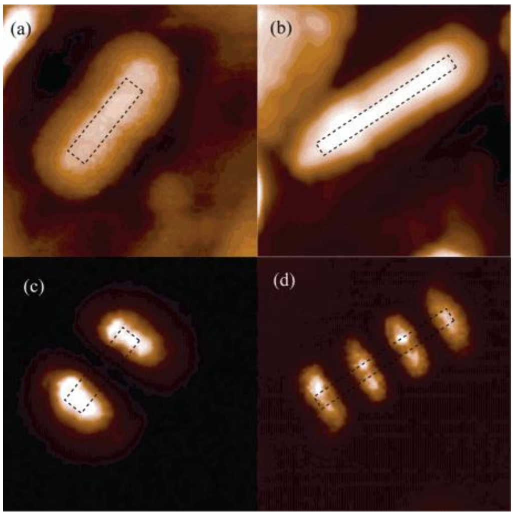

Figure 2.17: Example of SNOM images of Au nanorods, (a,b) topography image, (c,d) near-field image *[176]*. Outlined rectangles are a guide for the eye.

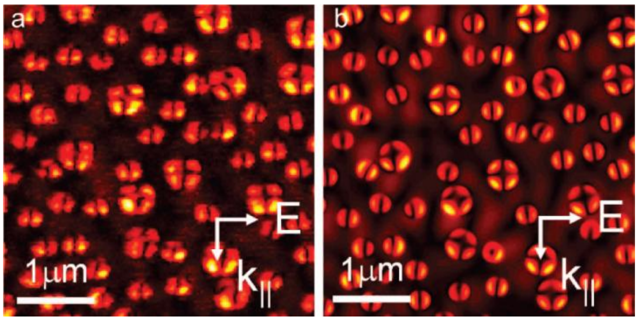

Figure 2.18: (a) SNOM image and (b) simulation of Ag nanodisc with double-peaked size distribution, showing dipolar and quadrupolar excitation *[178]*.

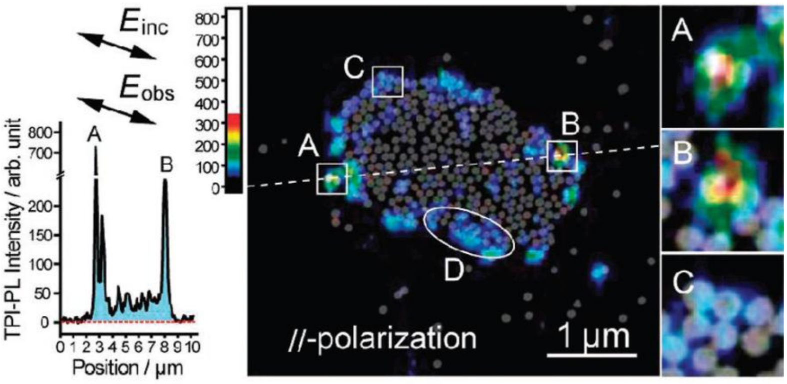

Figure 2.19: Two-photon-induced photoluminescence map of Au nanoparticle cluster correlated with SEM image *[181]*.

2.4 Optical properties of metal nanoparticles

The optical properties of metal nanoparticles are highly sensitive to the particle size, shape, composition, and the local dielectric environment. For solar cell applications we are interested in controlling the peak resonance wavelength and the relative contributions of absorption and scattering to extinction. Other factors such as polarization sensitivity and e-field intensity are also of interest.

2.4.1 Metal

Metal nanoparticles can support LSPs at wavelengths where their constituent metal's optical response is free-electron in nature. Damping by interband transitions weakens or prohibits LSPs. Table 2.1 lists the approximate interband threshold energies and wavelengths for Ag, Au, Cu and Al. The noble metals support LSPs at wavelengths longer than the threshold wavelength. The interband region for Al is centred around 830 nm, but the metal can be considered as free-electron for wavelengths either longer or shorter than this. As such, Al nanoparticles can support LSPs further into the UV than the noble metals.

Metal	**Energy**	**Wavelength**
Ag	3.9 eV	318 nm
Au	2.4 eV	521 nm
Cu	2.1 eV	590 nm
Al	1.5 eV	827 nm

Table 2.1: Interband transition regions for Ag, Au, Cu and Al (adapted from *[31]*).

Kreibig and Vollmer calculated extinction spectra for spheres of 41 elemental materials, with diameters of 10 nm and 50 nm, embedded in media with refractive indices of n = 1 and n = 2 *[31]*. Resonant extinction spectra were presented for many of the metals, not just the noble and alkali. No summary of peak position and magnitude for each metal was given, and so we do not attempt to present that data here. Blaber *et al.* theoretically investigated the absorption spectra of nanospheres made from Na, K, Al, Ag and Au *[182]*. The maximum absorption for each metal was found as a function of sphere size. Al, Na and K were found to exhibit the strongest optical absorption, while Au exhibited the weakest. The reported resonance peak of Al at 143 nm is at a far shorter wavelength than the other metals, with the next closest being Ag at 361 nm. The authors show that, counter-intuitively, absorption strength in metal nanoparticles is inversely proportional to the imaginary part of the dielectric function for a given metal. This is due to the fact that absorption losses in the metal damp the plasmon resonance, leading to a reduction in plasmon-induced absorption.

Stuart and Hall fabricated metal island films from Ag, Au and Cu *[14]*. Differences in film thickness and annealing condition rule out quantitative comparison of observed spectra (particularly as no study of particle size and shape was conducted). Qualitatively, the Au peak was weaker and red-shifted compared with Ag, and the Cu peak was weaker and red-shifted compared with both Ag and Au. Interestingly, Baba *et al.* demonstrated that an alloyed metal island film with a 1:1 mixture of Ag and Au features a resonance peak wavelength almost exactly half way between the respective Ag and Au peaks *[100, 101]*. Tuning of the peak position was achieved by varying the relative content of Ag and Au in the film.

Chan *et al.* fabricated ordered arrays of Al, Ag, Cu and Au nanotriangles by NSL *[121]*. The resonance peak positions of similarly sized triangles were found to be 508 nm, 639 nm, 698 nm and 787 nm for Al, Ag, Cu and Au respectively. Full-width half-maxima (FWHM) were found to increase in the order of Cu, Ag, Au then Al. Some differences in nanoparticle geometry were expected due to different wetting properties of the metal, and reduction of tip curvature due to oxidation of Cu and Al nanoparticles. Moderately good agreement with DDA calculations was found, supporting the notion that the principle reason for the optical properties was due differences in metal and not the resulting particle geometry. Langhammer *et al.* fabricated nanodiscs of Pt, Pd, Ag, Au and Al by HCL *[136, 156]*. Far-field extinction and absorption measurements were made using techniques discussed in the previous section. Strong resonant peaks were found for all metal types. The extinction spectra of Pd and Pt nanoparticles were found to be very similar, with resonant peaks that were broader and blue-shifted with respect to Au and Ag. Additionally, the optical spectra of Pt and Pd nanoparticles were found to be dominated by absorption, due to interband activity across the measured range. Ag, Au and Al nanoparticles exhibited a tuneable scattering to absorption ratio, dependent on particle size. Larger (> 120 nm diameter) Au and Ag nanoparticles feature very similar optical properties, with the exception of higher absorption in Au at shorter wavelengths due to the position of the interband threshold in Au. The spectra of Al nanoparticles were also found to feature a small increase in absorption around the interband transition region near 800 nm.

2.4.2 Size

The optical properties of large and small nanoparticles are markedly different. Kreibig and Vollmer define two types of size effects: extrinsic and intrinsic *[31]*. The threshold for the two regimes occurs for diameters of around 10 nm in the case of Au nanoparticles. The optical properties of nanoparticles with diameters above the threshold are dominated by extrinsic effects, which are related to the diameter and the bulk dielectric function of the metal. A red-shifting and broadening of the resonance peak is seen for increasing radius, due to retardation effects. For nanoparticles with diameters below the threshold several special considerations must be made due to intrinsic effects. This size range is clearly within the quasi-static regime, and so electrodynamic effects such as retardation do not play a role in the optical properties. However, surface scattering of electrons occurs due to the particle dimensions being smaller than the mean free path, leading to damping of the plasmon oscillation and a resulting attenuation and broadening of the resonance peak. Berciaud *et al.* experimentally observed intrinsic size effects in single particle spectroscopy studies of 5 nm radius Au nanoparticles *[183]*. Additionally, bulk dielectric functions are no longer valid for small nanoparticles and must be adjusted for finite-size effects. For very small nanoparticles (radius < 1 nm), quantum effects become important, and the optical properties can no longer be said to result from coherent oscillation of electrons.

Mie theory simulations show that as nanoparticle diameter is increased the dipolar extinction peak is red-shifted and broadened *[39]*. Optical transmission and absorption measurements of chemically synthesized Ag nanoparticles in solution show the same trend *[155]*. Additionally, the relative contribution of absorption to extinction decreases with size, resulting in predominantly scattering nanoparticles for diameters above 75 nm. A similar red-shifting of the resonance peak and increase in scattering for an increase in nanoparticle size has been reported nanodiscs fabricated by HCL *[156]*.

2.4.3 Shape

Haes *et al.* elegantly demonstrated the importance of particle shape by simulating the optical spectra of various Ag nanoparticle types with constant volume (Fig. 2.20) *[184]*. The largest difference occurs between the sphere and pyramid, with a ~200 nm shift in peak wavelength position. The peak position shift correlates well with an increase in the number of sharp tips or edges as the shape is changed from sphere to pyramid. Plots of $|\boldsymbol{E}|^2$ intensity in the same paper show that the near-field intensity is strongly confined at sharp features, which results in the red-shifting of the far-field response.

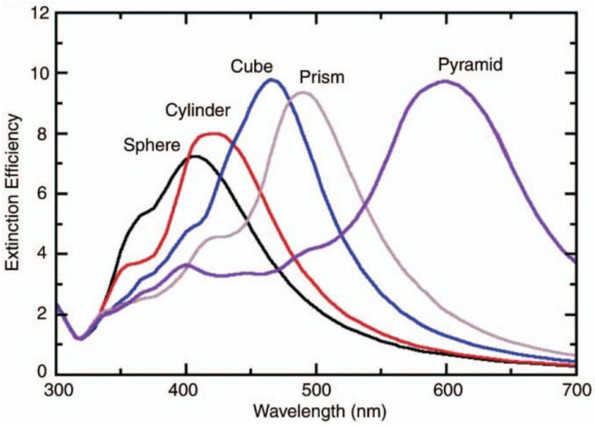

Figure 2.20: FDTD extinction simulations of Ag nanoparticles with identical volume *[184]*.

Zhang *et al.* studied the effect of electrochemical oxidation on the optical properties of nanotriangles fabricated by NSL *[185]*. The oxidation process reduced the in-plane size of the nanoparticle and also reduced the tip radius of curvature. The oxidation process caused the particle to change from a triangular cross-section to circular, and the resonance peak to shift from 654 nm to 506 nm. The height of the nanoparticle was relatively unaffected by the oxidation process, and so the cause of the shift was primarily due to a change in shape. Kelly *et al.* used DDA simulations to study the sensitivity of triangular prisms to changes in tip geometry *[24]*. Tip truncation introduces a strong blue-shift, with approximately a 100 nm decrease in peak wavelength per 5 nm truncation for a triangular prism with 100 nm sidelength. The authors attribute this sensitivity to the strong localization of electric-field around the tips, as evidenced by simulated e-field enhancement plots.

Anisotropic nanoparticles support distinct LSP resonances for different polarization states. The simplest example of an anisotropic nanoparticle is the nanorod, which supports distinct transverse and longitudinal LSP resonances. Typically the longitudinal resonance dominates the optical response of the rod. DDA calculations by Lee and El-Sayed show that the longitudinal resonance red-shifts linearly with aspect ratio for a constant volume, with an approximately 100 nm shift in peak position for a unit increase of aspect ratio *[186]*. The ratio of scattering to absorption was found to sharply increase with increasing aspect ratio until a maximum at an aspect ratio of 3, after which the ratio decreased slowly. Comparisons were also made between spheroids and nanorods (defined as cylinders with hemispherical end caps), with spheroids exhibiting slightly blue-shifted resonances compared to nanorods of the same volume. This effect was found to be more pronounced for higher aspect ratios. Experimental measurements of nanorods exhibit similar trends. Kooij and Poelsema surveyed results from theoretical and experimental measurements of the optical properties of nanorods and found a linear fit between resonance peak wavelength and rod aspect ratio for nearly all reported results *[187]*. Prescott and Mulvaney used DDA to study the effect of nanorod shape, comparing the spectra of prolate spheroids, hemisphere-capped cylinders and uncapped cylinders *[188]*. A red shift was found as the curvature of the rod ends was varied from spherically capped to uncapped through intermediate oblate cap geometries.

Solutions of chemically synthesized nanoparticles often include a variety of sizes and shapes. Mock *et al.* were able to correlate TEM images of individual nanoparticles with their respective single particle spectrum by using dark-field spectroscopy and careful analysis of particle formations (Fig 2.21) *[163]*. In general the peak position was found to red-shift in the order of: sphere < pentagonal prisms < triangular prisms.

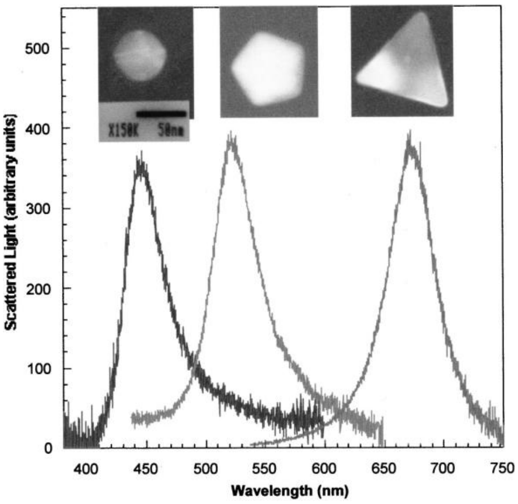

Figure 2.21: Dark-field single-particle spectra correlated with TEM images of particle shape *[163]*.

In practice fabricated nanoparticles exhibit a degree of nanometre scale surface roughness, which can also affect their optical properties. Wang *et al.* developed a method to roughen chemically synthesized polycrystalline metal nanoparticles by means of a site-selective chemical etch *[189]*. Experimental results and FDTD simulations showed that nanometre scale surface roughness results in a red-shifting of the peak position. A later paper also demonstrated a modification of the angular scattering pattern of the quadrupolar mode of due to surface roughness (although the dipolar mode was unaffected) *[190]*.

2.4.4 Higher-order modes

Particles that are small compared with the incident wavelength experience homogenous field strength across their surface and therefore only support dipolar LSP modes. However as the particle diameter is increased the field may become retarded across the particle surface, resulting in the excitation of higher-order oscillations (quadrupolar, octupolar *etc.*). These occur in extinction spectra as additional peaks at higher energies (shorter wavelengths) than the dipolar peaks. In modern derivations of Mie theory the contribution of each mode order is included separately in the summation of a_n and b_n, and so the modal contributions to extinction can be separated. Kelly *et al.* demonstrated that plots of dipole polarization (obtained by DDA simulations) can be used to identify the mode type of non-spherical particles *[24]*. Their study also illustrated the different field confinement of each mode for the case of triangular prisms: the dipolar mode is confined to the tips, while the quadrupolar mode is confined to the sides. SNOM measurements have identified quadrupolar and dipolar near-field intensity distributions in nanorods *[176]* and nanodiscs *[178]*.

In far-field measurements weak quadrupolar modes can be ‘hidden’ by stronger dipolar excitation if the two peaks occur at similar wavelengths. The quadrupolar peak position is less sensitive to particle size and surrounding refractive index than dipolar modes, and so is often ‘revealed’ when either of these parameters is increased. Each mode order has a distinct angular distribution of scattering intensity, and the angular scattering of a given particle is the weighted superposition of these modes *[25]*. Small particles support only dipolar modes and so scatter equally forwards and backwards, but larger particles become increasingly more forward-scattering due to the excitation of higher-order modes *[25, 31]*. Fragstein *et al.* measured the angular scattering dependence of dipolar and quadrupolar modes of spherical Ag nanoparticles, and achieved excellent quantitative agreement with simulations based on Mie theory *[31, 158]*. Importantly, Fragstein’s experimental results confirmed that larger particles scatter predominantly in the forward direction.

Higher-order modes are frequently observed in the extinction spectra of reasonably large nanoparticles. Evanoff and Chumanov observed an additional peak in the extinction spectra of spherical Ag colloids for diameters above 75 nm *[155]*. This quadrupolar peak was found to exhibit far higher absorption than the dipolar peak, and was less sensitive to particle size. Langhammer *et al.* fabricated nanodisc arrays of using a variety of metals by HCL, with disc diameters ranging from 38 nm to 530 nm *[156]*. Clear evidence of additional peaks due to quadrupolar and octupolar modes was found for Au and Ag disc diameters above 200 nm. The optical spectra of small nanorods also feature two peaks, but this is due to separate excitation of longitudinal and transverse LSPs. However, higher-order modes have also been reported for the case of nanorods. Krenn *et al.* varied the length of Ag nanorods fabricated by EBL from 100 nm to 1000 nm, with width fixed at 85 nm *[104]*. The number of extinction peaks and their respective wavelengths was found to increase with rod length. Lower order modes were found to red-shift more strongly for a given increase in particle length. Although the authors attributed each peak to a linearly increasing set of multipole orders (1, 2, 3, 4 *etc.*), later studies have in fact shown that only odd order modes are excited along the longitudinal direction. Payne *et al.* demonstrated using DDA simulations that all orders can be excited as the polarization state is rotated from transverse (where only one mode is supported) to longitudinal (where only odd modes are supported) *[146]*. An in-depth theoretical study of this phenomena is given by Khlebtsov *et al.* *[191]*. Multipole orders up to 9 have been observed experimentally for nanorods with lengths exceeding 500 nm *[192]*.

2.4.5 Dielectric environment

The optical properties of metal nanoparticles are strongly sensitive to the surrounding dielectric environment, which is useful for tuning their optical properties or for biosensing. In general, an increase of refractive index of medium surrounding a nanoparticle results in a red-shift of the LSP peak. Whitney *et al.* utilized atomic layer deposition of Al_2O_3 onto Ag nanotriangles to probe the sensitivity of nanoparticles to changes in refractive index *[193]*.

Detection of a single atomic layer (0.11 nm thick) was demonstrated. The effect of the overlayer was found to decrease strongly with layer thickness, although changes in thicknesses above 60 nm still had an observable effect on the peak position. McFarland and VanDuyne studied the scattering spectra of single Ag nanoparticles as a function of the surrounding refractive index *[194]*. A linear fit between peak position and refractive index of a surrounding solvent was demonstrated (Fig. 2.22).

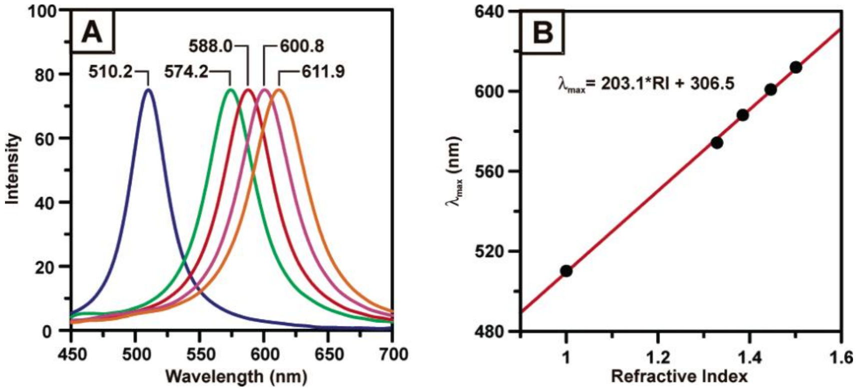

Figure 2.22: Single-particle scattering spectra of Ag nanoparticles as a function of surrounding dielectric environment *[194]*.

A thin oxide layer forms on the surfaces of Ag, Cu and Al form when these metals are exposed to air. Langhammer *et al.* considered the case of the self-limiting oxide that forms on Al, which was estimated to be 3 nm thick *[136]*. This oxide growth has two effects on Al nanoparticles: (1) the core Al particle is reduced in size during the oxide growth, (2) the local dielectric environment is changed by the outer alumina shell. SVM simulations showed that the change in dielectric environment has the strongest effect on the optical properties of the nanoparticle, and gives rise to a moderate red-shift for large particles, and a strong red-shift for small particles.

Metal nanoparticles are often deposited onto substrates prior to optical analysis, leading to a change in optical properties compared with those in vacuum or a homogenous fluid. Although a nanoparticle on a substrate is subject to an inhomogeneous dielectric environment, good results have been achieved by approximating the substrate as a homogenous effective medium. Various theories have been proposed to derive the refractive index of the medium, including averaging the refractive indices of the media above and below the particle, but agreement between these theories is poor. Kelly *et al.* included the substrate directly in DDA simulations, and found good agreement with experimental results *[24]*. A cylinder with width twice the particle diameter and length equal to particle height was found to be most suitable representation of a substrate in the DDA model. Although the substrate is substantially larger (semi-infinite in comparison with the nanoparticle size), only the region that affects the near-field region of the nanoparticle needs to be included in the model. The authors report a 100 nm red-shift for a nanoparticle on a mica substrate compared to the vacuum case. The authors also investigate the effect of gradually embedding an Ag nanoparticle into a mica sphere. After an initial strong red-shift in wavelength the peak red-shifts linearly with contact area.

Sherry *et al.* used single-particle spectroscopy and FDTD simulations to demonstrate that the presence of a substrate induces higher order modes in Ag nanocubes *[195]*. The nanocubes were produced by chemical synthesis and had an average side length of 30 nm. The scattering spectra of single nanocubes on a glass substrate was found to have two peaks, while the extinction spectra of nanocubes suspended in water only had a single peak. The additional peak was also present in FDTD simulations, and was found to develop as a function of distance from the substrate. The simulations also showed that the two peaks had considerably different field intensity distributions: the short wavelength peak is concentrated around the top of the particle, while the longer wavelength peak is concentrated around the bottom (at the Ag/glass interface).

Noble metals adhere poorly to Si and SiO2, and so a thin transition metal layer (typically Ti or Cr) is used to provide improve adhesion. This is particularly important during lithographic processes, to ensure the metal is not removed during lift-off. However, the transition metal layer damps the LSP resonance of the particle. Zheng *et al.* studied the influence of Cr adhesion layers on Au nanodiscs using DDA *[129]*. They found that even a 2.5 nm Cr layer significantly attenuates and broadens the extinction peak, and a slight blue shift of the peak position was also noted. All of these effects were found to increase with thickness of the Cr layer.

2.4.6 Intraparticle coupling

So far we have only discussed simple nanoparticle shapes, but more complex nanoparticle structures can feature distinct plasmon resonances on different surfaces. An example is the core-shell nanoparticle, where the inner and outer surfaces of the shell support different resonances. Coupling between the two surfaces leads to an alteration of the overall optical response of the nanoparticle. Prodan *et al.* developed a hybridization model that can explain the interaction between elementary plasmons supported by complex nanoparticles *[196]*. For example, the optical response of a core-shell nanoparticle can be considered as the hybridization of a shell plasmon and a cavity plasmon. The strength of the interaction is controlled by the shell thickness. The optical properties of core-shell nanoparticles can be tuned by modifying the core material, core diameter, shell material and shell thickness. Increasing the refractive index or diameter of the core leads to a red-shift of the resonance *[197, 198]*. Decreasing the shell thickness also results in a resonance red-shift, which is particularly dramatic for very thin shells. Standard Mie theory models for core-shell particles do not include the effect of surface scattering, which can be important for thin shells. Moroz developed an extension to Mie theory to model the effects of surface scattering in core-shell nanoparticles. The effect is the same as for very small solid spheres, *i.e.* damping that leads to attenuation and broadening of the peak. The toroid or nanoring can be considered as a 2D core-shell structure, and also features intraparticle coupling between the inner and outer surfaces *[130, 199]*. Nanorings are more readily fabricated by lithographic means than core-shell nanoparticles.

The effect of particle height of prism-shaped metal nanoparticles has been investigated by simulations based on the FDTD *[106]* and DDA *[129]* methods. A strong red-shift was reported for decreasing particle height in both cases. Although the authors do not suggest a physical reason for this shift, the trend is the same as that observed for decreasing the shell thickness of core-shell nanoparticles, and so is most likely due to coupling of the top and bottom surfaces of the particle.

2.4.7 Interparticle coupling

Systems composed of multiple particles may exhibit optical properties different than that of an isolated particle, even if each particle in the group is identical. In the near-field, evanescent fields of proximate nanoparticles can interact. At larger distances nanoparticles interact in the far-field through their scattered fields, which is particularly relevant for periodic arrays.

Jensen *et al.* investigated near-field coupling between two identical Ag nanospheres using DDA simulations (Fig 2.23). For a particle radius of 30 nm, an interparticle spacing of 30 nm results in a 10 nm red-shift of the resonance peak. For much smaller spacing the effect is much more dramatic, resulting in 100 nm and 125 nm red-shifts for a spacing of 4 nm and 2 nm respectively. Gunnarsson *et al.* experimentally investigated coupling between two Ag nanodiscs fabricated by EBL, with gap diameters ranging from 400 nm down to approximately 10 nm *[200]*. For disc diameters of 95 nm and 80 with light polarized parallel to the pair axis, reducing the interparticle distance from 400 nm to 100 nm had little effect on the peak position. However, for interparticle distances of the order of the diameter of the particle and below a strong red-shift was recorded that increases with decreasing gap. The results were in good agreement with DDA simulations, but CDA simulations were found to underestimate the effect of coupling for small interparticle separations. Closely-spaced nanoparticle pairs exhibit strong polarization sensitivity, as coupling effects are much weaker for incident light polarized perpendicular to the particle pair axis. Complete transfer of energy from one nanoparticle can occur via dipole-dipole interaction, leading to the idea of subwavelength waveguides based on linear chains of metal nanoparticles *[201-203]*. The principle interest in coupled metal nanoparticle dimers is the intense electric field enhancement observed in the gap between the particles, which is far larger than those obtained around isolated particles *[204]*. These are found to be strongly related to the interparticle separation, with smaller distances producing larger field enhancement *[205]*.

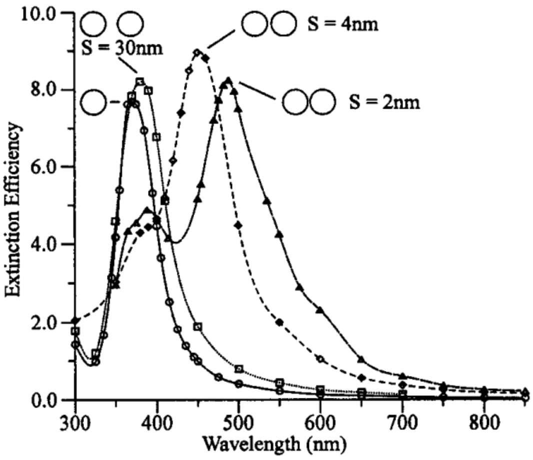

Figure 2.23: DDA simulations of 30 nm radius Ag sphere with various interparticle distances *[39]*.

Particles arranged in a periodic pattern will scatter photons coherently, leading to a change in the observed far-field scattering spectrum due to interaction between scattered photons. Periodic arrangements of nanoparticles form a diffraction grating, and coupling of LSPs to evanescent or radiating grating modes alters the extinction spectrum from that of isolated nanoparticles. Essentially the diffraction grating imposes restrictions on the angular distribution of scattering, and so inhibits or strengthens scattering at given wavelength. Therefore the optical properties of a periodic array of nanoparticles depend on the grating period in addition to the properties of the individual nanoparticles. For wavelengths longer than the grating period only the zero order grating mode exists, and so scattering is attenuated. For wavelengths shorter than the grating periods many grating modes exist, and so scattering can occur in specific angles defined by the properties of the relevant grating order. Therefore the extinction spectrum of an isolated particle will be modified when it is part of a periodic array *[206]*. It is worth noting that for particles on a substrate two sets of grating conditions exist: one for light scattered into air, and one for light scattered into the substrate. The theory of light scattering by periodic arrays of nanoparticles was recently reviewed by García de Abajo *[207]*. Good qualitative agreement with experimental results have been found for T-matrix and CDA simulations *[208]*, and good quantitative agreement was demonstrated using FDTD simulations with periodic boundary conditions *[209]*.

Special consideration must be given to the case where the grating period is similar to the wavelength, as the first grating order will be evanescent. Simulation studies have predicted extremely sharp resonances for 1D and 2D arrays of particles near the onset of the first grating order *[210, 211]*. Recently several groups confirmed the existence of these peaks experimentally *[208, 209, 212, 213]*. The extremely narrow diffraction peaks are only found for periodic arrays of highly scattering particles in homogenous geometries with a well collimated incident light source *[208]*. The effect on the extinction spectrum is a weakening of the dipolar peak, and emergence of a sharp interference peaks that red-shift with increasing grating period. Auguié and Barnes have shown that introducing disorder into the particle position or particle size can inhibit or completely suppress these effects *[213]*.

Near-field coupling occurs for nanoparticles with interparticle spacing of the order of the particle size or less. The result is a strong red-shift of the peak position a giant increase the e-field intensity. Far-field coupling occurs for periodically structured arrays, even with large (> 1 µm) particle separations. Peak suppression and additional peaks can occur, depending on the array period and the LSP peak of the isolated particle.

2.4.8 Interaction with planar waveguides

Thin dielectric and semiconductor films can support waveguide propagating modes provided they have a higher refractive index than the surrounding medium, while planar metal films can support propagating surface plasmon (PSP) modes. Both systems support laterally propagating modes, and can therefore act as an additional channel for coupling energy between nanoparticles. Additionally, the metal nanoparticles can couple selectively to waveguide propagating modes if they are situated in the range of a mode's evanescent field. Therefore the optical properties of metal nanoparticles can be modified by coupling to nearby waveguides, and also by waveguide-mediated coupling between the metal nanoparticles themselves. The field experienced by each particle will be the super-position of the incident field, the field reflected from the interface of the waveguide, any near-field contribution from proximate nanoparticles, and the evanescent field of modes trapped in the waveguide. A number of studies have been made to investigate which of these modes dominate the optical response of the metal nanoparticle / waveguide structure.

Stuart and Hall investigated the optical properties of an Ag MIF deposited onto a silicon-on-insulator (SOI) wafer with an Si thickness of 160 nm *[157]*. The diffuse reflectance of the sample was found to be markedly different from the case of a similar Ag MIF on a glass substrate. The modified spectrum features numerous peaks, most notably one centred at ~1250 nm where the on-glass MIF has near zero optical response (Fig. 2.24a). The authors attribute this to waveguide-mediated coupling, where the detected scattered signal is proportional to the amount of light trapped in the waveguide. The peaks observed in the reflectance spectrum were found to be in good qualitative agreement with a CPS-based model of the spectral efficiency of coupling into discrete waveguide-propagating modes supported in the Si layer. This interpretation is further strengthened by a second experiment where an Ag MIF film is deposited onto a thick Ag film, with a separating layer of LiF (Fig. 2.24b). For thin layers of LiF the only available waveguide mode is a PSP on the Ag mirror. For LiF layers above 150 nm an additional waveguide mode is available within the LiF layer. The authors interpret the broad peak for LiF < 150 nm to coupling to a PSP mode, which is broadened and attenuated with increasing LiF thickness due to a weakening of the coupling. For LiF > 150 nm an additional high energy peak is observed, which the authors ascribe to coupling to a LiF waveguide mode.

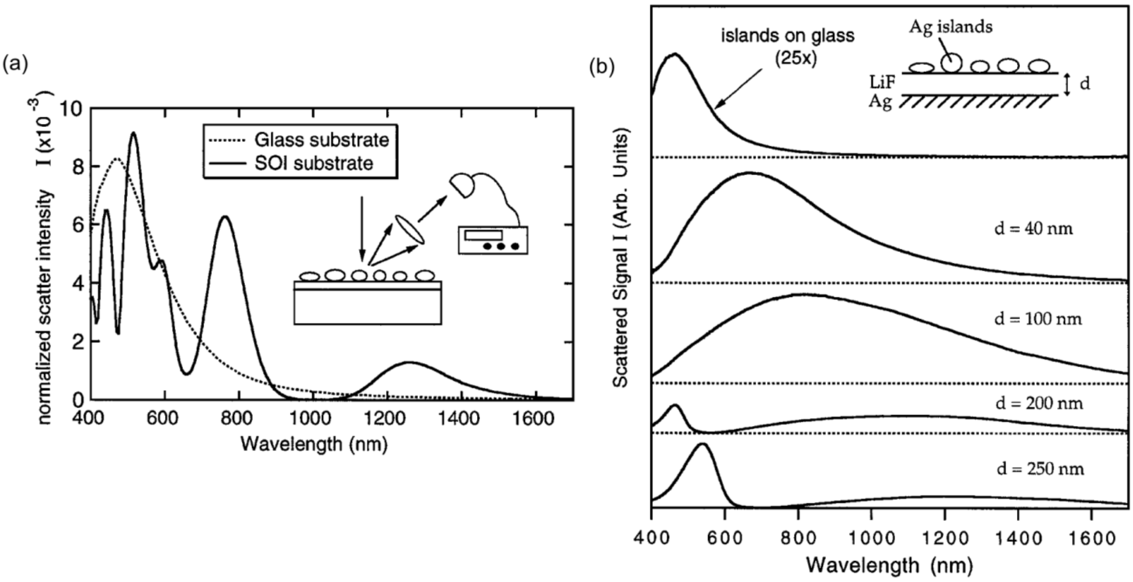

Figure 2.24: (a) Diffuse reflectance of Ag island film on glass and on SOI, (b) Diffuse reflectance of Ag island film separated from an Ag mirror by a LiF layer *[157]*.

Several other experimental and theoretical studies have been performed on similar geometries. Most notably, the theoretical study of Johansson specifically aimed to further understand the results of Stuart and Hall *[214]*. Johansson developed an analytical model of the system that included effects of multipolar excitation, interparticle coupling and distribution of particle size and shape. Good agreement between a simulated diffuse reflectance spectrum and the experimental spectrum presented by Stuart and Hall was found. Johansson ascribed the observed scattering peaks to maxima in the field driving the LSP oscillations, which derive from constructive and destructive interference between incident photons and those reflected from the Si-SiO$_2$ interface. Further corroboration for this interpretation is given by Leitner *et al.*, who studied the specular reflectance of an Ag island film separated from a planar Ag layer by a SiO$_x$ layer of variable thickness *[215]*. The spectra reported by Leitner *et al.* feature dips in reflectance where the second part of Stuart and Hall's study show peaks, but otherwise the trends are very similar. Good agreement with stratified medium theory, which only includes interference effects, was also demonstrated. The nanoparticles used by Leitner *et al.* were small enough (~ 20 nm diameter) that absorption was the dominant optical property, and so the authors conclude that absorption is enhanced or suppressed by constructive or destructive interference, leading to numerous minima in the specular reflectance data. Therefore the trends observed in Stuart and Hall's experiments are most likely due to interference effects: scattering of light by the metal nanoparticles is enhanced or suppressed by interference within the SOI structure, leading to peaks and dips in the diffuse reflectance spectra.

Although these studies suggest that waveguide-mediated coupling does not strongly affect the optical properties of metal nanoparticles on planar layers, this does not discount the possibility of the metal nanoparticles coupling light into waveguide-propagating modes. Catchpole and Pillai developed a model developed to estimate the fraction of incident photons guided into waveguide-propagating modes by metal nanoparticles on an SOI structure *[216]*. This model treated the nanoparticles as non-interacting ideal dipoles (*i.e.* dipole-dipole interactions are ignored) on the surface of an SOI structure. Modification of scattering intensity by the waveguide was modelled using theory developed by Mertz *[217]*. Interestingly, Catchpole and Pillai use experimentally derived scattering data as input to the Mertz model, which circumvents the need to model the complex optical properties of a MIF. The model alters the angular distribution and wavelength dependence of the input spectrum to account for effects due to the waveguide. A transfer matrix approach is then used to calculate the diffuse reflectance and the absorption within the top silicon layer, based on the approach used by Leblanc *et al. [218].* Despite the simplicity of the model very good qualitative agreement is found with previously presented experimental results.

So far we have only considered random arrangements of metal nanoparticles on planar layers, but experimental studies of periodic arrangements have also been made. In this case the interaction is more complex due to coherent far-field coupling. Linden *et al.* studied the optical properties of periodic arrays of metal nanoparticles on ITO waveguides *[219]*. They observed a series of sharp spectral features that shift through the extinction peak as a function of the array period. This cannot be due to substrate-induced interference effects as a change was observed by modifying the array period, not the waveguide thickness. Instead the authors suggest that constructive and destructive interference occurs between incident light and light propagating along the waveguide. Due to the periodic arrangement of nanoparticles light is coupled coherently into waveguide-propagating modes, resulting in the formation of a standing wave within the waveguide. Therefore in the case of periodic arrangements of metal nanoparticles, waveguide-mediated coupling plays an important role.

2.4.9 Summary of the optical properties of metal nanoparticles

The optical properties of metal nanoparticles are a strong function of the particle composition, size, shape, dielectric environment and the orientation and proximity of particles with respect to each other.

Increasing the size of a particle results in a red-shift and broadening of the peak position, and an increase in the ratio of scattering to absorption. Large particles also support higher-order modes, which occur at progressively shorter wavelengths, and have a larger absorption to scattering ratio than the corresponding dipolar peak.

Near-field coupling between nanoparticles results in a red-shift, but is only relevant for interparticle spacing of the order of the particle diameter or less. Waveguide-mediated interparticle coupling is only relevant for periodic arrangements of particles situated on slab waveguides, and results in the appearance of fringes in the extinction spectrum.

Increasing the refractive index of a homogenous medium surrounding a particle results in a linear red-shift of extinction peak position. Inhomogeneous mediums such as substrates and multilayers can result in the excitation of higher-order modes or dramatically change the extinction spectrum due to interference effects.

The strongest field enhancement occurs for particles with sharp tips (*e.g.* triangular prisms) or particle dimers with extremely small gaps. Interestingly, there appears a loose correlation between field enhancement and red-shifting of the LSP peak position.

Chapter 3

Recent progress in metal nanoparticle enhancement of inorganic photodiodes and solar cells

Metal nanoparticles have found use in a broad range of applications due to their strong and highly tuneable optical properties. These applications usually relate to intense absorption or scattering of light, the sensitivity of the optical properties (particularly extinction peak position) to the local dielectric environment, and the strong confinement and subsequent giant local enhancement of electromagnetic field strength. To understand the potential enhancement methods for solar cells, it is instructive to discuss a number of prominent applications of metal nanoparticles and their distinct modes of operation.

Surface enhanced Raman spectroscopy (SERS) has been the predominant driving force for metal nanoparticle research in recent decades *[220]*. Raman spectroscopy can be used to gain information on the type and orientation of molecular bonds in a sample, but the signal strength is very weak. Dramatic enhancements of Raman signal is found when samples are situated on a roughened metal substrate or near metal nanoparticles, due to enhancement of the local electric field strength. Enhancement factors up to 10^{15} have been reported *[221]*.

Another form of biosensor is based on the strong sensitivity of the optical properties of metal nanoparticles to the refractive index (RI) of their surrounding medium *[184]*. In this method the metal is functionalized to have a high affinity for a given biomolecule, and binding is detected by a change in refractive index in the extinction or scattering spectrum. The sensitivity of the sensor is a function of the particle geometry and the FWHM of the bare particle extinction peak. Sensors based on dark-field single particle spectroscopy have been demonstrated to have sensitivity in the Zeptomole range *[194]*. This raises the interesting prospect of using a variety of nanoparticles as real-time refractive index sensors at different points of complex biological systems.

Metal nanoparticles can also be used as contrast agents in light microscopy, as they feature far larger scattering cross-sections than correspondingly-sized dielectric nanoparticles (*i.e.* they provide a higher scattering signal per particle volume). Similarly, they can be used as labels for biological molecules *[162]*. Importantly, Au nanoparticles are biocompatible and their peak scattering wavelength can be tuned into the infrared region where water and blood are maximally transparent.

A new form of photothermal cancer therapy utilizes highly absorbing metal nanoparticles to selectively heat cancerous tumours *[222, 223]*. In this procedure metal nanoparticles are functionalized to selectively bind with cancerous tumours, and then injected into the body. A laser tuned to an IR wavelength, where tissue and blood are highly transparent, is shone through the body. The nanoparticles absorb the incident photons, and transfer the energy as heat to the surrounding tissue, thereby destroying it. Typically Au nanorods or core-shell nanoparticles are used, as these can readily be tuned to be strongly absorbing in the IR *[5]*.

For each of these applications it is vital that the correct size and shape of nanoparticle are used. For absorption-based applications, small nanoparticles are required, while for scattering-based applications larger particles are required. High e-field enhancements are found for particles with high degrees of curvature (*i.e.* sharp tips). For RI sensing extremely low FWHMs are needed. Additionally, in each case the size, shape and composition must be adjusted to provide a strong optical interaction across the desired wavelength range.

Therefore for solar cell applications we need to indentify which of these properties (scattering, absorption and e-field enhancement) are beneficial, and then design suitable nanoparticles (or ensembles of nanoparticles) to maximise these effects while minimizing unwanted optical properties. In this section we review recent progress in integration of metal nanoparticles with inorganic solar cells with the aim of identifying key enhancement mechanisms. We note that good progress has also been made in applying metal nanoparticles to organic solar cells *[224]* and dye-sensitized solar cells *[225]*, but these are considerably different physical systems to inorganic solar cells, and so the enhancement mechanisms are not necessarily applicable.

We consider the cases of wafer-based and thin-film solar cells separately, as the optical properties of thin-films are more complex.

3.1 Wafer-based devices

Schaadt *et al.* reported an enhancement in photocurrent for silicon photodiodes coated with Au nanospheres *[67]*. The spheres were deposited from colloid and adhered to the substrate using poly-l-lysine, *i.e.* via electrostatic attraction. Spheres with diameters of 50, 80 and 100 nm, were deposited on the devices with a surface coverage of 1.3%, 0.8% and 0.6% respectively. Extinction measurements taken of the particles in solution show clear resonant peaks, with a red-shifting with increasing size (Fig. 3.1a). The red-shifting behaviour is also seen in Mie theory simulations (by the author), but the relative extinction magnitudes exhibit opposite trends (Fig. 3.1b). This is most likely due to differences in concentrations of the solutions, which are not stated in the paper. When deposited on devices the peak photocurrent enhancement (defined as the ratio of photocurrent in a coated photodiode to a reference photodiode) was found be a factor of approximately 1.60, 1.85 and 1.55 for the 50, 80 and 100 nm spheres respectively (Fig. 3.2). No attempt to account for differences in surface coverage for the each nanoparticle size was made, resulting in the misleading appearance of the enhancement being strongest for the smallest particles. In fact, accounting for surface coverage, the peak photocurrent enhancement increases with nanoparticle size.

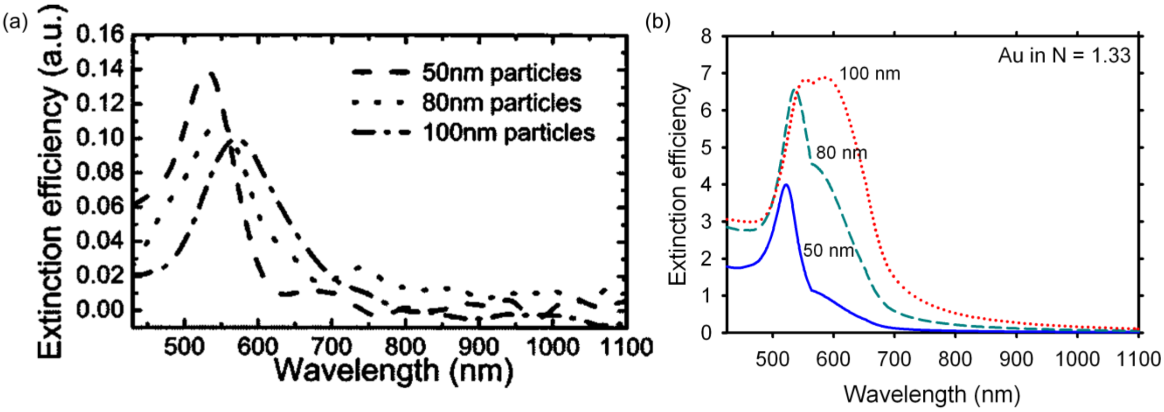

Figure 3.1: (a) Measured extinction of Au particles in water *[67]*, (b) corresponding Mie theory simulations.

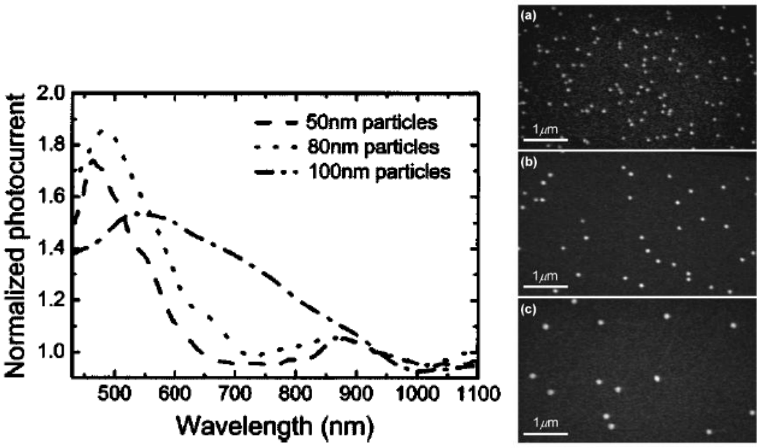

Figure 3.2: (Left) Normalized photocurrent of photodiodes coated with nanoparticles. (Right) SEM images of particle coverage: (a) 50 nm, (b) 80 nm, (c) 100 nm *[67]*.

The authors discuss various possible causes of the enhancement. Methods that do not relate to surface plasmon resonance, such as photoexcitation, are discounted due to the clear similarities between the extinction spectra and the spectral photocurrent measurements. Additionally, the authors discount the possibility of carrier injection, due to the electrical isolation of the particles by the native SiO_2 layer. Instead, it is proposed that the strength and 'interaction time' of the electric field is enhanced by the metal particles, which gives rise to an increase in optical absorption. However, the quoted peak values for normalized photocurrent are improbable given the optical cross-section of the nanoparticles. For a surface coverage of 1.3% and a peak extinction factor of 10 (higher than any of the simulated values), the nanoparticles would only interact with 13% of incident photons at the peak wavelenth. Therefore the authors claim a 50-80% increase in photocurrent response by improving the absorption of less than 13% of incident photons. The normalization process, which is based around the response of all devices over 950-1100 nm, is clearly inaccurate. Additionally, the observed photocurrent peaks for the two smallest nanoparticles occur well in the interband region of Au, where LSPs are not supported.

In a later paper by the same group, Lim *et al.* investigated the effect of depositing a sparse coating of 100 nm diameter Au nanospheres on silicon photodiodes *[9]*. The photodiodes under investigation were similar to those presented by Schaadt *et al.* but with a junction depth of 500 nm of instead of 80 nm. The nanoparticles were adhered in the same way, but a higher surface coverage of 2.74% was achieved by repetition of the deposition process. Spectral photocurrent was recorded before and after deposition of nanoparticles. A plot of the ratio between coated and uncoated photodiodes shows a decrease in photocurrent at shorter wavelengths down to a factor of 0.96, and an increase at longer wavelengths up to a factor of 1.03 (Fig 3.3). The maximum ratio is far lower than reported by Lim *et al.*, and also shows a region where the nanoparticles have a negative effect on the photocurrent. Also the peak photocurrent enhancement occurs at 700 nm for Lim *et al.*, but 600 nm for Schaadt *et al.*, despite the use of identical nanoparticles. Curiously, no mention is made of the substantial disparities between the results presented in the two papers.

Lim *et al.* used FEM simulations to model the effect of the nanoparticles on absorption within a silicon slab. The experimental geometry was approximated by a periodic array of 100 nm diameter Au spheres with a lattice constant of 600 nm (corresponding to a surface coverage of 2.18%), separated by 2 nm from a silicon substrate. This model was used to provide field intensities around the spheres and within the substrates, and field enhancement. The spectral features –a trough near 500 nm and a peak near 700 nm- are reported to be due to interference between forward-scattered photons and transmitted photons (Fig 3.4). The phase of the scattered photons is changed due to interaction with the nanoparticles. When the scattered and transmitted photons are in phase, constructive interference occurs, and the electric-field intensity within the silicon is increased (Fig. 3.4a). However, when they are out of phase, destructive interference occurs, and the electric-field intensity within the silicon is decreased (Fig. 3.4b). The phase delay is wavelength dependent, as it depends on the polarizability of the nanoparticle, and so the nature of the interference (constructive or destructive) varies across the spectrum. A good qualitative agreement between simulation and theory is shown (Fig. 3.3). The simulated peak is 100 nm blue-shifted compared with experiment, and the enhancement values are higher - particularly considering the lower surface coverage in the simulation compared to the experiment. The authors do not discuss the effect of absorption by the nanoparticle. Below approximately 575 nm Au nanoparticles are predominantly absorbing, which may account for the decrease in photocurrent at shorter wavelengths, rather than the suggested destructive interference. Reflectance data would help identify which mechanism is responsible, but unfortunately this is not presented.

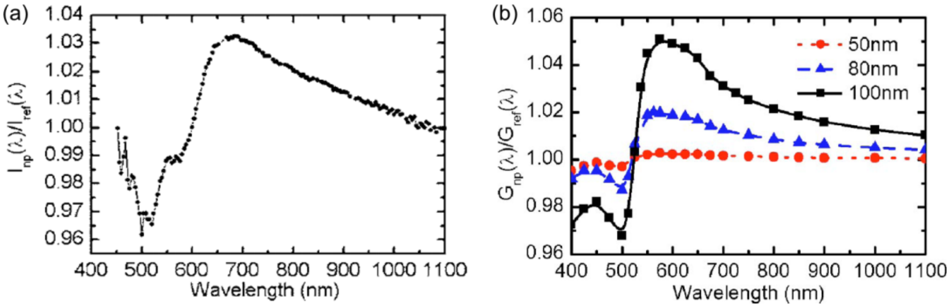

Figure 3.3: (a) experimentally obtained photocurrent ratio, (b) results obtained by FEM simulations *[9]*.

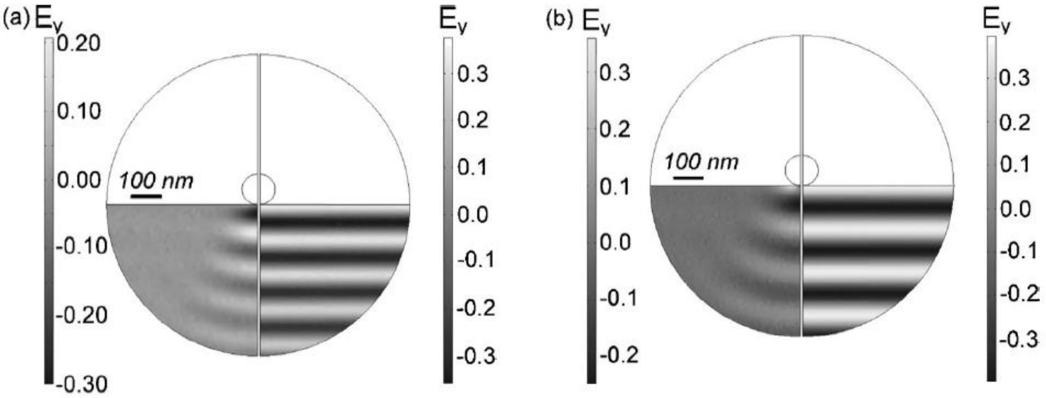

Figure 3.4: Simulated y component of electric field in silicon slab, separated into scattered (lower left quadrant) and transmitted (lower right quadrant) components at wavelengths (a) 500 nm, (b) 575 nm *[9]*.

Pillai *et al.* investigated the effect of depositing an Ag island film on a silicon solar cell *[13]*. The nanoparticles were separated from the active area of the device by a 30 nm thick SiO_2 layer. Different thicknesses of Ag were used to study the effect of varying the average island size. Extremely large photocurrent enhancement factors centred at the band edge were reported for the thickest MIFs (Fig 3.5). Enhancement factors up to 6.0 at 1200 nm were reported, with a 19% increase in photocurrent across the AM1.5 spectrum. Although the absorption coefficient of silicon near the band edge is extremely weak, a six-fold increase in absorption can still be considered significant. Importantly, it is higher than could be expected from a reduction in reflection alone, and therefore the metal nanoparticles must also be enhancing absorption within the silicon or improving light trapping. Optical measurements were carried out on plain double-side polished silicon wafers to further investigate the phenomenon. The same Ag island films were deposited as on the solar cell, and transmission and reflectance measurements gave an indication of optical enhancement mechanisms. The samples with metal islands all have a higher diffuse component of reflectance than plain silicon (Fig. 3.6b). If forward scattering also has a large diffuse component then the optical path length experienced by photons will increase on average, *i.e.* nanoparticles can improve light-trapping by coupling light into a solar cell at an angle.

The role of absorption is also clearly evident: in the photocurrent enhancement plot a dip is seen centred around 350 nm, but a peak is seen in the same area of the absorption enhancement plot. Therefore absorption by the nanoparticles reduces reflection, but does not increase photocurrent, and so is a loss mechanism.

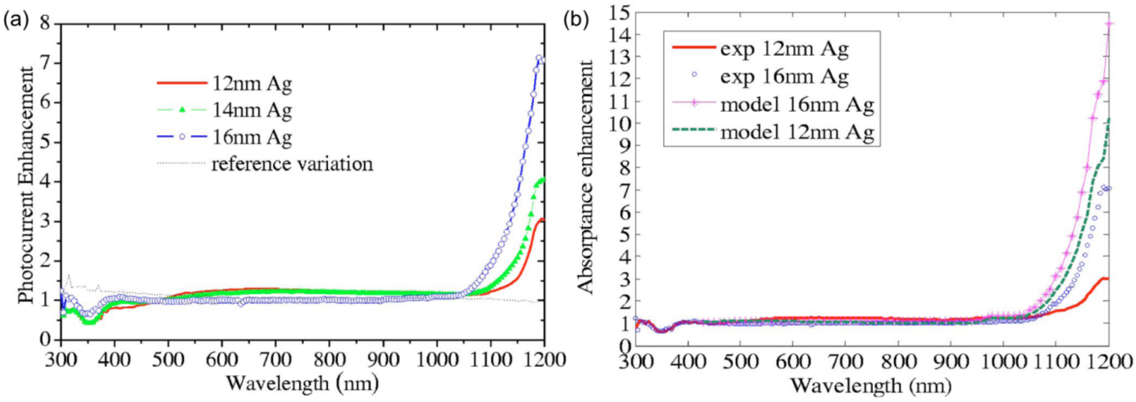

Figure 3.5: (a) Experimental photocurrent enhancement and (b) comparison to model for Ag island films on silicon solar cells *[13]*.

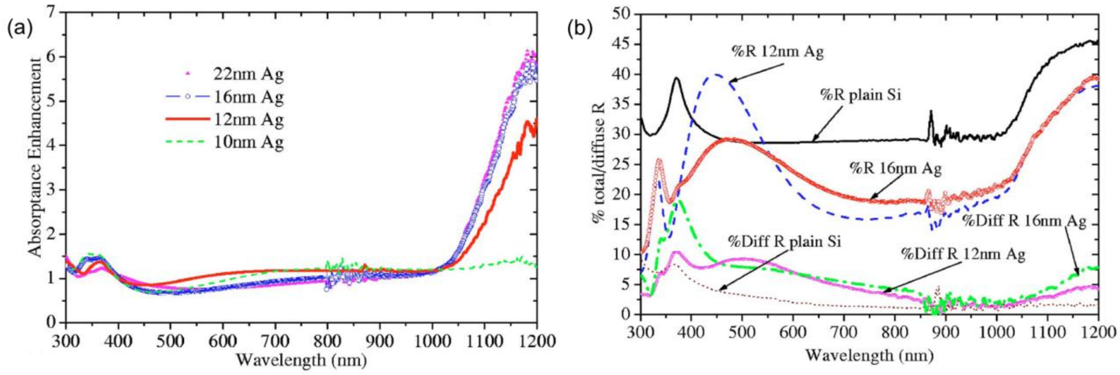

Figure 3.6: (a) Absorptance enhancement of Ag island film on DSP silicon wafer, (b) diffuse and total reflectance of corresponding samples *[13]*.

To achieve a greater control over particle orientation and morphology, Hägglund *et al.* used EBL to define Au nanodiscs on the surface of *pn* silicon photodiodes *[8]*. The Au discs were elliptical in shape, with a major axis of 92 nm and a minor axis of 40 nm, arranged in a square lattice with a period of 150 nm. These structures support two distinct polarization-sensitive LSP resonances, and so polarization-resolved QE measurements were taken. The unpolarized reflectance spectrum of the coated devices was found to feature two peaks, corresponding to excitation of separate LSPs along each axis. Each peak corresponded to an *increase* in reflectance of approximately 30%. QE measurements were made at two orthogonal polarizations, to selectively excite the minor and major axis. In each case a strong decrease in photocurrent was found, centred at different wavelengths for each axis, both corresponding to one of the peaks in reflectance. The minor-axis (shorter wavelength) LSP resulted in an enhancement factor of 0.7, while the major-axis (longer wavelength) LSP resulted in an enhancement factor of 0.55. We note that enhancement factors less than 1 correspond to a reduction of photocurrent, for example a 50% reduction of photocurrent results in an ‘enhancement’ factor of 0.5. FEM simulations identified the two major loss mechanisms as absorption of light by the nanoparticle and backscattering. Absorption was the dominant process for the minor-axis peak, while back-scattering was the dominant process for the major-axis peak.

Studies have also been performed on non-silicon inorganic solar cells. Nakayama *et al.* deposited Ag nanoparticles on GaAs solar cells using a porous alumina template *[12]*. The active GaAs layer was only 200 nm thick (substantially thinner than conventional devices) to provide a weakly absorbing device. The layer was grown on a bulk GaAs wafer, but separated by a region with a high band gap to limit photocurrent generation to the top, thin GaAs layers. The mean diameter of the Ag nanoparticles was 110 nm, and the height was varied to provide hemispherical and conical particles. Suppression of photocurrent was observed for wavelengths below 600 nm (but most significant < 400 nm), while a moderate improvement was found for wavelengths above this. Overall, an 8% increase in short circuit current density was achieved. The authors identify back-scattering and absorption by the nanoparticles as the primary loss mechanisms.

Yang *et al.* studied the effect of depositing Au nanoparticles onto the top surface of a triple junction InGaP/InGaA/Ge solar cell *[226]*. In contrast to all other studies of metal nanoparticles on inorganic devices, the authors used extremely small Au nanoparticles with an average diameter of 1.9 nm. These were produced by chemical synthesis, and deposited by simple drop-casting. The authors report a 15.3% increase in conversion efficiency (from 19.6% to 22.6%) after deposition of the nanoparticles. Photoluminescence was found to increase by factors varying from 1.5 to 2.0. The authors plot three points of PL enhancement versus photon energy, and fit this to a plot of radiative efficiency, calculated using the quasi-static approximation. The authors suggest that the excellent agreement between PL enhancement and modelled radiative efficiency confirms that the enhancement is due to scattering of light by the nanoparticles. Additionally, the authors claim that small nanoparticles provide a larger enhancement in photocurrent than the larger nanoparticles used in previous studies by other groups. However, the authors do not state for which particle size the radiative efficiency calculation is performed, and no relevant scale is given on the graph (radiative efficiency has values from 0 to 1, but the scale presented is for “enhancement”, and is plotted for values from 0 to 6). Both Mie theory and the quasi-static theory clearly show that the radiative efficiency of small (< 20 nm) nanoparticles is nearly zero for the range of wavelengths considered by Yang *et al.*, and therefore scattering can not be the reason for the observed increase in PL signal and solar cell efficiency, assuming the particles are well-separated on the device surface. In fact, Mie theory calculations of the radiative efficiency of a 2 nm diameter Au sphere yield a peak value of 0.00002, with an extinction efficiency of 0.05, suggesting that the particles exhibit only a weak interaction with light, and this interaction is predominantly (> 99.999 %) due to absorption. Although it should be stated that both of these calculations are not strictly valid for such small nanoparticles, the required corrections will not lead to an increase in radiative efficiency. A possible explanation for the observed enhancement is that the nanoparticles aggregated to form much larger clusters during drop-casting. These clusters would exhibit a much higher radiative efficiency, thereby resulting in a scattering-based enhancement. However, no reflection or quantum efficiency measurements were made of the devices, so it is difficult to conclusively investigate the enhancement process.

Numerous authors have suggested the use of non-metallic scattering particles, for example silica or latex nanospheres, in place of metallic nanoparticles. Matheu *et al.* argue that dielectric nanoparticles exhibit zero absorption and a much smaller phase mismatch than metal nanoparticles *[6]*. This hypothesis is supported by their experimental results comparing the effect of depositing either 100 nm diameter Au nanoparticles or 150 nm diameter silica nanoparticles onto *pn* silicon photodiodes. The short circuit current was found to increase by 2.8% for Au nanoparticles, and by 8.8% using silica nanoparticles. Therefore the authors conclude that silica nanoparticles are more suitable for use in solar cells than metal nanoparticles. However, we note a number of crucial points that are not raised in the paper. The first is that the surface coverage of each particle, using the concentration data from the paper these work out as approximately 33% for the silica nanospheres, and 7.8% for the Au nanospheres, and so the comparison is not even. Furthermore, according to Mie theory the scattering efficiency of a 150 nm diameter silica nanoparticle is unity at 300 nm, and falls off sharply for longer wavelengths (0.1 at 600 nm, 0.01 at 900 nm). Therefore the enhancement is most likely not due to scattering. Instead, we propose that the subwavelength-sized silica spheres act as an effective medium, *i.e.* as a planar layer with a refractive index between that of air and silica. A layer of 150 nm diameter silica spheres covering 33% of the surface has the same volume as a 10.7 nm planar layer of SiO_2. Although this is considerably thinner than an optimized SiO_2 anti-reflection coating, it would still lead to a modest reduction in surface reflectance.

The case for dielectric nanoparticles was further promoted by Sundararajan *et al.*, who compared four types of nanoparticle: 120 nm diameter silica spheres; 50 nm diameter Au sphere; core-shells with a 76 nm diameter silica core and a 124 nm diameter Au shell; and core shells with a 196 nm diameter silica core and a 232 nm Au diameter shell *[227]*. Interestingly the group made use of a novel QE measurement system based on a confocal microscope retrofitted with an AFM attachment. In this way the excitation can be localized to diffraction-limited spots, and raster-scanned across the surface to achieve a 2D plot of photocurrent (in a similar manner to LBIC, but with higher spatial resolution *[228]*). The requirement of a laser source restricted the excitation wavelengths to four discrete values: 532 nm, 633 nm, 785 nm and 980 nm. Aligned topographic information was recorded by AFM after the photocurrent scan, and used to identify the size and shape of nanoparticles. By using a sparse coverage of nanoparticles the authors present photocurrent enhancement data for *individual* nanoparticles. Individual nanoparticles were evident in the

2D photocurrent maps, and while silica resulted in enhancement at all four wavelengths, Au nanoparticles resulted in photocurrent suppression at some wavelengths and enhancement at longer wavelengths. The photocurrents were normalized to the average background signal, and a maximum suppression of -15% at 532 nm was found for the smaller core-shell nanoparticle, and a maximum enhancement of +20% at 980 nm was found for the larger core-shell nanoparticle. A large spread in values was found for each nanoparticle type, and the background signal also seems to vary considerably due to the low signal level. Aggregated metal nanoparticles (identified by AFM) were found to reduce photocurrent at all wavelengths. The general trend for Au nanoparticles is similar to that reported by Lim *et al.* Similar sized silica nanoparticles were used as in the study by Matheu *et al.*, and so we again argue that they also have too low an optical cross-section to scatter incident photons.

In a related work to that presented by Matheu *et al.* (and by the same group), Derkacs *et al.* studied the effect of depositing 100 nm diameter Au nanoparticles and 150 nm silica nanoparticles onto a InP/InGaAsP quantum-well (QW) solar cell *[229]*. Their devices feature a series of ten 10 nm thick $In_{0.81}Ga_{0.19}As_{0.4}P_{0.6}$ quantum wells, separated by an equal number of 10 nm thick $In_{0.91}Ga_{0.09}As_{0.2}P_{0.8}$ barrier layers. These were grown on top of a 300 µm thick n-type InP substrate. The InP device absorbs photons up to around 850 nm, and the QWs extend this range to 1200 nm (Fig. 3.7a). The authors report an efficiency increase of 17% for silica nanoparticles, but only an increase of 1% for Au nanoparticles. The photocurrent enhancement ratio for silica is relatively constant from 700 nm to 1200 nm, and does not drop below 1.0 at any wavelength (Fig. 3.7b). The photocurrent enhancement for Au nanoparticles is much more dependent on wavelength. For wavelengths below 900 nm (*i.e.* for photocurrent due to the InP wafer) the photocurrent ratio is very similar to that observed for the same size Au nanoparticles on a silicon photodiode by Lim *et al.* (also by the same group). However the photocurrent ratio sharply increases for wavelengths > 1100 nm (*i.e.* for photocurrent due to the QWs) (Fig. 3.7b). The QWs have a slightly higher refractive index than the surrounding material and so can support slab waveguide modes. The authors attribute the increase in photocurrent at longer wavelengths to scattering into waveguide-propagating modes. However, the refractive index difference between the quantum wells and the surrounding material is relatively small (~0.5) and so photons would need to be scattered to very large angles to achieve total internal reflection. Therefore we would expect a low efficiency of coupling to waveguide modes for this geometry. We note that the photocurrent at 1150 nm is extremely small, and so any increase in path length will appear significant. Therefore we do not believe it is possible to convincingly identify this additional peak as evidence of coupling to waveguide-propagating modes, although this is certainly a possible method. An interesting observation not made by the authors is that no such long wavelength peak occurs for the silica nanoparticles. Therefore it appears that silica nanoparticles reduce surface reflection, but do not scatter (*i.e.* do not improve light-trapping). This supports our claim that small silica nanoparticles act as an effective medium. Au nanoparticles can increase or decrease surface reflection, but also scatter light to propagate through the device at more oblique angles, and potentially into waveguide-propagating modes.

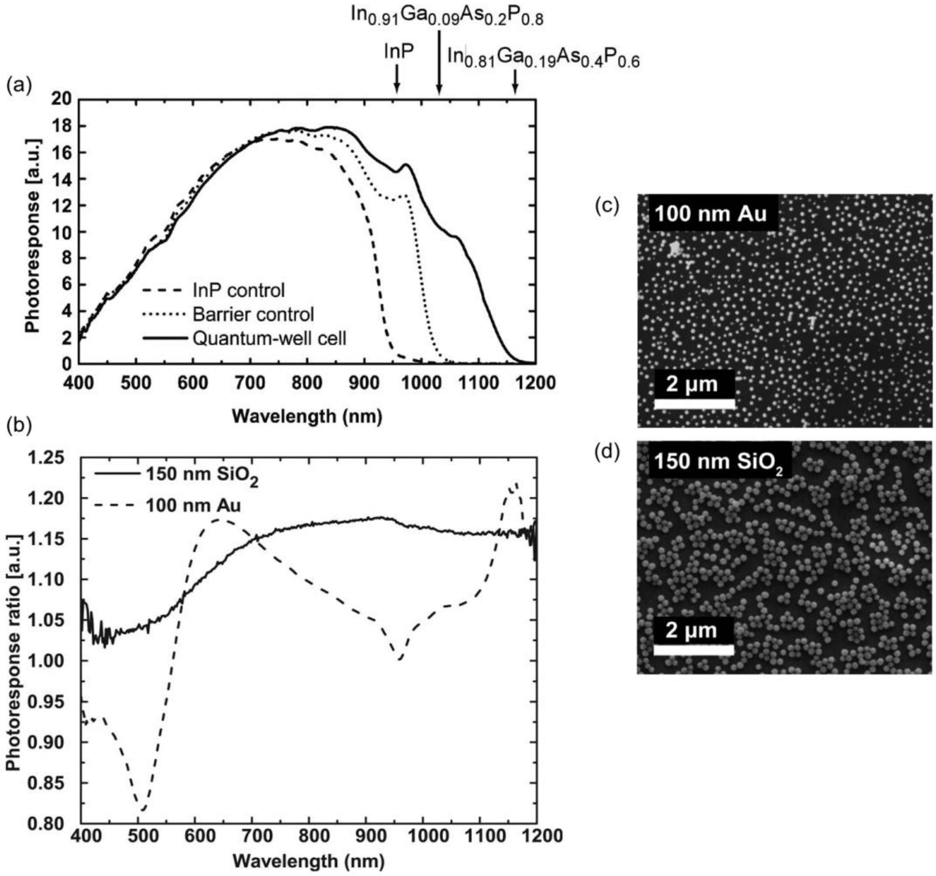

Figure 3.7: (a) Photoresponse, (b) photoresponse ratio, (c) SEM image of Au nanoparticle coating, (d) SEM image of silica nanoparticle coating *[229]*.

3.2 Thin-film devices

Extremely large enhancement factors are found for island films on solar cells based on silicon-on-insulator (SOI) substrates. SOI substrates consist of a bulk silicon wafer separated from a thin silicon layer by a SiO_2 layer *[230]*. SOI substrates are commonly used in microelectronics, but are not suitable for commercial photovoltaics applications due to their high cost compared with other silicon substrates. However they are useful for proof-of-concept studies of thin-film monocrystalline silicon solar cells. For SOI devices the active layer is much thinner than a bulk wafer, leading to greatly reduced absorption in the active layer. However, the planar layer can also act as an optical slab waveguide. Stuart and Hall observed strong photocurrent enhancement for metal island films on SOI photodiodes with 160 nm thick active layer (Fig. 3.8) *[14, 99]*. The peak enhancement was found to centre around 800 nm, far from the on-glass resonance positions of the MIFs investigated. Additionally, the enhancement peak was not strongly spectrally shifted by changes in metal type or mean particle diameter. Pillai *et al.* reported similar results for Ag MIFs on SOI solar cells with 1.25 μm thick active layer (Fig. 3.9) *[13]*. Numerous enhancement peaks were found, and overall enhancement increased with increasing mass thickness of the metal layer. Both groups concur that the effect is due to coupling of light to waveguide propagating modes. This has two effects: increased light-trapping, and a modification of the scattering efficiency at certain wavelengths. This latter effect is now believed to be due to interference effects *[216]*, and not due to waveguide-mediated interparticle coupling, as is claimed in the paper. Increasing the nanoparticle size increases the scattering efficiency, and therefore also the efficiency of coupling to waveguide modes.

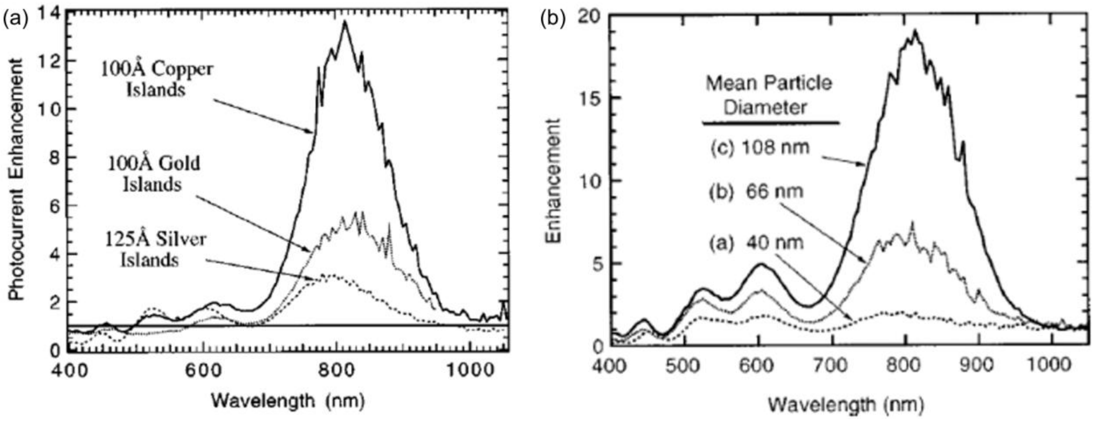

Figure 3.8: Photocurrent enhancement for metal island films on SOI photodiode with 190 nm thick active layer, varying (a) metal type *[14]*, (b) mean particle diameter of Ag island film *[99]*.

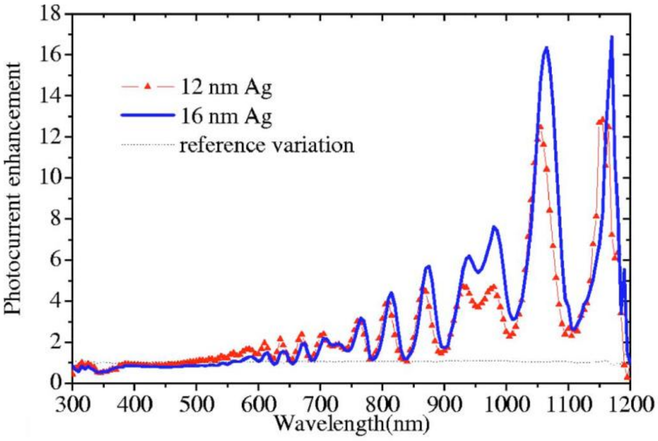

Figure 3.9: Photocurrent enhancement due to Ag island films on SOI solar cells with 1.25 µm thick active layer *[13]*.

Currently SOI substrates are too expensive to consider for commercial photovoltaic applications, but these results may be of interest as Si epitaxy techniques become more flexible and lower cost. Currently non-epitaxial silicon thin-films are of more interest commercially, and these include amorphous silicon (a-Si:H) and microcrystalline silicon (µc-Si:H). The first report of metal nanoparticles on amorphous silicon solar cells was given by

Derkacs *et al.*, who observed an 8.3% increase in efficiency after coating the device with a sparse layer of 100 nm diameter Au nanoparticles *[7]*. However no spectral data on reflectance or QE were presented and so no conclusions can be made about the cause of the observed enhancement.

In a series of more detailed studies Moulin *et al.* investigated the effect of integrating Ag nanoparticles at various positions in a-Si:H and µc-Si:H solar cells. In addition to QE and reflectance measurements, the authors also employed Raman measurements. As the intensity of a Raman signal is proportional to the forth power of the e-field intensity, it can be used to provide a qualitative measure of e-field intensity within the silicon layer. In the first paper the authors reported the effects of depositing a 3 nm Ag island film between the *i* and *n* layers of a 135 nm thick *p-i-n* a-Si:H solar cell *[231]*. The reflectance was found to decrease for wavelengths greater than 600 nm and a two-fold increase in Raman intensity was observed. However, the electrical properties of the device were severely degraded, and a 15.3% decrease in photocurrent was observed. The authors suggest that the metal nanoparticles may act as recombination sites, or introduce defects into the a-Si:H layers. A similar result was given in a later publication for the case of a 3 nm Ag film deposited between the back contact ITO and the *i* layer (Fig. 3.10) *[11]*. The average size of particles in the 3 nm Ag island film was not stated, but from the SEM images appears to be less than 20 nm. These particles will be predominantly absorbing, which would result in both a reduction of QE and of reflectance. The increase in Raman intensity suggests that the particles also enhanced the near-field intensity, but that this does not result in an increase in photocurrent.

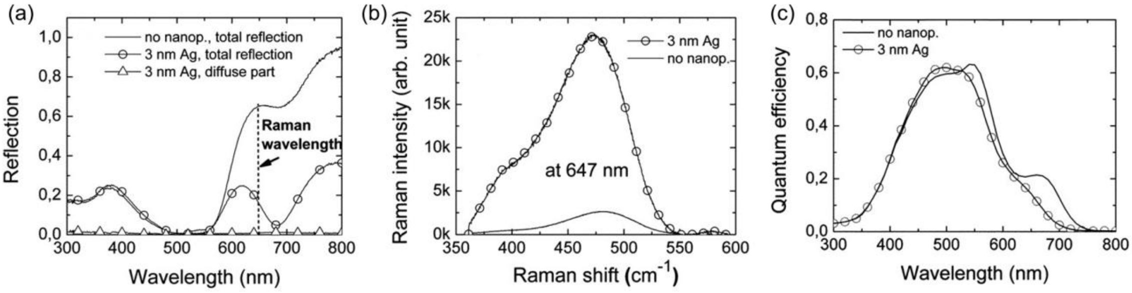

Figure 3.10: Effect of depositing a 3 nm Ag island film on a 160 nm thick a-Si:H solar cell: (a) reflection, (b) Raman intensity, (c) QE *[11]*.

Moulin *et al.* also studied the effect of integrating a 20 nm Ag island film in the rear reflector of a µc-Si:H solar cell, with an active layer thickness of 1000 µm *[10, 11]*. The average particle size was not stated, but we estimate it to be larger than 100 nm from the AFM images. The authors report a sharp drop in reflectance at long wavelengths, from approximately 85% to 25%, but only a relatively modest increase in QE. Therefore the authors conclude that the primary mechanism that reduces reflectance does not lead to an increase in QE. It is possible that the nanoparticles are coupling light into propagating plasmon modes in the rear contact, where they are dissipated as heat. In addition, the electrical properties of the device were slightly degraded by the presence of the metal nanoparticles. The authors attribute this to a change in the μc-Si:H growth process due to the nanoparticles, but we note that the nanoparticles are not separated from the silicon layers (*e.g.* by an ITO over-layer), and so diffusion of Ag into the active layer or recombination at the particle surface are also possible explanations.

3.3 Discussion of the enhancement of inorganic solar cells by metal nanoparticles

Interpretation of results is complicated by several factors, including incorrect or misleading interpretation of data and incomplete characterisation. In addition, only a relatively small amount of parameter space (device type, particle size and shape, particle location within the device) has been investigated to date. To clearly identify the role of metal nanoparticles on the efficiency of a given device we ideally require information on the nanoparticle size and shape (*i.e.* SEM inspection), and reflectance, QE and IV measurements. However in most of case one or more of these measurements are lacking, which makes conclusive interpretation of the results challenging.

The trend in the literature is to judge the relative merits of nanoparticle schemes by their maximum photocurrent enhancement factor, which is the ratio of the photocurrent of an uncoated device to the photocurrent of a device coated with metal nanoparticles (*i.e.* $I_{coated} / I_{uncoated}$). This can be extremely misleading as it tends to minimize the appearance of negative effects and exaggerate the positive effects (particularly for weakly absorbed photons). For ratio plots the loss scale is bounded from 0 to 1, but the gain scale is unbounded and can be many decades. A fairer form of normalization is to subtract the photocurrent of the coated device from the photocurrent of the uncoated device. This way the losses and gains are plotted to the same scale, with losses negative and gains positive.

Analysis of the current literature leads us to conclude that scattering of light by metal nanoparticles is the only relevant efficiency enhancement mechanism for conventional silicon solar cells. Several theoretical studies have suggested that direct carrier injection from metal nanoparticles into silicon will lead to an increase in device efficiency *[232, 233]*, but there is currently no experimental evidence to support this claim. For direct carrier injection the nanoparticles must be embedded within the active layer. This was attempted by Moulin *et al.* and resulted in severe degradation of the electrical properties of the device *[231]*. Embedding metal nanoparticles into the active layer creates additional recombination sites, and the metal can diffuse into the semiconductor material to create trap states. Although passivation of the nanoparticles by a thin dielectric layer may help alleviate these problems, carrier-injection does not seem to be a promising method of enhancement. For similar reasons, electric-field confinement also seems an improbable enhancement mechanism, despite simulation studies that support this approach *[234, 235]*. Importantly, we note that simulation studies usually do not consider the effect of defects and trap states within the silicon layer. The field enhancement drops off exponentially, and so absorption will primarily be increased in the semiconductor material closest to the nanoparticle –*i.e.* in an area most likely to have increased recombination and/or defects. E-field enhancement has been studied using Raman spectroscopy, and was not found to correlate with device efficiency enhancement *[11]*. However, the particles used in this study were not ideally suited to e-field enhancement, and so it is possible that further progress could be made by employing optimized particle geometries. Closely-spaced particles or particles with large radii of curvature (*e.g.* triangles, pyramids) would provide a larger e-field enhancement, but absorption by the particle would also need to be minimized.

It is our view that absorption by the nanoparticle acts as a loss mechanism and e-field enhancement is either unimportant or can also act as a loss mechanism. Scattering of light by metal nanoparticles can improve efficiency in one of two ways: by reducing front-surface reflection, and/or by improving light-trapping. Therefore, we require metal nanoparticles that exhibit high scattering (*i.e.* have a high radiative efficiency) at wavelengths where the solar cell is most weakly absorbing, and low absorption across the solar spectrum. For metal nanoparticles situated on the front surface of a solar cell, back-scattering also acts as a loss mechanism and so must be minimized.

Absorption losses can be eliminated by using dielectric nanoparticles instead of metal nanoparticles. However, as the scattering of dielectric nanoparticles is due to geometry instead of excitation of LSPs, it is a much weaker process for small (< 300 nm particles), and cannot easily be spectrally tuned. The enhancement results for dielectric nanoparticles that are presented in the literature most likely arise due to an effective medium based reduction of surface reflectance. Given the high refractive indices of semiconductors almost any dielectric layer will serve to reduce surface reflection, and therefore increase photocurrent.

3.4 Optimization of metal nanoparticles for silicon solar cell applications

To date there has been little effort to optimize or systematically investigate the size of nanoparticles for solar cell applications, and many studies make use of Au nanoparticles with diameters of 100 nm or less. The low radiative efficiency of this size particle and issues with interband transitions in Au at short wavelengths make it far from the optimum choice of nanoparticle for enhancement of solar cell efficiency.

Stuart and Hall used quasistatic theory to demonstrate that a high radiative efficiency (defined as the ratio of scattering to extinction) can be obtained by increasing the size of Ag nanoparticles, and can exceed 80% for metal nanoparticles with a diameter greater than 100 nm *[99]*. Considerably lower radiative efficiencies were found for Au and Cu at all wavelengths studied. This is surprising given the similarity of the dielectric constants of Ag, Au and Cu in the IR, and perhaps suggests an error in the author’s calculations. Cole and Halas used a downhill simplex optimization method to determine optimum distributions of

Ag spheres or core-shells for scattering of the solar spectrum *[236]*. Their calculations allowed for mixtures of up to three different kinds of nanoparticle, with a total surface coverage limited to 40%. The optimum particle distribution for scattering wavelengths between 380 nm and 820 nm was found to be a single type of Ag nanosphere with an overall diameter of 210 nm and a surface coverage of 30%.

In addition to studies focusing on solar cell applications, close parallels may be drawn with optimization of metal nanoparticles for scattering-based biological applications. These require resonances with wavelengths between 700 nm and 1100 nm as both haemoglobin and water have absorption minima in this range (Chp. 8, *[17]*). Biological studies focus on Au nanoparticles, as other metals are less biocompatible. Jain *et al.* studied the simulated optical spectra of Au nanospheres, nanorods and core-shell nanoparticles with the aim of optimizing scattering the IR *[5]*. A relatively small range of particle sizes were investigated, with spheres up to 80 nm diameter and rods up to a an effective diameter of 44 nm. Much larger core-shell nanoparticles were considered, with a total particle diameter up to 300 nm. Sharp increases in the ratio of scattering to absorption were found as the particle size was increased, although very low overall radiative efficiencies were found for rods and spheres. An increase in absorption was noted for increasing the ratio of core diameter to shell diameter (*i.e.* decreasing the shell thickness), but almost no change in scattering to absorption ratio was found for increasing the aspect ratio of nanorods.

Optimization of nanoparticle properties to minimize back-scattering is vital for metal nanoaparticles situated on the top surface of devices, but has not been widely investigated. In vacuum, dipolar LSP modes scatter equally forwards and backwards, while higher order modes become progressively more forward scattering. As such, we would not expect metal nanoparticles to increase the reflectance of a solar cell, but this is often observed experimentally, *e.g.* by Hägglund *et al. [8]*. Therefore the presence of the substrate affects the angular distribution of light scattered by the nanoparticles. Lim *et al.* suggested that the increase in reflectance could be due to interference with non-scattered photons *[9]*. Interference effects occur due to the induced phase delay which is related to the polarizability of the nanoparticle.

Catchpole and Polman studied the theoretical angular scattering distribution of ideal point dipoles *[237]*. They found that ideal dipoles scattering 100% of incident photons into a silicon layer when situated directly on it, but they have a small optical cross-section. The optical cross-section was found to increase with distance from the substrate, but the percentage of photons scattered into the silicon layer decreases (Fig. 3.11a). Further work by Catchpole and Polman used FDTD simulations to model the scattering of light by Ag nanoparticles separated from a substrate by a 10 nm SiO^2 layer *[238]*. Considerably lower coupling efficiencies were found than for the point-dipole, with a general trend relating the contact area of the nanoparticle with the fraction of light scattered into the silicon (*i.e.* disc-like particles couple more than spherical particles) (Fig. 3.11b). Numerical simulations by Hägglund *et al.* suggested that increased back-scattering can occur if the upper and lower parts of a nanoparticle oscillate out of phase *[8]*. For the case of a disc-like particle in direct contact with the substrate the upper and lower internal fields were found to be different due to the influence of the substrate on the lower part of the particle. Therefore the authors suggest that spherical particles are preferable to disc-like particles, as they have a smaller contact area with the substrate. Their simulation results agreed with this assumption, showing that discs are highly back-scattering, while spheres are predominantly forward-scattering above ~550 nm. Alternatively the authors suggest the use of a thin dielectric layer to mediate coupling with the substrate for disc-like nanoparticles, which can also reduce back-scattering.

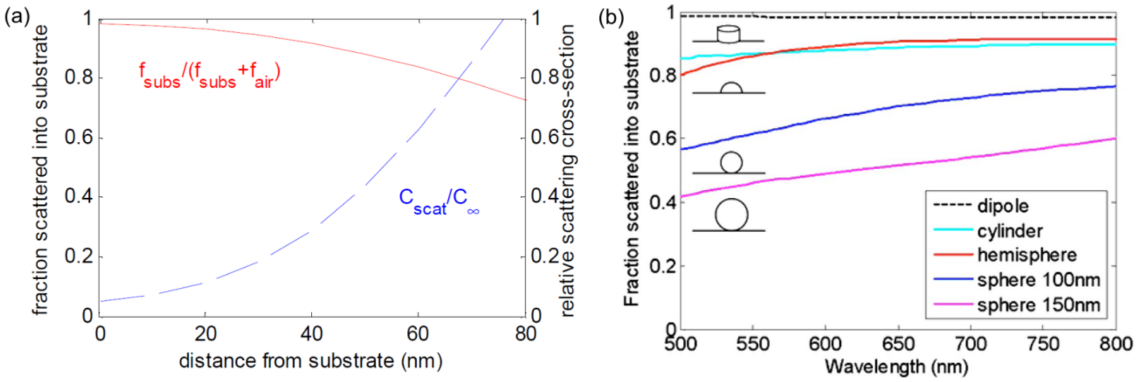

Figure 3.11: (a) Fraction of light scattered into silicon substrate by an ideal point dipole *[237]*, (b) Fraction of light scattered into a silicon substrate by Ag nanoparticles situated on a 10 nm SiO_2 layer *[238]*.

Clearly the results of Hägglund *et al.* and Catchpole and Polman are contradictory. We note that both studies investigated different metals (Au for the former, Ag for the latter), and that the shapes investigated by Catchpole and Polman had differing volumes. However, we can at least conclude that both studies show that substrates have a strong effect on the angular distribution of scattering by metal nanoparticles. This is further demonstrated by FEM simulations by Sundararajan *et al.*, who show vortex behaviour of the Poynting vector (*i.e.* power flow) around Au nanoparticles on a silicon substrate (Fig. 3.12). Further investigation is required to fully elucidate the optical properties of metal nanoparticles on silicon substrates. However, we can see that the 3D shape of the nanoparticle and the separation of nanoparticle from the substrate are crucial parameters to minimize back-scattering.

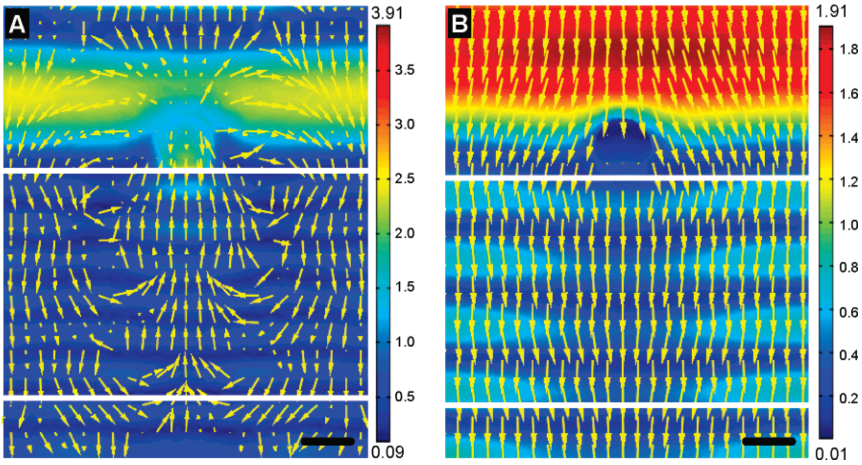

Figure 3.12: Poynting vector field plots of Au nanoparticle on Si slab at (a) 633 nm (b) 980 nm *[227]*. The upper and lower white lines denote the substrate surface and a depth of 500 nm within the substrate, respectively.

3.5 Conclusions

The interaction of metal nanoparticles with solar cells is a complex function of the particle size, shape and composition, and also of the position of the nanoparticle within the device. Integration of metal nanoparticles with inorganic solar cells can both enhance and suppress photocurrent, depending on the device geometry and the incident wavelength. Integration of metal nanoparticles has been demonstrated for the following device types: crystalline silicon, ultra-thin crystalline silicon (SOI), amorphous silicon, microcrystalline silicon, GaAs, triple junction InGaP/InGaA/Ge, and InP/InGaAsP QW solar cells. The predominant design is that of ~ 100 nm Au nanoparticles situated on the front surface of a device, which is far from optimal. Further improvements are expected for optimized nanoparticle size, shape and placement.

Enhancement of photocurrent is primarily due to scattering of light by the nanoparticles. Reduction of photocurrent is due to absorption by the nanoparticle, back-scattering of light, or by degradation of the electrical properties of the semiconductor material. Further work is required to optimize the design of metal nanoparticles for silicon solar cell applications.

Chapter 4

Simulated optical properties of metal nanoparticles

The optical properties of metal nanoparticles are highly dependent on the particle size, shape, chemical composition, and the local dielectric environment. Therefore it is possible to selectively tune these properties to suit a given application. For silicon solar cell enhancement, we require high scattering and low absorption across the solar spectrum. Scattering in the near-infrared (NIR) is particularly desirable as this is where conventional light-trapping techniques for thin-film devices perform poorly (Fig. 1.4).

Although many studies have explored the optical properties of metal nanoparticles using simulations, there has as yet been no cohesive investigation of the optical properties across a broad range of all parameters. In particular, the relative contributions of absorption and scattering are usually overlooked in favour of overall extinction, but these are of critical importance for solar cell applications. We define the radiative efficiency (also known as the scattering yield) as the ratio of scattering to extinction. A value of 1 denotes an entirely scattering particle, while a value of 0 denotes an entirely absorbing particle. For solar cell applications we wish to achieve extinction peak positions across the solar spectrum, with corresponding radiative efficiencies close to unity.

The magnitude of the extinction efficiency is also an important parameter. For inorganic solar cell applications the optimum configuration is a sub-monolayer of particles on the front or rear surface of the device. This maximises interaction with the device, and minimizes multiple particle interactions. As the extinction efficiency of metal nanoparticles often exceeds unity it is possible for a submonolayer to interact with all incident photons. The minimum surface coverage to achieve 100% interaction is defined by the extinction efficiency: an extinction efficiency of 10 requires a minimum surface coverage of 10%, while an efficiency of 5 requires a minimum surface coverage of 20%. Most fabrication techniques can readily achieve surface coverage of up to 30% to 40%, and so we require extinction efficiencies of at least 2.5 to 3. Larger extinction efficiencies are desirable as this allows the mixing of multiple particle types. For example, we can mix two nanoparticle types that interact with different parts of the solar spectrum provided they both have extinction efficiencies greater than 5 (*i.e.* a surface coverage of 20% for each type, resulting in a total surface coverage of 40%).

In this chapter we explore the trends in the optical properties of metal nanoparticles, with the aim of optimising the design of metal nanoparticles for silicon solar cell applications. We explore the optical properties of four major particle groups: spheres, coated spheres, spheroids and prisms. Simulations were performed using Mie theory and the discrete dipole approximation (DDA). Identical refractive index data and interpolation methods were used for all techniques, enabling direct comparison of results from different simulation methods.

The effects of near-field and far-field coupling are not considered in this chapter. The simulations presented are for the case of isolated nanoparticles, which are valid for randomly orientated arrays of nanoparticles with interparticle spacing greater than the particle size. We expect some deviation from these results for moderately high surface coverage (> 20 %) but a full study of these effects is beyond the scope of this work. A red-shifting of the extinction peak is expected for interparticle spacing of the order of the particle diameter or less (see Section 2.4.7). We limit our consideration of the surrounding medium to non-absorbing material with a refractive index ranging from 1.0 to 2.0. In typical solar cells the surrounding environment with likely be a passivation layer of SiO_2 (n = 1.5) or Si_3N_4 (n = 2.0) in the case of c-Si, and a TCO layer such as ITO (n = 2.0) in the case of a-Si:H. All of the particle geometries considered can feasibly be produced by current fabrication methods.

4.1 Simulation methods

Mie theory codes BHMIE and BHCOAT from Bohren and Huffman were used to simulate the optical properties of spheres and coated spheres respectively *[25]*. An implementation of the separation of variables method (SVM) by Voshchinnikov and Farafonov was used to simulate the optical properties of spheroids *[34]*. Finally, prism-shaped particles were simulated using an implementation of DDA, DDSCAT 6.1, by Draine and Flatau *[37]*. All codes were adapted to use the same wavelength looping and refractive index interpolation code. Refractive index data was obtained from Palik (see Section 9.1.2) and fitted using parabolic interpolation *[29, 30]*. Peak positions were found by identifying the highest value turning point of each spectrum. Dimensionless extinction efficiencies were calculated by dividing the calculated cross-sections by the ‘shadowing area’ of the particle. The shadowing area is defined as the largest cross-section through a plane of the particle that is perpendicular to the illumination direction. Note that this is different to the default output of DDSCAT, which uses the cross-sectional area of a sphere with equal volume to the particle. This latter approach gives misleading values, particularly for the case of large, flat particles. A comparison between DDA and Mie theory is given in the Appendix (Section 9.1.3).

Mie theory and SVM simulations were performed at 1 nm intervals from 200 nm to 1200 nm. DDA simulations were performed over the same range, but at an interval of 10 nm due to the greatly increased computation time.

Simulations are restricted to nanoparticles with diameters above 10 nm, and so finite size effects are not considered. However, we note that thin shells or layers may be subject to surface scattering effects, which are not included in our simulations. The effect of surface scattering is to damp the resonance, and so the spectral positions presented here are still expected to be valid. None of the particle sizes investigated are large enough to induce rounding errors in the Mie theory codes used. Extinction peaks occurring at wavelengths longer than 1200 nm have been discarded from all summary plots, due to inaccuracies caused by a discontinuity at around 1250 nm in refractive index data for Au and Ag given by Palik. Although this problem could have been alleviated by smoothing algorithms or by use of a different data source, peak positions greater than 1200 nm are currently not of interest for Si-based applications. Wavelengths greater than 1200 nm may be of interest in the future for multi-junction devices, but these are beyond the scope of this work.

4.2 Dielectric spheres

First we begin with a brief discussion of the optical properties of dielectric nanoparticles. Dielectric spheres are non-absorbing (*i.e.* have a radiative efficiency of unity) across most of the solar spectrum, and so have been proposed by numerous authors as a more suitable scattering medium than metal nanoparticles *[227, 229]*. However, to date none of the experimental studies have considered the optical properties of dielectric nanospheres using simulation techniques. The scattering of light by dielectric nanoparticles is due to geometry and not excitation of LSPs. The scattering strength of a dielectric nanoparticle is related to the refractive index contrast between it and the surrounding medium, and also to its size (Fig. 4.1a). A 400 nm diameter sphere is required to obtain a high scattering efficiency in the NIR for the case of a particle with a refractive index of 2 in a vacuum. Such large spheres offer little practical benefit over conventional surface texturing approaches as they also result in a substantially roughened substrate. Additionally, it is important to consider the practical dielectric environment in a realistic solar cell. In this case the nanoparticle will either be embedded in the passivation layer (typically SiO_2) or in the encapsulent material (which is typically index-matched to glass). Therefore it is unlikely that the dielectric environment surrounding the nanoparticles will be less than 1.5, and in this case scattering is substantially reduced compared with a vacuum surrounding (Fig. 4.1b). An alternative is to embed low index nanoparticles in a high index layer (*i.e.* air-filled cavities). Although this slightly improves scattering at longer wavelengths, the overall optical interaction is weak.

Metal nanoparticles can exhibit stronger scattering at IR wavelengths with much smaller nanoparticle sizes, and are not negatively affected by the typical dielectric environment present in a solar cell - in fact this provides a highly beneficial effect. However, absorption of light by metal nanoparticles is a potential loss mechanism and so must be minimized.

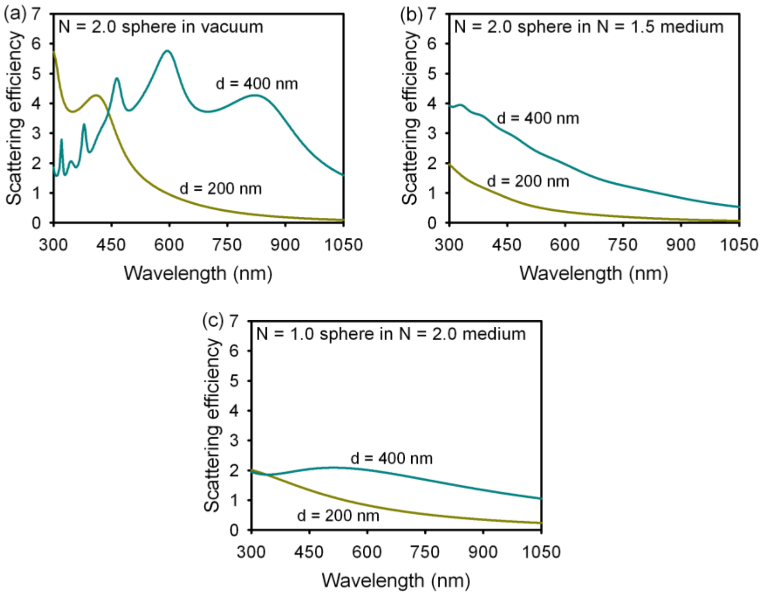

Figure 4.1: Optical properties of dielectric nanospheres.

4.3 Optical properties of metal nanoparticles made from different metals

In the quasisatic limit the spectral position of the LSP resonance is a function of the particle volume and the bulk dielectric function of the metal. Therefore the optical properties of metal nanoparticles are strongly affected by the bulk dielectric of the consituient metal, as we would expect. Figure 4.2 shows plots of extinction, scattering and absorption by 100 nm diameter metal nanoparicles, calculated using Mie theory. All of the metals show a resonant extinction peak, implying the excitation of LSPs. The spectra of Ag, K, Na, Li, Al and Cr all feature scattering-dominated extinction. K gives the strongest optical response, with an extinction factor of nearly 16. The shortest wavelength peak is observed for Al at 300 nm and the longest for K at 610 nm.

The extinction spectra of Al, Pt and Cr are very similar, with a similar spectral position and overall efficiency. However, the scattering and absorption spectra of these metals are markedly different. Al features a high radiative efficiency, while Pt and Cr feature a large absorption component. While most of the metals have near zero extinction at wavelengths greater than 800 nm, Pt and Cr also feature a high absorption component in this region, due to interparticle transitions. An additional minor peak is also seen for Al at around 800 nm, due to a narrow interband region in this region of the spectrum.

Ag features a strong extinction peak, similar to that of Na. Au and Cu have substantially weaker responses, and the structure of the Cu peak is markedly different to the other metals. The resonant peaks of 100 diameter particles of both Au and Cu metals is spectrally very close to their respective interband thresholds. As such, the resulting LSP resonances are substantially damped.

Increasing the particle size red-shifts the LSP resonance wavelength, and so enables investigation of the effect of metal choice for a different part of the spectrum. The extinction, scattering and absorption spectra of 200 nm diameter nanoparticles of each metal are given in Figure 4.3. The extinction efficiencies are generally weaker, broader and red-shifted in comparison with the 100 diameter spheres. The strongest optical cross section is still found for the K nanosphere, but the efficiency has halved to 8 in comparison to the 100 nm sphere. Only Au and Cu nanoparticles exhibit a larger extinction efficiency at 200 nm than 100 nm, due to red-shifting of the peaks away from the respective interband transition regions. The red-shifted peaks of the 200 nm diameter nanoparticles also reveals the remarkable similarity of the optical properties of the noble metals at wavelengths above 700 nm. This is because the dielectric functions of these metals are very similar in the NIR.

In addition to red-shifting the peak position, the radiative efficiency is generally increased for the larger particles. Most of the 200 nm spheres feature extremely low contributions from absorption. Au, Cu and Li see a sharp rise in absorption below their respective interband transition thresholds, but otherwise exhibit a high radiative efficiency. The larger Pt and Cr nanoparticles still feature relatively high absorption across the solar spectrum, with radiative efficiency dropping below 0.5 above a wavelength of 1000 nm. Most of the 200 nm spheres feature multiple peaks due to the excitation of higher-order modes. The higher-order modes exhibit stronger absorption than the dipolar mode, leading to a small increase in absorption at shorter wavelengths.

Nanoparticles of all metals feature extinction efficiency peaks of 3 or higher, and so can be used in sub-monolayers while maintaining 100% optical interaction. However, the scattering peaks are much lower than 3 for Pt and Cr, even for particles with a diameter of 200 nm. Therefore Pt and Cr are most likely not suitable for use in scattering-based applications. The alkalai metals are highly reactive and therefore not suitable for use in practical experiments or devices. We present them here only as an indication of the optical properties of free-electron metals. Therefore, of the metals studied only Ag, Au, Cu and Al are promising candidates for solar cell applications. For the remainder of this chapter we will focus on Ag and Au. Ag exhibits the highest extinction efficiency of the transition metals, and is widely studied. We include Au to investigate the effects of the interband threshold region, which also affects Cu and Al.

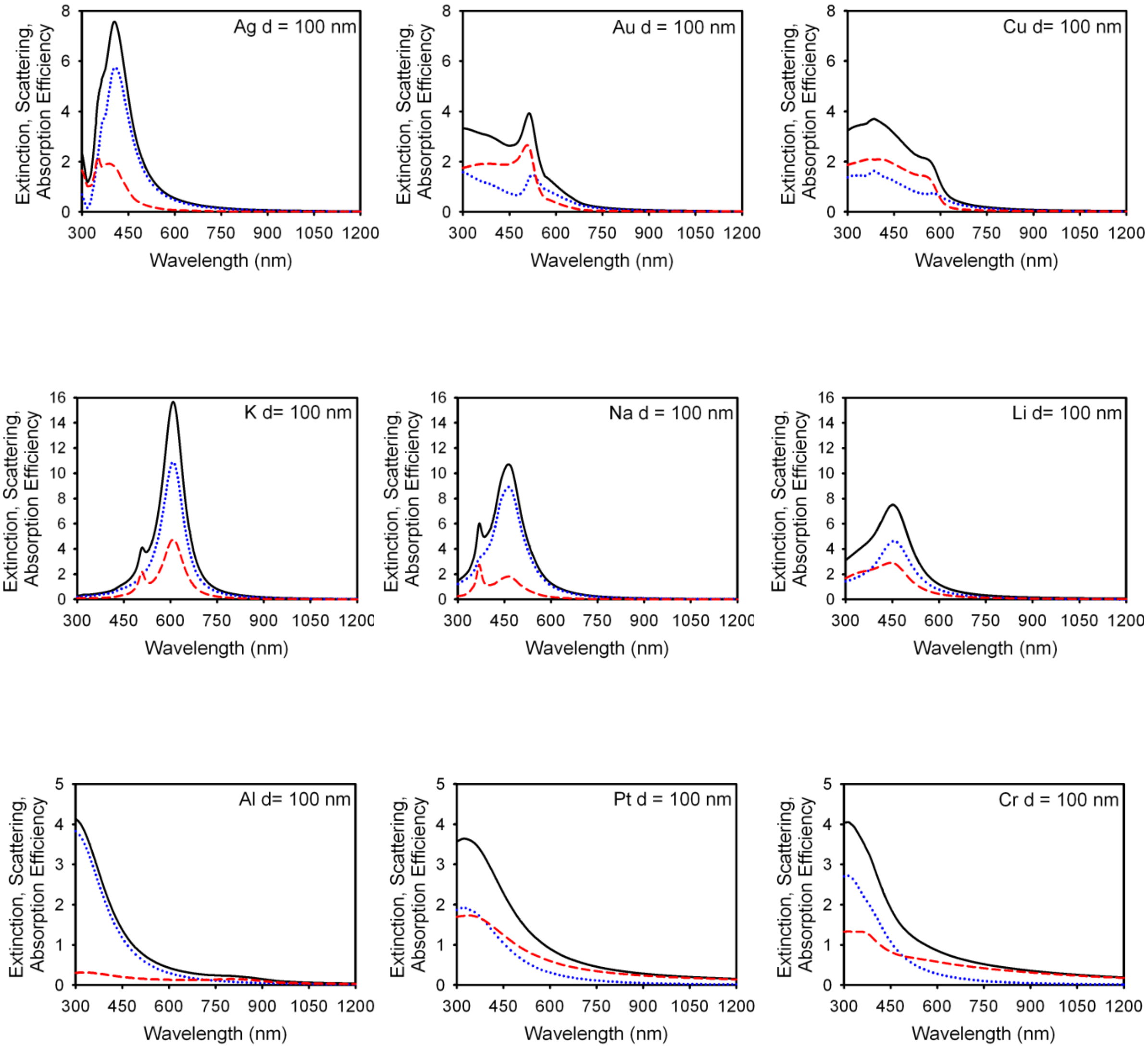

Figure 4.2: Simulated optical extinction (black lines), scattering (blue lines) and absorption (red lines) efficiencies of 100 nm diameter metal spheres. Note the differences in y-axis scaling.

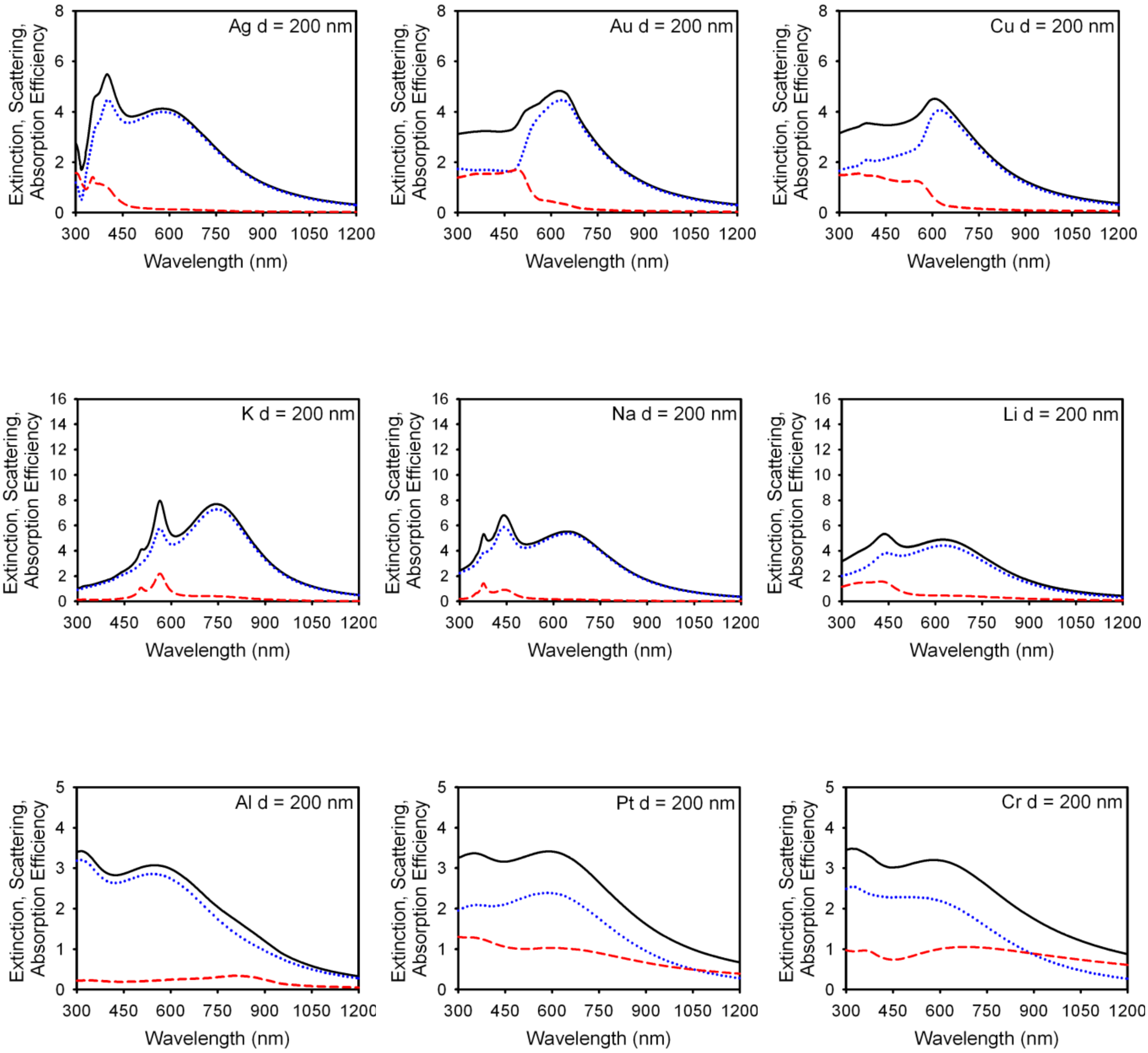

Figure 4.3: Simulated optical extinction (black lines), scattering (blue lines) and absorption (red lines) efficiencies of 200 nm diameter metal spheres. Note the differences in y-axis scaling.

4.4 Effect of particle size and dielectric environment

Extinction spectra of Ag and Au spheres with three different diameters are given in Fig. 4.4. For Ag spheres the peak is broadened and attenuated with increasing diameter. The 50 nm Ag particle has a peak extinction efficiency nearly double that of the 250 nm particle. For Au the smallest sphere exhibits a very weak response, which is considerably strengthened for larger diameters. The peak position of the smallest Au sphere is very close to the interband threshold, which weakens the plasmon resonance. Resonances further away from the threshold, *i.e.* those for larger particle sizes, are not attenuated by interband effects. Above 750 nm the spectra of Au and Ag particles are nearly identical, due to similarities of their dielectric functions in this wavelength range.

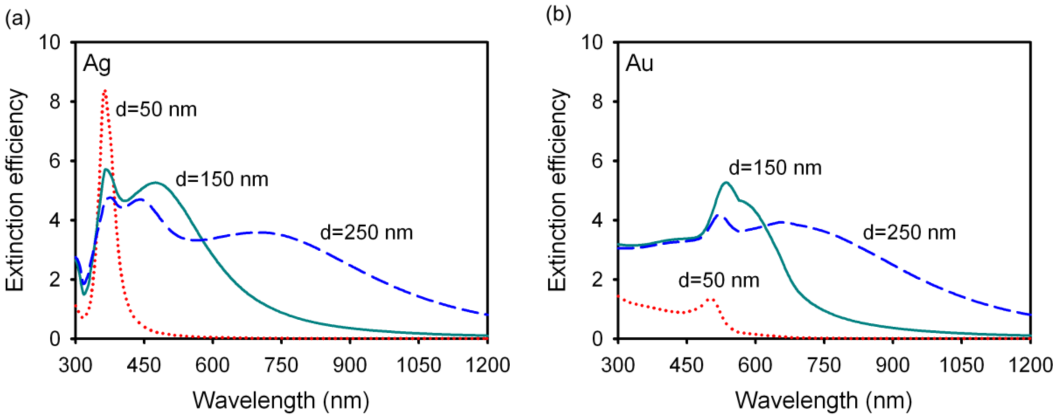

Figure 4.4: Simulated optical extinction spectra of Ag and Au spheres with diameter 50 nm, 150 nm and 250 nm, in vacuum.

Increasing the refractive index of the surrounding medium linearly red-shifts the extinction peak, and the magnitude of this red-shift increases with particle size (Fig. 4.5). For a 50 nm Ag sphere the peak is red-shifted by 195 nm per refractive index unit, while for a 300 nm sphere this increases to 860 nm per refractive index unit. The extinction peak is also red-shifted with increasing particle diameter, and this dependence is linear for particles larger than 150 nm, with a red-shift of 36 nm for every 10 nm increase in diameter. For Au the dependence on refractive index is not linear for resonances below 700 nm due to attenuation and modificaiton of the extinction peak by interband-related effects. The minimum peak position is 362 nm for Ag and 502 for Au, with maximum values exceeding 1200 nm for both metals.

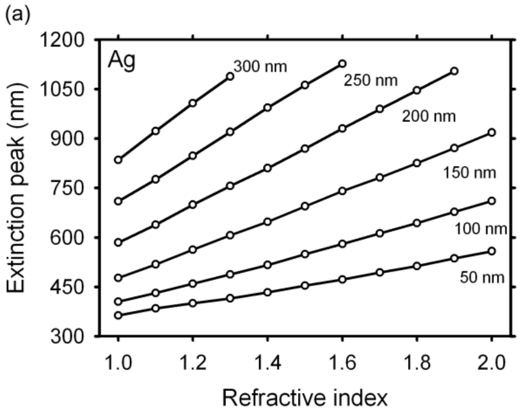

Figure 4.5: Extinction peak position of Au and Ag spheres as a function of refractive index and diameter.

In addition to peak position, the nanoparticle size and the refractive index of the surrounding medium also affect the magnitude of the extinction efficiency and the ratio of scattering to absorption. The trends for an embedding medium of n = 1.5 are given in Fig. 4.6. Ag exhibits a peak extinction efficiency of 12.4 at a sphere diameter of 43 nm, while Au peaks at 8.8 for a sphere size of 87 nm. For Ag spheres scattering becomes the dominant mechanism for diamters above 50 nm, and for Au the cross-over occurs at 75 nm. Absorption becomes almost negligible for spheres larger than 150 nm diameter for both metals. The peak extinction efficiency for Ag occurs with a high absorption component, and low absorption is only achieved at relatively low extinction efficiencies.

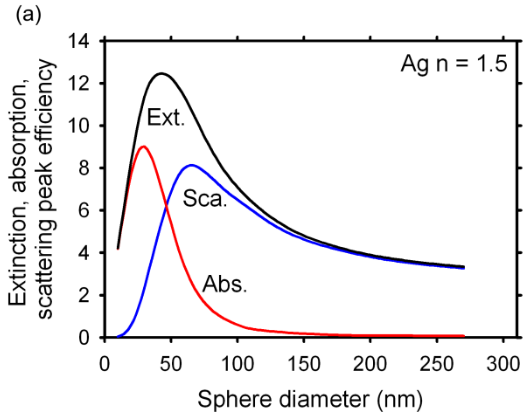

Figure 4.6: Relative contribution of absorption and scattering to extinction as a function of diameter.

Expanding these trends for other embedding media shows that for Ag spheres the extinction peak efficiency increases in size and occurs at smaller diameters for increasing refractive index (Fig 4.7a). A maximum extinction efficiency of 16.7 is seen for a sphere size of 30 nm embedded in a medium with n = 2.0. The cross-over from absorption-dominatated to scattering-dominated extinction occurs at smaller diameters for increasing refractive index. The maximum radiative efficiency occurs for the largest particle diameter, with a peak value of around 0.98 for all embedding media (Fig. 4.7b). For a given particle diameter, the radiative efficiency increases with increasing refractive index, but this effect is negligible for particles larger than 200 nm.

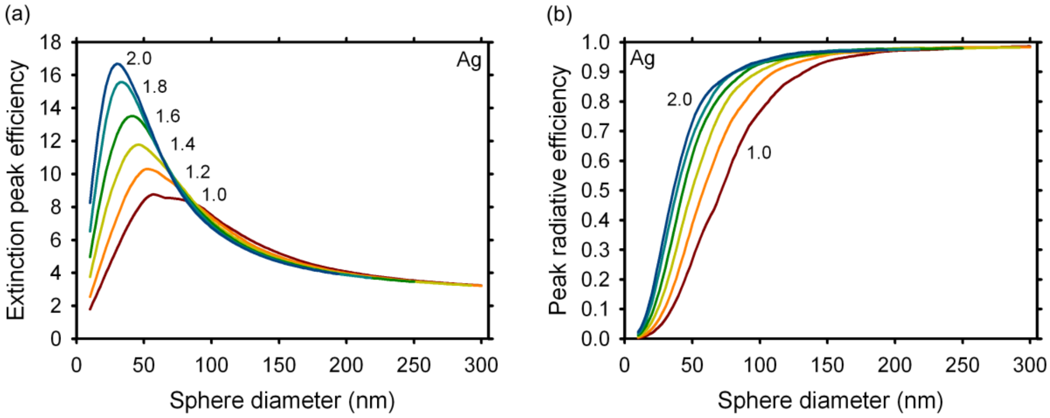

Figure 4.7: Trends of (a) extinction peak efficiency and (b) peak radiative efficiency for Ag spheres as a function of diameter and surrounding refractive index.

4.5 Higher-order modes

For small nanoparticles only dipolar modes are excited as the phase of the incdient wave is nearly constant across the particle surface. As the particle size is increased the wave becomes retarded across the particle surface, leading to excitation of higher-order modes. In Mie theory calculations the mode order is defined by the sufficies of the parameters a_n and b_n. Truncation of the series leads to restriction of the number of contributing modes used for the calculation. Therefore by truncating the series at n = 1, 2, 3 *etc.* the relative contribution of dipolar, quadrupolar, octupolar *etc.* modes can be identified. For simplicity we will focus on Ag spheres in this section.

Figure 4.8 shows the calculated extinction spectrum of a 150 nm diameter Ag sphere embdedded in a medium with n = 1.5. The spectrum exhibits three distinct peaks. Separation of the spectrum into modal contributions shows that the peaks are due to separate dipolar (I), quadrupolar (II) and octupolar (III) excitation (Fig. 4.8a). The peaks become smaller and more blue-shifted as the order is increased. The overall extinction spectrum is the superposition of all three peaks. Although the quadrupolar peak appears strongest in the extinction spectrum, the dipolar mode is seen to be dominant when the individual contributions are separated. Analysis of the separate scattering and absorptiong spectra shows that the dipolar mode is predominantly scattering, the quadrupolar mode contributes to both scattering and absorption, and the octupolar mode is predominantly absorbing (Fig. 4.8b).

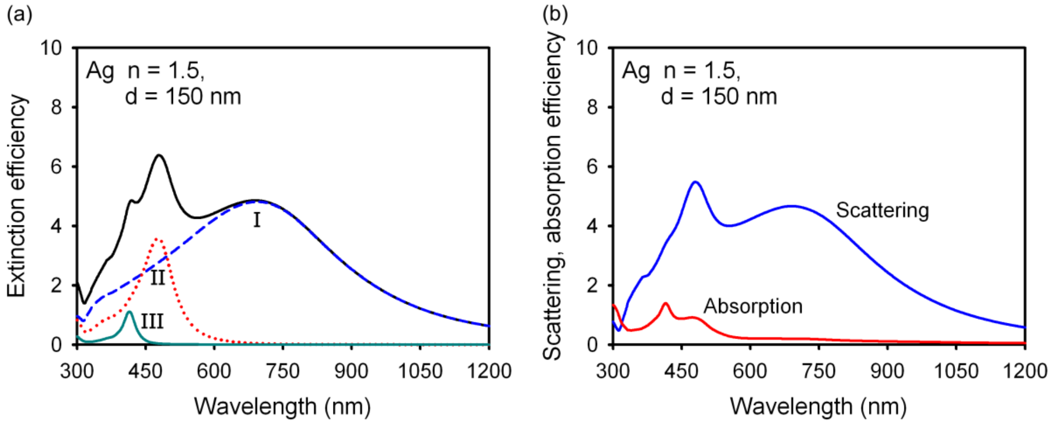

Figure 4.8: (a) Contribution of higher order modes to extinction, (b) resulting absorption and scattering.

An analysis of peak position reveals that successively more orders become excited as the sphere diameter and/or refractive index is increased (Fig. 4.9). Modes up to order 5 are recorded for the largest nanoparticles (d > 225 nm) embeded in a medium with n = 1.5. Higher-order peaks are red-shifted in a similar manner to the dipolar peak, but the relative shift is smaller for a given increase in diameter or refractive index. The relative spectral position of the different orders is always fixed such that the longest wavelength peak is dipolar, and then higher order peaks occur at successively shorter wavelengths.

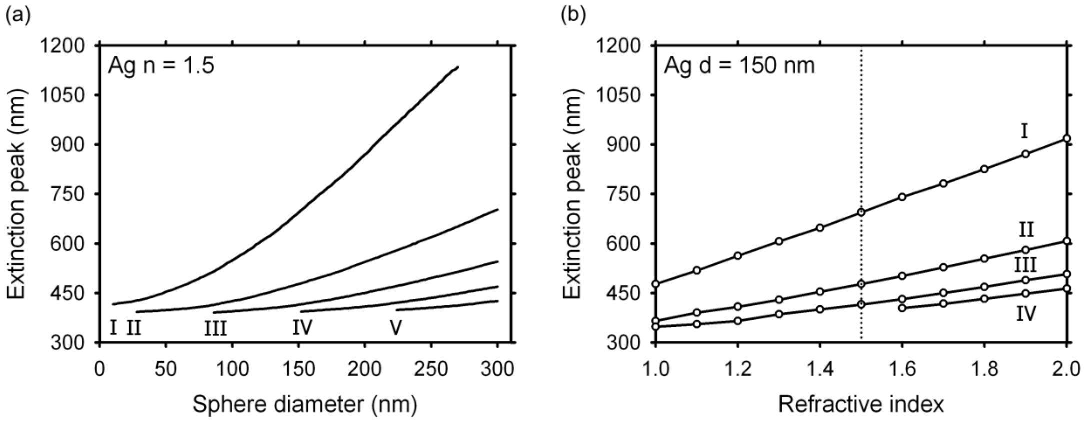

Figure 4.9: Peak position of higher order modes as a function of (a) diameter and (b) refractive index. Excitation orders are denoted by Roman numerals. Each mode is only plotted if it contributes 0.1 or more to the extinction efficiency.

The results presented in Fig 4.8 indicate that higher order modes have a considerably lower radiative efficiency than dipolar modes, and also that their relative contribution to extinction is weaker. Figure 4.10a shows that higher orders also experience extinction efficiency maxima, and these occur at larger diameters as the order is increased. The excitation strength of a given mode never exceeds any lower order mode, *e.g.* the contribution of the octupolar mode is always lower than that of the quadrupolar mode. It is important to note that higher order excitations are important even for relatively small particles. For a 100 nm Ag sphere the quadrupolar mode has nearly half the extinction efficiency of the dipolar mode. This contribution may not always be evident on extinction spectra, particularly when the dipolar and quadrupolar peaks have similar spectral positions. Interestingly, the radiative efficiency of higher-order modes is seen to increase with sphere diameter (Fig. 4.10b). This increase is slower for each successive mode, but high radiative efficiencies can still be achieved for higher-order excitations. For an embedding medium of n = 1.5, the dipolar mode is predominantly scattering for diameters above 47 nm, the quadrupolar mode is predominantly scattering for diameters above 113 nm, and the octupolar mode is predominantly scattering for diameters above 185 nm.

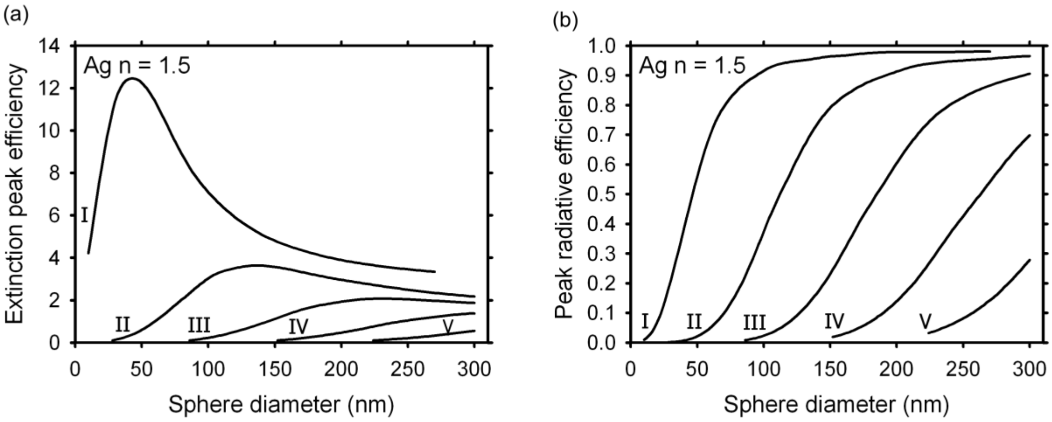

Figure 4.10: (a) Peak extinction efficiency and (b) radiative efficiency as a function of diameter.

4.6 Coated (core-shell) spheres

A coated sphere, also known as a core-shell nanoparticle, offers an additional tuning mechanism in the form of intraparticle coupling between the inner and outer surface. This effect is strongest in the case of a metal coating on a dielectric sphere, and therefore this is the geometry we will focus on. Different LSP excitations occur on the inner and outer surfaces, which hybridize to produce the overall extinction spectra. The coupling strength is determined by the shell thickness, leading to a red-shift for decreasing shell thickness (Fig. 4.11).

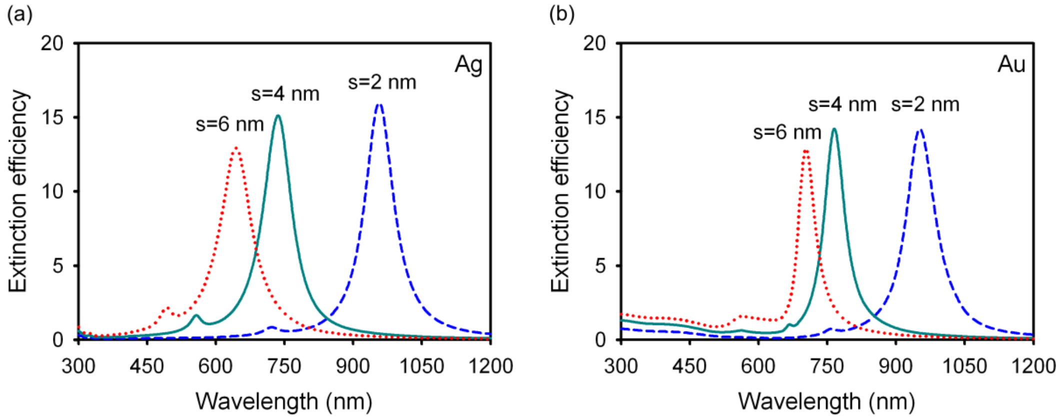

Figure 4.11: Simulated optical extinction spectra of Ag and Au shells of thickness 2 n, 4 nm, 6 nm on vacuum cores of diameter 100 nm.

Figure 4.12 gives an overview of the influence of core diameter size and shell thickness on the extinction peak position of a core-shell nanoparticle. Two peak-shifting regimes are observed. For shell thicknesses over 30 nm, the peak positions red-shifts with increasing shell thickness, and the peak positions are nearly identical to those for solid spheres of identical overall diameter. Below 30 nm the peak position red-shifts with decreasing shell thickness, with the largest shifts occurring for the thinnest shells. The shortest wavelength resonance of a given core diameter occurs at a shell thickness between the two regimes. For a given shell thickness the peak position is red-shifted for increasing core diameter. The Au trends are similar to Ag for peak positions above 750 nm, but below this are distorted by interband effects.

The two trend regimes are due to the coupling strength of the inner and outer surfaces of the shell. For a thick shell the two surfaces are poorly coupled, and so the outer surface resonance dominates the optical response. This resonance is identical to that of a solid sphere of the same overall diameter, and so the peak position red-shifts with increasing shell thickness, and therefore also with increasing overall particle size. As the shell thickness is decreased the two surfaces interact more strongly, leading to a red-shifting of peak position. The penetration depth for an electric field into Ag is approximately 30 nm *[22]*. Therefore with thick shells the electric fields cannot interact with the core and so the inner LSP is not excited, resulting in the same optical response as a solid sphere.

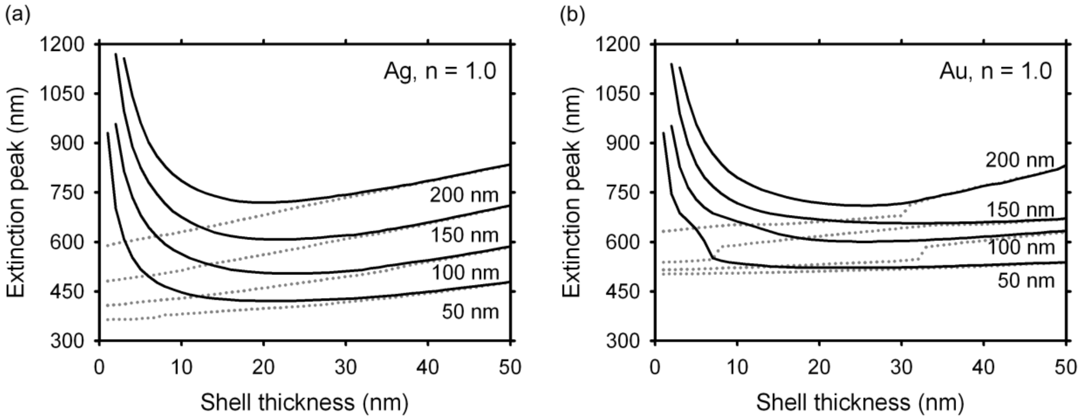

Figure 4.12: Extinction peak position as a function of Au and Ag core-shell particles (vacuum core), as a function of core diameter and shell thickness. The dotted lines represent the peak position of solid Ag and Au spheres with diameter equal to the overall diameter of the core-shell.

The effect of embedding medium follows trends observed for solid spheres, with a general red-shift for all shell thicknesses (Fig. 4.13).

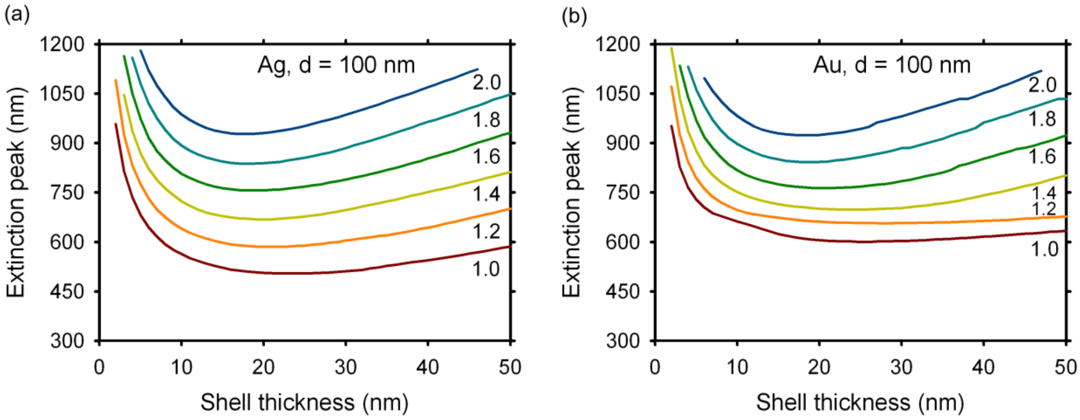

Figure 4.13: Extinction peak position as a function of 100 nm diameter Au and Ag core-shell particles (vacuum core), as a function of shell thickness and embedding medium.

The refractive index of the dielectric core also affects the optical spectra. In the previous graphs we have only considered a vacuum (or air) core. Increasing the core refractive index results in a strengthening of the red-shift caused by decreasing the shell thickness. This allows the peak position to be tuned further into the red for a given shell thickness. The core refractive index has no effect for thick shells as we would expect. Increasing the refractive index of the core enables tuning into the NIR without the need for extremely thin shells, which are difficult to fabricate consistently.

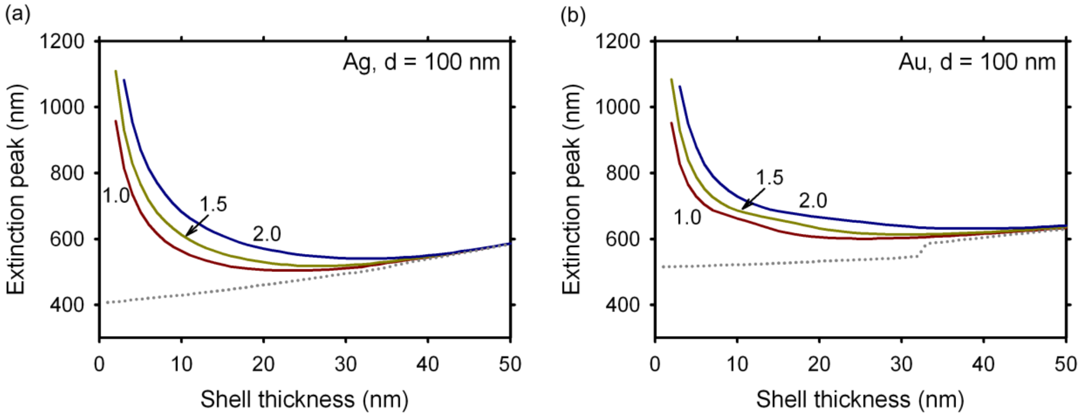

Figure 4.14: Extinction peak position as a function of 100 nm diameter Au and Ag core-shell particles, for core refractive index of 1.0, 1.5 and 2.0. The dotted line gives the peak position for a solid sphere of the same diameter.

Due to the sharp increase of peak position for thin shells, core-shell nanoparticles are extremely sensitive to changes in size, shell thickness, core refractive index, and medium refractive index. For a 50 nm core diameter, changing the shell thickness from 2 nm to 1 nm results in a 228 nm shift in the peak position. Similarly, for a shell thickness of 2 nm a change in core diameter from 50 nm to 100 nm results in a 255 nm shift. For a core diameter of 100 nm and a shell thickness of 2 nm, an increase in core refractive index from 1.0 to 1.5 results in a 202 nm shift. For the same size particle, increasing the refractive index of the embedding medium from 1.0 to 1.2 results in a 133 nm shift. Therefore the refractive index of the embedding medium has a stronger effect on the resonance position than the refractive index of the core.

Core-shell particles are highly tuneable and enable extinction peaks in the IR even for relatively small particles. However, as Fig. 4.15 shows, the radiative efficiency also decreases as the shell thickness is reduced. The sharpest decrease in radiative efficiency is seen for the thinnest shells, *i.e.* those that give rise to the largest peak shifts. Although radiative efficiency decreases with overall particle size (Fig. 4.10b), the effect is far more pronounced for decreasing shell thickness. The radiative efficiency of a core-shell particle with a 50 nm core and 2 nm Ag shell is 0.13, while a 54 nm diameter solid Ag sphere has a radiative efficiency of 0.32. Therefore the advantages of increasing tuning capability of core-shells particles are offset by considerably increased absorption.

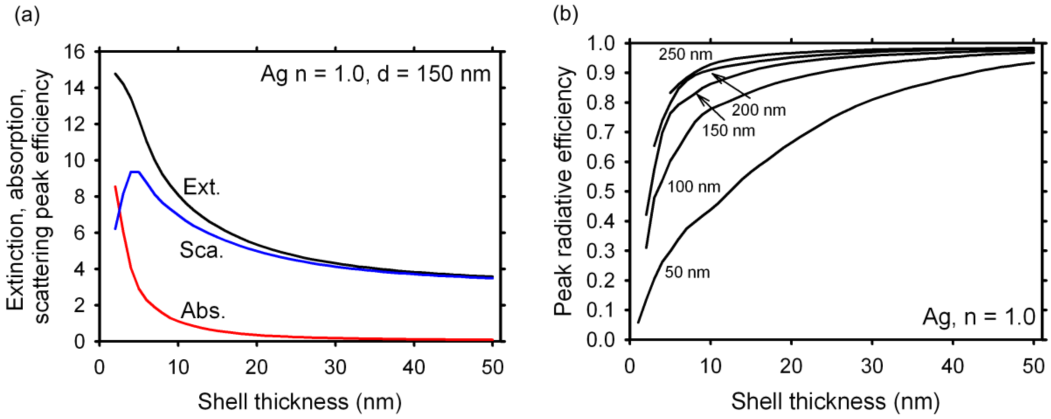

Figure 4.15: (a) Extinction, scattering and absorption peak efficiency for 150 diameter Ag core-shell particle as a function of shell thickness, (b) peak radiative efficiencies for core-shell particles with core diameters ranging from 50 to 250 nm.

4.7 Spheroids

Shape anisotropy gives rise to excitation of multiple polarization-dependent LSP modes. In the case of a prolate spheroid two perpendicular resonances related to the long and short axes are excited (assuming illumination normal to a plane containing one short axis and the long axis). We define the aspect ratio as the ratio of the long axis length to the short axis length. As seen in Fig 4.16 the major peak position is red-shifted for increasing aspect ratio. For Ag, the extinction peak for a sphere (aspect ratio = 1) features a side-lobe, which is due to quadrupolar excitation. Spheroids with aspect ratio of 2.5 and 5 also feature an additional peak at low energy, but these are due to transverse modes. The longitudinal mode is dominant for all aspect ratios, and occurs at longer wavelengths than the transverse mode. The transverse peak is weakened and blue-shifted with increasing aspect ratio.

The tuning of peak position for spheroids is more spectrally selective than for spheres. The entire peak is spectrally shifted without broadening for spheroids with increasing aspect ratio. As such it is possible to achieve NIR resonances in spheroids without significant optical activity at shorter wavelengths. The aspect ratio 5 spheroids have a weak optical response below 750 nm, and so the optical properties for both Ag and Au are nearly identical across the entire spectrum.

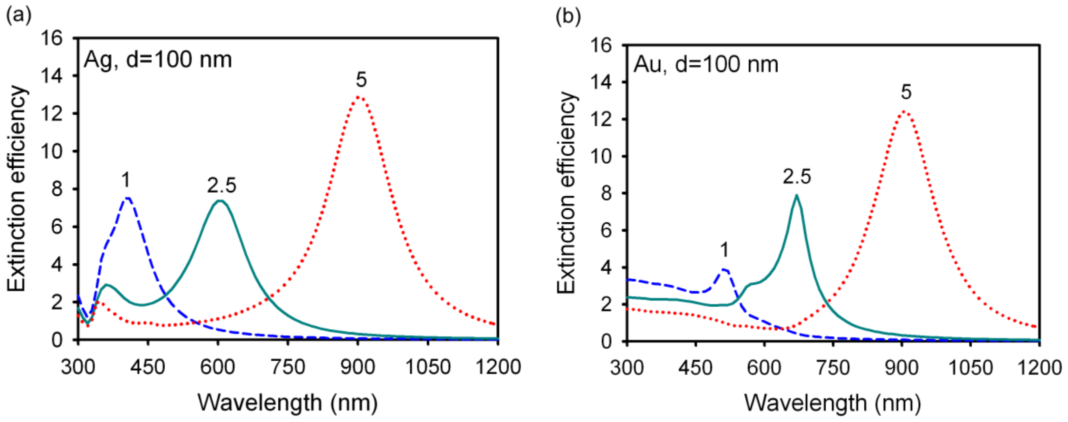

Figure 4.16: Simulated optical extinction spectra of Ag and Au spheroids with aspect ratios of 1, 2.5 and 5, and volume equal to that of a 100 nm diameter sphere, illuminated by unpolarized light.

We can consider increasing the aspect ratio in two distinct ways: either by increasing the long axis length while keeping the short axis length constant, or by increasing the long axis length while keeping the volume constant. For a constant short-axis length the peak position of Ag spheroids is linearly related to the aspect ratio (Fig. 4.17a). For a short-axis of 50 nm, increasing aspect ratio from 1 (*i.e.* a sphere) to 5 red-shifts the peak position by 480 nm. As for spheres, larger particles are more sensitive to aspect ratio, resulting in larger shifts of peak position. For a constant short axis the volume is increased with aspect ratio, and so the shift is due to a combination of both size and particle anisotropy. By keeping the volume constant while changing the aspect ratio we can observe trends due solely to aspect ratio and not to overall particle size (Fig. 4.18a). These trends are similar to those for constant short-axis, but smaller shifts are observed. Additionally the constant volume trends are slightly bowed compared with the linear shift of the constant short axis. The trends for Au spheroids exhibit the same distortion at short wavelengths as were found for spheres and core-shell particles (Figs. 4.17b, 4.18b).

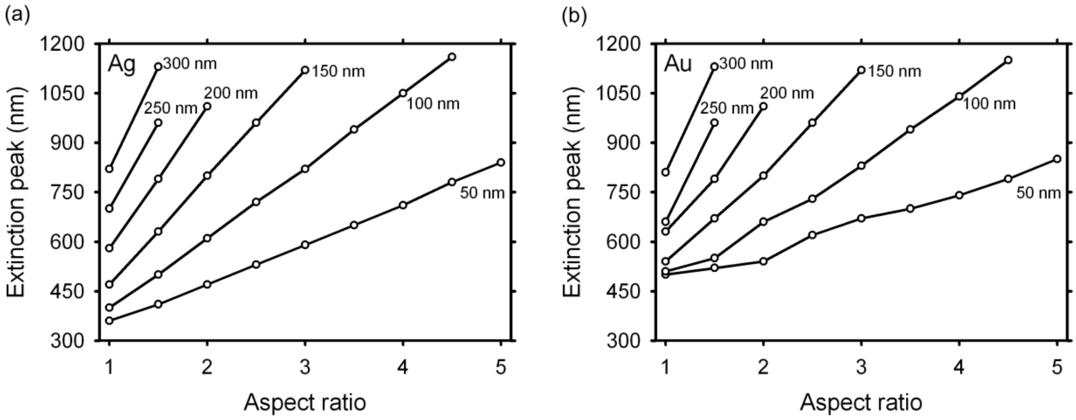

Figure 4.17: Longitudinal extinction peak position of Au and Ag spheres as a function of aspect ratio and short axis length.

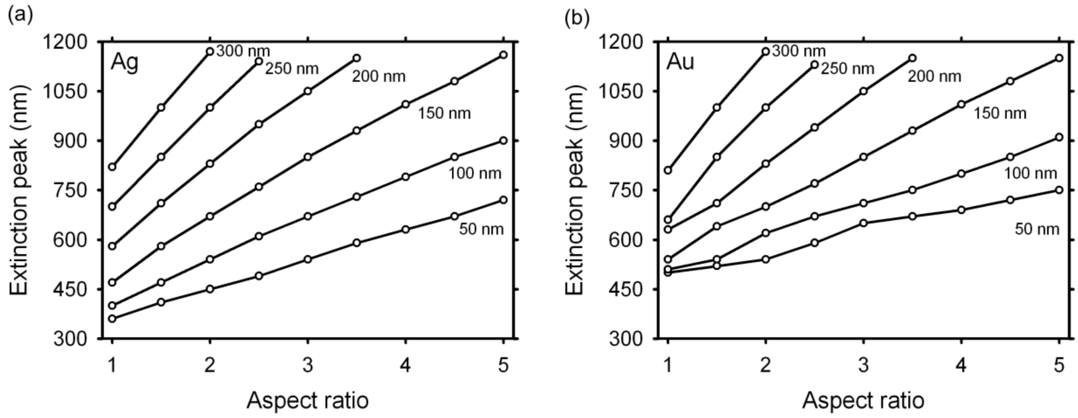

Figure 4.18: Longitudinal extinction peak position of Au and Ag spheres as a function of aspect ratio and size, with total particle volume fixed to that of the sphere with the indicated diameter.

The sensitivity of the peak position to the refractive index of the surrounding medium also increases with aspect ratio (Fig 4.19). For Ag particles with constant volume, an increase in refractive index from 1.0 to 1.2 red-shifts the peak by 90 nm for a sphere, and by 160 nm for a spheroid of the same volume and an aspect ratio of 3.

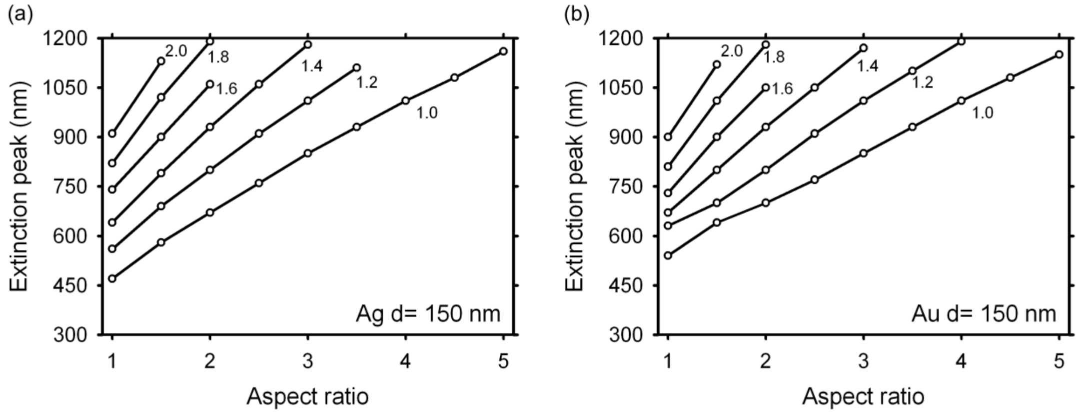

Figure 4.19: Longitudinal extinction peak position of Au and Ag spheres as a function of aspect ratio and embedding medium refractive index, for spheroids with a constant volume equal to that of a 150 nm sphere.

The magnitude of the extinction efficiency of the longitudinal mode increases linearly with aspect ratio, for both constant volume (Fig 4.20a) and constant short axis (Fig. 4.21a). For an increase of aspect ratio with constant volume, absorption initially decreases until reaching a minimum, and then increases. For a 100 nm spheroid the minimum occurs at an aspect ratio of 1.5 (Fig 4.20a). A similar trend is seen for other spheroid sizes, with a general decrease in radiative efficiency for high aspect ratios. For an increase of aspect ratio with a fixed short-axis length the volume of the particle is increased, and therefore we see a more substantial decrease in absorption (Fig. 4.21a). However, the extinction efficiencies of the constant short-axis are lower than the corresponding constant volume efficiencies for a given aspect ratio. This is similar to the trends observed for spheres, where a decrease in extinction efficiency occurs for increasing diameter of larger spheres (Fig. 4.10a).

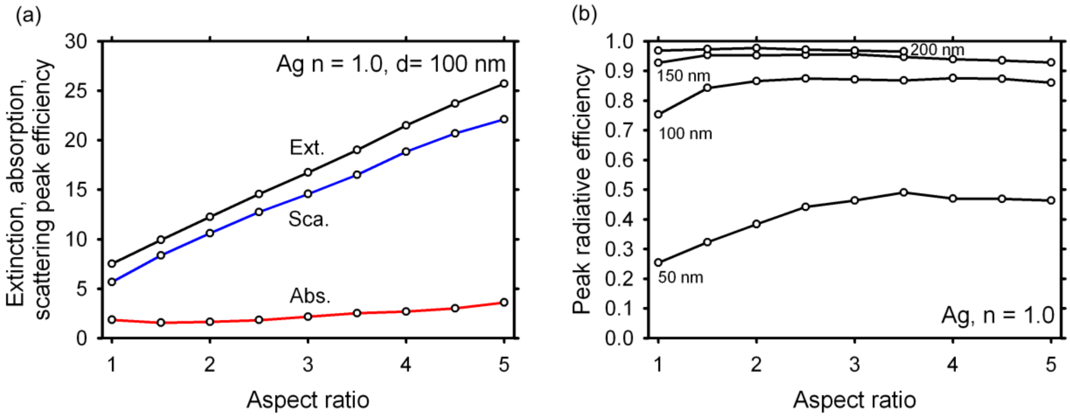

Figure 4.20: (a) Longitudinal extinction, scattering and absorption peak efficiency for Ag spheroids with volume equal to that of 150 diameter Ag sphere, (b) peak radiative efficiencies for spheroids with volumes equal to 50 nm, 100 nm, 150 nm and 200 nm spheres.

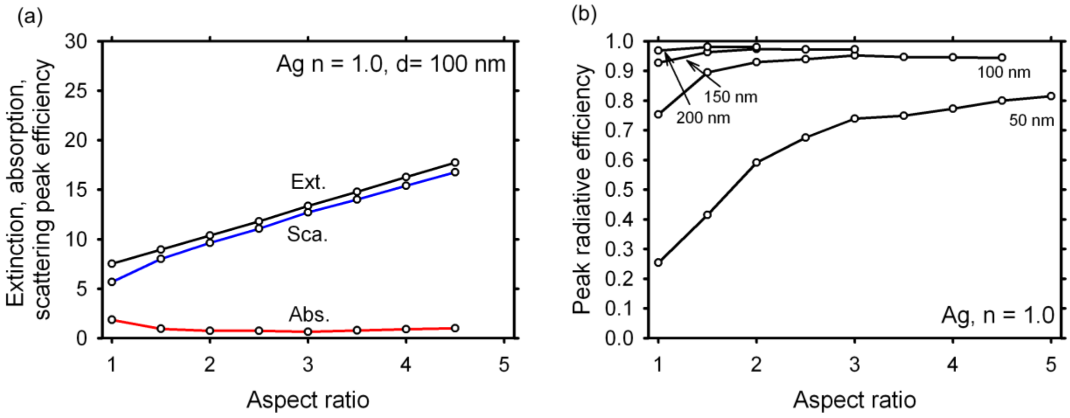

Figure 4.21: (a) Longitudinal extinction, scattering and absorption peak efficiency for Ag spheroids with 100 nm short-axis length, (b) peak radiative efficiencies for spheroids with short-axis equal to 50 nm, 100 nm, 150 nm and 200 nm.

4.8 Cross-sectional shape

To explore the influence of particle shape we will now investigate the optical properties of Ag prisms with identical height and similar cross-sectional area, but different cross-sectional shapes. We consider the response to unpolarized light incident normal to the prism cross-section. Fig. 4.22 gives the extinction spectra of Ag prisms with height 50 nm and cross-sections of: circle with diameter 115 nm, square width side length 100 nm, and equilateral triangle with side length 150 nm. Shape clearly has a strong influence on extinction peak position, and the peak wavelength increases in the order of circle, square and then triangle. This correlates with the angle of the vertices present in the shapes, which become smaller –*i.e.* sharper– from circle to square to triangle. This suggests that the trend is related to e-field confinement.

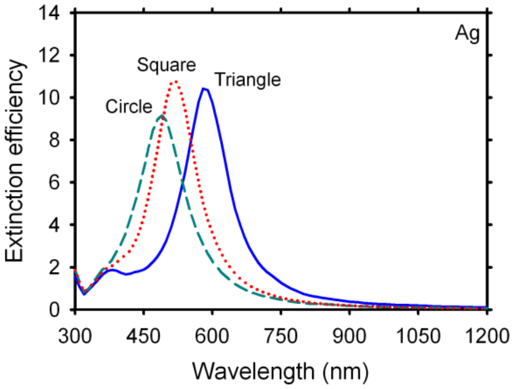

Figure 4.22: Simulated extinction spectra of Ag prisms with height 50 nm and cross-sections of: circle with diameter 115 nm, square width side length 100 nm, and equilateral triangle with side length 150 nm. These dimensions correspond to cross-sectional areas of 10387 nm^2, 10000 nm^2, and 9743 nm^2 respectively.

The relative peak positions for the three shapes remain the same as they are shifted by a change in refractive index (Fig. 4.23a). The triangular prism is more strongly red-shifted by an increase in the surrounding refractive index than the other two shapes. The radiative efficiency of prisms with square and circular cross-sections remain almost identical, with a maximum values of 0.88 and 0.89 respectively for an embedding medium of n = 2 (Fig. 4.23b). The triangular prism exhibits a substantially lower radiative efficiency, with a maximum value of 0.67. The reason for this change in radiative efficiency is most likely due to the differences in field distribution for the three shapes. For triangles it has been shown that the field is mainly concentrated at the tips, and therefore much larger field enhancement values are found for triangular nanoparticles than other shapes. This field enhancement may give rise to larger intraparticle absorption, resulting in a lower radiative efficiency.

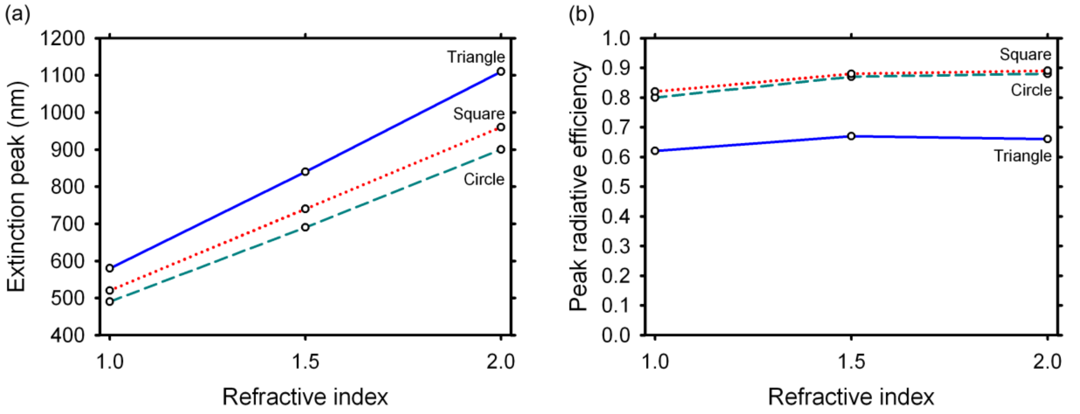

Figure 4.23: (a) Peak positions and (b) radiative efficiencies for geometries described in Fig 4.22 as a function of embedding medium refractive index.

Aside from cross-sectional shape, the height of the prism also plays an important role. As shown in Figure 4.24 the extinction peak position is red-shifted by a decrease in prism height. This effect is particularly strong for thin layers, with a 400 nm red-shift for a decrease of height from 50 nm to 5 nm. We note the similarity to the trends observed for decreasing metal shell thickness, and so suggest a similar mechanism is responsible: *i.e.* coupling between the upper and lower particle surfaces. Unfortunately, as with core-shells, although decreasing height enables tuning of the resonance well into the NIR, it also comes at the cost of a substantial reduction in radiative efficiency.

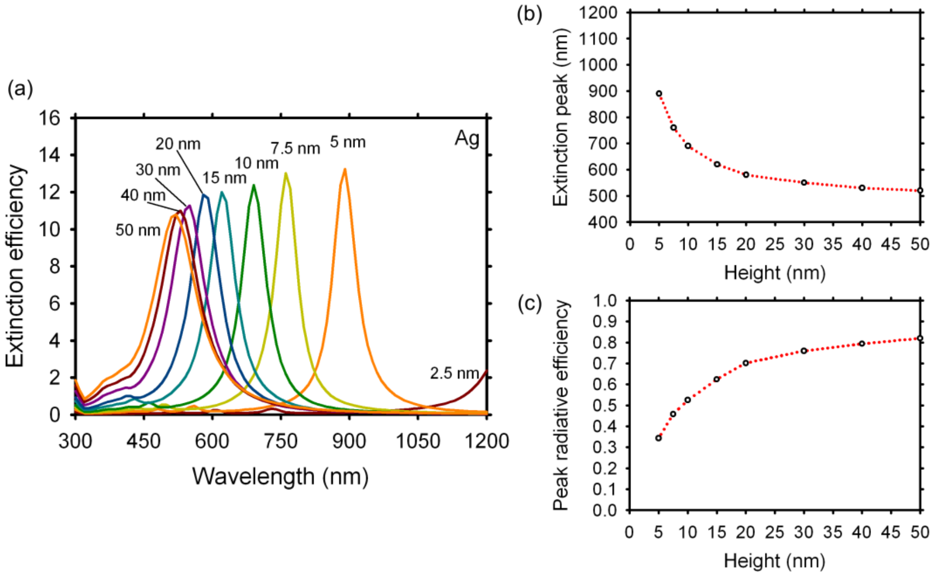

Figure 4.24: (a) Extinction peaks of a prism with a 100 nm square cross-section, and height ranging from 2.5 nm to 50 nm. The 2.5 nm peak occurs > 1200 nm. (b) Extinction peak position and (c) radiative efficiency.

4.9 Conclusions

For silicon solar cell applications we require a tuneable extinction peak position with a high radiative efficiency. From our preliminary studies the metals Ag, Au, Cu and Al all seem to be good candidates for this purpose. Nanoparticles of the noble metals exhibit nearly identical optical properties at wavelengths greater than 700 nm. Below this the interband regions of Au and Cu weaken the optical response and reduce radiative efficiency. For nanoparticles situated on the front surface Ag is the preferred metal, but for rear surface (particularly if photons < 700 nm have been absorbed), all three noble metals perform equally well. Al nanoparticles exhibit a broader, blue-shifted extinction peak compared with identical nanoparticles of the noble metals. The radiative efficiency of Al nanoparticles at short wavelengths appears to be higher than Ag nanoparticles with resonances in the same part of the spectrum, but further study is required to confirm this. Additionally, Al can support LSPs further into the UV than Ag. However, Al nanoparticles feature increased absorption around a narrow interband region in the NIR. This occurs at wavelengths beyond the bandgap of a-Si:H, and so will only affect c-Si applications.

Extinction peak position can be tuned across the solar spectrum by a wide variety of methods. Increasing the refractive index of the surrounding medium results in a red-shifting of the peak position, with the highest peak shift occurring for larger nanoparticles. Peak positions are also a strong function of particle geometry. In the case of spheres increasing the diameter results in a broadening and red-shifting of the extinction peak. Extinction peaks of core-shell particles can be red-shifted by decreasing shell thickness, and similarly the peak position of prisms can be red-shifted by decreasing the out-of-plane height. These effects are particularly strong for very thin layers. Increasing the aspect ratio of spheroids red-shifts the longitudinal extinction peak position, and it is this mode that dominates the overall extinction spectrum. In contrast to spheres, the peak position of core-shell nanoparticles and spheroids can be tuned without significant broadening, resulting in a spectral shift of the entire peak. As the extinction efficiencies of core-shells and spheroids generally exceed those of spheres, we can envisage two methods of spanning the solar spectrum. The first is to use large spheres with broad resonances, and the second is to use an ensemble of discrete types of spheroid or core-shells, each with an extinction peak at a different part of the spectrum.

Aside from tuning the extinction peak position, we also wish to minimize absorption. Absorption can be decreased by increasing the particle size and/or increasing the refractive index of the surrounding medium. For core-shells and prisms, decreasing the metal thickness leads to a large increase in absorption. For spheroids an initial increase in aspect ratio lowers absorption, but further increase of the aspect ratio results in increased absorption. Triangular prisms have larger absorption than similarly sized circular or square prisms. We note that there appears to be a correlation between an increase in tip-curvature and an increase in absorption. Therefore, it is likely that the use of metal nanoparticles with sharp tips to increase absorption in silicon layers by e-field enhancement will also result in an increase in losses due to absorption by the nanoparticles. The increased absorption in spheroids is also likely due to an increase in tip curvature. However, rods fabricated by chemical synthesis resemble hemispherically-capped cylinders and not spheroids. Therefore it is likely that in practice the decrease in radiative efficiency for increasing aspect ratio will be lessened or even negligible, while still maintaining a high degree of tuneability.

Tuning the optical properties by modifying shape rather than size helps to suppress the excitation of higher-order modes. Large nanoparticles feature higher-order modes at short wavelengths, which have a lower radiative efficiency. The extinction efficiency decreases with mode order, so that the optical response is always dominated by the dipolar resonance. However, higher-order modes can still significantly decrease the net radiative efficiency at short wavelengths. The radiative efficiency of all modes increases with particle size, but the increase diminishes with mode order. Interestingly, the quadrupolar radiative efficiency of an Ag nanoparticle exceeds 0.9 for diameters larger than 200 nm. Quadrupolar modes scatter predominantly in the forward direction, and so could be used to reduce front-surface reflection. However, quadrupolar modes are more difficult to spectrally tune, and the dipolar mode may introduce significant back-scattering losses.

This study has shown that tuning the spectral response by means of core-shell particles, tip curvature and prisms height are not suitable for solar cell applications due to the corresponding decrease in radiative efficiency. Spheres and spheroids offer both a high degree of tuneability and minimum absorption values of around 1-2%. Ag spheres and spheroids can support resonances from 390 nm to over 1200 nm. In the case of spheres, long wavelength resonances are achieved by considerably broadening the dipolar peak. However, this gives rise to excitation of higher-order modes, which increase absorption at lower wavelengths. In the case of spheroids, the peak can be tuned without significant broadening, but additional absorption can occur at high aspect ratios. The optimum nanoparticle for high scattering across the solar spectrum appears to be large spheroids with modest aspect ratios, enabling tuning to the NIR while maintaining a high radiative efficiency.

Chapter 5

Optical properties of metal nanoparticles fabricated by electron-beam lithography

Electron-beam lithography (EBL) enables precise definition of nanometre scale patterns in planar resist layers. Transfer of the pattern to metal layers can be achieved by lift-off or anisotropic etching. In the case of lift-off, the pattern is defined in the resist as a series of holes, and the resist is used as a deposition mask. The main advantage of EBL over other fabrication techniques is an extremely precise control over particle size, shape and orientation. Additionally, the technique is applicable to virtually any material that can be vapour-deposited, enabling the study of a wide range of metals. In addition to process cost, the limitations of EBL concern minimum feature size, limitations on achievable particle geometries, and the maximum write area achievable. Conventional EBL is restricted to the fabrication of planar structures with height less than the resist thickness. All particles in a given array must be made of the same material and have the same out-of-plane height, but the in-plane width and structure is virtually unrestricted. Some tapering of out-of-plane height may occur due to narrowing of the hole during deposition. The minimum feature size of EBL is not limited by diffraction, due to the extremely short wavelength of the electron beam at high accelerated voltages, but is instead limited by scattering of electrons in the resist layer. Feature sizes down to around 20 nm can be routinely fabricated. The major limitation of EBL is the high cost of the process. EBL machines are very expensive, and as the write process is serial the exposure of a pattern can be extremely time-consuming (*e.g.* hours per mm^2).

EBL is clearly unsuitable for commercial solar cell fabrication processes. Even the process of coating a modestly sized 1 cm^2 laboratory cell with an array of nanoparticles by EBL is a formidable and costly task. However, the precise control offered by EBL enables an experimental clarity that is not available by any other fabrication technique. Variations in particle size and shape can be minimized, particle aggregation limited, and array structure precisely controlled. Therefore, EBL is an ideal tool to pioneer the study and optimization of nanoparticle structures for silicon solar cells, and we use it in particular to gain confidence in the accuracy of results obtained by simulation. Provided we restrict our studies to aperiodic arrays of simple structures the results are equally applicable to low-cost techniques such as chemical synthesis.

5.1 Fabrication overview

1.5 x 1.5 mm^2 arrays of metal nanoparticles were fabricated using conventional EBL and lift-off by NILT, Denmark. Patterns were defined in ZEP520 resist layers, working with a spot size of 4 nm and typical accelerating voltage of 100 kV. ZEP520 was spun-cast onto cleaned 150 mm fused-silica wafers with a layer thickness of around 115 nm. Each array contained 9,006,001 particles, corresponding to an average interparticle distance of 500 nm. Particle dimensions ranged from 50 nm to 200 nm, and the layer thickness (*i.e.* out-of-plane particle height) was kept constant at 40 nm. After fabrication of the metal nanoparticle arrays, the wafers were diced into 22 x 22 mm^2 squares, each containing nine 1.5 x 1.5 mm^2 particle arrays.

The original design specified three sets of identical particles each made from a different metal: Ag, Au and Al. Au and Ag are known to adhere poorly to silica and so an adhesion layer is required to prevent complete removal of metal during lift-off. Ti and Cr layers are often used to improve adhesion of noble metals to surfaces, but these layers also degrade the optical properties of metal nanoparticles and so their thickness must be minimized. As such, 2 nm layers were used in this experiment. However, the initial run of samples fabricated using a 40 nm Ag layer deposited on top of a 2 nm Ti adhesion layer failed during lift-off, resulting in complete removal of the Ag layer. For the second set of samples, a 40 nm Au layer on 2 nm Cr was used, and lift-off was achieved successfully. The reason for the failure of the Ag samples is not clear. Ag could adhere poorly to Ti, or the extremely thin Ti could have been poorly formed (*e.g.* incomplete surface coverage). Arrays of Al nanoparticles were successfully fabricated without an adhesion layer.

Array designs were defined using a custom CIF file generation program. CIF (Caltech Intermediate Form) is a simple, plaintext descriptive language that can be used to define the geometry of a mask. A custom program was required to generate CIF files containing pattern definitions of pseudo-random arrays of nanoparticles. Conventional mask layout software only supports generation of periodic arrays. Initially the program was written in the internal TCell code available within the program L-Edit, but substantial improvements in execution speed and stability were achieved by moving to direct generation of CIF files by native C code. A grid perturbation method was used to generate pseudo-random particle positions with a consistent average surface coverage. In this method the particles are initially arranged in a periodic array, and then each particle is moved from its position by randomly assigned x and y offsets ranging from 0 to the period length. To avoid closely-spaced or overlapping particles the position of the particle is checked with the eight nearest neighbours. If the centre to centre distance between particles is lower than a given bounding value (250 nm for all particles in this experiment) then the x and y offsets are recalculated. The advantages of this approach are that overlap checks are limited to the eight nearest neighbours, and that surface coverage density is evenly distributed. However, for large particles and small period lengths the range of offsets is limited by the bounding value, and so some degree of order may remain.

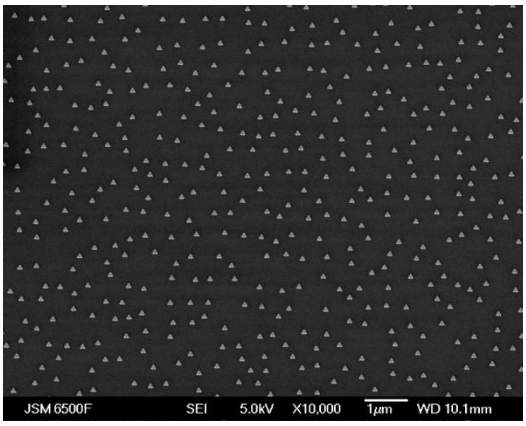

Figure 5.1: SEM image of typical Au nanoparticle array fabricated by EBL.

5.2 Characterisation

Optical measurements were made using a bespoke fibre-coupled transmission setup. Light from a tungsten-halogen bulb (Bentham IL1) was coupled to a 100 µm core silica fibre (Ocean Optics) and focused on the sample using a 100 mm focal length lens. The spot size is estimated to be less than 1 mm^2, and no measurement on beam divergence was made. Light from the input fibre was directed into a 600 µm silica fibre (Ocean Optics) by a collimating lens with a small acceptance angle. This fibre was connected directly to a VIS-NIR spectrometer (HR4000, Ocean Optics). Measurements were normalized to the transmission of the uncoated areas of the fused-silica substrates. Extinction efficiencies were calculated by dividing the obtained extinction percentage by the surface coverage. For example, if we obtain 50% extinction for a 10% surface coverage then the extinction efficiency is 5.

The fabricated samples could not be inspected directly by SEM due to the use of an insulating substrate, which was necessary for optical transmission measurements. Conventionally a thin Au, Pt or C over-layer is used to alleviate charging, but this would lead to substantial modification of the optical properties of the film. Instead, a single set of identical samples were fabricated on a silicon wafer, and these were used for SEM inspection. A 30 nm SiO_2 layer was used to limit differences between particles fabricated on the two substrates. The silicon samples were made using a 40 nm thick layer of Au. We do not expect large discrepancies in obtained geometries between these samples and Au particles fabricated on fused silica. Other metals will have a different grain size and so there may be small differences in surface and edge roughness, but this is not likely to result in a large change in optical properties. We do not expect any differences in lateral dimensions as a result of differing wetting potentials of metals, as is commonly reported for NSL, due to the fact that EBL patterned resist masks are not severely undercut like NSL masks.

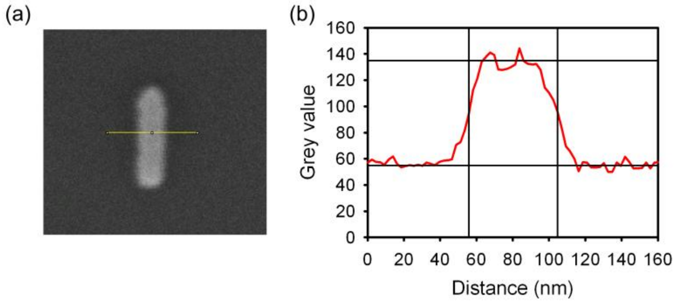

Figure 5.2: (a) SEM image of an Au nanoparticle, and (b) the corresponding greyscale intensity plot.

An example SEM image of a 50 nm wide, 200 nm long Au nanoparticle is given in Figure 5.2a. The outline of the particle is blurred due to charging effects arising from the 30 nm SiO_2 layer. As such, exact determination of particle dimensions is challenging. The greyscale intensity of a line through the short-axis of the rod is noisy, and the boundary between the nanoparticle and the background is sloped (Fig. 5.2b). To calculate the particle width we can measure the width at the middle grey value between the background and the peak foreground values, which results in a value of 48 nm in this case. However, automated analysis is complicated by the high degree of noise. In addition to the critical measurements (*e.g.* length and width) we are also interested in other aspects such as edge roundness. In effect we wish to know how close the size and shape of the fabricated particle is to the design. As such we have found it more useful to overlay a scale drawing of the designed particle onto the SEM image than to list critical dimensions.

5.3 Experiment overview

The purpose of this project was to study the optical properties of metal nanoparticles fabricated by EBL, and to optimize their size and shape for silicon solar cell applications. Therefore our aim was to achieve high scattering efficiencies across the solar spectrum, particularly near the band-edge regions of crystalline silicon (~1100 nm) and amorphous silicon (~715 nm).

To date the majority of experiments have focused on Au and Ag nanoparticles, but we also wish to extend our investigations to Al as it can offer certain benefits over Au and Ag, such as improved adhesion to substrates and LSP resonances at shorter wavelengths than are possible in the noble metals. As such, identical arrays of nanoparticles were fabricated in all three metals. However, the Ag nanoparticles were destroyed during lift-off, and so we restrict our investigation to Al and Au. All nanoparticles were fabricated with a nominal height (*i.e.* metal layer thickness) of 40 nm.

In addition to the choice of metal, we also wish to explore the effect of particle size, particle shape and shape anisotropy. To achieve this we employed a pseudo-random arrangement of nanoparticles within each array, to minimize far-field (*e.g.* diffractive) coupling effects.

Near-field coupling was minimized by ensuring that each particle was not in close proximity to any other particle. In this way the optical response of a large array of nanoparticles should be the same as an isolated nanoparticle, which enables comparison with single particle simulations. The list of nanoparticle geometries studied in this experiment is given in Table 5.1. An array containing 9,006,001 particles was fabricated for each nanoparticle geometry, both in Al and Au. Anisotropic nanoparticles were aligned vertically except for an additional 50 x 200 nm array which was randomly-assigned one of two orthogonal orientations.

Cross-section	**Dimensions**	**Surface area**	**Surface coverage**
Square	50 nm x 50 nm	2500 nm^2	1.00%
Square	100 nm x 100 nm	10000 nm^2	4.00%
Square	150 nm x 150 nm	22500 nm^2	9.00%
Square	200 nm x 200 nm	40000 nm^2	16.00%
Rectangle	50 nm x 100 nm	5000 nm^2	2.00%
Rectangle	50 nm x 150 nm	7500 nm^2	3.00%
Rectangle	50 nm x 200 nm	10000 nm^2	4.00%
Rectangle	80 nm x 130 nm	10400 nm^2	4.16%
Circle	Diameter 115 nm	10387 nm^2	4.15%
Triangle	Side 150 nm	9743 nm^2	3.90%

Table 5.1: List of nanoparticle arrays fabricated to investigate nanoparticle size and shape.

5.4 Comparison between simulated and experimental spectra

Simulations were performed using DDSCAT, a freely available implementation of the discrete dipole approximation (DDA) *[37]*. Each model contained between 20,000 and 50,000 dipoles to ensure that the target geometry was suitably represented. Dielectric data was obtained from Palik *[29]*, and fitted using parabolic interpolation. The simulations were performed with a wavelength step of 10 nm at normal incidence. The spectra presented are the average between two orthogonal polarizations, which approximate the response of the particle to unpolarized light, as is used in the experiment. The simulations modelled a simplified version of the experimental geometry, and in this section we discuss the resulting discrepancies between experimental and simulated extinction spectra.

In the experimental transmission measurements it was necessary to use a converging beam to get a small spot size, but in the simulations we assume an ideal plane wave at normal incidence. This changes the excitation conditions, as LSP resonances related to the sides of the prism are also excited by a converging beam. Due to the relatively long focal length of the focusing lens we expect this effect to be minimal. A more important discussion concerns the detector used. Due to the large size of the detector collimating lens in comparison with the spot size, a high percentage of forward-scattered light was most likely detected and therefore not included in the extinction spectra. This leads to an underestimation of the extinction efficiency with respect to the simulations.

The simulation model assumes a perfectly-defined particle with the exact dimensions specified in the design file, smooth sides and sharp edges. However, the fabricated nanoparticles are noticeably rounded with comparison to the original design. As we have seen in Chapter 4, smoothing of sharp edges in a nanoparticle results in a blue-shift of the extinction peak. The surface roughness of the fabricated nanoparticles was not measured but is not expected to be high enough to significantly alter the optical properties of the array. Small changes in particle height, width and length from the designed values will undoubtedly lead to small shifts in the extinction position.

The DDA simulations are for isolated nanoparticles, but each of the fabricated arrays contains over 9 million particles. The simulations do not account for near-field and far-field coupling between particles, but as the fabricated nanoparticles are positioned in a pseudo-random layout and spaced far apart we expect these effects to be minimal. However, of more importance is inhomogeneous broadening of the extinction peak, due to small changes in the size and shape of the fabricated nanoparticles. EBL is capable of precise and consistent definition of each nanoparticle, but small changes in substrate topography, resist thickness or metal structure (*e.g.* grain size and location) will result in unavoidable variation in particle size and shape.

Finally, the models do not account for the surrounding dielectric environment of the fabricated samples. Most notably the silica substrate is absent from the models. The primary effect of the substrate is to raise the average refractive index of the volume surrounding the nanoparticle. For Au nanoparticles we must also consider the effect of the thin Cr layer used for adhesion, and for Al nanoparticles we expect a thin alumina oxide layer to form on the particle surface after exposure to air. Although these effects could be included directly in the DDA model, the simulation time scales with the number of dipoles used and quickly becomes prohibitively long. Including a substrate greatly increases the number of dipoles required due to the added volume in the sample. Including a thin adhesion or oxide layer does not add much volume, but still considerably raises the required number of dipoles due to the need for a substantially reduced interdipole spacing to accurately define the thin layer. The interdipole spacing is constant throughout a given DDA model, and so the number of dipoles used to define the metal nanoparticle must be greatly increased when adhesion layers are modelled. In the following two sections we discuss the effects of substrate, adhesion layer and native oxide layers in more detail, and compare simulation results with experimentally obtained spectra.

5.4.1 Cr adhesion layer

Au adheres poorly to most substrates, and without a layer to improve adhesion it would be entirely removed during lift-off. Typically thin layers of Cr and Ti are used to improve adhesion of Au to substrates, but these affect the optical properties of the nanoparticles. In Figure 5.3 we show the results of DDA simulations performed to model the effect of adding a 2 nm, 3 nm and 4 nm layer of Cr underneath Au nanorods. Each of the models including a Cr layer required the use of more than 200,000 dipoles, almost a factor ten higher than for models that do not include a Cr layer.

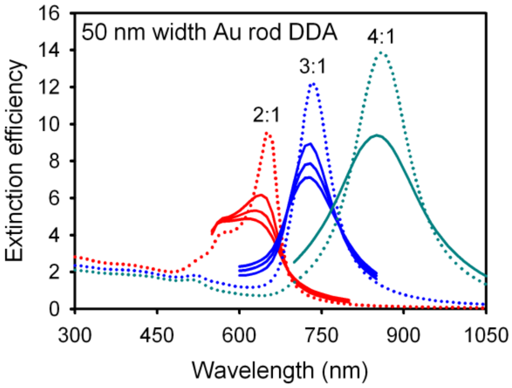

Figure 5.3: Simulated extinction spectra of Au nanorods with short-axis of 50 nm, and long-axes of 100 nm (2:1), 150 nm (3:1) and 200 nm (4:1). Solid lines are results from simulations that include a thin layer of Cr underneath the particle, dotted lines exclude Cr. Results are given for 2 nm, 3 nm and 4 nm Cr layers under the 2:1 and 3:1 nanorods, and a 4 nm layer under the 4:1 nanorod.

The Cr layer has only a weak effect on the spectral position of the extinction peak, with a weak blue-shift of 5 – 10 nm. Increasing the Cr layer thickness does not affect the peak position. However, the Cr layer significantly attenuates and broadens the extinction peak. The effect is stronger for thicker Cr layers, but even the thinnest Cr layer results in a substantial attenuation of the extinction peak. Additionally, the radiative efficiency of the peak is strongly reduced by the addition of a Cr layer (Fig. 5.4c).

To model the substrate we can use a homogenous medium to account for the increase of the average refractive index in the volume surrounding the nanoparticle. For Au nanoparticles an embedding medium with a refractive index of 1.10 gives a good agreement with experimental results (Fig 5.4a). This accounts for the strong red-shift due to the substrate and the weak blue-shift due to the Cr layer. However, the extinction efficiency of the experimental results is much lower than the simulated values (Fig. 5.4b). Although including a Cr layer in the simulation also results in attenuation of the extinction efficiency, the obtained values are still considerably larger than the experimental values. Either the Cr layer is substantially thicker than assumed, or the optical measurements are not correctly recording extinction. The latter is more likely given the large size of the detector collimating lens.

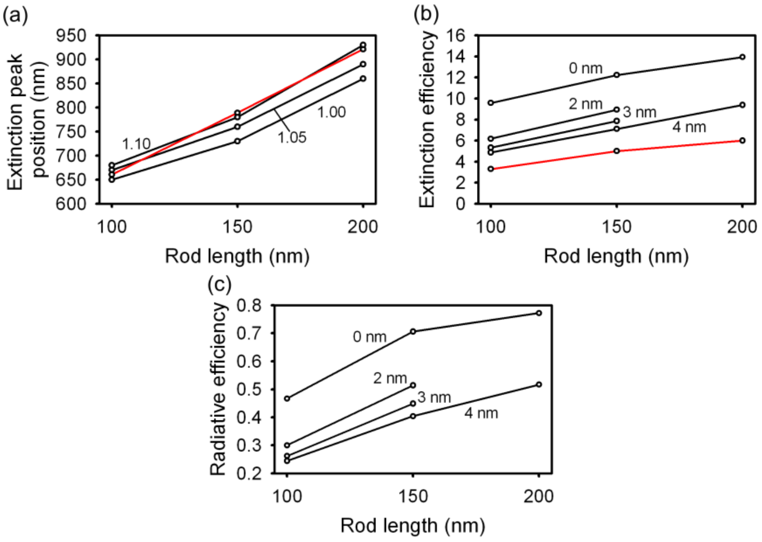

Figure 5.4: (a) Effect of refractive index of the surrounding medium on the extinction peak position of 50 nm wide Au nanorods. Effect of Cr on (b) extinction efficiency and (c) peak radiative efficiency of the rods. Experimentally obtained values are shown in red.

We cannot include Cr in all simulation models as it considerably increases the simulation time. Therefore we omit effects due to Cr in the simulations presented in the remainder of this chapter, but note that the presented simulated spectra will be attenuated and broadened by Cr. An interesting possibility is to include the effect of Cr directly in the dielectric function, for example by including additional damping terms in a Drude-Lorentz model. This would enable simulation of Cr-coated nanoparticles without increasing the simulation time. However, Cr clearly degrades the optical properties of Au nanoparticles for solar cell applications, by weakening interaction strength and increasing absorption. Therefore we consider the development of a non-metallic adhesion layer a crucial part of optimizing Au nanoparticles for use with solar cells. For example, self-assembled organosilane monolayers provide a promising alternative *[72, 73]*.

As it is not possible to fully model the effects of the Cr layer by means of changing the embedding medium, for the remainder of this chapter we will present results for the case of Au nanoparticle in a vacuum. We note that the substrate will lead to a red-shifting of peak position, and the Cr layer will lead to a broadening and attenuation of the peak.

5.4.2 Aluminium oxide

Al adheres well to silica substrates and so does not require an adhesion layer. However, on exposure to air a thin, self-limiting layer of oxide forms on the surface. Previous studies have estimated this layer thickness to be between 2 nm and 3 nm. This layer will reduce the size of the nanoparticle and also increase the average refractive index of the surrounding medium, leading to a blue-shift and a red-shift of peak position respectively. A thin layer of alumina can be included in DDA simulations directly, but again the computational time is considerably extended. Figure 5.5 shows the effect of including a 2 nm and a 3 nm layer of alumina in the simulations. The overall dimensions of the particle were kept the same, and so both the effect of reducing the nanoparticle size and of increasing the surrounding refractive index are included. A moderate red-shift of the peak position is observed, and so we conclude that the increase of surrounding refractive index has a stronger effect on peak position than the reduction of particle size.

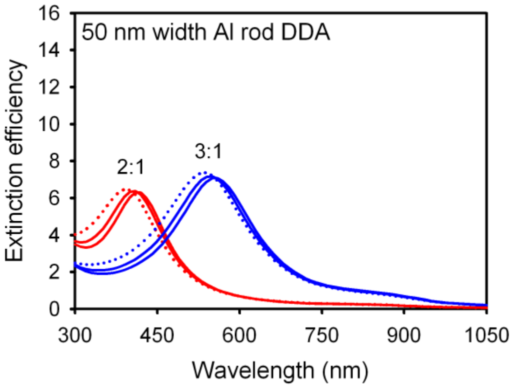

Figure 5.5: DDA simulations of 50 nm wide Al nanorods, with lengths of 100 nm (2:1) and 150 nm (3:1). The dotted line represents solid Al particles, and the solid lines are for models including 2 nm and 3 nm of alumina.

Figure 5.6 gives a comparison of experimental and simulated results. The peak positions of simulated spectra for particles in vacuum do not agree well with experimental results (Fig. 5.6a). Including the effect of oxidation in the simulations decreases the separation between the two sets of values, but agreement is still poor. Excellent agreement is found for the case of solid Al nanoparticles embedded in a medium with a refractive index of 1.2, without inclusion of oxide in the model. We believe that this value accounts for influences due to the substrate in addition to the oxide layer. Given the small increase in peak position caused by the oxide, it appears that the substrate is the dominant cause of peak red-shift. The extinction efficiencies of the simulations are far higher than the experimentally obtained values. Increasing the local refractive index does lead to a slight reduction in extinction efficiency, but the experimental values are still considerably lower (Fig 5.6b). As for the results for Au nanoparticles in the previous section, we attribute this to the detection of scattered photons resulting in a decrease of extinction efficiency.

To compare the influence of the two effects of the oxide (reduction of particle size, increase in local refractive index), simulations for the case of a decrease in particle size but no oxide were also modelled (Fig 5.6c). A very slight blue-shift was observed, with similar values for both a 2 nm and 3 nm decrease in all dimensions.

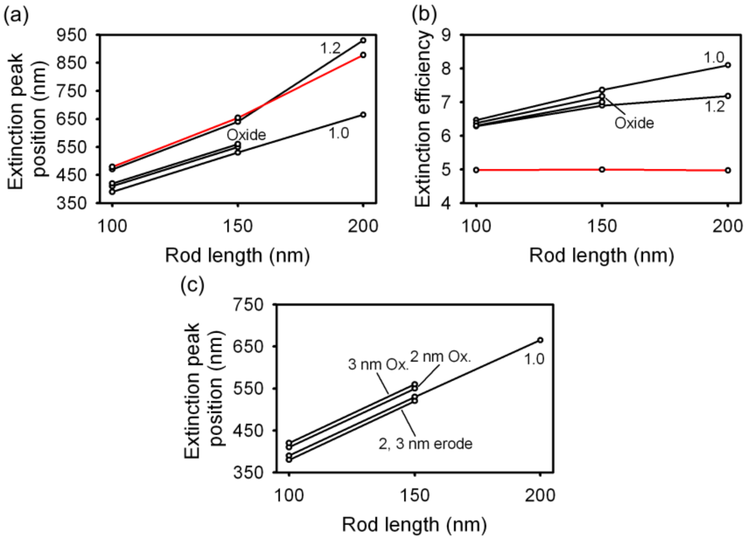

Figure 5.6: (a) Effect of refractive index of the surrounding medium on the extinction peak position of 50 nm wide Al nanorods, and (b) extinction efficiency. (c) Comparison of the effect of the oxide layer and eroding particle size on peak position. Experimentally obtained values are shown in red.

For the remainder of this chapter we will use a surrounding medium with a refractive index of 1.2 for all Al simulations, to account for the substrate and the native oxide layer.

5.5 Metals

Al and Au feature very different dielectric functions, and so Al and Au nanoparticles with identical geometry have markedly different optical properties (Fig. 5.7). The simulated spectra show that Al has a broader, weaker and blue-shifted peak in comparison with Au. There is excellent quantitative agreement between the features of the simulated and experimental Al nanoparticle spectra, with the exception that the experimental extinction efficiencies are lower. However, the experimental Au peak is noticeably broadened and red-shifted in comparison with the simulated spectrum. The Al simulation was performed with an embedding medium of n = 1.2, and so accounts for the substrate and surface oxide as described in the previous section. The Au simulation was performed assuming a vacuum environment, and so does not account for the substrate or Cr layer.

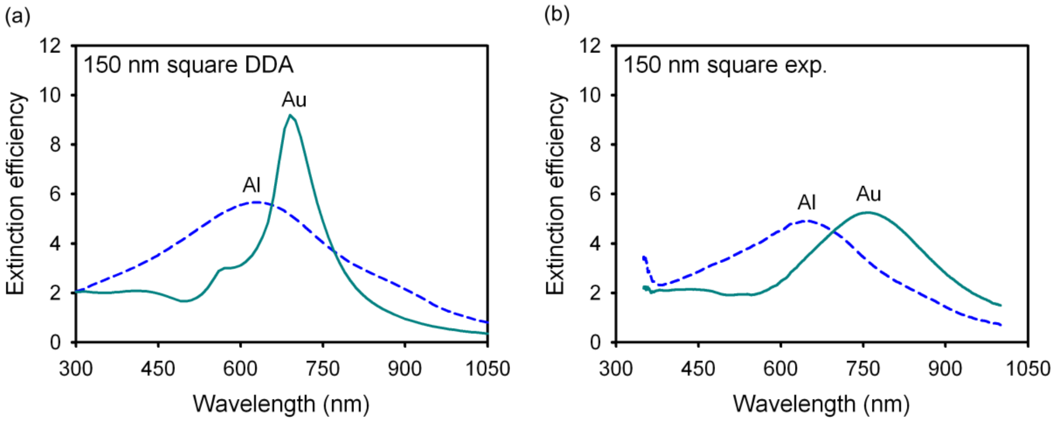

Figure 5.7: (a) DDA simulations of Al and Au nanoparticles with a 150 nm square cross-section, (b) corresponding extinction spectra of fabricated arrays.

To compare the effect of array structure a square array of 150 nm square particles was fabricated for each metal, with a period of 500 nm. An identical number of particles and total surface coverage was used in both the randomly-orientated and periodic arrays, and so the differences between the two spectra are entirely due to the position of the nanoparticles within the array (Fig. 5.8). The periodic Al array spectrum is considerably different to the random array, featuring a distorted and asymmetric peak. The Au array is less strongly affected, but is also asymmetric. The periodic array of nanoparticles effectively forms a diffraction grating, and so extinction is enhanced or suppressed at different wavelengths. For wavelengths below approximately 500 nm the random and periodic arrays feature a very similar optical response. This corresponds well with the array period, and so confirms that the distortions are due to diffraction effects. Therefore, to achieve good agreement with single particle simulations it is essential that the nanoparticles are randomly positioned on the substrate.

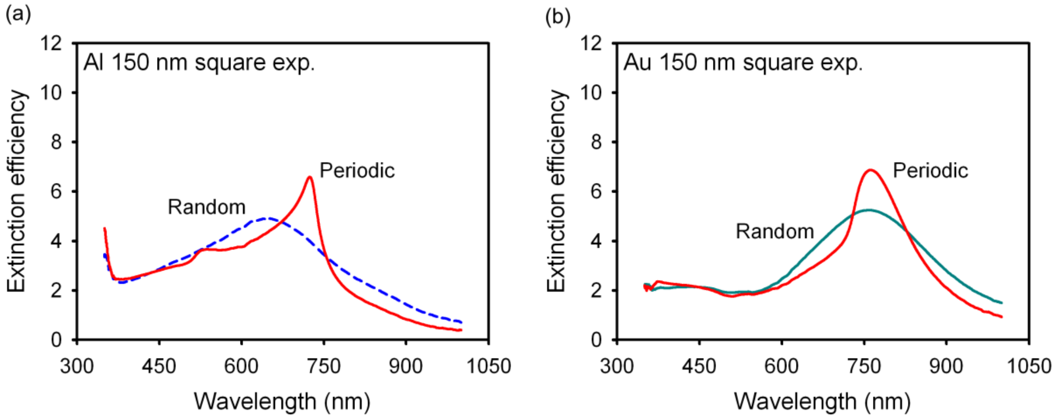

Figure 5.8: Comparison of the extinction spectra of fabricated nanoparticles arranged in a periodic grid and a pseudo-random, (a) Al, (b) Au.

5.6 Shape

Uniquely, EBL can be used to fabricate arrays of nanoparticles with the same height but different lateral size and shape. Therefore it is an ideal tool to isolate and explore the effect of cross-sectional shape on the optical properties of metal nanoparticles. In this section we investigate the optical properties of four cross-sectional shapes: triangle, circle, square and rectangle (Fig. 5.9). Each has a similar cross-sectional area (Table 5.1), and so any differences in optical properties are primarily due to shape.

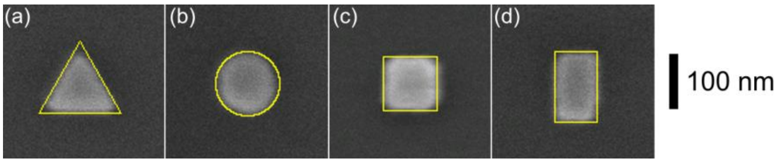

Figure 5.9: SEM images of the four shapes investigated: (a) triangle with 150 nm side length, (b) circle with diameter 115 nm, (c) square with 100 nm side length, (d) rectangle with short-axis 80 nm and long-axis 130 nm. All images are overlaid with their 'as-designed' dimensions in yellow.

As previously noted in Chapter 4 we anticipate a correlation between edge sharpness and peak position. This is the case for both Al and Au simulations, with a red-shift in peak position observed as we progress from circle to square to triangle (*i.e.* progressively higher degree of curvature) (Fig. 5.10a). As was found for spheroids, the rectangular nanoparticle supports two LSP resonances, along the major and minor axes. Two peaks are clearly evident in the Au simulation of a rectangular nanoparticle, and also present but less easy to identify in the Al simulations. However, we note that the short wavelength peak for the Au rectangle is close to the interband region, and so could also be due to increased absorption at this part of the spectra. This is supported by the observation of short-wavelength distortions in the extinction peaks for circular and square Au nanoparticles, which are also most likely due to interband effects. For Al nanoparticles the long-axis resonance of the rectangle occurs at a longer wavelength than the triangle, but they both occur at a similar wavelength for Au.

The experimental results for Al nanoparticles agree well with the simulations. The notable differences are the red-shifting of the triangle peak, and a weaker response for the long-axis peak of the rectangle. The fabricated triangles feature considerably rounded tips compared to the simulations, which results in a red-shifting of the peak position. The reason for the weaker long-axis peak is not known. The experimental spectrum for an Au triangle is also red-shifted, for the same reason. The experimental Au spectra do not share the same interband-related peak asymmetry for the circle and square particles due to broadening effects.

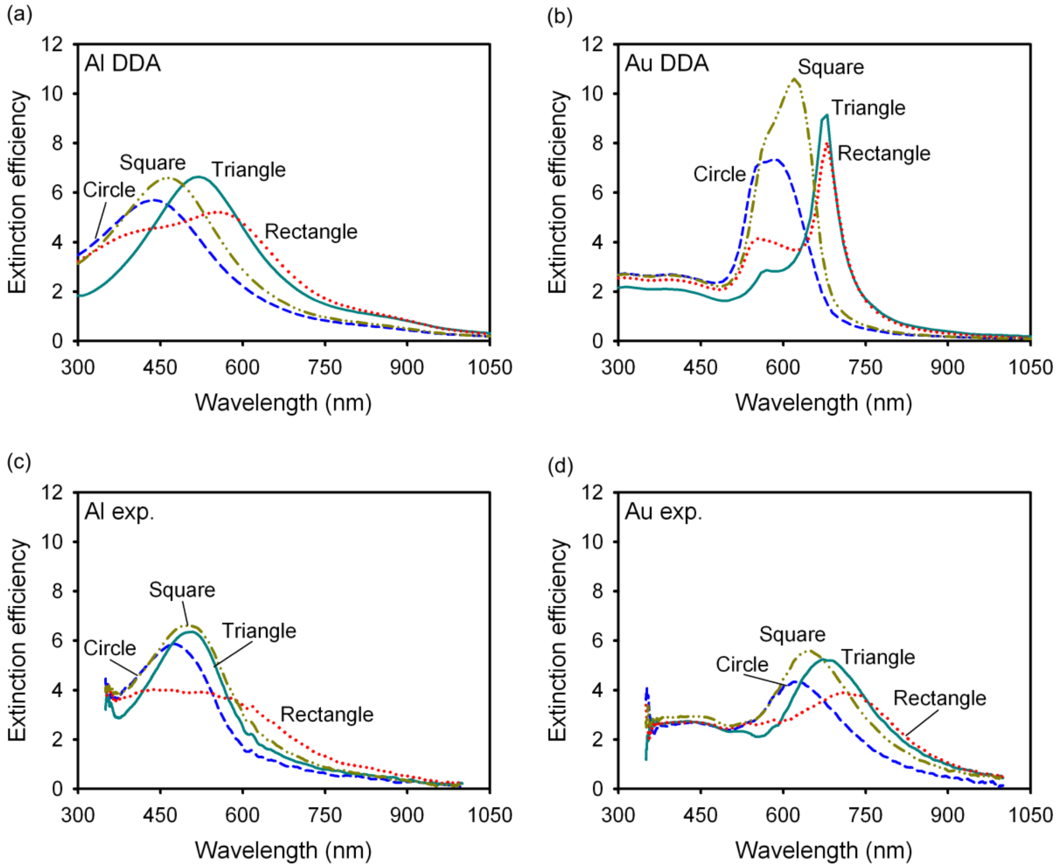

Figure 5.10: (a,b) DDA simulations and (c,d) experimental extinction spectra of the particle shapes shown in Fig. 5.9. DDA calculations were performed for n = 1.2 for Al, and n = 1.0 for Au.

5.7 Aspect ratio

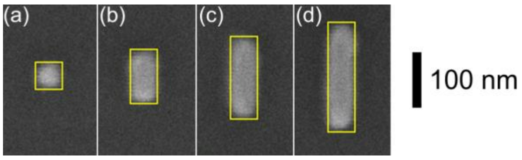

Figure 5.11: SEM images of the four rod lengths investigated: 50 nm width with (a) 50 nm length, (b) 100 nm length, (c) 150 nm length, (d) 200 nm length. All images are overlaid with their 'as-designed' dimensions in yellow.

In the previous section nanoparticles with a rectangular cross-section were shown to exhibit the longest wavelength extinction peak of the shapes investigated. The extinction peak position of rectangular nanoparticles can be readily tuned by changing the aspect ratio, and so rectangular (*i.e.* rod-like) nanoparticles are a promising method for achieve a large extinction efficiencies across the solar spectrum. In this section we investigate the effect of aspect ratio on the optical properties of rectangular nanoparticles.

The simulated extinction spectra show a strong red-shifting of extinction peak position for increasing rectangle length (Fig. 5.12a,b). The spectra of the 3:1 and 4:1 Al rectangles both exhibit an anomaly around 800-900 nm. In the case of the 3:1 spectrum a minor peak is present, while for the 4:1 rod a localized attenuation occurs in the extinction peak. These are both due to the narrow Al interband region in this part of the spectrum. The minor peak for the 3:1 rectangle is due to an increase of absorption due to increased interband transitions. The 4:1 peak is primarily due to scattering, which is attenuated by interband transitions, leading to a local minimum of extinction.

In all cases the Al nanoparticles exhibit broader peaks than Au. With the exception of the square Au nanoparticle, all of the Au rectangles feature larger extinction efficiencies than the corresponding Al nanoparticles. The extinction peak of the smallest Au nanoparticle is close to the interband transition region of Au and so is attenuated. Interestingly the extinction efficiency of Au rectangles increases with length, while for Al it remains at a similar value. Al nanoparticles support resonances at much shorter wavelengths than Au, and experience a larger red-shift for a given increase in rectangle length.

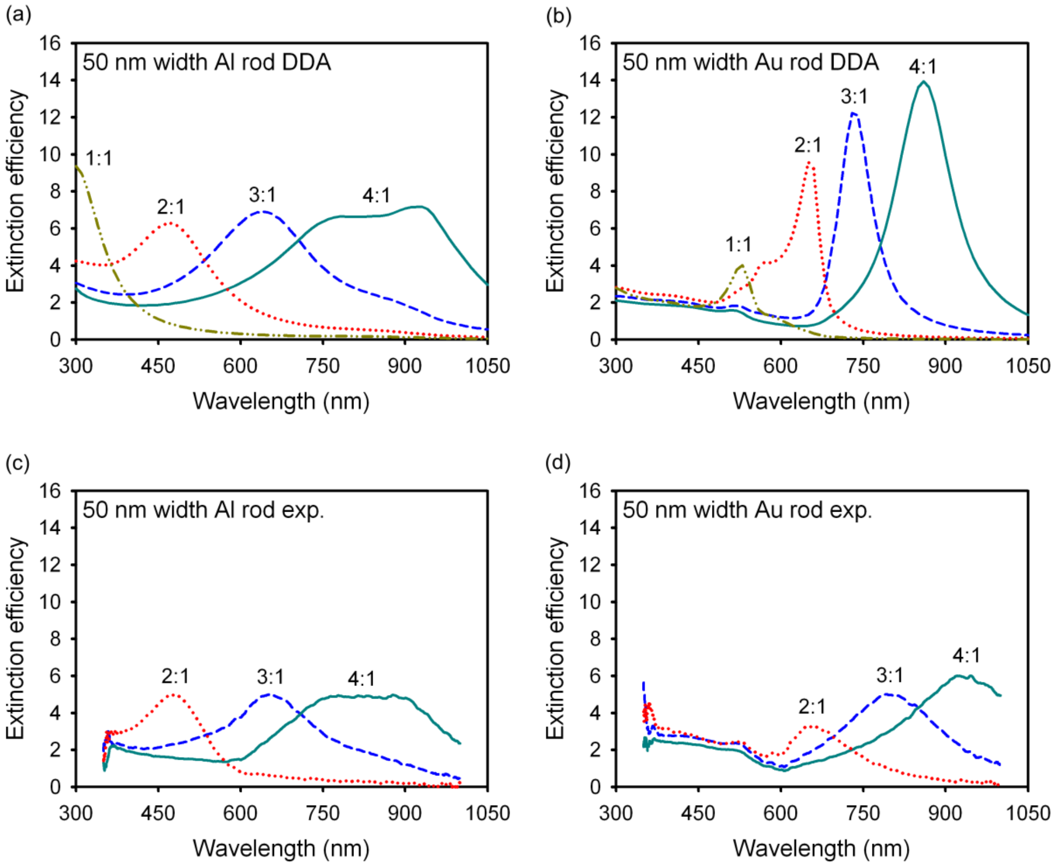

Figure 5.12: (a,b) DDA simulations and (c,d) experimental extinction spectra of the particle shapes shown in Fig. 5.11. DDA calculations were performed for n = 1.2 for Al, and n = 1.0 for Au.

No extinction spectrum was obtained for the 1:1 square nanoparticle for either metal. In both cases the optical response of the 1:1 array was within the noise limit of the detector. From the simulation results we can see that the 1:1 Al nanoparticle exhibits an extinction peak at around 300 nm, which is below the detection limit of the spectrometer used in this experiment. The simulated spectrum of the 1:1 Au nanoparticle has a weak optical response, which we expect to be further attenuated by the Cr layer. Therefore we conclude that the optical response of the 1:1 Au nanoparticle was too weak to be detected in our experiments.

The trends of the 2:1, 3:1 and 4:1 rectangles agree well with the simulations. The extinction efficiencies of the Al nanoparticles remain nearly constant, while those Au nanoparticles increase with rod length. However, the peak position of the 2:1 Au rectangle is blue-shifted with respect to the simulation results. This is unexpected as we expect the blue-shifting due to the Cr layer to be out-weighed by the red-shifting of the substrate, as is the case for the other nanoparticles investigated. However, the simulated extinction peak of the 2:1 Au nanoparticle features a complex shape due to proximity to the interband threshold. It is likely that the minor short-wavelength peak close to the interband region will not be strongly damped by the Cr (as it is predominantly due to absorption), and therefore the average peak position the two peaks will occur at a shorter wavelength.

5.8: Orientation

The orientation of polarization-sensitive nanoparticles is an important consideration for solar cell applications. Previously we have considered the case of arrays of vertically-aligned rectangular nanoparticles. The extinction spectra of these arrays are dominated by the long-axis extinction peak, and are therefore very sensitive to the polarization state of incident photons. This is not desirable for solar cell applications, where we require polarization-insensitive interaction to maximize absorption of all photons. To remove polarization sensitivity the rectangles can be randomly orientated. However, random orientation of rectangular nanoparticles by rotation results in inaccurate nanoparticle definition to the nature of the raster scan and the constrictions of the design grid size. Instead, we investigate the case where the rectangles are randomly designated one of two orthogonal orientations, which also removes polarization sensitivity (Fig. 5.13).

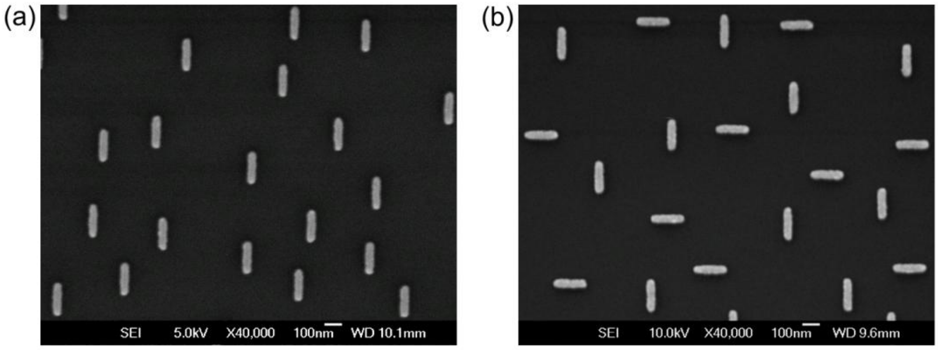

Figure 5.13: SEM images of 50 nm x 200 nm Au nanorods, with (a) parallel and (b) crossed alignment.

The extinction efficiency of 50 nm x 200 nm rectangles is primarily due to excitation of longitudinal modes along the long-axis (Figs. 5.14a,b). The extinction spectra for incident light orientated parallel to the long-axis (pol. A) feature strong extinction peaks in the IR for both metals. The extinction spectra of the orthogonal polarization are near zero for much of the spectrum investigated, with the short-axis Al peak occurring in the UV, and the short-axis Au peak occurring near the Au interband region. The minor-axis peaks of both metals are negligible in comparison with the major-axis peaks. Therefore the extinction spectrum for unpolarized light is essentially just half of the extinction spectrum for light polarized along the long-axis.

The experimental results for cross-aligned and parallel nanorods are very similar (Fig. 5.14). The maximum deviation is at longer wavelengths, where the noise level in the spectrometer is highest. Interestingly, the cross-aligned Al nanorods exhibit a spectrum that is much closer to the simulated spectrum than the parallel orientation.

As the optical spectra of both arrays are identical it is tempting to conclude that orientation is not important. However, the experiments feature a low surface coverage and therefore a low overall interaction with incident photons. As the surface coverage is increased the extinction percentage of the aligned array will saturate at 50%, but the crossed array will not. Essentially the long-axis mode of the parallel array can only interact with half of the incident photons, as the other half can only excite short-axis modes. For the cross-aligned, incident light can excite long-axis modes on either orientation, and so light that does not excite short-axis modes on one rod orientation (due to the low extinction efficiency of the short-axis mode) can excite a long-axis mode on the orthogonal orientation.

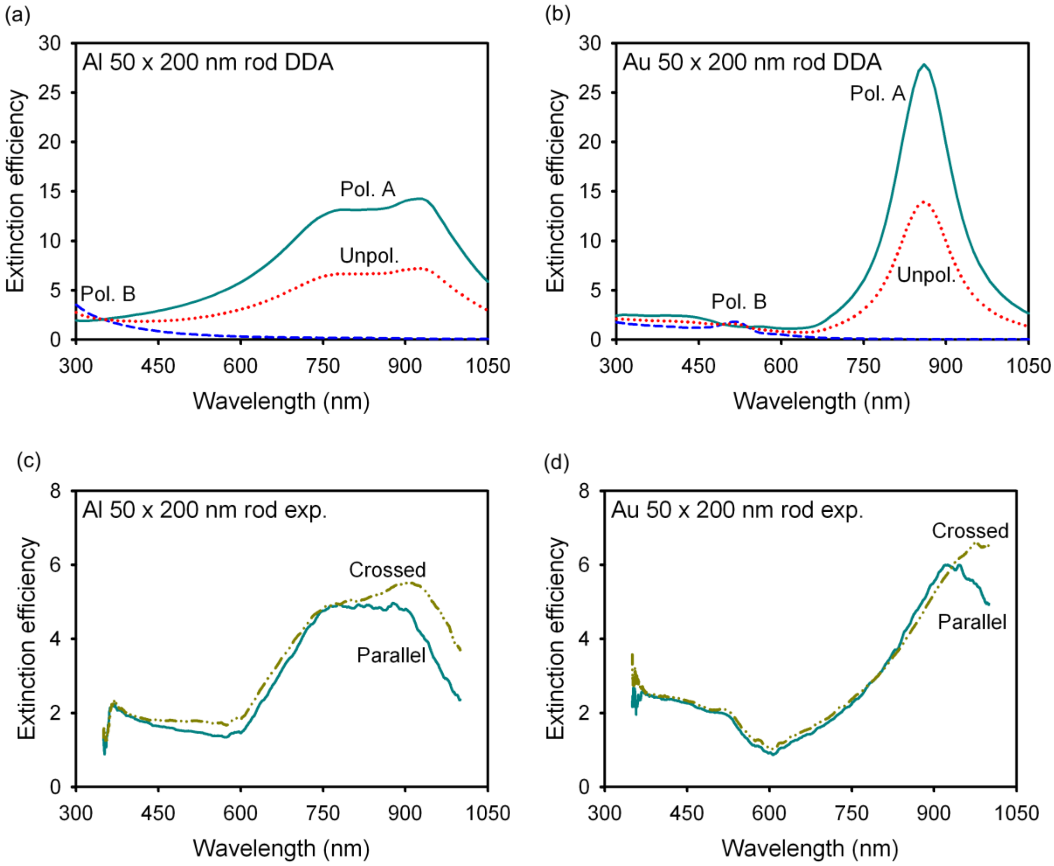

Figure 5.14: (a,b) DDA simulations of 50 x 200 nm rods, with light polarized along the long-axis (Pol. A), short-axis (Pol. B) or unpolarized (Unpol.), (c,d) extinction spectra of the geometries given in Fig. 5.13.

5.9: Lateral size

Increasing the volume of a spherical metal nanoparticle results in a red-shifting and broadening of the extinction peak. Therefore it is logical that the same trend will hold for planar metal nanoparticles. To investigate the effect of lateral particle size, arrays were fabricated with three sizes of square nanoparticle: 100 nm, 150 nm and 200 nm. Arrays containing 50 nm squares were also fabricated, but these were not detected experimentally and so will not be discussed further.

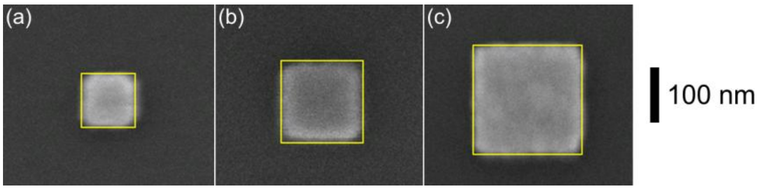

Figure 5.15: SEM images of the three square geometries investigated, each width sidelength of: (a) 100 nm, (b) 150 nm, (c) 200 nm. All images are overlaid with their ‘as-designed’ dimensions in yellow.

The simulation results show a red-shifting and broadening of extinction peak for increasing the lateral size of the nanoparticles. Additionally, as for spheres, the extinction efficiency decreases with increasing particle size. The effects of the narrow Al interband region are lessened in comparison with those observed for rectangular nanoparticles. Although these results show that it is possible to achieve a strong extinction response in the NIR by increasing the lateral particle size, we note that the extinction efficiencies are smaller than rectangles with peaks in the same wavelength range.

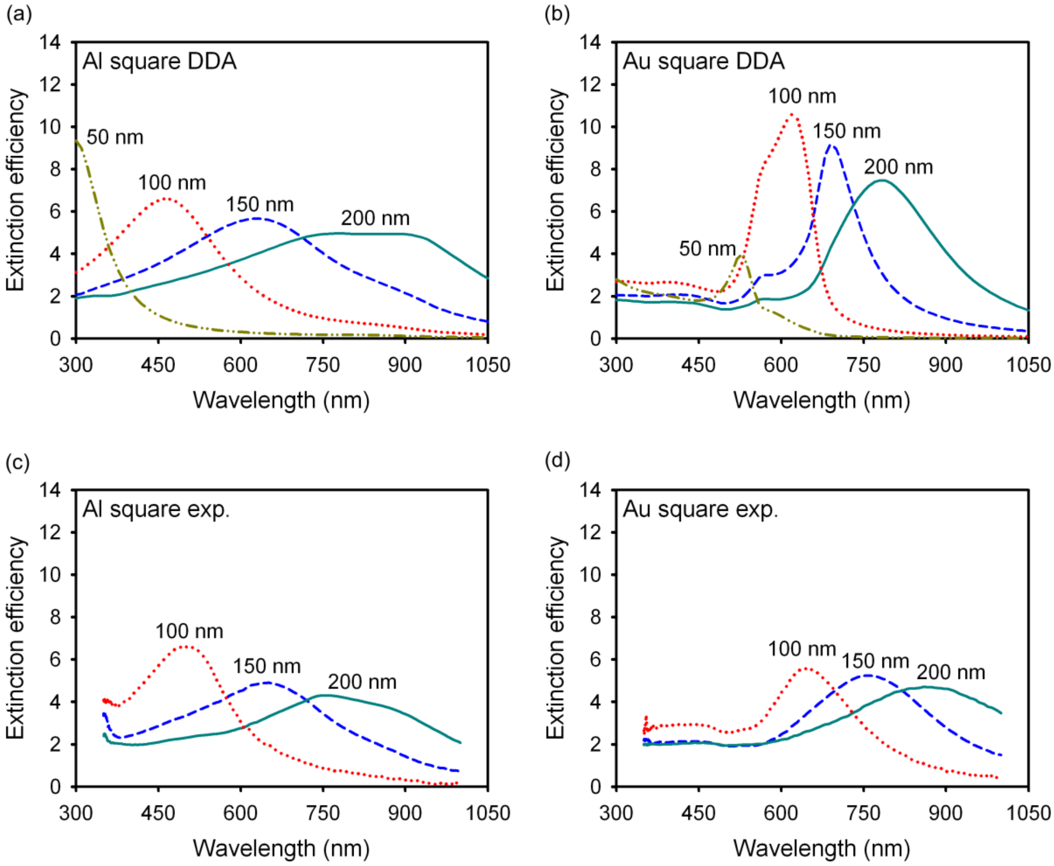

Figure 5.16: (a,b) DDA simulations and (c,d) experimental extinction spectra of the particle shapes shown in Fig. 5.15. DDA calculations were performed for n = 1.2 for Al, and n = 1.0 for Au.

The experimental results show similar trends, with particularly good agreement for the Al nanoparticles (Fig. 5.15c,d). The extinction efficiencies are attenuated for increasing lateral size for both metals, but the effect is weaker for Au than is predicted by simulations.

5.10 Particle ensembles

We have demonstrated that it is possible to selectively tune the extinction peak of metal nanoparticles by varying their size and shape. To increase the spectral range of extinction we can combine nanoparticles with different geometries into the same array. To confirm this an array was fabricated containing all four rectangle types investigated in Section 5.7. This array was designed to have the same average interparticle spacing of 500 nm, but each nanoparticle was given a width of 50 nm and then randomly assigned a length of 50 nm, 100 nm, 150 nm or 200 nm. Therefore the resulting array was composed of 25% of each of these rectangle lengths.

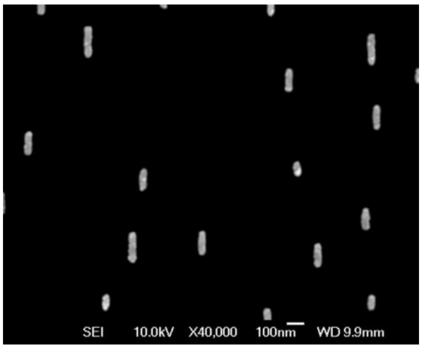

Figure 5.17: SEM images of an ensemble containing four types of rectangular nanoparticle.

The experimental results are given in Figure 5.18. For comparison we include the spectra of arrays containing each individual type of nanoparticle, normalized to have the same surface coverage (*i.e.* divided by four). The contribution of the 1:1 particle is expected to be negligible. Note that the results are presented as an extinction percentage and have not been converted to efficiencies. Extinction by the ensemble is closely correlated with the sum of the extinction signals from the individual particle types.

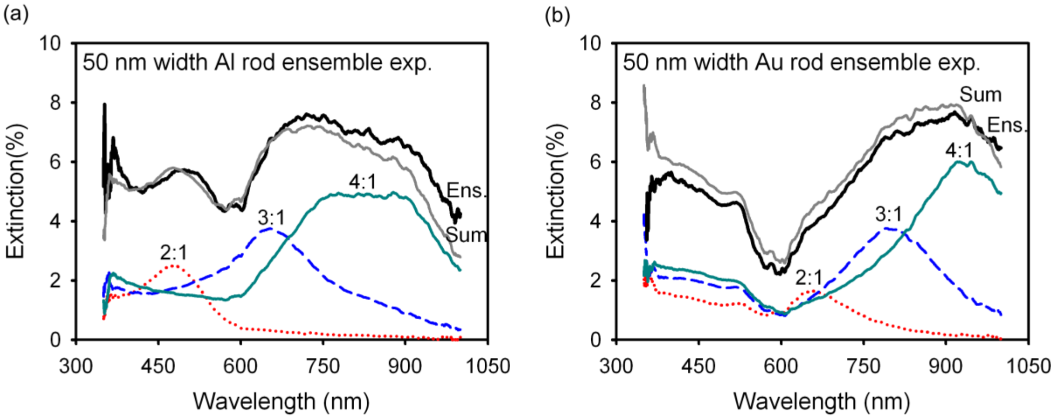

Figure 5.18: Experimental extinction measurements of (a) Al and (b) Au nanoparticle ensembles. The individual peaks are of arrays containing a single particle type, with extinction divided by four to normalize the surface coverage. The black line is the measured spectrum of the ensemble, and the grey line is the sum of three separate spectra.

These results demonstrate that the optical response of an ensemble of nanoparticles is the superposition of the optical properties of each individual nanoparticle type within the ensemble. The optical response of the fabricated array is very weak due to the low surface coverage of nanoparticles. Increasing the surface coverage will increase the optical response, but may also introduce spectral changes due to near-field coupling between nanoparticles. However, as near-field coupling has only a moderate effect on peak position for all but the smallest (< 50 nm) interparticle distances, it should still be possible to predict and therefore design the optical properties of ensembles by means of single particle simulations.

5.11 Radiative efficiency

So far we have only considered the extinction peak position of the fabricated nanoparticles, but clearly radiative efficiency also is an essential consideration for solar cell applications. Experiments to measure the absorption of the fabricated arrays by means of an integrating sphere were not successful. Problems were encountered due to the large size of the sphere, the small spot size required, and the low sensitivity of the detection equipment used. Improved results are expected for a smaller (*i.e.* less attenuating) integrating sphere and a more sensitive, lower noise detector.

The simulation results also contained values on absorption and scattering cross-sections and so we can investigate the radiative efficiency for all of the models studied. We present the data for Au nanoparticles in the absence of Cr, but note that Cr layers substantially reduce radiative efficiency (Fig. 5.4c). Even without Cr, the radiative efficiency of Au is lower than Al for most geometries discussed here (Fig 5.19). However, the radiative efficiency of Al nanoparticles decreases with increasing size, while the opposite trend is seen for Au. These effects can be correlated with the spectral shifts induced by an increase of the particle size. Al is more absorbing at longer wavelengths, while Au is more absorbing at shorter wavelengths. Again we note that triangular particles have a low radiative efficiency, although the radiative efficiency of the fabricated triangles is likely to be much higher due to the rounder tips. Red-shifting the extinction peak by size rather than aspect ratio results in a higher radiative efficiency.

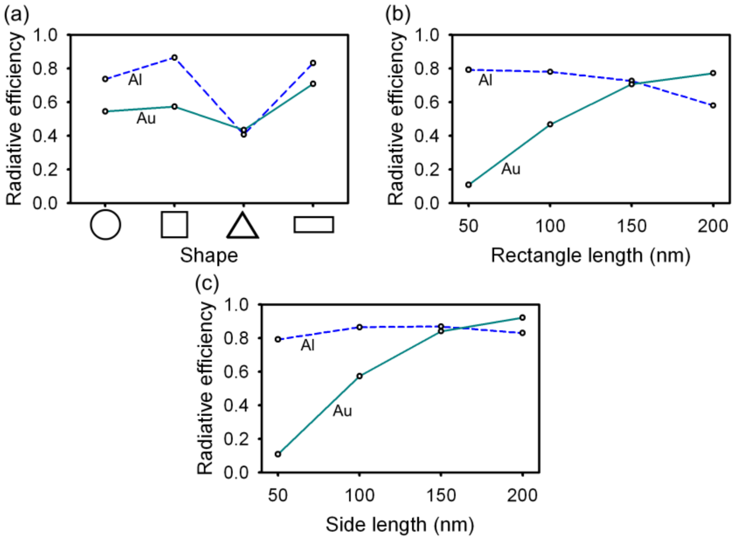

Figure 5.19: Simulated radiative efficiencies for geometries discussed in the previous section (a) shape, (b) aspect ratio, (c) size.

5.12 Conclusions

Good quantitative agreement has been demonstrated between DDA simulations and experimental extinction measurements of Al nanoparticle arrays. This was obtained by careful design of the array structure to minimize near-field and far-field coupling, and inclusion of effects due to the substrate and native oxide layer by means of an effective medium. The effects of inhomogenous broadening are thought to be minimal due to the good agreement with simulations.

Poorer agreement between experiment and simulation was found for Au nanoparticles, but the major trends were still well represented. Greatly improved agreement was found by including a Cr layer within the model, but this resulted in unacceptably long simulation times. The effect of Cr is to weakly blue-shift and strongly attenuate and broaden the extinction peak. Additionally, the radiative efficiency is substantially reduced by the presence of a Cr layer. Therefore it is essential that a non-metallic adhesion layer is used for solar cell applications. We expect that this will also give rise to much improved agreement with simulation results.

Extinction peaks of Al nanoparticles are generally blue-shifted, attenuated and broadened with respect to identical Au nanoparticles. Similar trends for all geometries were found for both metals, with the exception that increasing rectangle length results in an increase in extinction efficiency for Au but not for Al. The radiative efficiency of Al nanoparticles is higher than Au at short wavelengths, but is lower for long wavelengths. Both metals are strongly affected by their respective interband transition regions. These regions cause a decrease in radiative efficiency and an attenuation of extinction peaks.

Large extinction efficiencies in the NIR were demonstrated for both metals. However, none of the nanoparticles investigated in this study exhibited extinction peaks near the bandgap of crystalline silicon (~1100 nm). All of the nanoparticles were situated on a fused-silica substrate with no over-layer, and so there is considerable scope for further red-shifting by increasing the surrounding refractive index. Another possibility is to increase the size of the nanoparticle studied. This will result in red-shifting and, in the case of Au, will also increase the radiative efficiency. The use of Al nanoparticles for scattering of NIR photons is limited by the interband region.

We have demonstrated that nanoparticle ensembles exhibit a hybrid optical response, but have as yet not attempted to optimize the design of the ensemble. Given the excellent agreement between simulations and experiment, we can use simulations to design ensembles optimized for solar cell applications, both in terms of spectral coverage and radiative efficiency. Further work is required to investigate the maximum surface coverage of nanoparticles that can be used before near-field effects become important.

Chapter 6

Morphology and optical properties of silver island films

Metal island films offer a low cost, large-area method for creating dense arrays of metal nanoparticles on silicon solar cells. The optical properties of MIFs depend heavily on the deposition process and post-deposition anneal. For solar cell applications we require high scattering and low absorption across the solar spectrum. In particular, for a-Si:H solar cells the anneal temperature must be restricted to around 200^{o}C, to avoid damaging the a-Si:H layer.

In this chapter we investigate the optical and morphological properties of Ag island films, with the aim of developing a suitable process for use on a-Si:H solar cells. Ag was chosen for this study as it exhibits the strongest optical interaction strength of the noble metals, does not significantly oxidise at 200^{o}C, and does not suffer from interband absorption problems. To avoid degrading the electrical properties of the a-Si film it is important to isolate the nanoparticles from the active layer. This is best achieved by means of the TCO layer, which is part of all a-Si:H solar cell designs. Therefore, it is also necessary to study the influence of the TCO layer on the properties of the island film. For our studies we choose ITO, and investigate the effect of layers situated above and below the nanoparticles.

As with previous chapters, our aim is to achieve a high scattering efficiency across the solar spectrum, with a particular emphasis on the band-edge region of a-Si:H.

6.1 Experimental method

All samples were prepared on 50 x 50 mm^2 Corning glass substrates. The substrates were cleaned by sonication in DI water, then in Senico solution, and again in water, and finally dried in flowing nitrogen. ITO was RF-sputtered (Model SBR-2306, ULVAC) at a power of 100W, with 200 sccm O_2 and 0.75 sccm Ar. The chamber was pumped down to around 3 x 10^{-5} Torr prior to introduction of the gases. The target was exposed to plasma for five minutes with the shutter closed prior to deposition, to ensure a clean target surface. Nine substrates were loaded in the chamber in each run, and were rotated at 10 RPM during deposition. A calibration layer thickness of 76 nm was obtained using a step-profile measurement of a layer after a deposition time of 12 minutes. All other thicknesses were calculated by assuming a constant deposition rate during the process, and scaling the step-profile measurement accordingly. The three thicknesses used in this experiment are 12 nm, 24 nm and 36 nm, which were obtained by deposition times of 2 min, 4 min and 6 min respectively. No in-situ thickness monitoring was used.

Ag films were deposited by electron-beam evaporation at a pressure of around 10^{-7} Torr (custom design, ULVAC). Four samples were loaded in each run, positioned in a square array equidistant from the crucible. No rotation was used during deposition, and the substrate temperature was not controlled. An in-situ quartz balance was used to determine layer thickness. Calibration was performed by a step-profile measurement of an Al film, and a ‘tooling factor’ was calculated based on the difference between the quartz balance and step-profile readings. The quartz balance rate monitor used in this experiment has a lower display limit of 0.001 nms^{-1}. Deposition speeds below this value were calculated by timing the duration of the deposition process until the final thickness was obtained. For all runs the crucible was heated enough to melt the Ag prior to deposition (*i.e.* with the shutter closed) to remove contamination. The beam was turned off prior to shutter opening, after which the beam current was slowly increased until the required deposition speed was achieved. Film thicknesses are denoted by the ‘mass thickness’, which is the thickness of a planar, continuous film that has an identical mass to the island film.

Annealing was performed in a vacuum oven. Samples were placed in the centre of the oven on metal sheets to promote even dissipation of heat. The chamber was pumped down for approximately 30 minutes prior to heating. A ramp rate of approximately 5°C/min was used to achieve the target temperature (ranging from 150°C to 250°C). After two hours at the target temperature the samples were left to cool in vacuum until the chamber temperature was lower than 50°C.

6.2 Characterisation

Fabricated samples were optically characterized by a spectrophotometer (Perkin-Elmer Lambda 950) with an integrating sphere attachment. Spectra were recorded at 1 nm intervals from 400 nm to 800 nm. Diffuse transmission and diffuse reflectance were obtained by mounting the sample on the front and rear ports of the integrating sphere respectively, with the coated side of the glass facing towards the light source. A dual-beam configuration was used, with a reference beam directed at the interior surface of the sphere. Extinction measurements were taken using the same spectrophotometer, but samples were placed directly in the beam path and away from the integrating sphere. An aperture of approximately 4 mm^2 was used to limit transmission of scattered light. In all cases the beam was directed at the centre of the sample. Spectra are normalized to a blank reference, and therefore include effects (*i.e.* reflection) due glass and ITO. Absorption spectra were calculated by subtracting the sum of diffuse transmission and diffuse reflectance from 100%, using the assumption that photons not detected in reflection or transmission measurements have been absorbed. This method of measuring absorption is prone to error, and is strictly only valid for sparse coatings of nanoparticles. In particular the effect of the substrate is difficult to account for, as it can induce multiple scattering due to reflection at the rear-surface or TIR. Additionally, inconsistencies in the optical configuration for diffuse transmission and diffuse reflectance measurements (including differences in beam divergence and spot size) also affect the accuracy of these measurements. However, these measurements still provide a useful semi-quantitative measure of absorption. Optical measurements were performed within two weeks of sample fabrication.

The geometric properties of the fabricated samples were analysed using a FEG-SEM operating at 10 kV with a working distance of approximately 10 mm (JSM-6500F, JEOL). No charge dissipation layer was used, and charging effects were found to be minimal even for the thinnest ITO layer. Regions near the centre of the substrate were imaged at magnifications of 20k, 40k and 60k. SEM analysis was performed approximately two months after sample fabrication.

Image analysis was performed using a custom ImageJ macro. First, the SEM image is converted to a binary image by a process outlined in Figure 6.1. A Gaussian blur was found to improve the thresholding process by smoothing the boundary between the background and particle, therefore limiting the noise-induced edge roughness (Fig. 6.2). A binary image is created by setting a grey value threshold: below this value pixels are set to white, above the value pixels are set to black. The choice of threshold value defines the particle boundary, and is subjectively chosen. This step is the major source of error in size and shape analysis, as a small change in threshold value gives rise to a change in all particles sizes in an image, and can therefore bias mean values. After the threshold has been applied edge particles are removed from the image as they would lead to incorrect average values of size and shape. Edge particles are not removed for surface coverage calculations.

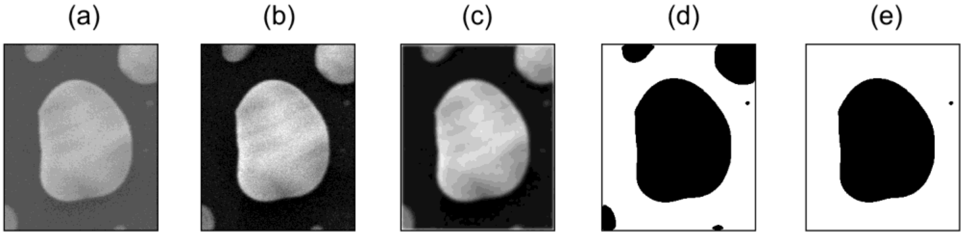

Figure 6.1: Process of extracting particle geometry: (a) SEM image, (b) brightness and contrast adjustment, (c) Gaussian blur, (d) threshold, (e) remove edge particles.

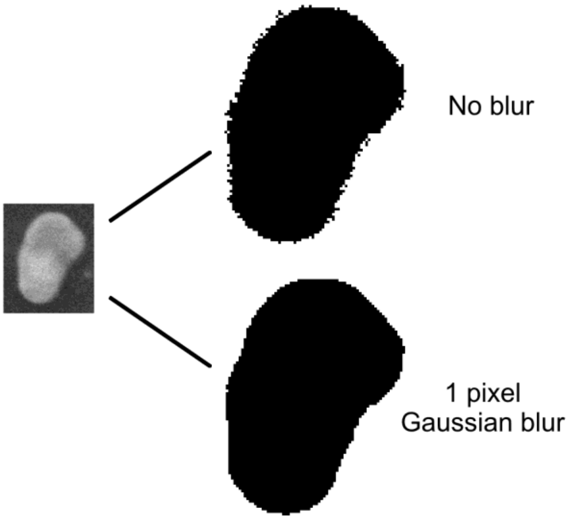

Figure 6.2: Effect of applying Gaussian blur prior to threshold.

The choice of threshold value is particularly important for ensuring separation. This is complicated by a spread in intensity across the image, which results in a local variation of suitable threshold value. Unfortunately the developed software was not sophisticated enough to account for this variation, and so only a global threshold value could be applied. Setting the threshold value too high results in under-estimation of particle size, while setting it too low can result in over-estimation of particle size or incomplete separation of particles. This latter effect occurs when the grey value between two particles is above the threshold, and so they are treated as a single particle. This strongly affects measurements of the average particle diameter and the aspect ratio, leading to an increase in the former and a decrease in the latter. One method of separated conjoined particles is to use a watershed segmentation algorithm *[239]*. Watershed segmentation operates by first calculating a distance map for each pixel in a particle (*i.e.* the distance from a given black pixel to the nearest white pixel), assigning the pixels with the largest values as 'ultimate eroded points' (UEPs). Once the UEPs for each particle are found they are dilated along the distance map until they are just about to come into contact with a neighbouring expansion. This reforms the original image, but separates neighbouring particles. Unfortunately because the watershed algorithm only operates on binary images it cannot distinguish between a true elongated particle and a conjoined particle pair, resulting in splitting of elongated particles. As such this method is only suitable for images that feature nearly circular particles prior to thresholding. An alternative is to manually draw single pixel thick white lines to separate conjoined nanoparticles, but this is extremely time-consuming. We used a mixture of these two approaches to ensure separation of particles.

Size and shape information can be calculated from the binary image by automatic analysis routines. All values are converted from pixel dimensions to nanometres by manual measurement of the scale bar. Useful particle properties include area, equivalent diameter (the diameter of a circle with identical area), aspect ratio and circularity. For optical studies the equivalent diameter (hereafter referred to as diameter) and aspect ratio are of particular interest. Aspect ratio analysis was performed by measuring Feret lengths, *i.e.* lengths that pass through the centre of mass of the particle, at 1° interval across 180° (Fig. 6.3). The centre of mass of a particle is the average of the x-y positions of all pixels comprising it. We define the aspect ratio as the ratio of the shortest Feret length to the longest, therefore values range from near zero to unity. Note that this is the inverse of the definition used in previous chapters. For MIF analysis it is useful to constrain the range of aspect ratios between 0 and 1, and therefore the inverse notation is preferable.

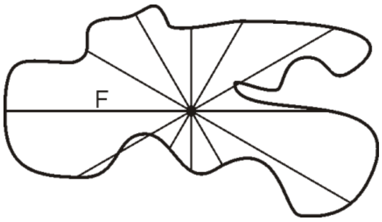

Figure 6.3: Example of Feret diameters through arbitrary particle. This particle has a circularity of 0.32 and aspect ratio of 0.39.

To visualize the extracted data we follow Heilmann's use of 3D histograms to show distribution of diameter and aspect ratio *[81]*. However, rather than using counts we weight the column binning by surface coverage. This is because the purpose of our size and shape analysis is to understand the optical properties of the island film, and these are related to the surface coverage of a given type of particle and not to their relative numbers. For example, if an image contains ten 10 nm diameter particles and one 300 nm particle, a count-based analysis would bias in favour of the 10 nm particles, but the optical response would be primarily related to the 300 nm particle. Weighting by surface coverage solves this disparity. In this scheme the height of a column represents the surface coverage of a given range of aspect ratio and particle diameter. Therefore the sum of all columns in the histogram is the surface coverage (%), and not the total number of particles as in the case of Heilmann. Standard deviation and mean values of particle properties are also calculated with a weighting factor:

$$\sigma = \sqrt{\frac{\sum_{i=1}^{N} P_i (x_i - \bar{x})^2}{\sum_{i=1}^{N} P_i}} \quad ; \quad \bar{x} = \frac{\sum_{i=1}^{N} P_i\, x_i}{\sum_{i=1}^{N} P_i} \tag{6.1}$$

Where σ is the weighted standard deviation, $\bar{x}$ is the weighted mean, x_i is a property (*e.g.* diameter or aspect ratio) of particle number i, P_i is the area (*i.e.* surface coverage) of particle i, and N is the total number of particles. The denominator of both equations represents the total surface coverage, excluding edge particles.

6.3 Experiment overview

Two groups of samples were fabricated. The first group of samples were fabricated to study the effect of process conditions and anneal conditions (Table 6.1). The second group were fabricated to study the effect of interaction with ITO undercoating and overcoating (Table 6.2).

To minimize variation in film morphology, all samples for a given mass thickness and deposition speed were deposited simultaneously, and the respective ITO layers were also deposited simultaneously. A 36 nm ITO layer was chosen for all samples in the first group as it is thick enough to contain most of the near-field region of a particle, but thin enough that waveguide-propagating modes are not supported.

	Glass, no anneal	**36 nm ITO, no anneal**	**36 nm ITO, 150°C**	**36 m ITO, 200°C**	**36 nm ITO, 250°C**
2.5 nm Ag	-	M	M	M	M
5.0 nm Ag	S, M, F	S, M, F	S, M, F	S, M, F	-
7.5 nm Ag	-	M	M	M	M
10.0 nm Ag	S, M, F	S, M, F	S, M, F	S, M, F	-
15.0 nm Ag	-	M	M	M	M
20.0 nm Ag	-	M	M	M	M

Table 6.1: Samples prepared to investigate effect of temperature, deposition rate and substrate. F, M and S represent deposition speeds of 0.2 nms^{-1}, 0.02 nms^{-1} and < 0.001 nms^{-1} respectively.

	Uncoated	**12 nm ITO**	**24 nm ITO**	**36 nm ITO**
Glass	5 nm, M, 200°C	5 nm, M, 200°C	5 nm, M, 200°C	5 nm, M, 200°C
36 nm ITO on glass	5n m, M, 200°C	5 nm, M, 200°C	5 nm, M, 200°C	5 nm, M, 200°C

Table 6.2: Samples prepared to investigate the effect of ITO undercoating and overcoating.

6.4 Optical properties of ITO layers

Transmission spectra of sputtered ITO films on glass are given in Fig. 6.4. Transmittance is reduced with increasing ITO layer thickness, particularly at short wavelengths. All MIFs were fabricated on glass coated with a 36 nm layer of ITO, unless otherwise stated.

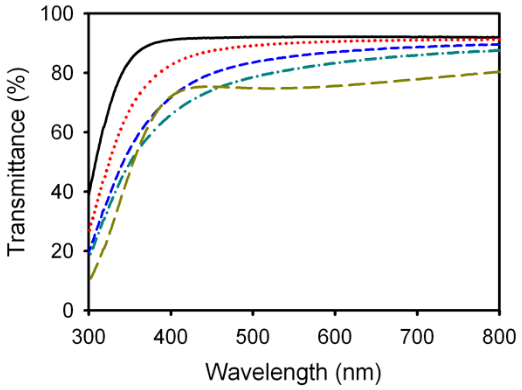

Figure 6.4: Transmittance spectra of glass coated with 0 nm, 12 nm, 24 nm, 36 nm and 72 nm of ITO.

The optical spectra of MIFs presented in this chapter have been normalized to the optical response of a bare glass sample, and so also include effects (*i.e.* extinction) due to the ITO layer. This is mainly due to an increase in surface reflectance caused by the higher refractive index of the ITO layer in comparison with glass.

6.5 Film thickness

SEM images of Ag island films with varying mass thickness are given in Figure 6.5. The percolation threshold is reached between 5.0 nm and 7.5 nm. For mass thicknesses of 7.5 nm and above a semi-continuous or porous film structure is seen. There appears to be no correlation between pore size and thickness. A clear multi-crystalline structure is seen in all semi-continuous films, with a general correlation between grain size and layer thickness. When annealed for 2 hours at 200°C all films consist of well-separated islands.

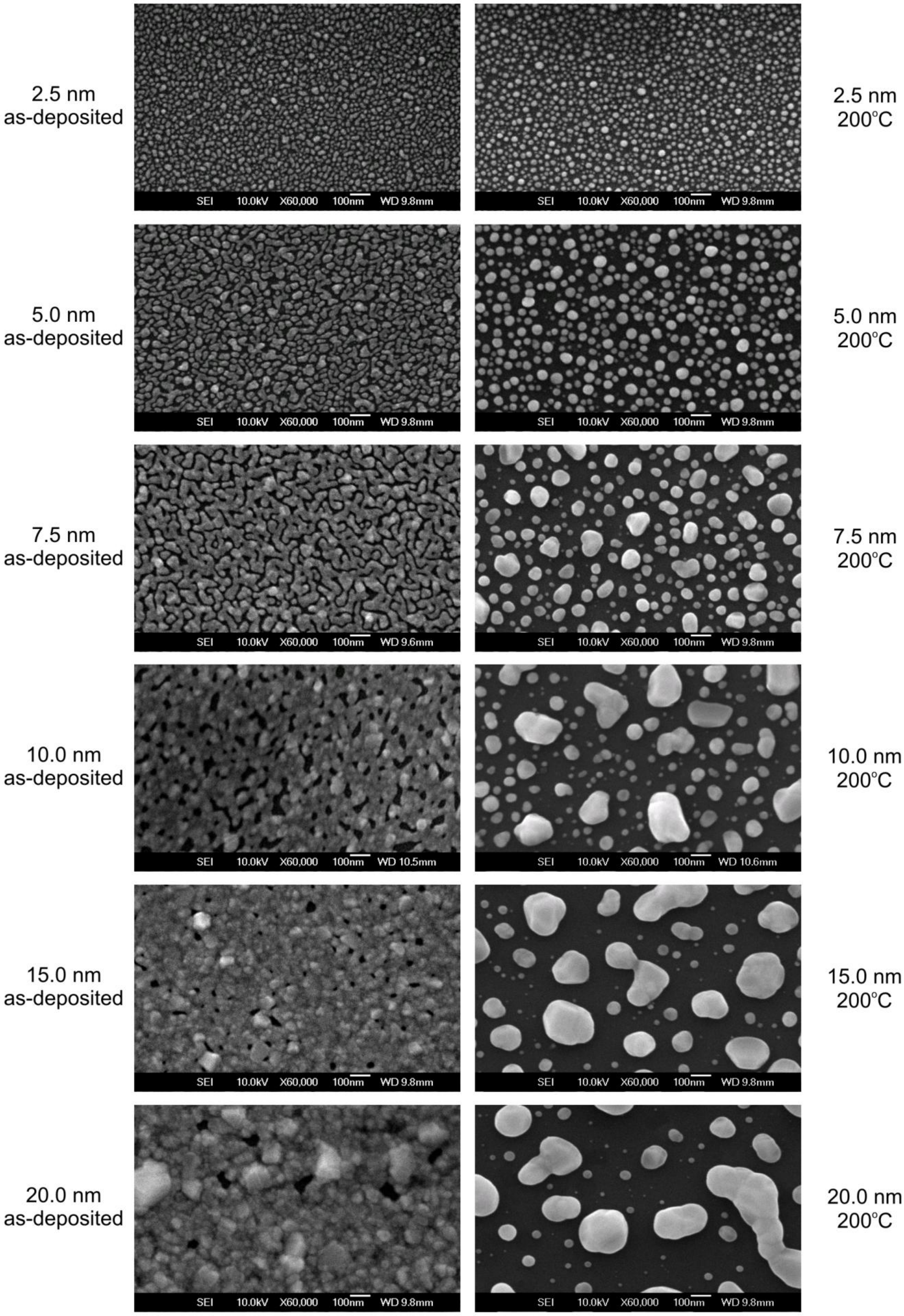

Figure 6.5: SEM images of Ag island films (left) as-deposited and (right) after a 2hr 200°C anneal, with mass thickness ranging from 2.5 nm to 20.0 nm

Figure 6.6 shows the distribution of particle diameter and aspect ratio in terms of surface coverage, and these results are summarized in Fig. 6.7. The extremely wide range of aspect ratios for the 2.5 nm film is unexpected as the particles appear to be nearly circular in the SEM image. This disparity is due to the limited number of pixels (around 200-300) used to represent each nanoparticle of this size. The limited resolution combined with noise effects can lead to substantial error in aspect ratio calculations. Additionally, the blurred outlines of nanoparticles can cause multiple particles to be combined together during conversion to a binary image, further decreasing aspect ratio. Particle separation techniques were not always successful for such small particle sizes.

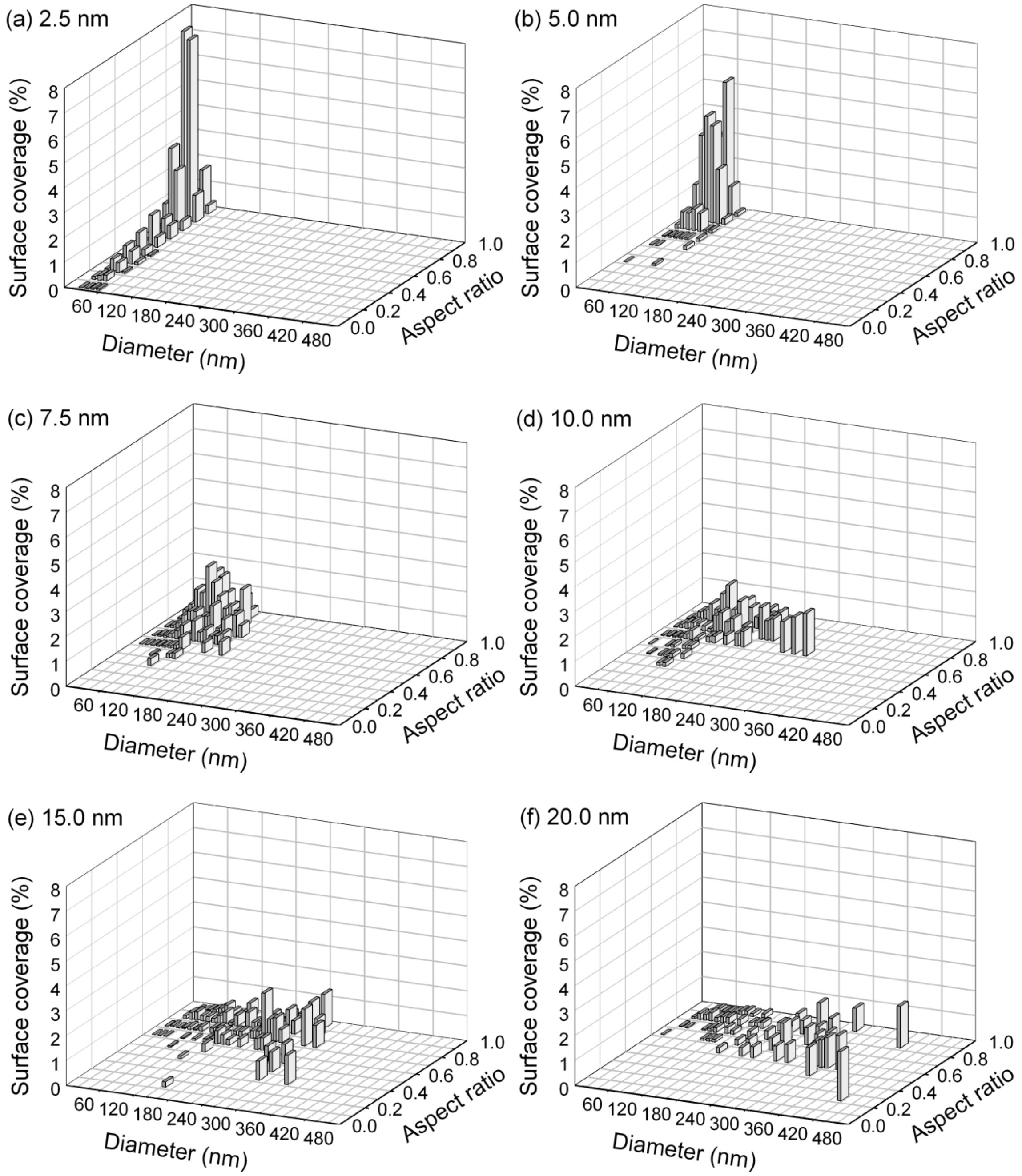

Figure 6.6: Particle size and shape distribution of Ag island films annealed at 200°C for 2hr.

The average particle diameter of annealed films increases with increasing mass thickness (Fig. 6.7). Aside from the 2.5 nm layer, the mean aspect ratio is seen to decrease with increasing layer thickness. The relationship between particle shape and layer mass thickness is due in part to the morphology of the as-deposited film. Very thin films already consist of well isolated nanoparticles, and so annealing leads to rounding (reshaping) of particles due to recrystallization. However, for thicker films the as-deposited layer is semi-continuous. In this case the recrystallization process initially serves to isolate particles by diffusion of atoms from low density areas to high density, and then reshaping can occur after separation, but to a lesser extent than for thinner films as it begins later in the process. Particles up to 420 nm diameter are observed in the 20 nm film. The lower limit of particle size is not known due to the limited resolution of the SEM images, but we estimate it to be less than 20 nm. Mean values of diameter range from 25 nm to 240 nm, and exhibit a nearly linear relationship with layer thickness. Aspect ratios ranging from 0.15 to 0.96 with mean values ranging from 0.65 to 0.8 are observed (excluding the 2.5 nm film). The standard absolute standard deviation of both properties increases with layer thickness, but in relative terms it remains fairly constant. We note the importance of quantitative measurement of nanoparticle geometry, particularly for thicker films. The SEM images of the two thickest annealed films look nearly identical by visual inspection (Fig. 6.5), but have considerably different size and shape distributions (Figs. 6.6, 6.7).

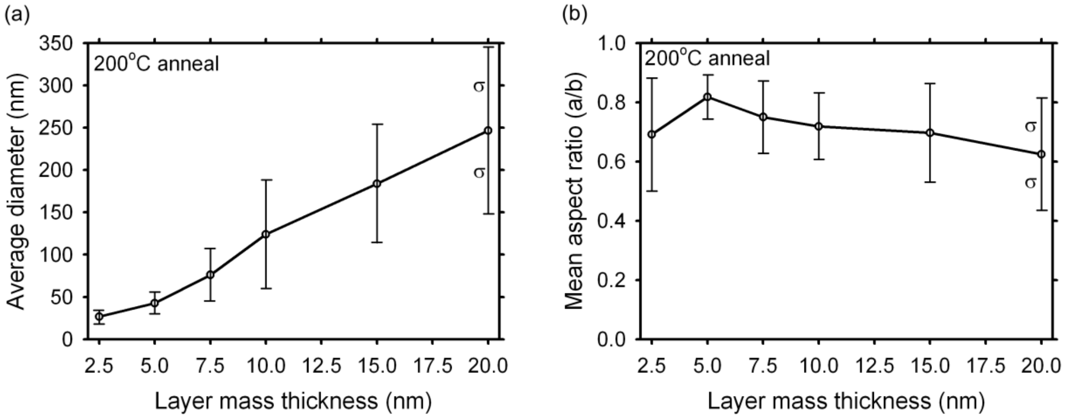

Figure 6.7: (a) Particle diameter and (b) aspect ratio of Ag island films annealed at 200°C for 2hr as a function of layer thickness, with the respective standard deviations represented by error bars.

Table 6.3 lists the calculated surface coverage of as-deposited and annealed films, as a function of mass thickness. The surface coverage of as-deposited films increases linearly with mass thickness. The percolation threshold occurs between 60% and 75% surface coverage. No clear trend is observed for surface coverage compared with layer mass thickness for annealed films, and values are contained within the relatively narrow range between 32% and 38%. Surface coverage is strongly affected by the choice of greyscale threshold value, and so an error of the order of 1-3 % absolute is expected.

	Surface coverage (%)	
Layer mass thickness (nm)	**As-deposited**	**200°C**
2.5	46.04	36.71
5.0	59.60	32.56
7.5	75.67	37.40
10.0	89.74	34.62
15.0	98.00	33.97
20.0	98.08	33.79

Table 6.3: Surface coverage of as-deposited and annealed Ag island films as a function of mass thickness.

The optical properties of metal island films are highly sensitive to the distribution of nanoparticle size and shape, as is seen in the optical spectra of fabricated samples (Fig. 6.8). 2.5 nm and 5.0 nm as-deposited layers feature broad extinction peaks between 550 nm and 600 nm. Beyond the percolation threshold the optical spectra of as-deposited films no longer feature resonant peaks, and gradually take on the characteristic properties of thin, continuous films. Absorption by as-deposited films is strongly reduced for films of 10 nm and higher due to increased reflectance, as is the case for continuous films. The effect of annealing on peak position of as-deposited layers will be discussed in the next section.

The resonance peak of annealed films is seen to broaden and red-shift with increasing layer mass thickness. The red-shifting is associated with an increase in mean particle diameter and decrease in mean aspect ratio, as evidenced by SEM analysis. Broadening of the peak is related to an increase of average particle diameter and also to an increase in the standard deviation of diameter and aspect ratio. As discussed in Chapter 4, increasing the diameter of a nanoparticle results in a broadening and red-shifting of peak position. Alternatively, as discussed in Chapter 5, a distribution of particle types that each exhibit peaks at different parts of the spectrum can also lead to a broad optical response. The annealed 7.5 nm and 10.0 nm samples have a strong peak asymmetry, which is a strong indication of a broad distribution of particle geometries, as peak broadening results in symmetrical peaks. In the extreme case, a nearly flat extinction spectrum is seen for the 20 nm sample, which is most likely due to a combination of the two processes.

Absorption of films from 2.5 nm to 10 nm is largely conformal to extinction, and is due to the innate absorption by small (< 100 nm) particles. Absorption in the infrared increases with particle size, and is zero for 2.5 nm and 5.0 nm annealed films above 600 nm, and so ‘extinction’ in this region is predominantly due to reflection by the ITO layer. The absorption peaks of the two thickest films feature markedly different lineshapes to their corresponding extinction peaks, and both peak at around 475 nm. This could be due to high absorption from small particles in the distribution, but both films have very low surface coverage of particles below 100 nm diameter. Instead, given the large average particle diameter, it is likely that the high absorption is due to excitation of higher-order modes.

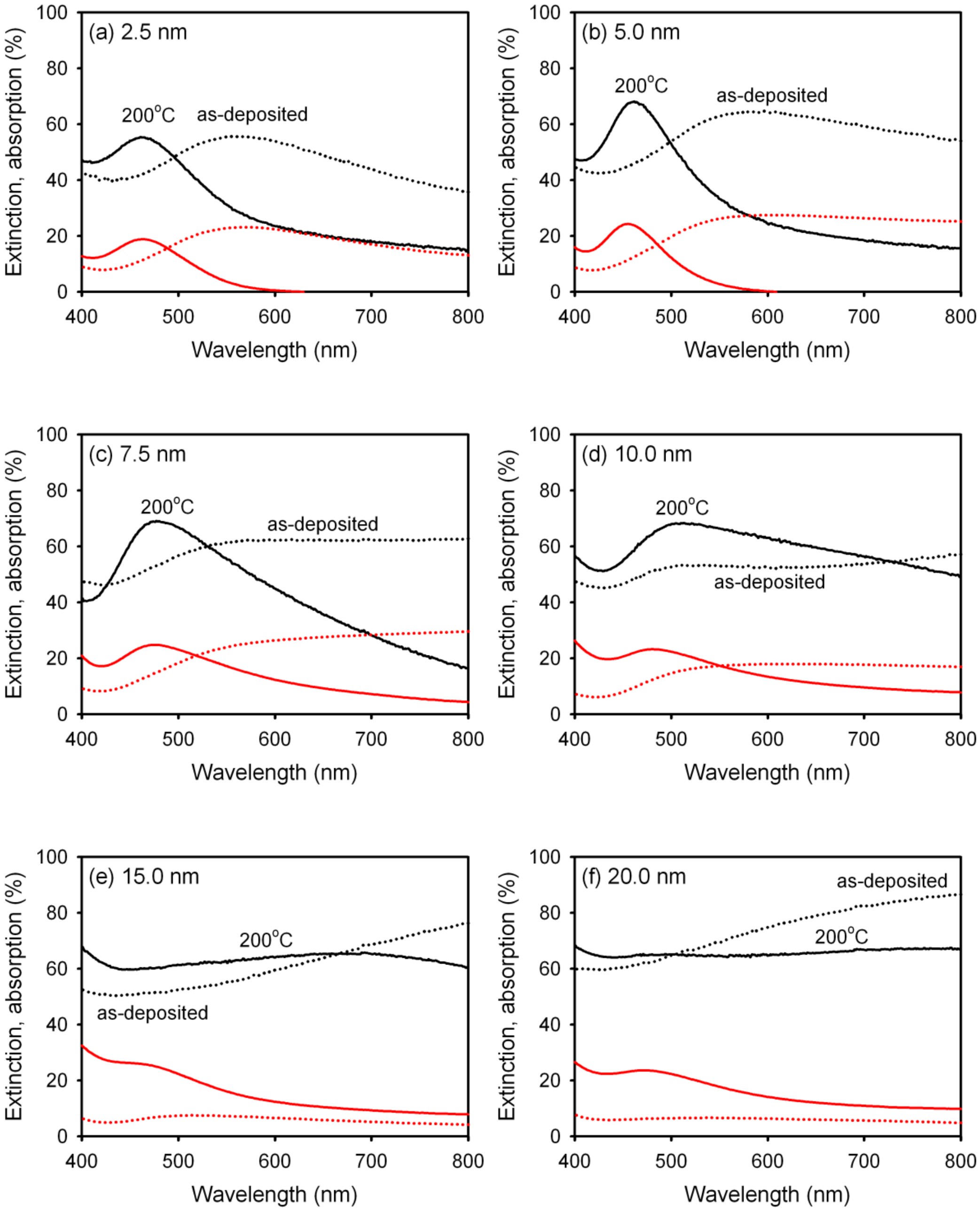

Figure 6.8: Optical extinction (black lines) and absorption (red lines) of as-deposited (dotted lines) and annealed (solid lines) films, with mass thickness ranging from 2.5 nm to 20.0 nm.

We define the term ‘spectral extinction’ as the extinction percentage averaged from 400 nm to 800 nm. This gives a measure of the optical interaction with photons across this wavelength range. As can be seen from Figure 6.9, spectral extinction increases sharply as the film thickness is increased from 2.5 nm to 10 nm, but saturates around 65% for films of 10 nm and higher. The increase in spectral extinction results from broadening of peak width, which we have discussed as a combination of an increase in the mean size and the standard deviation of particle diameter. The value of 65% is surprisingly low given the high surface coverage. Simulations of large (150 – 300 nm diameter) Ag spheres show that extinction factors of around 3-4 are expected across this wavelength range, which would correspond to 100% extinction for a 33% surface coverage. Given that the extinction also includes contributions from reflectance by the glass and ITO layers, these experimentally obtained values seem particularly low. Errors in extinction measurements due to detection of photons forward-scattered at small angles could lead to an underestimation of extinction values. Due to limitations of the spectrophotometer configuration the measurements were taken with a large beam size and a relatively large aperture size, and so a relatively large amount of forward-scattered light may have been detected.

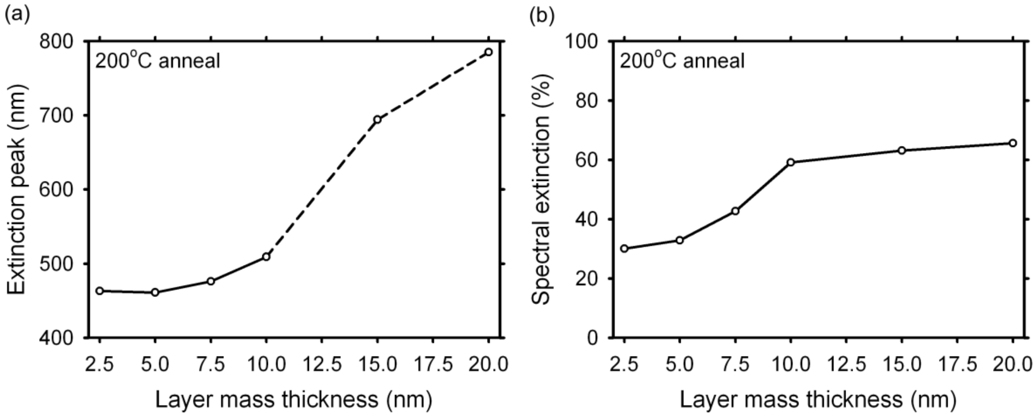

Figure 6.9: Summary of effect of layer mass thickness on (a) extinction peak position and (b) spectral interaction. The peak positions of the 15 nm and 20 nm films are difficult to determine accurately due to the broad widths of the extinction peaks of these films.

6.6 Anneal temperature

The anneal temperature also affects particle morphology and optical properties of a metal island film. For the case of a 5 nm film, the effect of increasing anneal temperature from 150°C to 200°C is not immediately clear from visual inspection of SEM images (Fig 6.10). However, a clear change in aspect ratio is seen in the corresponding 3D histograms (Fig 6.11). The as-deposited film consists of a wide distribution of particles diameters with very low aspect ratio. A 150°C anneal reduces the mean diameter, but many low aspect ratio particles remain. A 200°C anneal also reduces the mean diameter, but additionally substantially increases the mean aspect ratio. The morphological changes lead to a pronounced change in the extinction spectra of the three films. As the anneal temperature is increased the peak position red-shifts and the peak width decreases (Fig 6.11d).

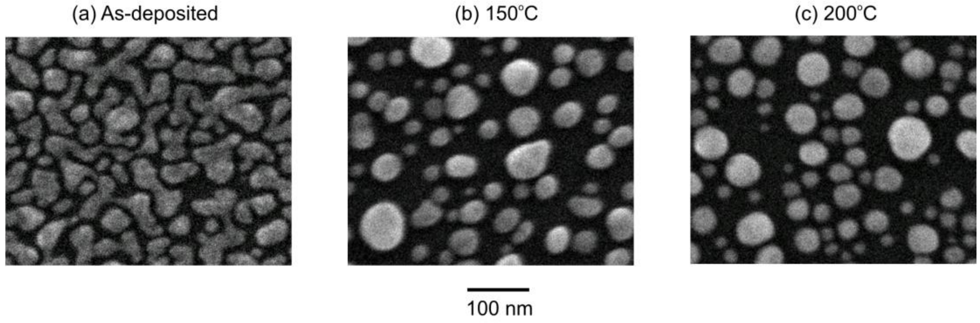

Figure 6.10: SEM images of 5 nm Ag films, (a) as-deposited, (b) after 2hr 150°C anneal, (c) after 2hr 200°C anneal.

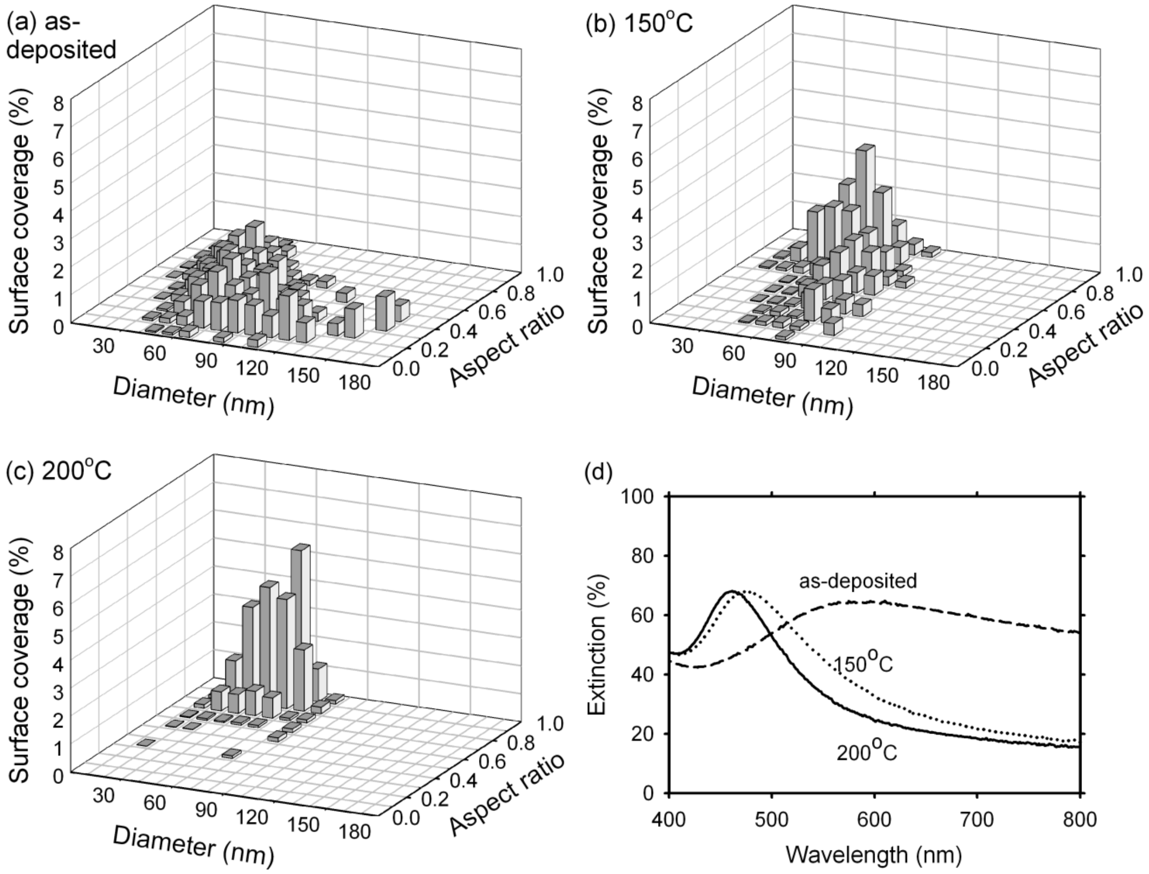

Figure 6.11: (a,b,c) 3D histogram of diameter and aspect distributions and (d) extinction spectra of samples given in Fig. 6.10.

These results highlight the relationship between the peak width and the standard deviations of both diameter and aspect ratio. The extinction peak of the as-deposited 5 nm film is broad and asymmetric (Fig. 6.11d). This is due to the broad spread of particle diameters and aspect ratios, as evidenced by the corresponding histogram (Fig. 6.11a). The extinction peaks of both annealed samples are considerably blue-shifted and narrowed. Although the mean diameter is seen to decrease the principle change is in the standard deviation of diameter and aspect ratio. The 150^{o}C sample is seen to have a much narrower spread of diameters, but still exhibits a reasonably broad range of aspect ratios (Fig. 6.11b). Increasing the anneal temperature to 200^{o}C has little effect on the spread of diameters, but a sharp increase in both the mean and standard deviation of aspect ratio is seen (Fig. 6.11c). Therefore we conclude that the extremely broad as-deposited peak is primarily due to the broad spread of particle diameters, which decreases upon annealing.

The physical mechanisms behind the temperature-induced change in morphology are related to atomic diffusion. The rate of atomic diffusion increases for higher anneal temperatures. Atomic diffusion gives rise to particle formation (from semi-continuous films), coalescence and reshaping. Coalescence results in an increase in particle size and a decrease in aspect ratio. Reshaping results in a decrease in aspect ratio and a decrease in lateral particle size. For a 5 nm film reshaping appears to be the dominant process, leading to a decrease in mean diameter and aspect ratio when the temperature is increased. The decrease in mean diameter is most likely due to an increase in out-of-plane height, *i.e.* the particles become more spherical with annealing.

To further investigate this effect of anneal temperature the 2.5 nm, 7.5 nm, 15 nm and 20 nm films were annealed at one of three temperatures: 150^{o}C, 200^{o}C and 250^{o}C. The trends are generally not linearly related to temperature, and are also quite different for each layer thickness (Fig. 6.12). Annealing an island film results in a complex series of reshaping and coalescence processes, which will affect each film morphology differently. For example in thin films we expect reshaping to dominate and affect only individual particles, while in thick films reshaping may result in the separation of one large particle into multiple smaller ones. Mean diameter generally decreases with increasing anneal temperature, with the exception of the 7.5 nm and 20 nm films, which show an increase in mean diameter when the temperature is increased from 200^{o}C to 250^{o}C (Fig. 6.12a). The standard deviation of diameter also generally decreases with temperature, with the strongest effect on the two thickest films (Fig. 6.12b). Aspect ratio increases for an increase in temperature from 150^{o}C to 200^{o}C, but decreases when the temperature is further increased to 250^{o}C for the 15 nm and 20 nm films. The standard deviation of aspect ratio decreases for all film thicknesses for increasing temperature. We exclude the 2.5 nm films from aspect ratio studies due to inaccuracies in the analysis of such small particles, as previously discussed.

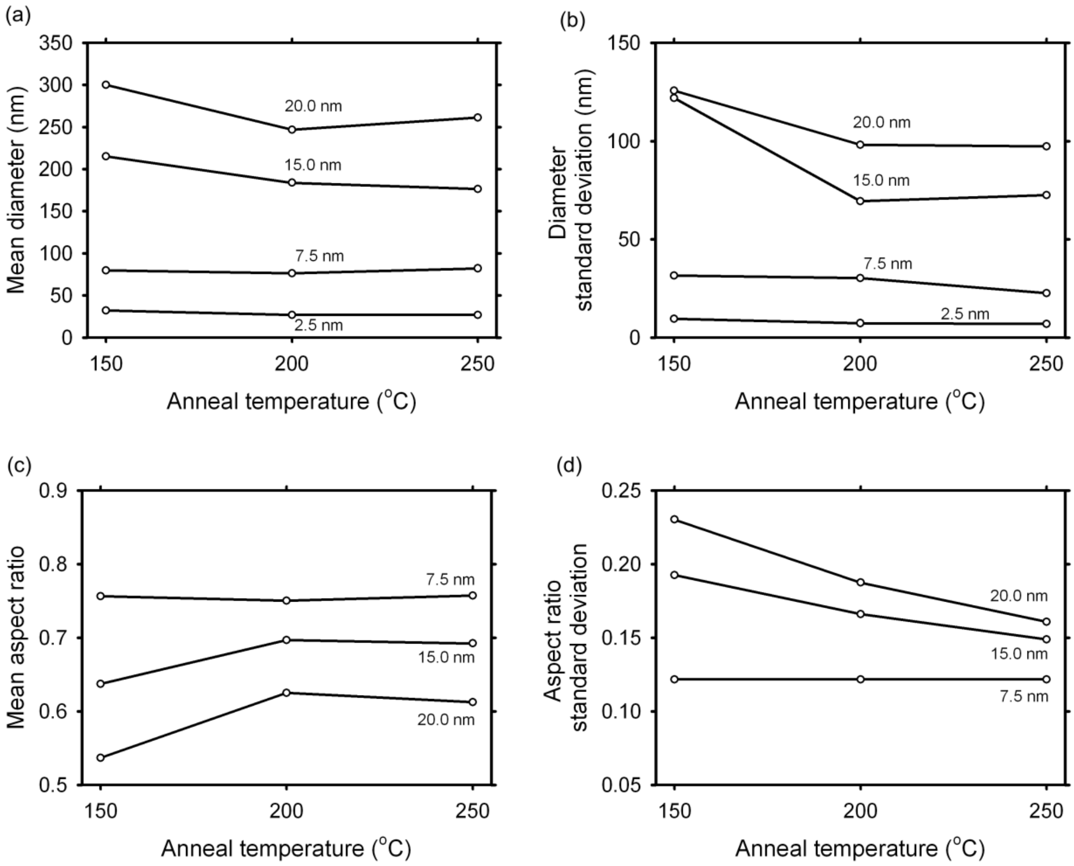

Figure 6.12: Mean values and standard deviation of (a,b) diameter and (c,d) aspect ratio, as a function of anneal temperature.

Given the large affect of anneal temperature on the overall film morphologies we would also expect a corresponding change in the optical properties. A summary of the optical properties of the films as a function of anneal temperature is given in Figure 6.13. Generally a blue-shift in peak position and a decrease in spectral extinction is seen for an increase in anneal temperature, similar to that observed for the 5 nm films (Fig. 6.11d). A decrease in spectral extinction is due to a decrease in peak width, which is related to the drop in standard deviation of diameter and aspect ratio (Fig. 6.12b,d). However, the extinction peak position trends are not well correlated with any of the morphological trends. The large changes in peak position for the two thickest films are misleading. Due to the nearly flat extinction profiles of these films (Fig. 6.8e,f), the peak position can change dramatically for only small changes in the extinction spectra. Indeed, the spectral extinction remains fairly constant for these films suggesting that the overall optical properties of these films are similar.

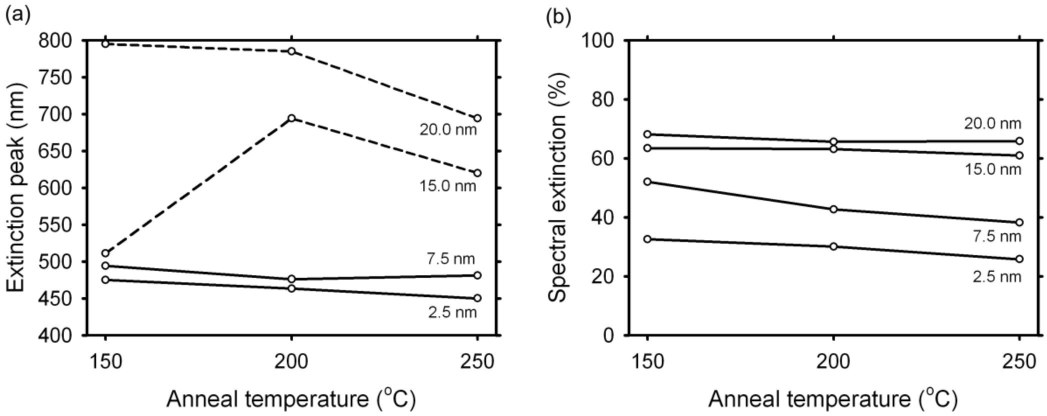

Figure 6.13: Summary of changes in (a) extinction peak position and (b) spectral extinction, as a function of anneal temperature. The peak positions of the 15 nm and 20 nm films are difficult to determine accurately due to the broad widths of the extinction peaks of these films.

In general, increasing the anneal temperature leads to a decrease in mean particle diameter and an increase in aspect ratio. There is also a corresponding decrease of the respective standard deviations. Spectral extinction is decreased and the extinction peak is blue-shifted for an increase in anneal temperature. Isolated particles were found for all layer thicknesses and temperatures investigated, demonstrating that low temperature anneals are suitable for MIF fabrication.

6.7 Deposition speed

Previous studies have shown that deposition speed can play a role in the particle geometry of MIFs, but its role is not yet well understood. Three deposition speeds were investigated in this experiment: 0.2 nms^{-1}, 0.02 nms^{-1} and 0.002 nms^{-1}. Due to the limited sensitivity of the quartz balance the slowest deposition speed was difficult to attain exactly, and values ranging from 0.0003 to 0.0009 nms^{-1} were achieved. SEM images of the fabricated samples are given in Fig. 6.14, and the corresponding 3D histogram plots of aspect ratio and diameter are given in Fig. 6.15. The low aspect ratio particles present in the histogram for the 5 nm slow deposition sample (Fig. 6.15a) are assumed to arise from errors in sample analysis due to the small particle size, as they are not present in the SEM images.

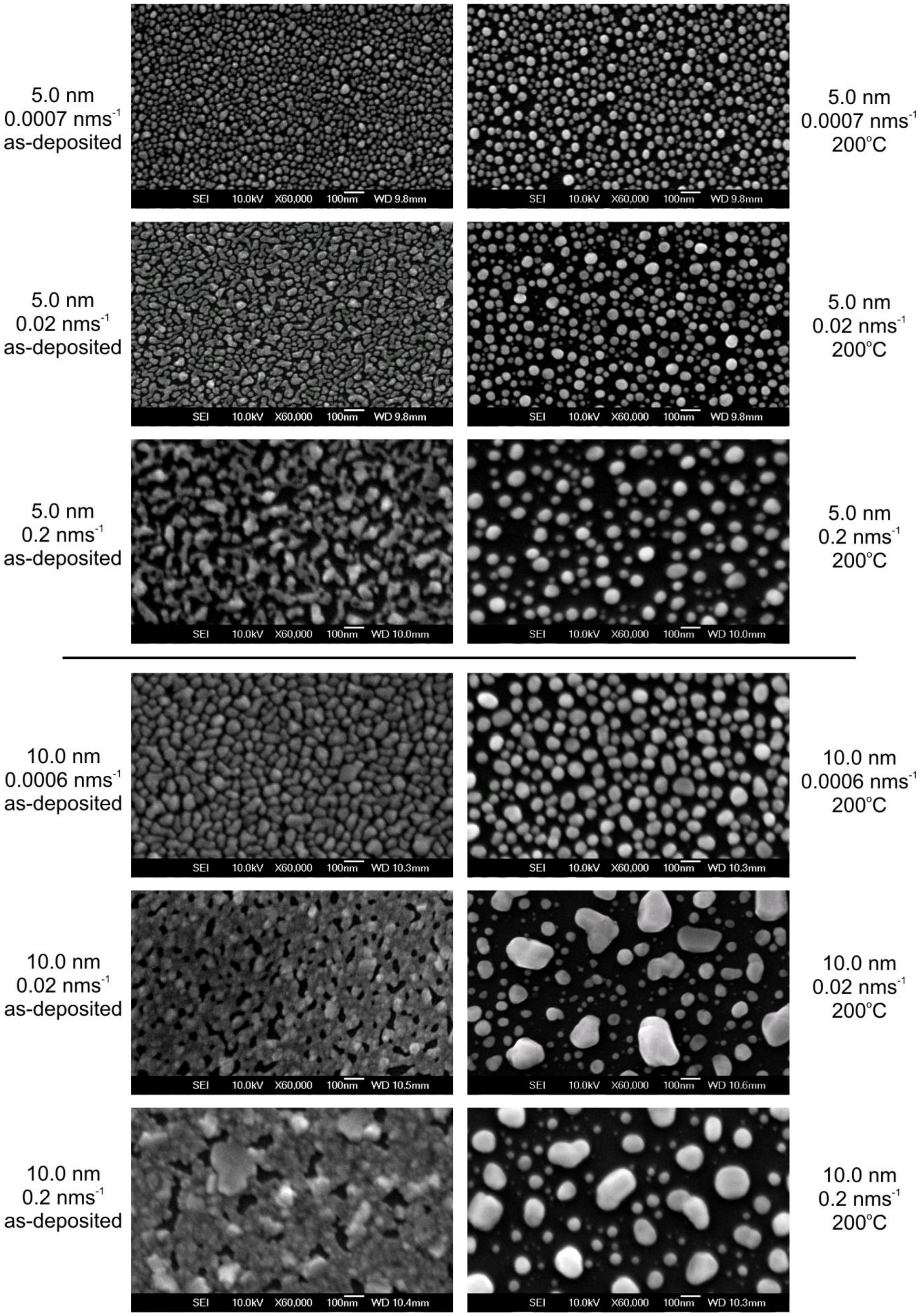

Figure 6.14: SEM images of (left) as-deposited and (right) annealed Ag island films, for films thicknesses of (top) 5 nm and (bottom) 10 nm, with deposition speeds ranging from 0.0006 nms^{-1} to 0.2 nms^{-1}.

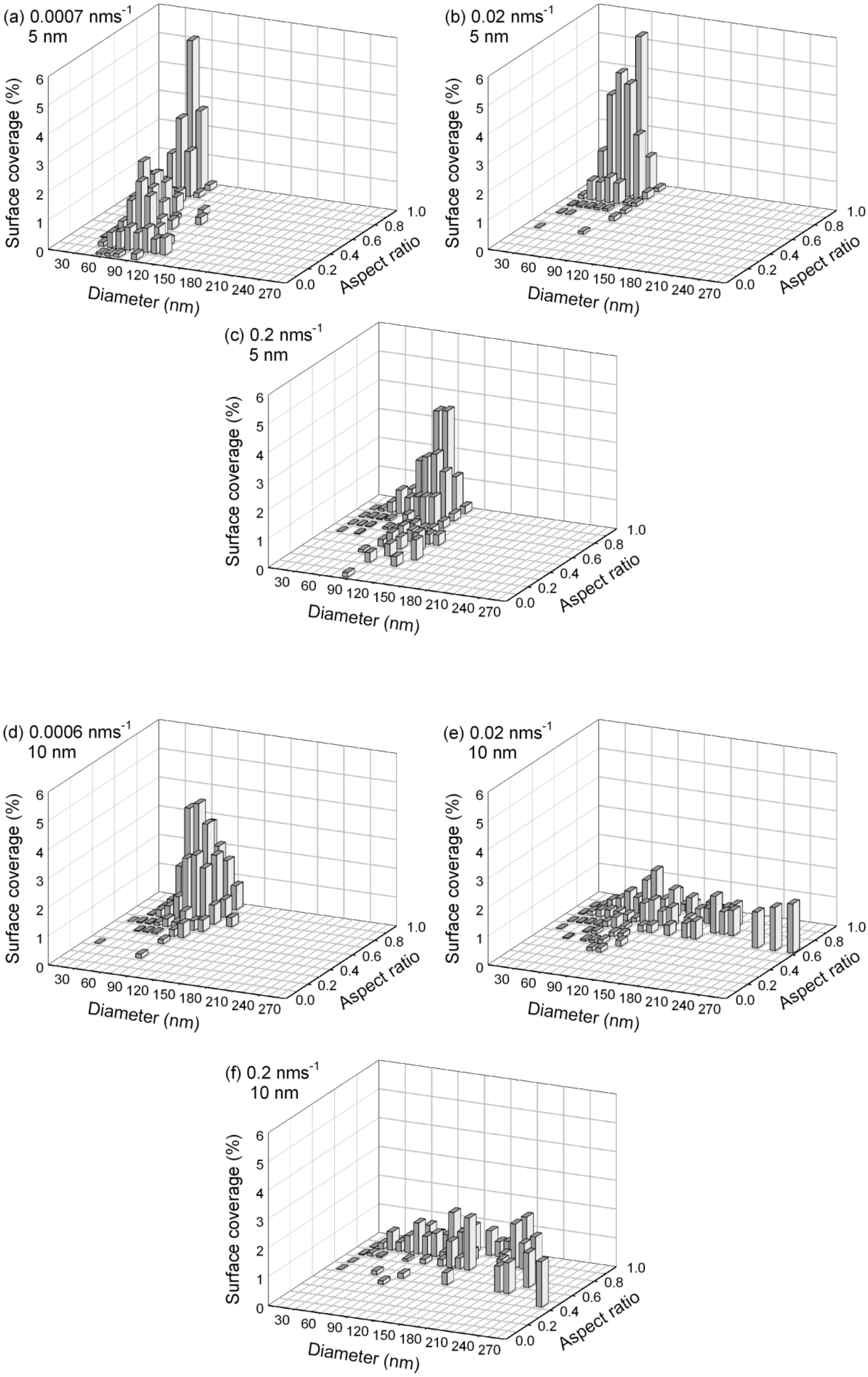

Figure 6.15: 3D histograms of 5 nm films deposited at rates of (a) 0.0007 nms^{-1}, (b) 0.02 nms^{-1}, (c) 0.2 nms^{-1} and 10 nm films deposited at rates of (d) 0.0006 nms^{-1}, (e) 0.02 nms^{-1}, (f) 0.2 nms^{-1}. All films were annealed at 200°C for 2 hrs.

Considerable differences in film morphology are seen for different deposition speeds. The as-deposited 5 nm films deposited at slow and medium speeds consist of isolated particles, with the medium sample containing larger and more irregular particles. In contrast the 5 nm film deposited at the fastest speed is semi-continuous. For the 10 nm films, the slow-deposited layer consists of isolated particles, while the other speeds produce porous films. Therefore, the percolation threshold is reached at smaller mass-thicknesses for faster deposition speeds. For annealed films the trends observed for increasing deposition speed are analogous to those for increasing the layer mass thickness: average particle size increases and average aspect ratio decreases. In particular we note the markedly different morphological properties of the annealed slow-deposited 10 nm film to the other two deposition speeds.

Deposition speed is expected to affect atomic migration time, with faster deposition speeds inhibiting surface diffusion of atoms. A slow deposition speed maximises atomic migration time, thereby promoting clustering and reshaping. Therefore faster deposition speeds result in a more continuous layer, and reach the percolation threshold for thinner layers than slow depositions. Annealing a semi-continuous film results in more irregularly-shaped nanoparticles than annealing a discontinuous film, as is the case for increasing mass layer thickness.

However, the role of substrate temperature during deposition must also be considered. For a 10 nm film, deposition speeds of 0.0007 nms^{-1}, 0.02 nms^{-1} and 0.2 nms^{-1} correspond to total deposition times of approximately 1 minute, 10 minutes, and 4 hours respectively. The crucible was heated throughout the deposition process, and so radiative heating of the substrate could have occurred. This would be more prominent for longer deposition runs, *i.e.* particularly for the slowest deposition speed. The sample temperature was not controlled or monitored during the deposition process, but the chamber was noticeably warmer after the slow deposition speed runs. Therefore we ascribe the differences in morphology to a combination of deposition speed and substrate heating, and cannot separate the effects of the two without further experiments.

Deposition speed also affects the optical properties of the film, as would be expected by the differences in corresponding particle geometry. Well-defined peaks are seen for as-deposited 5 nm and 10 nm films deposited the slowest rate (Figs. 6.16a,c). Increasing deposition speed results in a decrease of the resonant behaviour, and a move to the optical properties of a continuous film. The annealed 5 nm films feature very similar optical properties (Fig. 6.16b). All three samples have well-defined peaks, which are slightly red-shifted with increasing deposition speed due to a slight increase in particle diameter. For the annealed 10 nm films, the slowest deposition speed results in a very different spectrum to the other two speeds. The slow-deposited film features a well-defined, narrow peak, where as the other films exhibit broad, asymmetric peaks. This corresponds with the markedly different morphological features of the slow deposited 10 nm layer (Fig. 6.15).

Although a large difference in peak position is observed for the medium-deposited and fast-deposited 10 nm films, the overall spectra are very similar.

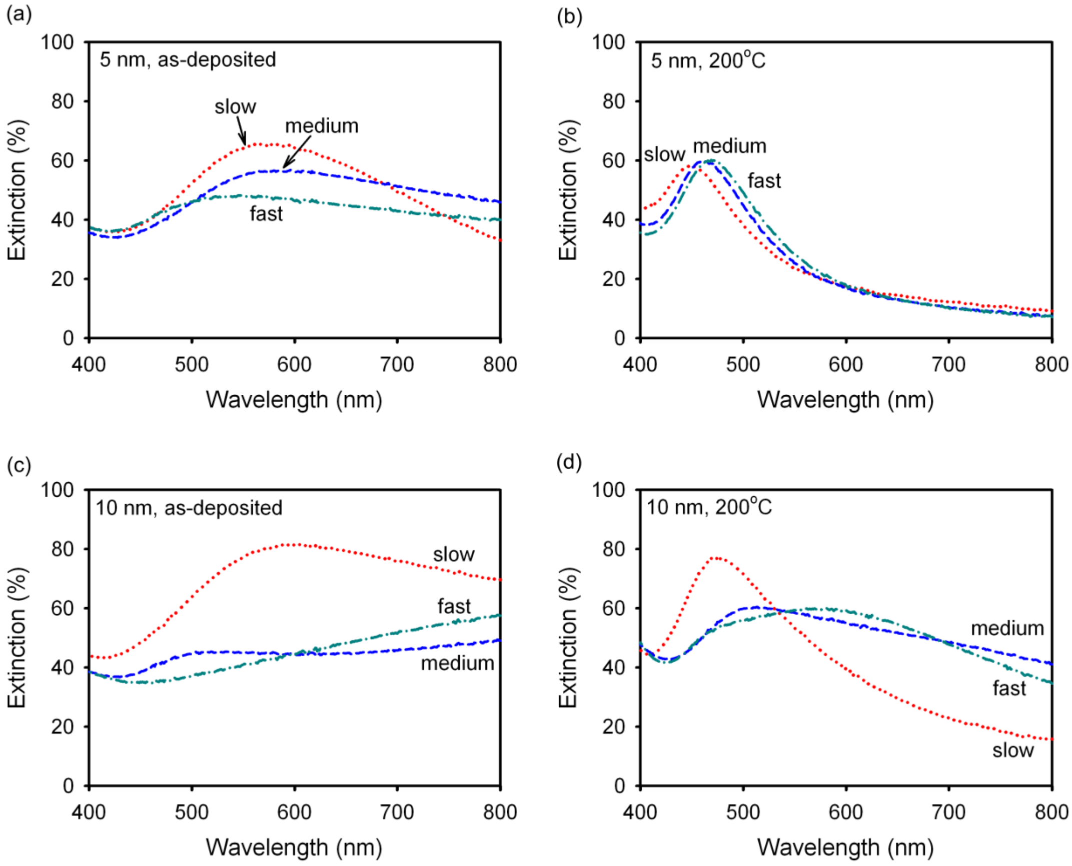

Figure 6.16: Extinction spectra of (a) 5 nm as-deposited films, (b) 5 nm films annealed at 200°C for 2hrs, (c) 10 nm as-deposited films, (d) 10 nm films annealed at 200°C for 2hrs.

Deposition speed has the strongest effect on the as-deposited films, where each of the three speeds result in films with distinct optical properties. However, after annealing the optical properties of the 5nm and 10 nm films deposited at medium and fast speed are very similar. Therefore we conclude that the optical properties of annealed films are not strongly sensitive to the deposition speed provided it is of the order of 0.2 nm^{-1} or higher. Significantly slower deposition speeds will result in narrower, blue-shifted peaks. This agrees well with previously reported results.

6.8 Substrate and overcoating

The samples investigated in the previous sections were all deposited on a 36 nm layer of ITO. The influence of this layer on the optical and morphological properties of a film is an important consideration. An ITO overcoating can also act as an additional method to tune the optical response by further changing the local dielectric environment of the nanoparticles. The interaction of metal nanoparticles with their local environment can be thought of in terms of a 'sensing volume', *i.e.* a volume around the particle that is sensitive to change in refractive index. In the examples studied here the sensing volume contains regions of air, glass and ITO. The sensitivity of a nanoparticle is expected to decrease exponentially with distance, and so the material closest to a nanoparticle has the largest impact on its optical properties. The refractive index of air, glass and ITO are roughly 1, 1.5 and 2.0 respectively. Therefore ITO will lead to a larger red-shift in peak position than glass. In this section we will investigate the influence of ITO layers above and below a 5 nm Ag island film, annealed at 200^{o}C.

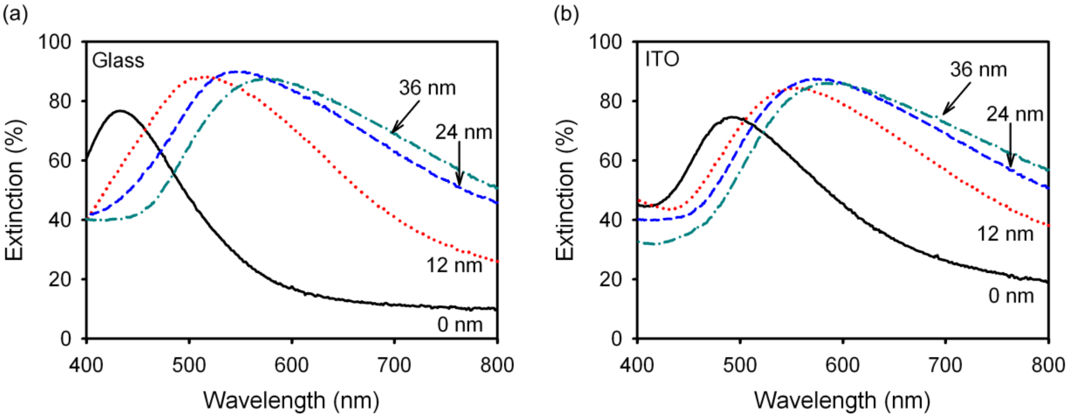

Figure 6.17: Extinction spectra of 5 nm films on (a) bare glass and (b) 36 nm ITO coated glass, with ITO overcoating of 0 nm, 12 nm, 24 nm and 26 nm. All films were annealed for 2hr at 200^{o}C prior to overcoating.

A 5 nm Ag film deposited onto a 36 nm ITO layer results in a 59 nm red-shift in the peak position in comparison with a film on bare glass (Fig. 6.17). This shift is due to an increase in the average refractive index of the medium surrounding the particles. Overcoating annealed island films also results in a strong red-shifting of the extinction peak. No significant change in particle morphology was found after deposition of the overcoating layer, and so the effect is thought to be solely due to the increase of the average refractive index of the surrounding medium. The effect of further increasing the thickness of the ITO layer gradually decreases at higher thicknesses (Fig. 6.18). Identification of the peak position is complicated by the broad peak widths, but inspection of the extinction spectra confirms that the largest change occurs for the first 12 nm overcoating, and then the effect of depositing thicker layers gradually decreases. This fits with the notion that the sensitivity of a nanoparticle to its surrounding drops off exponentially. A change in the extinction peak is still seen when increasing the ITO thickness from 24 to 36 nm, giving an indication of the sensing volume size for these particles. This must be considered when embedding nanoparticles into multilayer systems, such as in silicon solar cells.

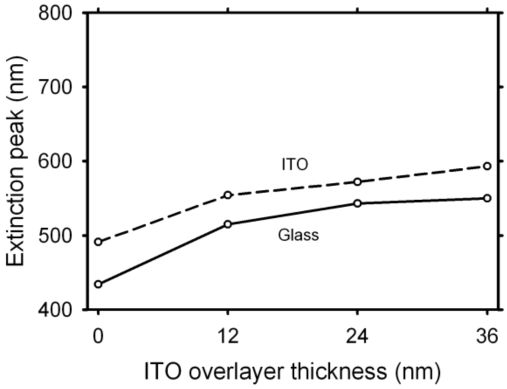

Figure 6.18 Extinction peak position for ITO overlayers on 5 nm Ag films, deposited onto bare glass or glass coated with 36 nm ITO.

An ITO layer deposited over the island film affects the peak position more strongly than a layer deposited before the island film. A 36 nm ITO *under*-layer results in a 59 nm red-shift, while a 36 nm ITO *over*-layer results in a 114 nm red-shift. An ITO over-layer expected to be conformal to the particle surface, and will therefore have a higher surface contact area than an under-layer. Additionally, the top surface of a nanoparticle deposited on an ITO under-layer is exposed to air, where as an overcoated particle is entirely in contact with either ITO or glass. Therefore the average refractive index within the sensing volume of a given particle is larger for overcoated films (Fig. 6.19). The largest shift in extinction peak comes from a combination of undercoating and overcoating.

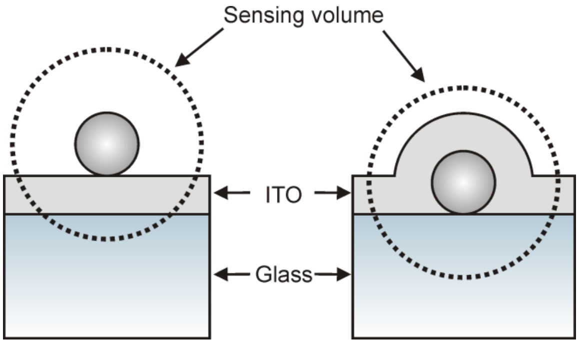

Figure 6.19: Representation of different dielectric environment for ITO under-layers and over-layers.

6.9 Conclusions

For all but the thinnest films investigated formation of isolated nanoparticles required an annealing stage. Isolated particles were observed for all annealed samples, *i.e.* for annealing temperatures ranging from 150^{o}C to 250^{o}C and film thicknesses ranging from 2.5 nm to 20 nm. These anneal temperatures are compatible with standard a-Si:H fabrication processes, and so this technique can readily be applied to coat solar cells. The fabricated film exhibit a reasonably low (~ 65%) extinction across the measured range, but the actual extinction may be higher than the measured value due to limitations of the characterisation configuration.

The optical properties of the island films were found to correlate strongly with mean diameter and mean aspect ratio, and the standard deviation of the distribution of both of these values. Thicker films give rise to larger nanoparticles with lower aspect ratios, which leads to a red-shifting and broadening of the extinction peak. Additionally, the standard deviation of diameter and aspect ratio also increases with film thickness, which contributes to peak broadening. Increasing the anneal temperature decreases the mean and standard deviation of the aspect ratio, leading to a decrease in peak width. Annealed films deposited at rates above approximately 0.2 nms^{-1} exhibit very similar optical properties. A substantial reduction of deposition rate results in the formation of smaller, more regularly-shaped particles. Additionally, the thickness at which percolation is reached is reduced for very slow deposition rates.

We have demonstrated that NIR extinction peaks can be obtained by control of numerous deposition parameters. The peak position red-shifts with increasing film thickness, but blue-shifts with increasing anneal temperature. These shifts are due to changes in particle diameter and aspect ratio. The presence of ITO also red-shifts the extinction peak position, with a stronger effect for overlying films than for underlying. The distance sensitivity of MIFs to their surroundings appears to exceed 30 nm, which must be considered when including MIFs in multilayer structures. The nearly flat extinction spectra of the 15 nm and 20 nm films are of particular interest for solar cell applications.

All of the fabricated films were found to exhibit a strong absorption component of extinction (*i.e.* a poor radiative efficiency). Absorption decreases with increasing particle size (Fig. 4.10b), and so we would expect to see a decrease in absorption for thicker films. However, the thickest films also feature a large absorption peak at short wavelengths, and a relatively flat band of absorption at longer wavelengths. The most likely cause for the strong absorption at short wavelengths is the excitation of higher-order modes, but the cause of the absorption at longer wavelengths is not clear. Single particle simulations suggest that the absorption at longer wavelengths should be close to zero for the largest films studied (Fig. 4.10b), but these do not account for interactions between nanoparticles. Metal island films feature a complicated structure, with a large number of different nanoparticle geometries situated very close to each other. Therefore absorption may also be increased by multiple scattering events and near-field coupling. Multiple scattering occurs if the nanoparticles scatter light laterally or if the scattered photon reflects from the substrate layer and back into the film. Near-field coupling occurs when particles are separated by distances of the order of their diameters, which is the case in most of the films studied. Near-field coupling results in an increase in local electric field intensity, which may also lead to an increase in absorption by the particle. Additionally, complete transfer of energy from one particle to another may occur due to dipole-dipole interaction, which will also result in an increase of absorption. Increasing the average inter-particle spacing will lead to a decrease in absorption due to near-field coupling. This can be achieved by an isotropic etch, but will also result in a reduction of surface coverage and therefore a reduction in optical interaction.

Questions remain over the accuracy of the optical measurements used, in particular the magnitudes of extinction and absorption. Improved optical characterisation will most likely lead to larger values of extinction (due to a reduction of the amount of detected scattered light) and perhaps smaller values for absorption. We note that an improved experimental setup would not change the spectral information obtained in these experiments, only the intensity of the signal, and so the observation of extinction peaks in the NIR is accurate.

For solar cell applications the optimum film thickness is between 15 – 20 nm, with an anneal temperature of between 150^{o}C and 200^{o}C. These parameters will result in an extremely broad extinction peak, but also moderately high absorption at shorter wavelengths. Further work is required to find methods to reduce this absorption. Use of a moderately high deposition speed provides a high-throughput process and improved consistency between samples.

Chapter 7

Influence of silver island films on the spectral response of amorphous silicon solar cells

To date there have been few published studies on the effect of metal nanoparticles on the efficiency of silicon solar cells. Currently the mechanisms of photocurrent enhancement and suppression are poorly understood, and only a small amount of the parameter space (device type, metal nanoparticle size and shape, position of particles within the solar cell) has been investigated. In particular there are no studies on the effect of depositing nanoparticles on the front surface of a-Si:H solar cells. Additionally, there are no conclusive studies on the effect of varying the nanoparticle size and the separation of the nanoparticle from the silicon layer.

The interaction of metal nanoparticles with silicon solar cells is complicated by many factors. The optical properties are highly sensitive to changes in the local dielectric environment, and are therefore closely related to the structure of the solar cell. Additionally, a-Si:H cells are comprised of extremely thin layers of conductors and semiconductors, which support Fabry-Pérot cavity resonances that additionally complicate analysis. However, the principle effect of the metal nanoparticles will be to scatter or absorb light. In this respect it is instructive to compare spectral plots of external quantum efficiency and hemispherical reflectance for coated and uncoated devices. This enables separation of contributions of forward-scattering, backward-scattering and intra-particle absorption. Forward scattering is identified by an increase in QE and a decrease in reflectance. Conversely, both back-scattering and intra-particle absorption lead to a decrease in QE, and can be separated by comparison of reflectance.

In this chapter we discuss the effect of depositing dense arrays of Ag nanoparticles onto the front surface of large area (1 cm^2) a-Si:H solar cells. Three thicknesses of MIF are used, which result in arrays with three different average diameters of nanoparticle. The front ITO layer serves as a front-contact and an anti-reflection coating, but in this experiment also serves to mediate the interaction of the nanoparticles with the a-Si:H layers. We explore four ITO thicknesses, including a layer that acts as an optimized AR layer. The fabricated devices were made without standard light-trapping texturing and identical sets of solar cells without nanoparticles were fabricated on the same substrate to provide reference values.

7.1 Fabrication process

Nanoparticle coated NIP a-Si:H solar cells were fabricated and characterised during a two month JSPS-funded placement at the institute of Advanced Industrial Science and Technology (AIST), Tsukuba, Japan. The devices were fabricated using a standard AIST process. Deposition of the a-Si:H layers was performed by an AIST technician, Ms. Yoko Takeyama. A schematic of the layer structure of the fabricated devices is given in Figure 7.1.

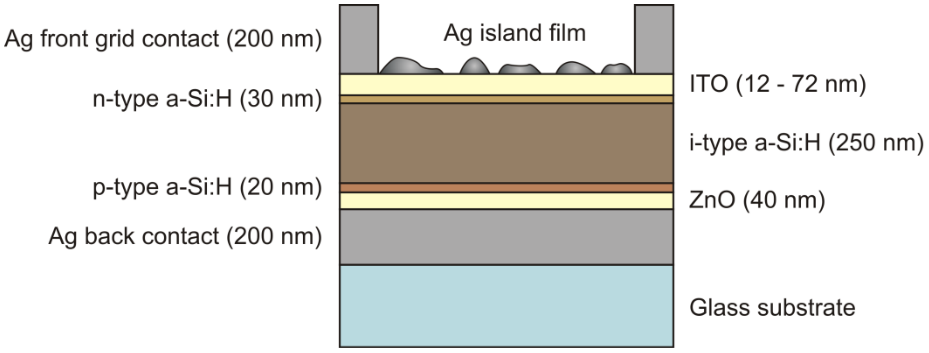

Figure 7.1: Side-on schematic of cell layer structure.

All devices were prepared on 50 x 50 mm^2 Corning glass substrates. Cells were defined as nine 1 cm^2 areas on each substrate. The substrates were cleaned by sonication in DI water, then in Senico solution, and again in water, and finally dried in flowing nitrogen. A 40 nm ZnO layer was deposited onto the substrates by DC sputtering to improve adhesion of the Ag back contact to the substrate. This first ZnO layer does not contribute to the electrical or optical properties of the device and so is not shown in the schematic. The following Ag layer serves as a rear-side contact and was deposited by DC sputtering an Ag target at a power of 100 W and an Ar flow rate of 200 sccm for 6 minutes, resulting in a layer approximately 200 nm thick. The next ZnO layer is used to reduce optical absorption losses at the metal surface, and was deposited by DC sputtering a ZnO target at a power of 200 W and Ar flow of 200 sccm for 2 minutes, resulting in a layer approximately 40 nm thick. All sputtering was performed in a model SBR-2306 from ULVAC, at a pressure of around 1 x 10^{-5} Torr.

An *n*-*i*-*p* a-Si:H layer structure was deposited by a conventional large-area PECVD process (model CME-400, ULVAC). The large chamber size permitted substrates up to 300 x 400 mm^2, and so six 50 x 50 mm^2 substrates were loaded in each run. Each layer was deposited in a separate chamber, without breaking vacuum. The *p*-layer was deposited in two stages. Stage one was deposited with gases SiH_4/B_2H_6(0.5% in H_2)/CH_4/H_2 at corresponding flow rates of 100/0/1000/100 sccm, at 80 W for 20 seconds. Stage two was deposited with gases SiH_4/B_2H_6(0.5% in H_2)/CH_4/H_2 = 100/100/250/100 sccm, at a power of 50 W for 27 seconds. The *i*-layer was deposited with 210 sccm of SiH_4 at a power of 40 W for 1312 seconds. The *n*-layer was deposited with gases SiH_4/PH_3(0.1% in H_2)/H_2 at corresponding flow rates of 100/200/100 sccm, at 40 W for 224 seconds.

Due to machine malfunction there was a one week delay between a-Si:H deposition and ITO overcoating. Usually ITO is deposited onto a-Si:H within a few hours (or ideally without breaking vacuum) to avoid oxidation of the a-Si:H layer. The effect of this delay is not fully known. Definition of each cell was achieved by DC sputtering of an ITO target through Mask A (Fig. 7.2) at a power of 100 W and Ar/O_2 flow rates of 200/0.75 sccm respectively. Deposition times of 2, 4, 6 and 12 minutes were used to deposit ITO films approximately 12, 24, 36 and 72 nm thick. Due to the poor carrier diffusion length in a-Si:H, each device can be considered as electrically isolated without etching away the a-Si:H material between devices. Therefore the active area of each device is defined by the lateral dimensions of the ITO, *i.e.* 1 cm^2. An Ag grid was used to provide a contact for the measurement probes, and was deposited by DC sputtering with the same parameters as the rear Ag contact, but masked by Mask B (Fig. 7.2). This mask defines front contact grids on seven of the devices, leaving two uncoated for optical measurements. To ensure consistency, all ITO layers and MIFs with the same thickness were deposited at the same time.

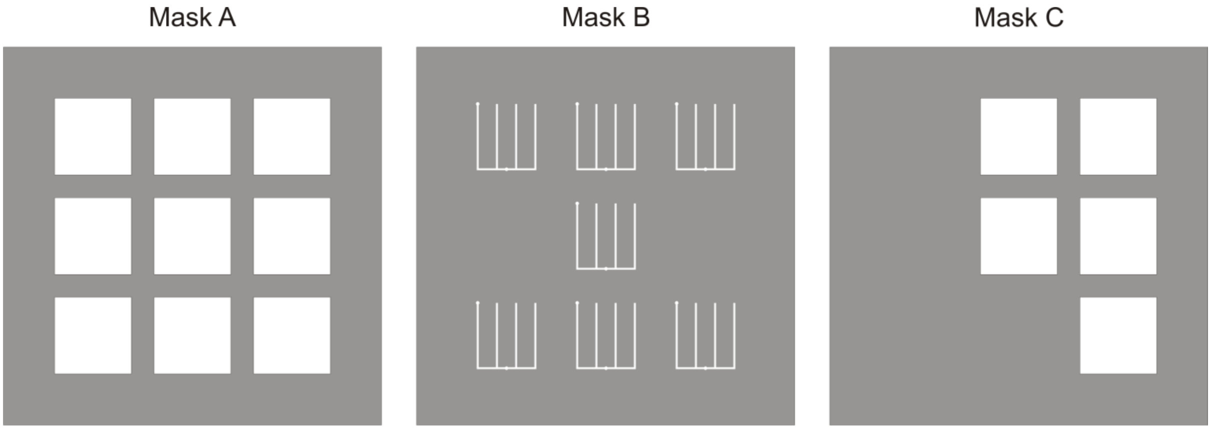

Figure 7.2: Scale drawings of the three masks used in this process:
Mask A, ITO; Mask B, front Ag contact; Mask C, MIF.

Contact was made to the rear of the device by scribing a channel through the a-Si:H with a diamond scribe and then soldering a contact lane (Fig. 7.3). Ag island films were fabricated using the technique describe in Chapter 6, *i.e.* evaporation and annealing. All films were deposited at a constant evaporation rate of 0.007 nms-1 (corresponding to ‘slow’ in the previous chapter) and annealed at 200^{o}C for 2 hr. The standard AIST process makes use of a 2 hr 150^{o}C anneal to reduce contact resistance, and so the annealing step is not expected to adversely affect device efficiency. As the annealed films are not continuous we do not expect any change in contact resistance due to the MIFs. At the end of the process each substrate contained nine 1 cm^2 solar cells. All nine devices have the same layer thicknesses, and five devices per substrate are coated with the same MIF. As the nanoparticle-coated and uncoated devices have experienced exactly the same processing steps their optical and electrical properties can be compared directly.

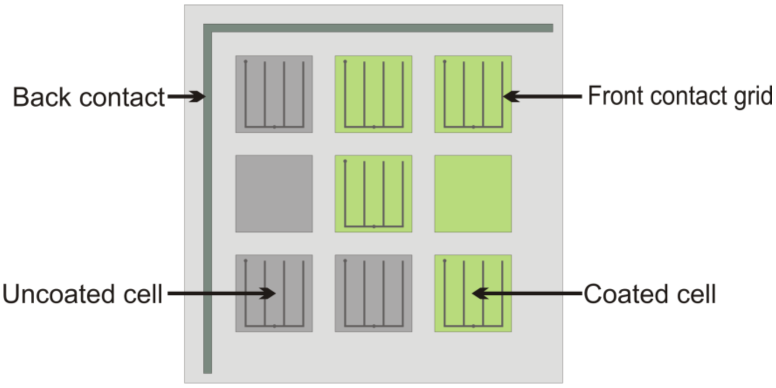

Figure 7.3: Top-down schematic of cell layout.

The complete list of samples fabricated during this experiment is given in Table 7.1. a-Si:H depositions were grouped into two runs with six substrates loaded into the chamber during each deposition, denoted as either A or B in the table. Four ITO thicknesses were investigated: 12 nm (D), 24 nm (C), 36 nm (E) and 72 nm (B). Three MIF layer thicknesses were deposited: 5.0 nm (3), 7.5 nm (6), 10.0 nm (5).

Sample label	**a-Si:H run**	**ITO thickness**	**Ag MIF thickness**
B3	A	72 nm	5.0 nm
B6	A	72 nm	7.5 nm
B5	A	72 nm	10.0 nm
E3	B	36 nm	5.0 nm
E6	B	36 nm	7.5 nm
E5	B	36 nm	10.0 nm
C3	A	24 nm	5.0 nm
C6	A	24 nm	7.5 nm
C5	A	24 nm	10.0 nm
D3	B	12 nm	5.0 nm
D6	B	12 nm	7.5 nm
D5	B	12 nm	10.0 nm

Table 7.1: List of fabricated solar cells.

7.2 Characterisation

Fabricated samples were optically characterized by a spectrophotometer (Perkin-Elmer Lambda 950) with an integrating sphere attachment. The diffuse reflectance spectra of the two devices per substrate without grid contacts were measured. The sample was orientated at an angle of 3^o to ensure that the specular component of reflectance was included in the measurement.

IV measurements were made using a solar simulator fitted with an AM1.5 filter and an intensity of 100 mW/cm^2. Contact was made to the device by four-point probe, so that contact resistance can be neglected. In this way the effect of changing the ITO thickness can be treated as purely optical. External quantum efficiency (QE) measurements were made using the spectrally filtered output of a tungsten halogen lamp. Measurements were recorded from 400 nm to 800 nm in steps of 10 nm. No optical or electrical bias was used.

7.3 Simulation of the optical properties of thin-film stack

Even without metal nanoparticles the optical properties of planar (*i.e.* untextured) a-Si:H solar cells is complex. The device structure is formed by planar layers of a few hundred nanometres or less, which show strong interference fringes due to Fabry-Pérot cavity resonances. To model the influence of each layer in the structure we used a transfer matrix approach for multilayer thin-films, implemented as a MATLAB script by Dr. Stuart Boden *[240]*. Using this technique the optical properties of a thin-film stack can be simulated by providing the layer thicknesses, layer order, and the respective dielectric constants of each layer. Dielectric constants of a-Si:H were obtained by ellipsometric measurements conducted by Dr. Fujiwara of AIST, while dielectric constants for the other materials were obtained from Palik *[29, 30]*. For simplicity we consider the case of an ITO layer between the rear contact and the a-Si:H layer, where as in the experiment ZnO was used. The results are given in Figure 7.4.

The reflectance of a planar a-Si:H layer on an Ag substrate exhibits strong interference fringes at wavelengths greater than approximately 500 nm (Fig. 7.4a). Shorter wavelengths are either reflected at the top surface or absorbed within a double pass of the a-Si:H layer. The position of the fringes is a strong function of the a-Si:H layer thickness, with three distinct minima that red-shift with increasing layer thickness. A rear ITO layer (*i.e.* between the Ag substrate and the a-Si:H) is seen to red-shift all of the minima, with a stronger shift for thicker layers (Fig. 7.4b). Adding an ITO layer to the top surface reduces overall the reflectance, with an increasing effect for thicker ITO layers (Fig. 7.4c). The 72 nm film exhibits near zero reflectance around 530 nm. This layer thickness is often used as an optimized anti-reflection coating. The top ITO layer does not strongly affect the interference fringes, and has the most effect at shorter wavelengths.

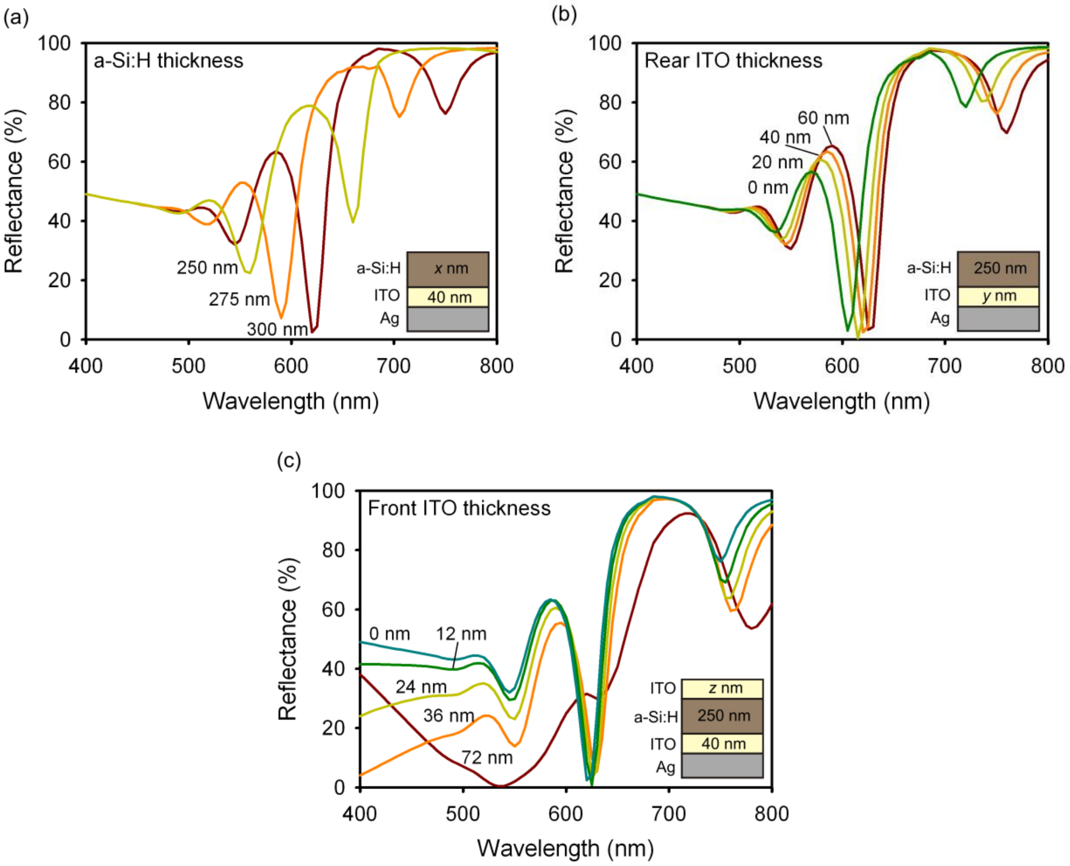

Figure 7.4: Simulated reflectance of a typical a-Si:H layer stack. All simulations contain an Ag substrate on top of which are planar layers of (a) 40 nm ITO, *x* nm a-Si:H thickness, (b) *y* nm ITO thickness, 250 nm a-Si:H, (c) 40 nm ITO, 250 nm a-Si:H, *z* nm ITO.

7.4 Electrical and optical properties of uncoated cells

The electrical and optical characteristics of solar cells not coated with nanoparticles are given in Figure 7.5. The presented results are for a single device on each substrate. A large percentage of the fabricated samples did not exhibit diode behaviour, most likely due to shunting faults in the active layer. The fault with the devices was not investigated further due to time constraints, but may be related to contamination issues or to complications arising from the exposure of the a-Si:H layer to air for a long period of time. Fortunately at least one working nanoparticle-coated device was present on each substrate, and so a complete investigation can still be conducted.

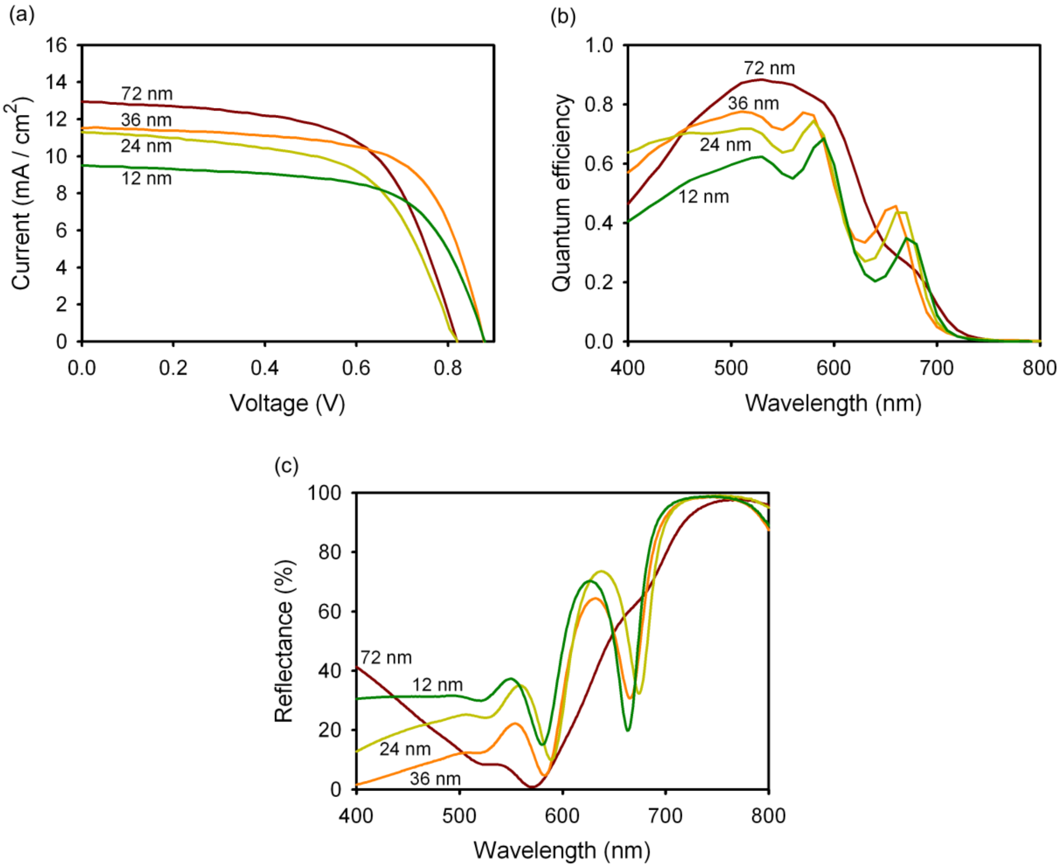

Figure 7.5: (a) IV, (b) external quantum efficiency, and (c) diffuse reflectance of the solar cells without metal nanoparticles. The ITO thickness is denoted in each plot.

From the I-V plot we can see that the two a-Si:H depositions result in markedly different electrical characteristics (Fig. 7.5a). The devices fabricated in run A (72, 24 nm ITO) have an open circuit voltage, V_{oc}, of 0.82 V, while the devices fabricated in run B (36, 12 nm ITO) have a V_{oc} of 0.88 V. The short-circuit current, I_{sc}, decreases with decreasing ITO thickness. V_{oc} is related to the material properties of the a-Si:H layers, and so we believe that the deposition parameters were slightly different between the two runs. The interference fringes of the 24 nm ITO sample are slightly offset from the 12 nm and 36 nm samples, which suggests the layer thicknesses of the type B devices are slightly different from the type A (Fig. 7.5c). I_{sc} is related to the number of photogenerated carriers, *i.e.* to the amount of light that is absorbed in the *i*-layer. The thickest ITO layer acts as a good anti-reflection coating, and so gives rise to the largest I_{sc} (Fig. 7.5b). As the ITO thickness is reduced the reflectance increases, resulting in a corresponding reduction of I_{sc}. The features observed in the QE spectra correlate closely to the interference fringes observed in the reflectance data (Figs. 7.5b,c). The reflectance spectra are in reasonable qualitative agreement with the simulations presented in Figure 7.4c. Further improvements could be made by using an ellipsometer to accurately measure the thicknesses and optical constants of the fabricated layers. The optical constants of ITO, ZnO and a-Si:H are a strong function of their deposition parameters, and the layer thicknesses used in the model were estimated.

7.5 Metal island films

SEM images of Ag island films fabricated on solar cells with a 36 nm ITO layer are given in Figure 7.6. No significant differences in average nanoparticle size and shape were found for a given MIF thickness on different ITO thicknesses. The average diameter and irregularity of the fabricated nanoparticles is seen to increase with layer mass thickness. Well-defined, isolated nanoparticles were fabricated in each case.

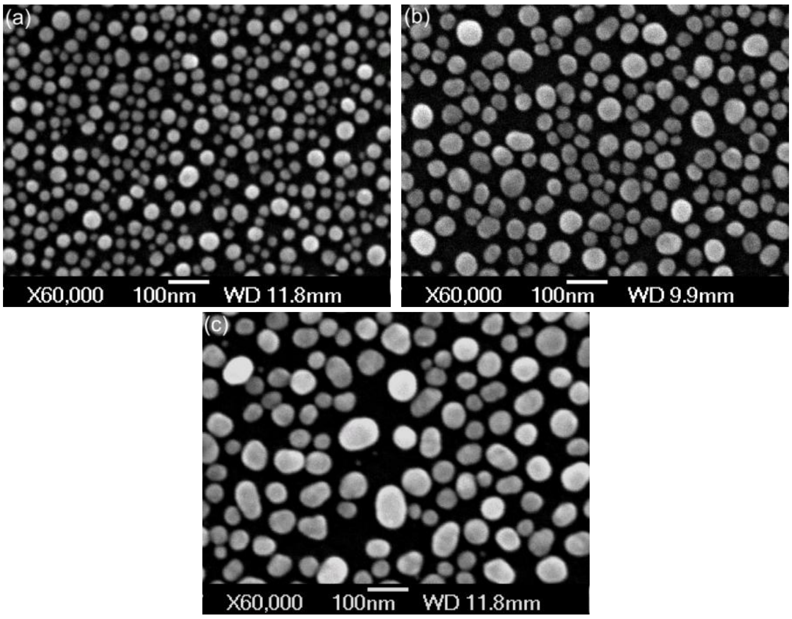

Figure 7.6: SEM images of Ag MIF on a solar cell with a 36 nm ITO layer, (a) 5 nm (b) 7.5 nm, (c) 10 nm.

The MIF deposition conditions were chosen mid-way through the series of experiments presented in Chapter 6, and so are not optimum. In hindsight, it would have been useful to include 15 nm and 20 nm films as well, to achieve larger particles and hence higher extinction in the NIR.

7.6 Effect of Ag nanoparticles on a-Si:H solar cells

Spectral QE and reflectance measurements of the fabricated devices are given in Figure 7.7, and I-V characteristics are given in the Appendix (Section 9.2.1). To improve clarity the spectra are normalized to those of a device with identical parameters but not coated with nanoparticles. As previously discussed, normalization based on ratios can be misleading, and so we have instead normalized the spectra by subtraction. For example a normalized reflectance of -15% means that the nanoparticles resulted in a 15% absolute drop in reflectance (*e.g.* from 40% to 25%). Both sets of spectra feature complex trends, and are difficult to interpret. Further simulation and experimental work is required to fully understand the effect of depositing nanoparticles onto thin-film devices. Here we attempt only a preliminary explanation of the results.

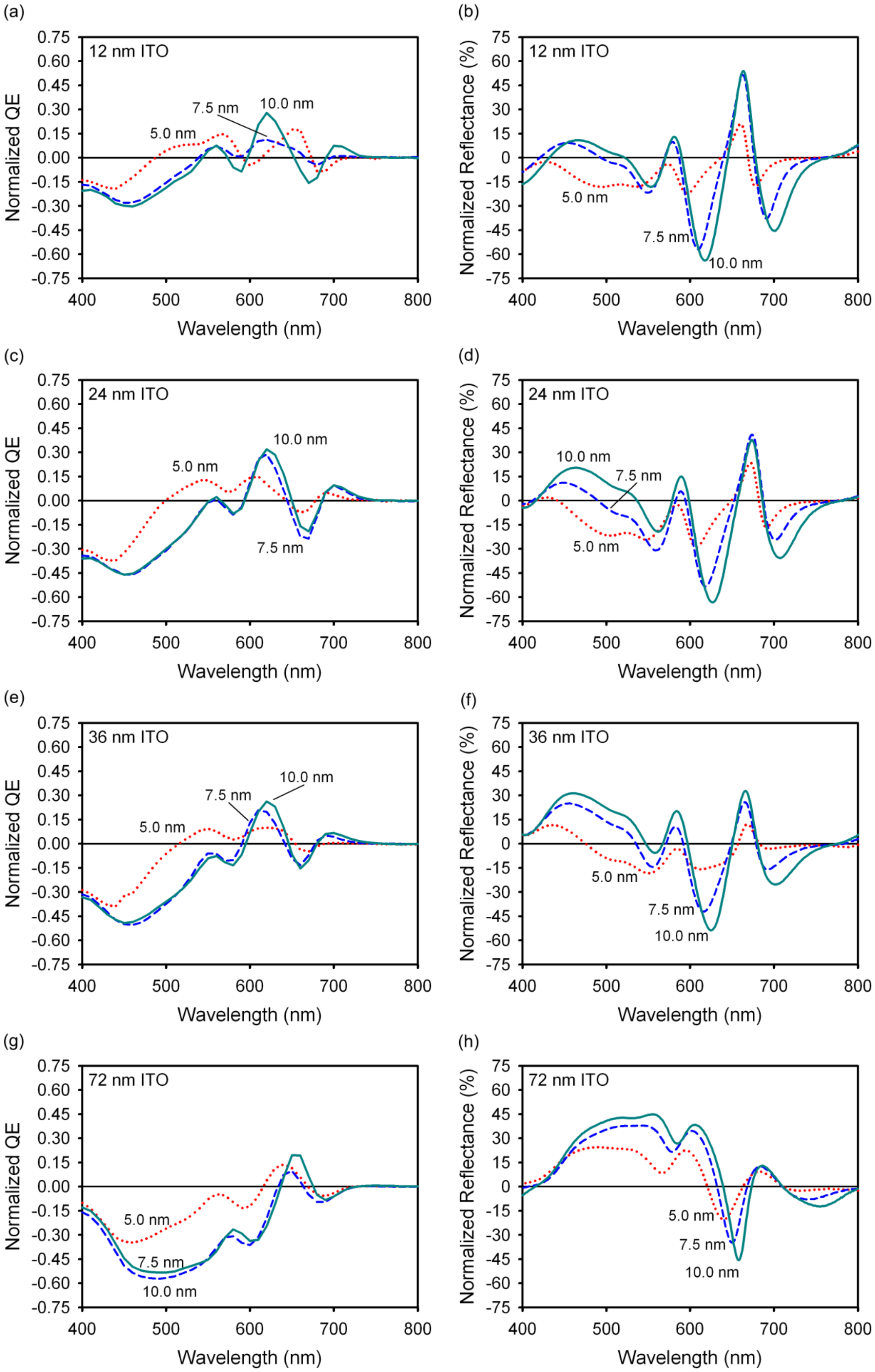

Figure 7.7: (Left) Normalized QE and (right) normalized reflectance of the fabricated solar cells, as a function of top ITO thickness and MIF thickness.

The reflectance of the 12 nm, 24 nm and 36 nm ITO solar cells are similar (Figs 7.7b,d,f). Each contains three maxima and three minima, and the position of these red-shifts with increasing thickness of MIF (*i.e.* increasing nanoparticle size). It is therefore tempting to conclude that the reflectance minima are due to plasmonic effects, as we would expect the scattering peak wavelength to red-shift with increasing particle size. However, the extinction spectra of 5 nm and 10 nm MIFs deposited at the same rate on ITO coated glass feature extinction peaks at 450 nm and 480 nm respectively, with a low optical activity at longer wavelengths. Although the optical properties of the MIFs fabricated onto solar cells will be different due to the substrate structure, we do not anticipate a significantly large change in peak position. Therefore we attribute the short-wavelength (< 500 nm) reflectance peaks to effects arising from absorption and scattering of light by the nanoparticles. The increase in reflectance is due to back-scattering by the nanoparticles, which becomes stronger for larger particles due to increased scattering efficiency and reduced absorption.

The remaining maxima and minima are better explained by analysis of the raw reflectance spectra rather than the normalized data (Fig. 7.8a). The effect of the metal nanoaprticles above ~ 550 nm is to shift the interference fringes, with a stronger shift for thicker layers. No additional maxima or minima are present, and so we do not attribute these shifts to resonant behaviour by the nanoparticles. The magnitude of the shift is related to the thickness of the MIF. Given that we expect the scattering efficiency of the fabricated devices to be low in the NIR, we propose that the presence of the nanoparticles alters the optical properties of the thin-film stack. At long wavelengths we can consider the nanoparticles as a homogenous effective medium, the presence of which changes the Fabry-Pérot cavity conditions, and so shifts the interference fringes. Raw reflectance and QE data for all of the solar cells studied are given in the Appendix (Section 9.2.2).

By comparing reflectance spectra with the QE spectra at wavelengths less than 500 nm we can identify the principle loss mechanisms of the metal nanoparticles. For the 7.5 nm and 10 nm films an increase of reflectance is observed for all ITO thicknesses, with a corresponding decrease in QE. Therefore for these larger particles back-scattering of light is the dominant mechanism. We note the surprisingly similarity of the QE spectra for 7.5 nm and 10 nm MIFs below 500 nm. The reason for this is not clear, as the reflectance of the 10 nm MIF is higher than the 7.5 nm film at longer wavelengths. The reason could be due to increased absorption of the 7.5 nm film, so that its reflectance is lower but the overall effect on QE is similar to the 10 nm film. It should be noted that the QE spectra were sampled at a coarser interval range than the reflectance spectra (10 nm c.f. 1 nm). The 5 nm films results in a decrease of reflectance for the 12 nm and 24 nm film, and a corresponding decrease in QE. An increase in reflectance is observed for the 5 nm Ag film. Therefore we conclude that the 5 nm film reduces QE due to both absorption and back-scattering, and that back-scattering appears as the dominant mechanism when the reflectance of the solar cell is reduced by the presence of a thicker ITO layer. This also provides clear proof that absorption by the nanoparticles is a loss mechanism.

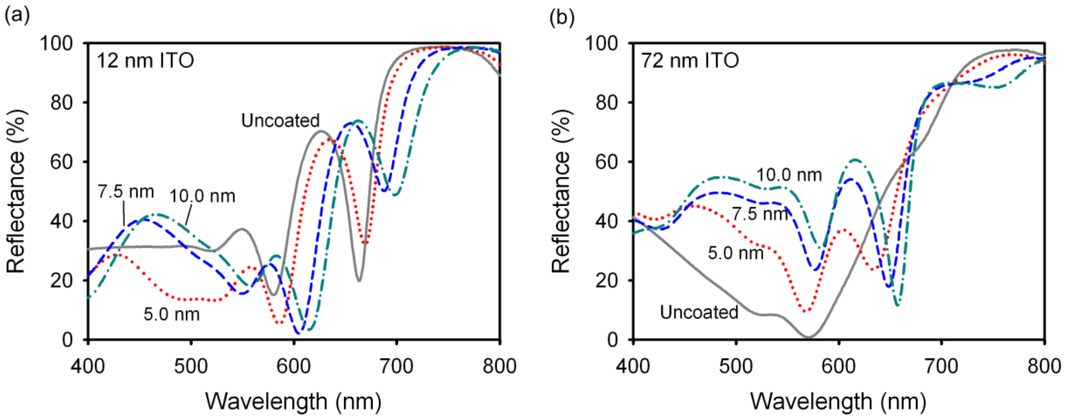

Figure 7.8: Reflectance spectra of solar cells coated with (a) 12 nm ITO and (b) 72 nm ITO, as a function of MIF thickness.

So far we have not discussed the solar cells coated by the 72 nm ITO layer. The reflectance spectra of these devices without the presence of Ag nanoparticles feature only minimal contribution from interference fringes. However, when coated with metal nanoparticles strong interference fringes develop (Fig. 7.8b). This demonstrates that caution should be taken when integrating metal nanoparticles with conventional anti-reflection coatings, as the AR properties of the film may deteriorate.

7.7 Conclusions

The presence of dense Ag nanoaparticle arrays on the front surface of a-Si:H results in a decrease of the device efficiency. The losses are primarily due to absorption in the case of small nanoparticles and back-scattering (*i.e.* increased reflectance) in the case of large particles. Deposition of nanoparticles results in substantial changes in reflectance and QE at longer wavelengths, due to the shifting of interference fringes. We tentatively ascribe these effects to a non-plasmonic, effective medium type mechanism. Importantly, this demonstrates the need for both reflectance and QE measurements when investigating the influence of metal nanoparticles on thin-film silicon solar cells. It is possible that in some geometries the shifting of interference fringes could result in a net improvement of device efficiency, which would be incorrectly ascribed to plasmonic effects if only I-V measurements were studied.

We estimate the extinction peak of the particles sizes investigated to be between 450 nm and 500 nm. The a-Si:H layers investigated are thick enough to absorb all incident photons at these wavelengths, and so the nanoparticles can only increase absorption by reducing reflection. We propose that larger particles will result in a red-shifting of the extinction peak to wavelengths that are poorly absorbed by a-Si:H. In this case the nanoparticles can also improve absorption by increasing light-trapping, and so this beneficial effect may outweigh the negative effect of back-scattering, leading to a net improvement of device efficiency.

Integration of the nanoparticles in the rear ZnO layer of the device will negate losses due to back-scattering, and so this is a more promising area of investigation. Improvement of device efficiency in this geometry will only be limited by absorption by the nanoparticles, although we note that this may be increased by interaction with the rear metal contact.

Chapter 8

Conclusions and future work

8.1 Conclusions

There is a motivation to reduce the thickness of silicon solar cells, both to reduce materials cost and to improve the efficiency of extracting excited carriers. However, reducing the thickness of a silicon cell also reduces the amount of light absorbed, which results in a decrease of the power generated by the device. To alleviate this problem we can use light-trapping techniques to increase the path length of photons within the device, and hence increase absorption. Conventional light-trapping techniques based on surface texturing result in degradation of electrical properties due to the creation of defects in the silicon layer. Additionally, surface texturing does not strongly scatter long wavelength (NIR) photons. Therefore there is a need for new light-trapping techniques that can strongly scatter NIR photons and do not require substantial roughening of the substrate.

Metal nanoparticles with dimensions far smaller than the incident wavelength can be tuned to strongly scatter infrared light, and so are a promising candidate for improving light-trapping in solar cells. The optical properties of metal nanoparticles are strongly dependent on their size, shape and by the local dielectric environment. This is both a help and a hindrance. We can tune the optical properties of metal nanoparticles to suit our purpose, *e.g.* to strongly scatter photons over a given range of wavelengths. However, the optical properties of metal nanoparticles are strongly dependent on the refractive index and the structure of their local environment. This greatly complicates the study of the interaction of metal nanoparticles with silicon solar cells, as the silicon layer changes the optical properties of the nanoparticle in numerous ways.

From the literature review and our own experiments we have identified two key loss mechanisms: back-scattering and absorption by the particle. Back-scattering is less widely studied and not yet well understood, but appears to be related to the 3D shape of the nanoparticle, the distance of the nanoparticle from the silicon surface and the presence of higher-order excitations. It is not possible to minimize back-scattering loses without understanding more about the effect that a proximate silicon layer has on the optical properties of metal nanoparticles. By contrast, absorption is a well understood process, and can be minimized by correct choice of particle size, shape and metal. We have shown that absorption decreases with particle size, until higher-order modes are excited, which initially have high absorption. However, we have demonstrated that the radiative efficiency of higher-order modes also increases with increasing sphere size. Surprisingly, the radiative efficiency of the quadrupolar mode approaches unity (*i.e.* near zero absorption) for Ag spheres larger than 200 nm. Shape also plays an important role in absorption, and we have shown that particles with sharp tips (*e.g.* triangular prisms) have a poorer radiative efficiency than circular nanoparticles of the same volume. Although dramatic red-shifts can be achieved by reducing the thickness of metal shells or the height of prisms, this also results in a marked increase in absorption. Therefore we conclude that triangular (or pyramidal, *etc.*) nanoparticles, core-shell nanoparticles and platelets are not suitable for inorganic solar cell applications.

To date studies of metal nanoparticle interaction with solar cells have focused on nanoparticles made of Ag and Au. By means of simulation studies we have shown that nanoparticles made from Ag, Au, Cu, and Al are all suitable for solar cell applications, provided they are used in the correct way. Optically, Ag is the best choice of the noble metals as it has the shortest interband transition wavelength. Au and Cu are poor choices of metal for nanoparticles situated on the front-surface of the device, as both have a high absorption component at shorter wavelengths due to interband transitions. The optical properties of Ag, Au and Cu are nearly identical for wavelengths above 700 nm. If the optical cross-section of a nanoparticle is low below 700 nm (*e.g.* high aspect ratio spheroids) then the choice between noble metals is arbitrary, and can be tailored to suit other considerations such as thermal stability or cost. Al nanoparticles are rarely studied and to date have not been used for solar cell applications. Part of the reason for this is that extinction peaks of small Al nanoparticles are too far into the UV to be useful for solar cell applications. However, we have shown that large Al nanoparticles can support resonances in the UV, visible and NIR. In general Al nanoparticles exhibit weaker but broader resonances than identical noble metal nanoparticles. Interestingly, Al nanoparticles support resonances at shorter wavelengths than the noble metals, and can exhibit high radiative efficiencies at regions where noble metals are highly absorbing due to interband effects. However, the narrow interband region of Al restricts its use in the NIR due to increased absorption. Al nanoparticles may be a desirable alternative to Ag for a-Si:H applications, as the Al interband region occurs beyond the band edge of a-Si:H.

We have demonstrated good agreement between DDA simulations and experimental measurements of arrays of Al nanoparticles fabricated by EBL. The dielectric environment due to the native oxide layer and the substrate was found to be an important consideration, and was suitably modelled by a homogenous embedding medium with a refractive index of 1.2. The agreement between experiment and simulations for Au was moderate. The Cr layer was found to strongly attenuate and broaden the extinction peak, and decrease radiative efficiency. Non-metallic adhesion layers, such as an organosilane SAMs, are an essential requirement for lithographically-defined Au and Ag nanoparticles on solar cells. The simulated radiative efficiencies of the prism-type nanoparticles investigated were less than 0.9 for all geometries considered. Further work is required to optimize the design of lithographic nanoparticles, but trends suggest that increasing the particle height and lateral size will most likely lead to an increase in radiative efficiency for Au and Ag nanoparticles.

Although very useful for academic research, EBL is clearly unsuitable for commercial solar cell processes and so a lower cost manufacturing method is required. Chemical synthesis is a low cost, large-area fabrication technique with a good control over particle size and shape. However, currently there are no existing recipes for high yield synthesis of large (> 150 nm), monodisperse Ag nanoparticles. Metal film islanding offers considerably poorer control over the particle geometry, but can be used to fabricate very large metal nanoparticles. Additionally, the process is very simple to integrate with existing solar cell fabrication processes. The main restriction of fabricating MIFs is the requirement of an annealing stage to form large nanoparticles. We have demonstrated that anneal temperatures of between 150^{o}C and 200^{o}C can be used to fabricate particles with average diameters ranging from 25 nm to 250 nm. These temperatures are low enough to not damage a-Si:H and ITO layers, and in fact are commonly used to reduce contact resistance in standard thin-film solar cell fabrication processes. We demonstrated that tuning of the extinction peak position into the NIR can be achieved by increasing the nanoparticle size, the aspect ratio, or by overcoating with ITO. To our knowledge no previous study has been conducted to measure the absorption of MIFs, which is of critical importance for the considered application. Measurements conducted using an integrating sphere indicated that the absorption of MIF layers was unacceptably high, even for large nanoparticles. We tentatively ascribe this absorption to the excitation of higher-order modes and near-field coupling between particles, although we note that the characterisation method was not robust. Further investigation, including more rigorous testing of the characterisation method, is required to fully explore this phenomenon. MIFs show good potential for improving light-trapping in the NIR provided that losses due to absorption can be minimized.

We were not successful in our attempts to improve the performance of a-Si:H using metal nanoparticles. Coatings of small nanoparticles were found to decrease QE due to absorption, while larger nanoparticles decreased QE by back-scattering. Large reductions of reflectance and corresponding increases of QE were found at longer wavelengths, but we do not believe that these are due to scattering by the nanoparticles. Analysis of integration of metal nanoparticles with thin-film solar cells is considerably complicated by Fabrey-Perot modes supported by the layer stack, resulting in interference fringes in the QE and reflectance spectra. These fringes are highly sensitive to the structure of the layers and so are modified by the addition of an additional layer, *e.g.* a layer of metal nanoparticles. The extinction peaks were at short wavelengths and so could be spectrally separated from the interference fringes. However, we wish to improve absorption of long-wavelength photons and so require larger nanoparticles with extinction peaks in the NIR. In this case the interference fringes and extinction efficiencies will overlap, making analysis of results difficult.

Given the losses due to absorption and back-scattering it seems unlikely that metal nanoparticle coatings on the front surface of solar cells will compete with the performance of optimized anti-reflection coatings based on dielectric layers. Instead, the optimum position for integration of metal nanoparticles with solar cells is on the back surface of the device. This mitigates loses arising from back-scattering and absorption of short-wavelength photons by higher-order modes, and localises interaction of the nanoparticles to weakly-absorbed photons. Passivation of the metal nanoaprticles can be achieved by embedding them in the rear oxide layer present in c-Si solar cells or the rear ITO layer often used in a-Si:H devices. Although a full optimization study was not conducted, our results indicate that the optimum nanoparticle type for solar cells are large (> 150 nm), prolate Ag particles with a modest aspect ratio. We note that the majority of previous studies have focused on much smaller particles made of Au, and so improvements in the reported enhancement factors should be possible by use of larger, Ag nanoparticles.

8.2 Future work

There is considerable scope to develop optimized arrays of nanoparticles using EBL and DDA. Higher radiative efficiencies and more red-shifted peak positions are expected for larger particles and higher refractive index surroundings. Therefore we propose extending the range of particle sizes investigated up to 300 nm, and also to coat fabricated arrays with dielectric layers, *e.g.* silicon dioxide and silicon nitride. With simulated spectra of Ag and Al particles with sizes ranging from 50 nm to 300 nm, optimized ensembles can be designed using procedures such as the downhill simplex method. In this way the scattering of light can be maximized across a broad range of wavelengths, and absorption minimized. We note that the optimum design will depend on the position of the nanoparticles within the device –for example nanoparticles on the front surface must exhibit low absorption across the solar spectrum, while those on the rear surface need only interact with weakly absorbed photons. Once optimum arrays are designed they can be fabricated by EBL. An important aspect of the assessment of fabricated arrays is the development of a characterisation method to separate the contributions of scattering and absorption. This is readily achieved by means of an integrating sphere, but improved optics and more sensitive detectors are required than were available during this study. For EBL fabrication involving Au and Ag the development of a non-metallic adhesion layer is an essential requirement. Much improved adhesion has been shown for planar Au films deposited onto organosilane SAMs, but to our knowledge this has not yet been combined with EBL patterning.

The simulation studies presented in this thesis have neglected the effect of near-field coupling between particles. To achieve 100% interaction with incident photons we typically require surface coverage of 30-40%. Therefore nanoparticles will be situated close to each other, and so near-field coupling may alter their optical properties. In particular the effect of near-field coupling on radiative efficiency is of critical importance for dense nanoparticle arrays, and may help explain the high absorption observed in MIF samples. Most numerical simulation methods can be used to study the interaction between a small number of particles, while the translational addition method is suitable for larger arrays.

Further work is required to minimize absorption in Ag island films. It is likely that absorption by arrays that predominantly consist of large particles is primarily due to excitation of higher-order modes and near-field coupling between metal nanoparticles. By measuring the angular distribution of scattering it should be possible to identify whether higher-order modes are being excited, as the scattering distribution will be considerably different (*e.g.* high-angle sidelobes for quadrupolar modes). To alleviate effects due to near-field coupling an isotropic etch could be employed. This will reduce the average nanoparticle size and also the interparticle spacing. As an additional benefit small particles will be completely removed. Further improvements of the absorption measurement technique are possible by ensuring the front and rear-port spot illumination conditions are the same, and by also taking centre-mount measurements as a comparison. The accuracy of the method can be checked by measuring samples that absorb but don’t scatter (*e.g.* thin, planar Cr films) and samples that scatter but don’t absorb (*e.g.* arrays of dielectric nanoparticles).

So far the effect of the supporting substrate was treated indirectly in simulations by means of an effective medium. This appears to give satisfactory results for nanoparticles deposited on fused-silica substrates, but does not account for the complicated interaction between silicon substrates and metal nanoparticles. There is considerable scope to explore this phenomenon further, both theoretically and experimentally. The effect of size, shape and distance from the substrate can be investigated by numerical simulation techniques such as FDTD or FEM. Experimentally it would be instructive to measure the reflectance of metal nanoparticles separated from a silicon layer, as a function nanoparticle shape and interlayer thickness.

The 15 nm and 20 nm silver island films exhibited nearly flat extinction spectra across a wide range of wavelengths, including the NIR. Therefore it would be promising to repeat the experiments of Chapter 7 with these thicker films. The larger particles may have reduced back-scattering due to the excitation of higher-order modes, but these modes may in turn cause losses due to absorption. The presence of interference fringes considerably complicates analysis of QE and reflectance data for thin-film devices, as the metal nanoparticles can also cause ‘non plasmonic’ effects by inducing shifts of the fringes. Therefore it would be interesting make use of metal nanoparticles with the same surface coverage and particle height, but different lateral size and shape. This could be achieved by EBL, for example. An alternative is to use an array of vertically-aligned rods, taking care to tailor the shape of the nanoparticles such that the short-axis mode is negligible. In this way the plasmonic contributions to device can be selectively investigated by polariation-resolved QE and reflectance measurements. The effect of the interference fringes will be the same for both polarizations, but for a polarization aligned to the short-axis there will be no contribution from plasmonic effects and so this can be used to normalize the long-axis polarization data.

A much more promising area of investigation is the integration of nanoparticles at the rear of silicon solar cells. It is important to ensure that the nanoparticles are isolated from the active layer to prevent diffusion of metal and/or increased carrier recombination. In the case of thin-film devices a good approach would be to embed metal nanoparticles in the rear TCO layer of a superstrate device. In this way the nanoparticles are deposited after the device layers, and so they do not affect the growth of the silicon layer. The nanoparticles must also be separated from the rear contact, which again we propose can be achieved by means of a thin TCO layer. Nanoparticles situated close to planar metal films can excite propagating surface plasmons, which will most likely act as a loss mechanism. Therefore the effect of changing the separation of the metal nanoparticles from the back contact should be studied, and also the effect of changing the type of back-contact metal. If embedding of nanoparticles in the rear of the device is successful then the technique can also be applied to other forms of thin-film solar cells such as μc-Si:H, μc-SiGe:H, nc-Si:H, CIGS and CdTe. In each case the peak scattering efficiency of the nanoparticles should be tuned (*e.g.* by control of size and shape) to the band-edge region of the semiconductor, where absorption is weakest. Metal nanoparticles are also promising for thin wafer-based solar cells. Usually the back surface of a crystalline silicon solar cell is covered by a SiO_2 layer to improve passivation (contact is made through small vias). Embedding metal nanoparticles in the SiO_2 layer could lead to scattering of NIR photons, leading to an improvement of light-trapping. This is most readily investigated using EBL, as nanoparticles featuring a high scattering efficiency at ~1100 nm are required, which is currently difficult to achieve by other techniques.

Chapter 9

Appendix

9.1 Additional simulation information

9.1.1 Choice of optical constants source

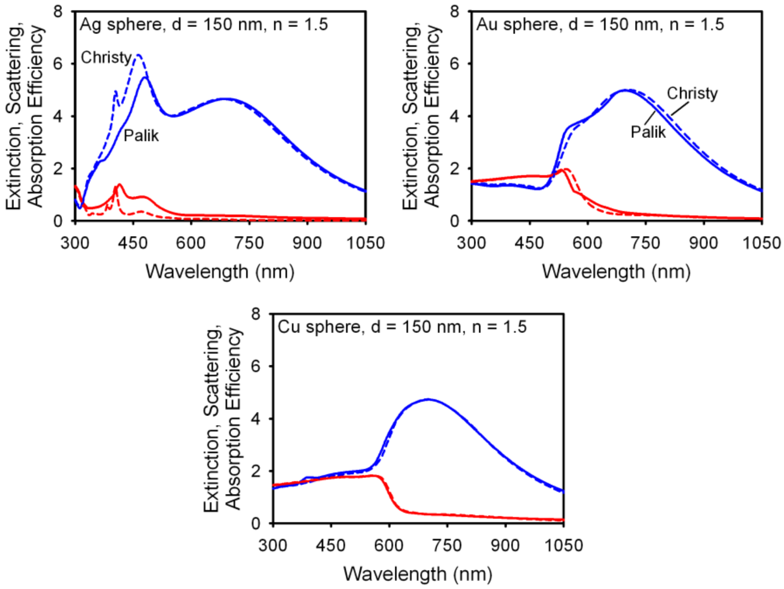

Figure 9.1: Mie theory simulations of scattering (blue) and absorption (red) of 150 nm spheres in N = 1.5 medium for optical constants obtained from Johnson and Christy *[241]* (dotted) and Palik *[29]* (solid).

9.1.2 Optical constants data

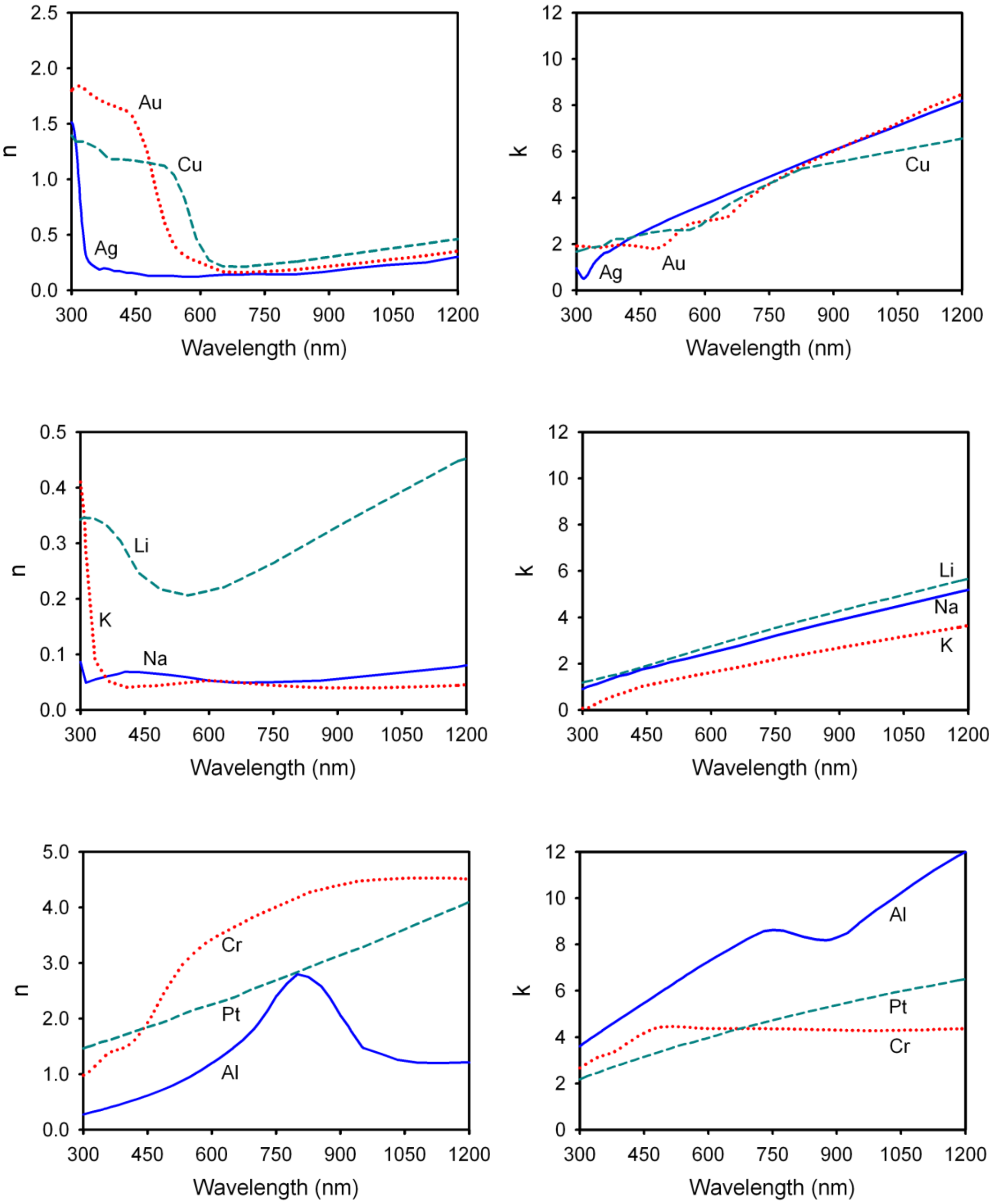

Figure 9.2: n and k plots for Au, Cu, Ag, Li, K, Na, Cr, Pt and Al (from Palik *[29]*).

9.1.3 Discrete dipole approximation

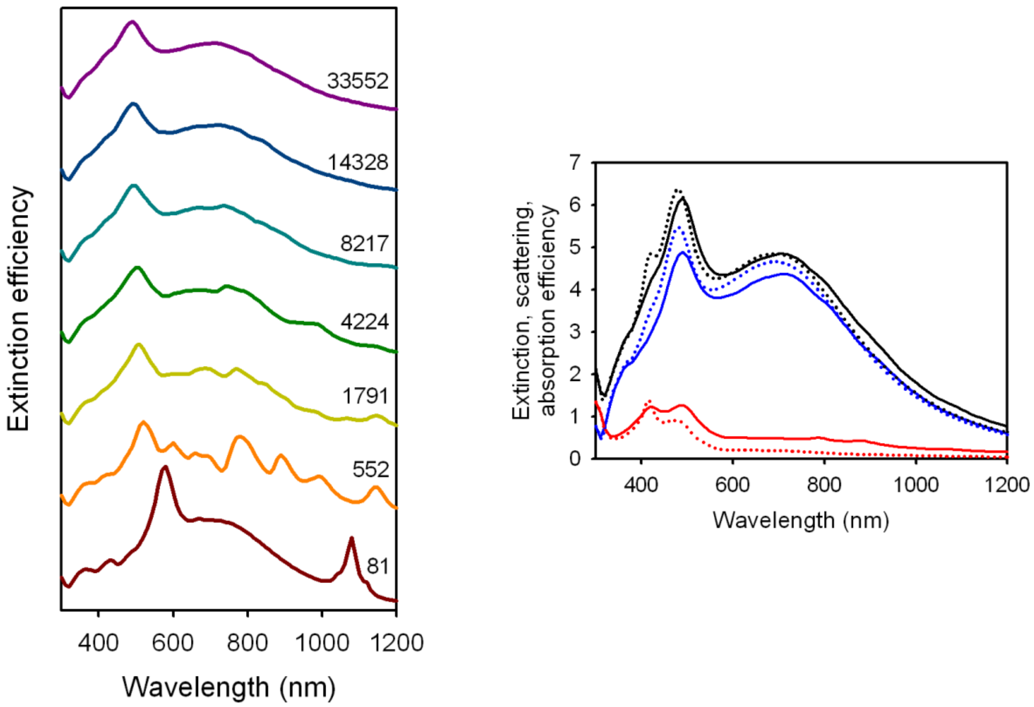

Figure 9.3: (Left) Effect of decreasing the number of dipoles on the simulated extinction spectrum of a 150 nm Ag sphere embedded in a medium with N = 1.5. (Right) The 33552 dipole model (solid lines) compared with Mie theory (dotted lines). Black = extinction, blue = scattering, red = absorption.

9.1.4 Details of DDA models used

Sample	D	d (nm)	A_{eff} (nm)
Triangle, 150 nm side	25472	2.33	42.63
Circle, 115 nm diameter	27088	2.48	46.29
Rectangle, 80 nm by 130 nm	26624	2.50	46.31
Square, 50 nm side	21600	1.66	28.79
Square, 100 nm side	25600	2.50	45.71
Square, 150 nm side	24300	3.33	59.89
Square, 200 nm side	43200	3.33	72.56
Rectangle, 50 nm by 100 nm	25000	2.00	36.28
Rectangle, 50 nm by 150 nm	37500	2.00	41.53
Rectangle, 50 nm by 200 nm	25600	2.50	45.71
Rectangle, 50 nm by 100 nm, 2 nm Cr	210000	1.00	36.87
Rectangle, 50 nm by 100 nm, 3 nm Cr	215000	1.00	37.16
Rectangle, 50 nm by 100 nm, 4 nm Cr	220000	1.00	37.45
Rectangle, 50 nm by 150 nm, 2 nm Cr	315000	1.00	42.21
Rectangle, 50 nm by 150 nm, 3 nm Cr	322500	1.00	42.54
Rectangle, 50 nm by 150 nm, 4 nm Cr	330000	1.00	42.87
Rectangle, 50 nm by 200 nm, 4 nm Cr	55000	2.00	47.18
Rectangle, 46 nm by 96 nm	19872	2.00	33.61
Rectangle, 46 nm by 96 nm, 2 nm Al_2O_3	200000	1.00	36.28
Rectangle, 44 nm by 94 nm	17578	2.00	32.26
Rectangle, 44 nm by 94 nm, 3 nm Al_2O_3	200000	1.00	36.28
Rectangle, 46 nm by 146 nm	30222	2.00	38.65
Rectangle, 46 nm by 146 nm, 2 nm Al_2O_3	300000	1.00	41.53
Rectangle, 44 nm by 144 nm	26928	2.00	37.19
Rectangle, 44 nm by 144 nm, 3 nm Al_2O_3	300000	1.00	41.53

Table 9.1: Details of the simulation models used. D: number of dipoles, d: interdipole spacing, A_{eff}: effective radius.

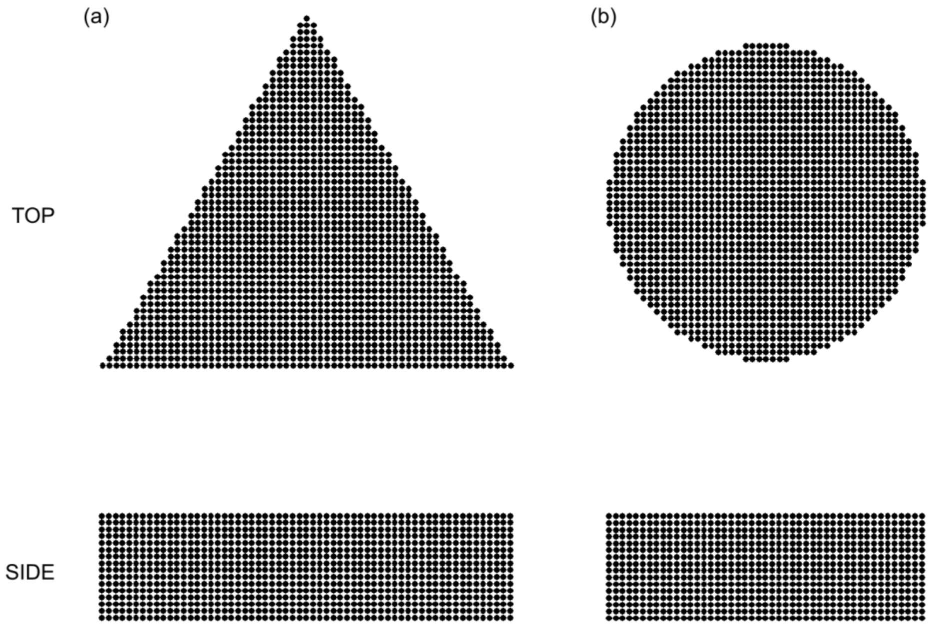

Figure 9.4: Examples of the dipole maps used for a 150 nm side length triangular prism and a 115 nm diameter cylinder.

9.2 Additional solar cell characterisation

9.2.1 I-V characteristics

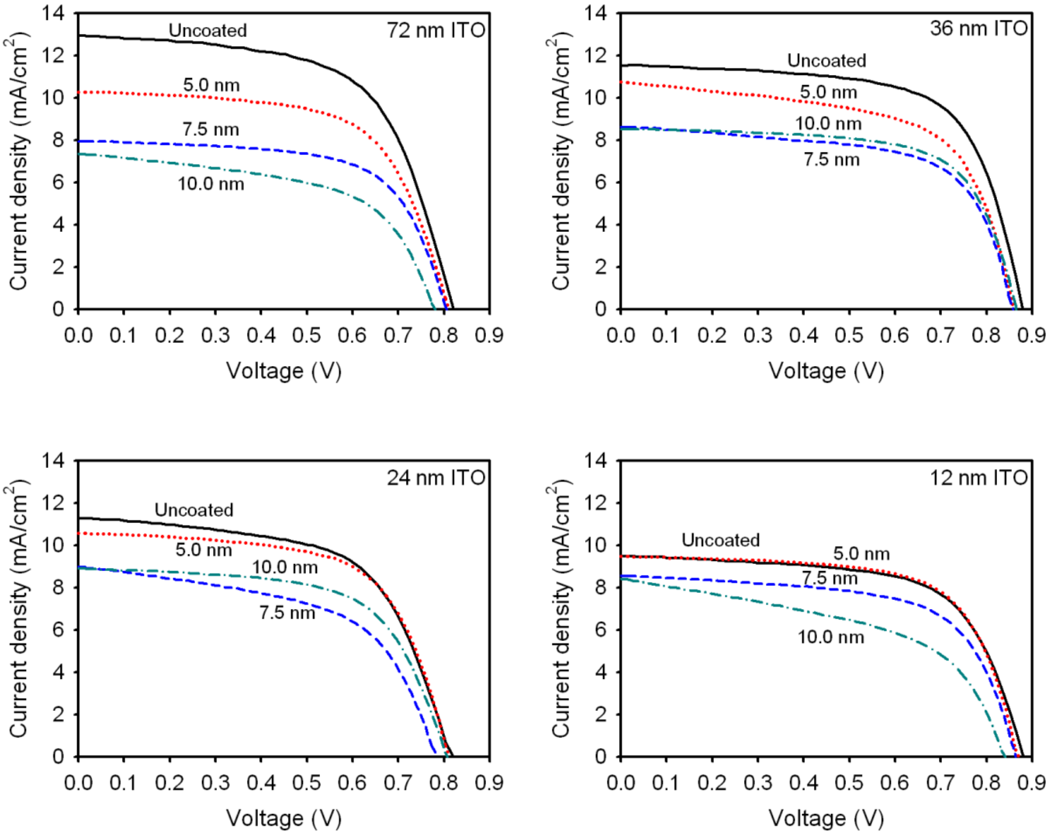

Figure 9.5: I-V characteristics of the fabricated solar cells, as a function of top ITO thickness and MIF thickness.

9.2.2 QE and reflectance

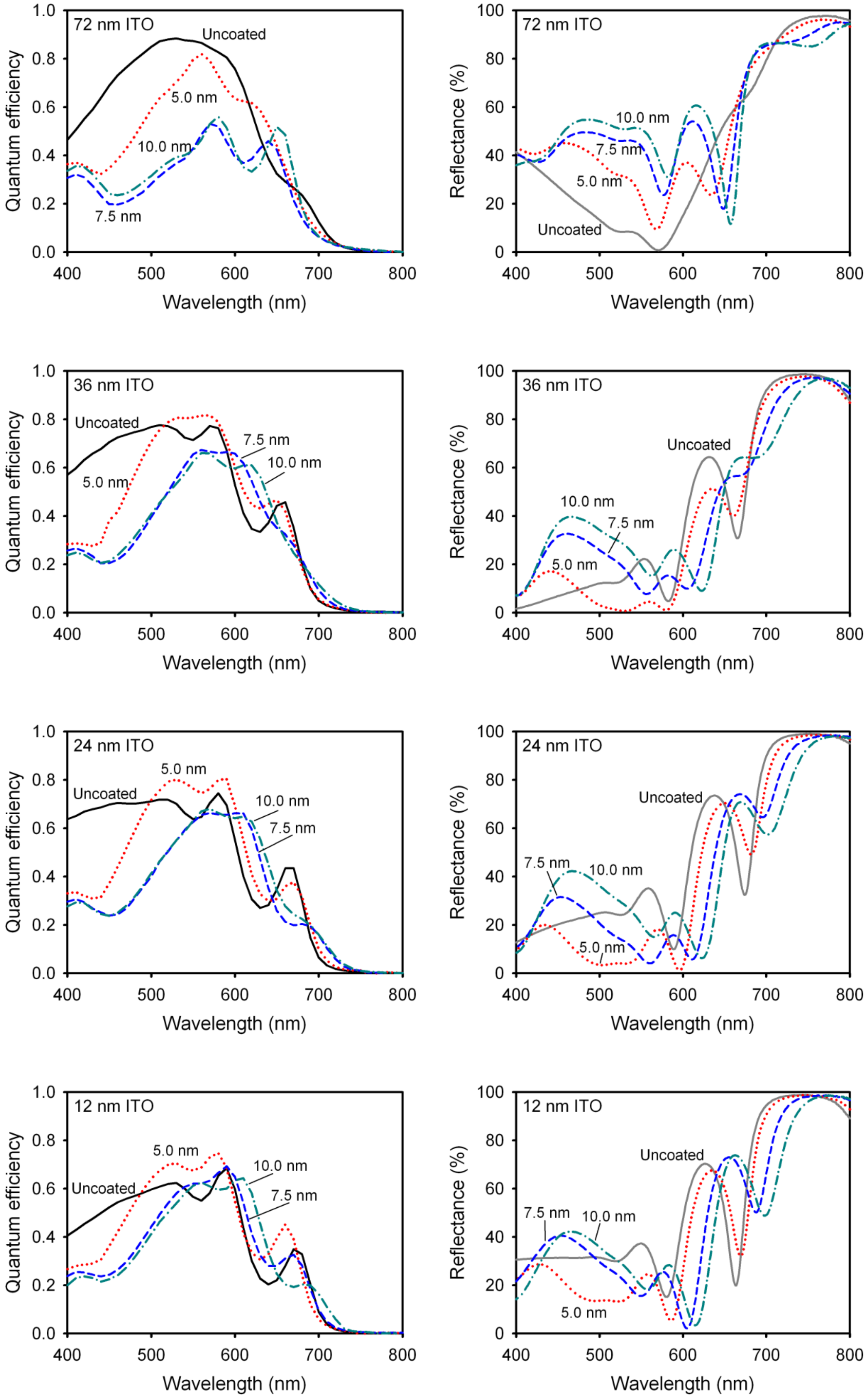

Figure 9.6: (Left) QE and (right) reflectance as a function of top ITO thickness and MIF thickness.

References

[1] E. Yablonovitch, G. D. Cody, "Intensity Enhancement in Textured Optical Sheets for Solar-Cells", *Ieee Transactions on Electron Devices*, **29**, 300 (1982).

[2] T. Markvart, L. Castaner, "*Practical Handbook of Photovoltaics: Fundamentals and Applications*", Elsevier Science, (2003).

[3] Y. Kim, S. K. Dhungel, S. Jung, D. Mangalaraj, J. Yi, "Texturing of large area multi-crystalline silicon wafers through different chemical approaches for solar cell fabrication", *Solar Energy Materials and Solar Cells*, **92**, 960 (2008).

[4] N. Taneda, T. Oyama, K. Sato, "*Light Scattering Effects of Highly Textured Transparent Conductive Oxides Films*", *Technical digest of International PVSEC-17*, Fukuoka, Japan (2007).

[5] P. K. Jain, K. S. Lee, I. H. El-Sayed, M. A. El-Sayed, "Calculated absorption and scattering properties of gold nanoparticles of different size, shape, and composition: Applications in biological imaging and biomedicine", *Journal of Physical Chemistry B*, **110**, 7238 (2006).

[6] P. Matheu, S. H. Lim, D. Derkacs, C. McPheeters, E. T. Yu, "Metal and dielectric nanoparticle scattering for improved optical absorption in photovoltaic devices", *Applied Physics Letters*, **93**, 113108 (2008).

[7] D. Derkacs, S. H. Lim, P. Matheu, W. Mar, E. T. Yu, "Improved performance of amorphous silicon solar cells via scattering from surface plasmon polaritons in nearby metallic nanoparticles", *Applied Physics Letters*, **89**, 093103 (2006).

[8] C. Hagglund, M. Zach, G. Petersson, B. Kasemo, "Electromagnetic coupling of light into a silicon solar cell by nanodisk plasmons", *Applied Physics Letters*, **92**, 053110 (2008).

[9] S. H. Lim, W. Mar, P. Matheu, D. Derkacs, E. T. Yu, "Photocurrent spectroscopy of optical absorption enhancement in silicon photodiodes via scattering from surface plasmon polaritons in gold nanoparticles", *Journal of Applied Physics*, **101**, 104309 (2007).

[10] E. Moulin, J. Sukmanowski, P. Luo, R. Carius, F. X. Royer, H. Stiebig, "Improved light absorption in thin-film silicon solar cells by integration of silver nanoparticles", *Journal of Non-Crystalline Solids*, **354**, 2488 (2008).

[11] E. Moulin, J. Sukmanowski, M. Schulte, A. Gordijn, F. X. Royer, H. Stiebig, "Thin-film silicon solar cells with integrated silver nanoparticles", *Thin Solid Films*, **516**, 6813 (2008).

[12] K. Nakayama, K. Tanabe, H. A. Atwater, "Plasmonic nanoparticle enhanced light absorption in GaAs solar cells", *Applied Physics Letters*, **93**, 121904 (2008).

[13] S. Pillai, K. R. Catchpole, T. Trupke, M. A. Green, "Surface plasmon enhanced silicon solar cells", *Journal of Applied Physics*, **101**, 093105 (2007).

[14] H. R. Stuart, D. G. Hall, "Absorption enhancement in silicon-on-insulator waveguides using metal island films", *Applied Physics Letters*, **69**, 2327 (1996).

[15] A. D. Rakic, A. B. Djurisic, J. M. Elazar, M. L. Majewski, "Optical properties of metallic films for vertical-cavity optoelectronic devices", *Applied Optics*, **37**, 5271 (1998).

[16] H. Raether, "*Surface Plasmons on Smooth and Rough Surfaces and on Gratings*", Springer, (1988).

[17] V. M. Shalaev, S. Kawata, "*Nanophotonics with Surface Plasmons*", Elsevier, (2007).

[18] M. L. Brongersma, P. G. Kik, "*Surface Plasmon Nanophotonics*", Springer, (2007).

[19] S. A. Maier, "*Plasmonics: Fundamentals and Applications*", Springer, (2007).

[20] W. L. Barnes, A. Dereux, T. W. Ebbesen, "Surface plasmon subwavelength optics", *Nature*, **424**, 824 (2003).

[21] E. Ozbay, "Plasmonics: Merging photonics and electronics at nanoscale dimensions", *Science*, **311**, 189 (2006).

[22] S. A. Maier, H. A. Atwater, "Plasmonics: Localization and guiding of electromagnetic energy in metal/dielectric structures", *Journal of Applied Physics*, **98**, 011101 (2005).

[23] W. A. Murray, W. L. Barnes, "Plasmonic materials", *Advanced Materials*, **19**, 3771 (2007).

[24] K. L. Kelly, E. Coronado, L. L. Zhao, G. C. Schatz, "The optical properties of metal nanoparticles: The influence of size, shape, and dielectric environment", *Journal of Physical Chemistry B*, **107**, 668 (2003).

[25] C. F. Bohren, D. R. Huffman, "*Absorption and Scattering of Light by Small Particles*", Wiley, (2004).

[26] H. Horvath, "Light scattering: Mie and More - commemorating 100 years of Mie's 1908 publication", *Journal of Quantitative Spectroscopy and Radiative Transfer*, **110**, 783 (2009).

[27] H. C. van de Hulst, "*Light Scattering by Small Particles*", Dover, (1981).

[28] J. A. Stratton, "*Electromagnetic Theory*", Wiley, (2007).

[29] E. D. Palik, "*Handbook of optical constants of solids*", Academic Press, (1985).

[30] E. D. Palik, "*Handbook of optical constants of solids II*", Academic Press, (1991).

[31] U. Kreibig, M. Vollmer, "*Optical Properties of Metal Clusters*", Springer: Berlin, (1995).

[32] L. Tonks, "Plasma-Electron Resonance, Plasma Resonance and Plasma Shape", *Physical Review*, **38**, 1219 (1931).

[33] S. Asano, G. Yamamoto, "Light-Scattering by a Spheroidal Particle", *Applied Optics*, **14**, 29 (1975).

[34] N. V. Voshchinnikov, V. G. Farafonov, "Optical-Properties of Spheroidal Particles", *Astrophysics and Space Science*, **204**, 19 (1993).

[35] N. V. Voshchinnikov, "Electromagnetic scattering by homogeneous and coated spheroids: Calculations using the separation of variables method", *Journal of Quantitative Spectroscopy & Radiative Transfer*, **55**, 627 (1996).

[36] E. M. Purcell, Pennypac.Cr, "Scattering and Absorption of Light by Nonspherical Dielectric Grains", *Astrophysical Journal*, **186**, 705 (1973).

[37] B. T. Draine, P. J. Flatau, "Discrete-Dipole Approximation for Scattering Calculations", *Journal of the Optical Society of America a-Optics Image Science and Vision*, **11**, 1491 (1994).

[38] B. T. Draine, J. Goodman, "Beyond Clausius-Mossotti - Wave-Propagation on a Polarizable Point Lattice and the Discrete Dipole Approximation", *Astrophysical Journal*, **405**, 685 (1993).

[39] T. Jensen, L. Kelly, A. Lazarides, G. C. Schatz, "Electrodynamics of noble metal nanoparticles and nanoparticle clusters", *Journal of Cluster Science*, **10**, 295 (1999).

[40] T. Wriedt, "A review of elastic light scattering theories", *Particle & Particle Systems Characterization*, **15**, 67 (1998).

[41] A. C. Ludwig, "The Generalized Multipole Technique", *Computer Physics Communications*, **68**, 306 (1991).

[42] E. Moreno, D. Erni, C. Hafner, R. Vahldieck, "Multiple multipole method with automatic multipole setting applied to the simulation of surface plasmons in metallic nanostructures", *Journal of the Optical Society of America a-Optics Image Science and Vision*, **19**, 101 (2002).

[43] J. L. Volakis, A. Chatterjee, L. C. Kempel, "Review of the Finite-Element Method for 3-Dimensional Electromagnetic Scattering", *Journal of the Optical Society of America a-Optics Image Science and Vision*, **11**, 1422 (1994).

[44] A. Taflove, "*Computational electrodynamics: the finite-difference time-domain method*", Artech House, (1995).

[45] J. P. Berenger, "A Perfectly Matched Layer for the Absorption of Electromagnetic-Waves", *Journal of Computational Physics*, **114**, 185 (1994).

[46] J. Bruning, L. Yuen, "Multiple scattering of EM waves by spheres part I--Multipole expansion and ray-optical solutions", *Antennas and Propagation, IEEE Transactions on*, **19**, 378 (1971).

[47] D. W. Mackowski, "Calculation of Total Cross-Sections of Multiple-Sphere Clusters", *Journal of the Optical Society of America a-Optics Image Science and Vision*, **11**, 2851 (1994).

[48] L. L. Zhao, K. L. Kelly, G. C. Schatz, "The extinction spectra of silver nanoparticle arrays: Influence of array structure on plasmon resonance wavelength and width", *Journal of Physical Chemistry B*, **107**, 7343 (2003).

[49] S. L. Zou, L. L. Zhao, G. C. Schatz, "Extinction spectra of silver nanoparticle arrays", *Plasmonics: Metallic Nanostructures and Their Optical Properties*, **5221**, 174 (2003).

[50] I. Freestone, N. Meeks, M. Sax, C. Higgitt, "The Lycurgus Cup - A Roman Nanotechnology", *Gold Bulletin*, **40**, 270 (2007).

[51] D. J. Barber, I. C. Freestone, "An Investigation of the Origin of the Color of the Lycurgus Cup by Analytical Transmission Electron-Microscopy", *Archaeometry*, **32**, 33 (1990).

[52] P. Mukherjee, A. Ahmad, D. Mandal, S. Senapati, S. R. Sainkar, M. I. Khan, R. Parishcha, P. V. Ajaykumar, M. Alam, R. Kumar, M. Sastry, "Fungus-mediated synthesis of silver nanoparticles and their immobilization in the mycelial matrix: A novel biological approach to nanoparticle synthesis", *Nano Letters*, **1**, 515 (2001).

[53] J. Turkevich, P. C. Stevnson, J. Hillier, "A study of the nucleation and growth processes in the synthesis of colloidal gold", *Discussions of the Faraday Society* **11**, 55 (1951).

[54] M. Brust, M. Walker, D. Bethell, D. J. Schiffrin, R. Whyman, "Synthesis of Thiol-Derivatized Gold Nanoparticles in a 2-Phase Liquid-Liquid System", *Journal of the Chemical Society-Chemical Communications*, 801 (1994).

[55] Y. W. Tan, X. H. Dai, Y. F. Li, D. B. Zhu, "Preparation of gold, platinum, palladium and silver nanoparticles by the reduction of their salts with a weak reductant-potassium bitartrate", *Journal of Materials Chemistry*, **13**, 1069 (2003).

[56] C. Radloff, N. J. Halas, "Enhanced thermal stability of silica-encapsulated metal nanoshells", *Applied Physics Letters*, **79**, 674 (2001).

[57] C. S. S. R. Kumar, J. Hormes, C. Leuschner, "*Nanofabrication Towards Biomedical Applications*", Wiley, (2005).

[58] D. G. Duff, A. C. Curtis, P. P. Edwards, D. A. Jefferson, B. F. G. Johnson, A. I. Kirkland, D. E. Logan, "The Morphology and Microstructure of Colloidal Silver and Gold", *Angewandte Chemie-International Edition in English*, **26**, 676 (1987).

[59] A. C. Curtis, D. G. Duff, P. P. Edwards, D. A. Jefferson, B. F. G. Johnson, A. I. Kirkland, A. S. Wallace, "A Morphology-Selective Copper Organosol", *Angewandte Chemie-International Edition in English*, **27**, 1530 (1988).

[60] D. G. Duff, P. P. Edwards, J. Evans, J. T. Gauntlett, D. A. Jefferson, B. F. G. Johnson, A. I. Kirkland, D. J. Smith, "A Joint Structural Characterization of Colloidal Platinum by Exafs and High-Resolution Electron-Microscopy", *Angewandte Chemie-International Edition in English*, **28**, 590 (1989).

[61] D. D. Evanoff, G. Chumanov, "Size-controlled synthesis of nanoparticles. 1. "Silver-only" aqueous suspensions via hydrogen reduction", *Journal of Physical Chemistry B*, **108**, 13948 (2004).

[62] M. M. Alvarez, J. T. Khoury, T. G. Schaaff, M. N. Shafigullin, I. Vezmar, R. L. Whetten, "Optical absorption spectra of nanocrystal gold molecules", *Journal of Physical Chemistry B*, **101**, 3706 (1997).

[63] M. Grzelczak, J. Perez-Juste, P. Mulvaney, L. M. Liz-Marzan, "Shape control in gold nanoparticle synthesis", *Chemical Society Reviews*, **37**, 1783 (2008).

[64] R. L. Whetten, J. T. Khoury, M. M. Alvarez, S. Murthy, I. Vezmar, Z. L. Wang, P. W. Stephens, C. L. Cleveland, W. D. Luedtke, U. Landman, "Nanocrystal gold molecules", *Advanced Materials*, **8**, 428 (1996).

[65] M. Brust, C. J. Kiely, "Some recent advances in nanostructure preparation from gold and silver particles: a short topical review", *Colloids and Surfaces a-Physicochemical and Engineering Aspects*, **202**, 175 (2002).

[66] S. Malynych, I. Luzinov, G. Chumanov, "Poly(vinyl pyridine) as a universal surface modifier for immobilization of nanoparticles", *Journal of Physical Chemistry B*, **106**, 1280 (2002).

[67] D. M. Schaadt, B. Feng, E. T. Yu, "Enhanced semiconductor optical absorption via surface plasmon excitation in metal nanoparticles", *Applied Physics Letters*, **86**, 063106 (2005).

[68] K. C. Grabar, K. J. Allison, B. E. Baker, R. M. Bright, K. R. Brown, R. G. Freeman, A. P. Fox, C. D. Keating, M. D. Musick, M. J. Natan, "Two-dimensional arrays of colloidal gold particles: A flexible approach to macroscopic metal surfaces", *Langmuir*, **12**, 2353 (1996).

[69] K. C. Grabar, R. G. Freeman, M. B. Hommer, M. J. Natan, "Preparation and Characterization of Au Colloid Monolayers", *Analytical Chemistry*, **67**, 735 (1995).

[70] K. C. Grabar, P. C. Smith, M. D. Musick, J. A. Davis, D. G. Walter, M. A. Jackson, A. P. Guthrie, M. J. Natan, "Kinetic control of interparticle spacing in Au colloid-based surfaces: Rational nanometer-scale architecture", *Journal of the American Chemical Society*, **118**, 1148 (1996).

[71] I. U. Vakarelski, C. E. McNamee, K. Higashitani, "Deposition of silica nanoparticles on a gold surface via a self-assembled monolayer of (3-mercaptopropyl)trimethoxysilane", *Colloids and Surfaces a-Physicochemical and Engineering Aspects*, **295**, 16 (2007).

[72] C. A. Goss, D. H. Charych, M. Majda, "Application of (3-Mercaptopropyl)Trimethoxysilane as a Molecular Adhesive in the Fabrication of Vapor-Deposited Gold Electrodes on Glass Substrates", *Analytical Chemistry*, **63**, 85 (1991).

[73] A. K. Mahapatro, A. Scott, A. Manning, D. B. Janes, "Gold surface with sub-nm roughness realized by evaporation on a molecular adhesion monolayer", *Applied Physics Letters*, **88**, 151917 (2006).

[74] S. J. Oldenburg, R. D. Averitt, S. L. Westcott, N. J. Halas, "Nanoengineering of optical resonances", *Chemical Physics Letters*, **288**, 243 (1998).

[75] J. B. Jackson, N. J. Halas, "Silver nanoshells: Variations in morphologies and optical properties", *Journal of Physical Chemistry B*, **105**, 2743 (2001).

[76] C. Charton, M. Fahland, "Optical properties of thin Ag films deposited by magnetron sputtering", *Surface & Coatings Technology*, **174**, 181 (2003).

[77] C. Charton, M. Fahland, "Growth of Ag films on PET deposited by magnetron sputtering", *Vacuum*, **68**, 65 (2002).

[78] R. S. Sennett, G. D. Scott, "The Structure of Evaporated Metal Films and Their Optical Properties", *J. Opt. Soc. Am.*, **40**, 203 (1950).

[79] J. G. Skofronick, W. B. Phillips, "Morphological Changes in Discontinuous Gold Films following Deposition", *Journal of Applied Physics*, **38**, 4791 (1967).

[80] G. L. Allen, R. A. Bayles, W. W. Gile, W. A. Jesser, "Small Particle Melting of Pure Metals", *Thin Solid Films*, **144**, 297 (1986).

[81] A. Heilmann, "*Polymer Films with Embedded Metal Nanoparticles*", Springer: Berlin, (2003).

[82] J. Werner, A. Heilmann, F. Mueller, "Electron-Beam-Induced Coalescence in Plasma Polymer Silver Composite Films", *Applied Physics Letters*, **66**, 3436 (1995).

[83] A. Heilmann, A. D. Muller, J. Werner, F. Muller, "Electron beam initiated oxidation and coalescence of metal particles embedded in a plasma-polymer thin film matrix", *Thin Solid Films*, **270**, 351 (1995).

[84] D. Dalacu, L. Martinu, "Optical properties of discontinuous gold films: finite-size effects", *Journal of the Optical Society of America B-Optical Physics*, **18**, 85 (2001).

[85] Y. Suzuki, Y. Ojima, Y. Fukui, H. Fazyia, K. Sagisaka, "Post-annealing temperature dependence of infrared absorption enhancement of polymer on evaporated silver films", *Thin Solid Films*, **515**, 3073 (2007).

[86] G. Kalyuzhny, A. Vaskevich, M. A. Schneeweiss, I. Rubinstein, "Transmission surface-plasmon resonance (T-SPR) measurements for monitoring adsorption on ultrathin gold island films", *Chemistry-a European Journal*, **8**, 3850 (2002).

[87] R. Gupta, M. J. Dyer, W. A. Weimer, "Preparation and characterization of surface plasmon resonance tunable gold and silver films", *Journal of Applied Physics*, **92**, 5264 (2002).

[88] S. E. Roark, K. L. Rowlen, "Thin Ag Films - Influence of Substrate and Postdeposition Treatment on Morphology and Optical-Properties", *Analytical Chemistry*, **66**, 261 (1994).

[89] S. Z. Malynych, G. Chumanov, "Vacuum deposition of silver island films on chemically modified surfaces", *Journal of Vacuum Science & Technology A*, **21**, 723 (2003).

[90] A. Vaskevich, T. Sehayek, I. Rubinstein, "Mass Thickness Analysis of Gold Thin Films Using Room Temperature Gas-Phase Chlorination", *Analytical Chemistry*, **81**, 2877 (2009).

[91] T. Karakouz, A. B. Tesler, T. A. Bendikov, A. Vaskevich, I. Rubinstein, "Highly Stable Localized Plasmon Transducers Obtained by Thermal Embedding of Gold Island Films on Glass", *Advanced Materials*, **20**, 3893 (2008).

[92] V. L. Schlegel, T. M. Cotton, "Silver-Island Films as Substrates for Enhanced Raman-Scattering - Effect of Deposition Rate on Intensity", *Analytical Chemistry*, **63**, 241 (1991).

[93] R. P. Vanduyne, J. C. Hulteen, D. A. Treichel, "Atomic-Force Microscopy and Surface-Enhanced Raman-Spectroscopy .1. Ag Island Films and Ag Film over Polymer Nanosphere Surfaces Supported on Glass", *J Chem Phys*, **99**, 2101 (1993).

[94] D. J. Semin, K. L. Rowlen, "Influence of Vapor-Deposition Parameters on Sers Active Ag Film Morphology and Optical-Properties", *Analytical Chemistry*, **66**, 4324 (1994).

[95] Z. Rakocevic, R. Petrovic, S. Strbac, "Surface roughness of ultra-thin silver films sputter depositedon a glass", *Journal of Microscopy-Oxford*, **232**, 595 (2008).

[96] D. N. Uan, A. Heilmann, "Determination of thermally induced microstructural changes of embedded metal nanoparticles by lateral and cross-sectional transmission electron microscopy", *Vacuum*, **49**, 51 (1998).

[97] M. Kawasaki, M. Hori, "Laser-induced conversion of noble metal-island films to dense monolayers of spherical nanoparticles", *Journal of Physical Chemistry B*, **107**, 6760 (2003).

[98] L. Eurenius, C. Haegglund, E. Olsson, B. Kasemo, D. Chakarov, "Grating formation by metal-nanoparticle-mediated coupling of light into waveguided modes", *Nature Photonics*, **2**, 360 (2008).

[99] H. R. Stuart, D. G. Hall, "Island size effects in nanoparticle-enhanced photodetectors", *Applied Physics Letters*, **73**, 3815 (1998).

[100] K. Baba, T. Okuno, M. Miyagi, "Silver-Gold Compound Metal Island Films Prepared by Using a 2-Step Evaporation Method", *Applied Physics Letters*, **62**, 437 (1993).

[101] K. Baba, T. Okuno, M. Miyagi, "Resonance wavelengths of silver-gold compound metal island films", *Journal of the Optical Society of America B-Optical Physics*, **12**, 2372 (1995).

[102] S. Kachan, O. Stenzel, A. Ponyavina, "High-absorbing gradient multilayer coatings with silver nanoparticles", *Applied Physics B-Lasers and Optics*, **84**, 281 (2006).

[103] A. Biswas, H. Eilers, F. Hidden, O. C. Aktas, C. V. S. Kiran, "Large broadband visible to infrared plasmonic absorption from Ag nanoparticles with a fractal structure embedded in a Teflon AF (R) matrix", *Applied Physics Letters*, **88**, 013103 (2006).

[104] J. R. Krenn, G. Schider, W. Rechberger, B. Lamprecht, A. Leitner, F. R. Aussenegg, J. C. Weeber, "Design of multipolar plasmon excitations in silver nanoparticles", *Applied Physics Letters*, **77**, 3379 (2000).

[105] C. L. Haynes, A. D. McFarland, L. L. Zhao, R. P. Van Duyne, G. C. Schatz, L. Gunnarsson, J. Prikulis, B. Kasemo, M. Kall, "Nanoparticle optics: The importance of radiative dipole coupling in two-dimensional nanoparticle arrays", *Journal of Physical Chemistry B*, **107**, 7337 (2003).

[106] J. Grand, P.-M. Adam, A.-S. Grimault, A. Vial, M. Lamy de la Chapelle, J.-L. Bijeon, S. Kostcheev, P. Royer, "Optical Extinction Spectroscopy of Oblate, Prolate and Ellipsoid Shaped Gold Nanoparticles: Experiments and Theory", *Plasmonics*, **1**, 135 (2006).

[107] P. P. Pompa, L. Martiradonna, A. Della Torre, L. Carbone, L. L. del Mercato, L. Manna, M. De Vittorio, F. Calabi, R. Cingolani, R. Rinaldi, "Fluorescence enhancement in colloidal semiconductor nanocrystals by metallic nanopatterns", *Sensors and Actuators B-Chemical*, **126**, 187 (2007).

[108] B. Lamprecht, A. Leitner, F. R. Aussenegg, "Femtosecond decay-time measurement of electron-plasma oscillation in nanolithographically designed silver particles", *Applied Physics B-Lasers and Optics*, **64**, 269 (1997).

[109] B. K. Canfield, S. Kujala, M. Kauranen, K. Jefimovs, T. Vallius, J. Turunen, "Remarkable polarization sensitivity of gold nanoparticle arrays", *Applied Physics Letters*, **86**, 183109 (2005).

[110] A. W. Clark, A. K. Sheridan, A. Glidle, D. R. S. Cumming, J. M. Cooper, "Tuneable visible resonances in crescent shaped nano-split-ring resonators", *Applied Physics Letters*, **91**, (2007).

[111] A. K. Sheridan, A. W. Clark, A. Glidle, J. M. Cooper, D. R. S. Cumming, "Multiple plasmon resonances from gold nanostructures", *Applied Physics Letters*, **90**, 143105 (2007).

[112] D. P. Fromm, A. Sundaramurthy, P. J. Schuck, G. Kino, W. E. Moerner, "Gap-dependent optical coupling of single "Bowtie" nanoantennas resonant in the visible", *Nano Letters*, **4**, 957 (2004).

[113] W. Y. Huang, W. Qian, P. K. Jain, M. A. El-Sayed, "The effect of plasmon field on the coherent lattice phonon oscillation in electron-beam fabricated gold nanoparticle pairs", *Nano Letters*, **7**, 3227 (2007).

[114] K. Ueno, S. Juodkazis, V. Mizeikis, K. Sasaki, H. Misawa, "Clusters of closely spaced gold nanoparticles as a source of two-photon photoluminescence at visible wavelengths", *Advanced Materials*, **20**, 26 (2008).

[115] S. Y. Chou, P. R. Krauss, "Imprint lithography with sub-10 nm feature size and high throughput", *Microelectronic Engineering*, **35**, 237 (1997).

[116] B. D. Lucas, J. S. Kim, C. Chin, L. J. Guo, "Nanoimprint lithography based approach for the fabrication of large-area, uniformly oriented plasmonic arrays", *Advanced Materials*, **20**, 1129 (2008).

[117] J. C. Hulteen, R. P. Vanduyne, "Nanosphere Lithography - a Materials General Fabrication Process for Periodic Particle Array Surfaces", *Journal of Vacuum Science & Technology a-Vacuum Surfaces and Films*, **13**, 1553 (1995).

[118] S. M. Weekes, F. Y. Ogrin, W. A. Murray, P. S. Keatley, "Macroscopic arrays of magnetic nanostructures from self-assembled nanosphere templates", *Langmuir*, **23**, 1057 (2007).

[119] T. R. Jensen, M. D. Malinsky, C. L. Haynes, R. P. Van Duyne, "Nanosphere lithography: Tunable localized surface plasmon resonance spectra of silver nanoparticles", *Journal of Physical Chemistry B*, **104**, 10549 (2000).

[120] G. H. Chan, J. Zhao, E. M. Hicks, G. C. Schatz, R. P. Van Duyne, "Plasmonic properties of copper nanoparticles fabricated by nanosphere lithography", *Nano Letters*, **7**, 1947 (2007).

[121] G. H. Chan, J. Zhao, G. C. Schatz, R. P. Van Duyne, "Localized surface plasmon resonance spectroscopy of triangular aluminum nanoparticles", *Journal of Physical Chemistry C*, **112**, 13958 (2008).

[122] B. J. Y. Tan, C. H. Sow, T. S. Koh, K. C. Chin, A. T. S. Wee, C. K. Ong, "Fabrication of size-tunable gold nanoparticles array with nanosphere lithography, reactive ion etching, and thermal annealing", *Journal of Physical Chemistry B*, **109**, 11100 (2005).

[123] J. C. Hulteen, D. A. Treichel, M. T. Smith, M. L. Duval, T. R. Jensen, R. P. Van Duyne, "Nanosphere lithography: Size-tunable silver nanoparticle and surface cluster arrays", *Journal of Physical Chemistry B*, **103**, 3854 (1999).

[124] A. Kosiorek, W. Kandulski, H. Glaczynska, M. Giersig, "Fabrication of nanoscale rings, dots, and rods by combining shadow nanosphere lithography and annealed polystyrene nanosphere masks", *Small*, **1**, 439 (2005).

[125] C. L. Haynes, A. D. McFarland, M. T. Smith, J. C. Hulteen, R. P. Van Duyne, "Angle-resolved nanosphere lithography: Manipulation of nanoparticle size, shape, and interparticle spacing", *Journal of Physical Chemistry B*, **106**, 1898 (2002).

[126] W. A. Murray, S. Astilean, W. L. Barnes, "Transition from localized surface plasmon resonance to extended surface plasmon-polariton as metallic nanoparticles merge to form a periodic hole array", *Physical Review B*, **69**, 165407 (2004).

[127] C. Haginoya, M. Ishibashi, K. Koike, "Nanostructure array fabrication with a size-controllable natural lithography", *Applied Physics Letters*, **71**, 2934 (1997).

[128] D.-G. Choi, S. Kim, S.-G. Jang, S.-M. Yang, J.-R. Jeong, S.-C. Shin, "Nanopatterned Magnetic Metal via Colloidal Lithography with Reactive Ion Etching", *Chemistry of Materials*, **16**, 4208 (2004).

[129] Y. B. Zheng, B. K. Juluri, X. L. Mao, T. R. Walker, T. J. Huang, "Systematic investigation of localized surface plasmon resonance of long-range ordered Au nanodisk arrays", *Journal of Applied Physics*, **103**, 014308 (2008).

[130] J. Aizpurua, P. Hanarp, D. S. Sutherland, M. Kall, G. W. Bryant, F. J. G. de Abajo, "Optical properties of gold nanorings", *Physical Review Letters*, **90**, 057401 (2003).

[131] J. S. Shumaker-Parry, H. Rochholz, M. Kreiter, "Fabrication of crescent-shaped optical antennas", *Advanced Materials*, **17**, 2131 (2005).

[132] J. Q. Liu, A. I. Maaroof, L. Wieczorek, M. B. Cortie, "Fabrication of hollow metal "nanocaps" and their red-shifted optical absorption spectra", *Advanced Materials*, **17**, 1276 (2005).

[133] P. Hanarp, M. Kall, D. S. Sutherland, "Optical properties of short range ordered arrays of nanometer gold disks prepared by colloidal lithography", *Journal of Physical Chemistry B*, **107**, 5768 (2003).

[134] H. Fredriksson, Y. Alaverdyan, A. Dmitriev, C. Langhammer, D. S. Sutherland, M. Zaech, B. Kasemo, "Hole-mask colloidal lithography", *Advanced Materials*, **19**, 4297 (2007).

[135] C. Langhammer, B. Kasemo, I. Zoric, "Absorption and scattering of light by Pt, Pd, Ag, and Au nanodisks: Absolute cross sections and branching ratios", *J Chem Phys*, **126**, (2007).

[136] C. Langhammer, M. Schwind, B. Kasemo, I. Zoric, "Localized surface plasmon resonances in aluminum nanodisks", *Nano Letters*, **8**, 1461 (2008).

[137] A. Dmitriev, T. Pakizeh, M. Kall, D. S. Sutherland, "Gold-silica-gold nanosandwiches: Tunable bimodal plasmonic resonators", *Small*, **3**, 294 (2007).

[138] Y. Ekinci, H. H. Solak, C. David, J. F. Loffler, "Plasmonic nanostructures made from aluminum fabricated by EUV interference lithography - art. no. 67170P", *Optomechatronic Micro/Nano Devices and Components Iii*, **6717**, P7170 (2007).

[139] J. Henzie, E. S. Kwak, T. W. Odom, "Mesoscale metallic pyramids with nanoscale tips", *Nano Letters*, **5**, 1199 (2005).

[140] J. Henzie, M. H. Lee, T. W. Odom, "Multiscale patterning of plasmonic metamaterials", *Nature Nanotechnology*, **2**, 549 (2007).

[141] C. R. Martin, "Membrane-based synthesis of nanomaterials", *Chemistry of Materials*, **8**, 1739 (1996).

[142] J. C. Hulteen, C. R. Martin, "A general template-based method for the preparation of nanomaterials", *Journal of Materials Chemistry*, **7**, 1075 (1997).

[143] S. Ono, M. Saito, H. Asoh, "Self-ordering of anodic porous alumina formed in organic acid electrolytes", *Electrochimica Acta*, **51**, 827 (2005).

[144] H. Masuda, M. Satoh, "Fabrication of Gold Nanodot Array Using Anodic Porous Alumina as an Evaporation Mask", *Japanese Journal of Applied Physics*, **35**, L126 (1996).

[145] K. Nakayama, K. Tanabe, H. A. Atwater, "Plasmonic nanoparticle enhanced light absorption in GaAs solar cells", *Applied Physics Letters*, **93**, (2008).

[146] E. K. Payne, K. L. Shuford, S. Park, G. C. Schatz, C. A. Mirkin, "Multipole plasmon resonances in gold nanorods", *Journal of Physical Chemistry B*, **110**, 2150 (2006).

[147] S. R. Nicewarner-Pena, R. G. Freeman, B. D. Reiss, L. He, D. J. Pena, I. D. Walton, R. Cromer, C. D. Keating, M. J. Natan, "Submicrometer metallic barcodes", *Science*, **294**, 137 (2001).

[148] C. D. Keating, M. J. Natan, "Striped metal nanowires as building blocks and optical tags", *Advanced Materials*, **15**, 451 (2003).

[149] M. S. Sander, L. S. Tan, "Nanoparticle arrays on surfaces fabricated using anodic alumina films as templates", *Advanced Functional Materials*, **13**, 393 (2003).

[150] T. Akita, M. Okumura, K. Tanaka, M. Kohyama, M. Haruta, "TEM observation of gold nanoparticles deposited on cerium oxide", *Journal of Materials Science*, **40**, 3101 (2005).

[151] F. Joachim, "*Electron Tomography: Three-Dimensional Imaging with the Transmission Electron Microscope*", Springer, (1992).

[152] D. L. Sedin, K. L. Rowlen, "Influence of tip size on AFM roughness measurements", *Applied Surface Science*, **182**, 40 (2001).

[153] L. W. Chen, C. L. Cheung, P. D. Ashby, C. M. Lieber, "Single-walled carbon nanotube AFM probes: Optimal imaging resolution of nanoclusters and biomolecules in ambient and fluid environments", *Nano Letters*, **4**, 1725 (2004).

[154] C. Lofton, W. Sigmund, "Mechanisms controlling crystal habits of gold and silver colloids", *Advanced Functional Materials*, **15**, 1197 (2005).

[155] D. D. Evanoff, G. Chumanov, "Size-controlled synthesis of nanoparticles. 2. Measurement of extinction, scattering, and absorption cross sections", *Journal of Physical Chemistry B*, **108**, 13957 (2004).

[156] C. Langhammer, B. Kasemo, I. Zoric, "Absorption and scattering of light by Pt, Pd, Ag, and Au nanodisks: Absolute cross sections and branching ratios", *J Chem Phys*, **126**, 194702 (2007).

[157] H. R. Stuart, D. G. Hall, "Enhanced dipole-dipole interaction between elementary radiators near a surface", *Physical Review Letters*, **80**, 5663 (1998).

[158] C. v. Fragstien, J. Meingast, H. Hoch, *Forschungsber. Wirtsch. und Verkehrsministerium Nordrhein-Westfalen, Koln*, **174**, (1955).

[159] W. B. Jackson, N. M. Amer, A. C. Boccara, D. Fournier, "Photothermal Deflection Spectroscopy and Detection", *Applied Optics*, **20**, 1333 (1981).

[160] U. Kreibig, B. Schmitz, H. D. Breuer, "Separation of Plasmon-Polariton Modes of Small Metal Particles", *Physical Review B*, **36**, 5027 (1987).

[161] C. Sonnichsen, S. Geier, N. E. Hecker, G. von Plessen, J. Feldmann, H. Ditlbacher, B. Lamprecht, J. R. Krenn, F. R. Aussenegg, V. Z. H. Chan, J. P. Spatz, M. Moller, "Spectroscopy of single metallic nanoparticles using total internal reflection microscopy", *Applied Physics Letters*, **77**, 2949 (2000).

[162] S. Schultz, D. R. Smith, J. J. Mock, D. A. Schultz, "Single-target molecule detection with nonbleaching multicolor optical immunolabels", *Proceedings of the National Academy of Sciences of the United States of America*, **97**, 996 (2000).

[163] J. J. Mock, M. Barbic, D. R. Smith, D. A. Schultz, S. Schultz, "Shape effects in plasmon resonance of individual colloidal silver nanoparticles", *J Chem Phys*, **116**, 6755 (2002).

[164] A. Curry, G. Nusz, A. Chilkoti, A. Wax, "Substrate effect on refractive index dependence of plasmon resonance for individual silver nanoparticles observed using darkfield micro-spectroscopy", *Optics Express*, **13**, 2668 (2005).

[165] A. Arbouet, D. Christofilos, N. Del Fatti, F. Vallee, J. R. Huntzinger, L. Arnaud, P. Billaud, M. Broyer, "Direct measurement of the single-metal-cluster optical absorption", *Physical Review Letters*, **93**, 127401 (2004).

[166] O. Muskens, D. Christofilos, N. Del Fatti, F. Vallee, "Optical response of a single noble metal nanoparticle", *Journal of Optics a-Pure and Applied Optics*, **8**, S264 (2006).

[167] J. J. Mock, D. R. Smith, S. Schultz, "Local refractive index dependence of plasmon resonance spectra from individual nanoparticles", *Nano Letters*, **3**, 485 (2003).

[168] C. L. Baciu, J. Becker, A. Janshoff, C. Sonnichsen, "Protein-membrane interaction probed by single plasmonic nanoparticles", *Nano Letters*, **8**, 1724 (2008).

[169] S. K. Eah, H. M. Jaeger, N. F. Scherer, G. P. Wiederrecht, X. M. Lin, "Plasmon scattering from a single gold nanoparticle collected through an optical fiber", *Applied Physics Letters*, **86**, 031902 (2005).

[170] R. C. Reddick, R. J. Warmack, T. L. Ferrell, "New Form of Scanning Optical Microscopy", *Physical Review B*, **39**, 767 (1989).

[171] J. Kim, K.-B. Song, "Recent progress of nano-technology with NSOM", *Micron*, **38**, 409 (2007).

[172] T. Klar, M. Perner, S. Grosse, G. von Plessen, W. Spirkl, J. Feldmann, "Surface-plasmon resonances in single metallic nanoparticles", *Physical Review Letters*, **80**, 4249 (1998).

[173] A. A. Mikhailovsky, M. A. Petruska, K. R. Li, M. I. Stockman, V. I. Klimov, "Phase-sensitive spectroscopy of surface plasmons in individual metal nanostructures", *Physical Review B*, **69**, 085401 (2004).

[174] J. R. Krenn, A. Dereux, J. C. Weeber, E. Bourillot, Y. Lacroute, J. P. Goudonnet, G. Schider, W. Gotschy, A. Leitner, F. R. Aussenegg, C. Girard, "Squeezing the optical near-field zone by plasmon coupling of metallic nanoparticles", *Physical Review Letters*, **82**, 2590 (1999).

[175] J. R. Krenn, J. C. Weeber, A. Dereux, E. Bourillot, J. P. Goudonnet, B. Schider, A. Leitner, F. R. Aussenegg, C. Girard, "Direct observation of localized surface plasmon coupling", *Physical Review B*, **60**, 5029 (1999).

[176] K. Imura, T. Nagahara, H. Okamoto, "Plasmon mode imaging of single gold nanorods", *Journal of the American Chemical Society*, **126**, 12730 (2004).

[177] H. Okamoto, K. Imura, "Near-field imaging of optical field and plasmon wavefunctions in metal nanoparticles", *Journal of Materials Chemistry*, **16**, 3920 (2006).

[178] R. Esteban, R. Vogelgesang, J. Dorfmuller, A. Dmitriev, C. Rockstuhl, C. Etrich, K. Kern, "Direct Near-Field Optical Imaging of Higher Order Plasmonic Resonances", *Nano Letters*, **8**, 3155 (2008).

[179] M. Rang, A. C. Jones, F. Zhou, Z.-Y. Li, B. J. Wiley, Y. Xia, M. B. Raschke, "Optical Near-Field Mapping of Plasmonic Nanoprisms", *Nano Letters*, **8**, 3357 (2008).

[180] V. A. Markel, V. M. Shalaev, P. Zhang, W. Huynh, L. Tay, T. L. Haslett, M. Moskovits, "Near-field optical spectroscopy of individual surface-plasmon modes in colloid clusters", *Physical Review B*, **59**, 10903 (1999).

[181] T. Shimada, K. Imura, M. K. Hossain, H. Okamoto, M. Kitajima, "Near-field study on correlation of localized electric field and nanostructures in monolayer assembly of gold nanoparticles", *Journal of Physical Chemistry C*, **112**, 4033 (2008).

[182] M. G. Blaber, M. D. Arnold, N. Harris, M. J. Ford, M. B. Cortie, "Plasmon absorption in nanospheres: A comparison of sodium, potassium, aluminium, silver and gold", *Physica B-Condensed Matter*, **394**, 184 (2007).

[183] S. Berciaud, L. Cognet, P. Tamarat, B. Lounis, "Observation of intrinsic size effects in the optical response of individual gold nanoparticles", *Nano Letters*, **5**, 515 (2005).

[184] A. J. Haes, C. L. Haynes, A. D. McFarland, G. C. Schatz, R. R. Van Duyne, S. L. Zou, "Plasmonic materials for surface-enhanced sensing and spectroscopy", *Mrs Bulletin*, **30**, 368 (2005).

[185] X. Y. Zhang, E. M. Hicks, J. Zhao, G. C. Schatz, R. P. Van Duyne, "Electrochemical tuning of silver nanoparticles fabricated by nanosphere lithography", *Nano Letters*, **5**, 1503 (2005).

[186] K. S. Lee, M. A. El-Sayed, "Dependence of the enhanced optical scattering efficiency relative to that of absorption for gold metal nanorods on aspect ratio, size, end-cap shape, and medium refractive index", *Journal of Physical Chemistry B*, **109**, 20331 (2005).

[187] E. S. Kooij, B. Poelsema, "Shape and size effects in the optical properties of metallic nanorods", *Physical Chemistry Chemical Physics*, **8**, 3349 (2006).

[188] S. W. Prescott, P. Mulvaney, "Gold nanorod extinction spectra", *Journal of Applied Physics*, **99**, 123504 (2006).

[189] H. Wang, G. P. Goodrich, F. Tam, C. Oubre, P. Nordlander, N. J. Halas, "Controlled texturing modifies the surface topography and plasmonic properties of au nanoshells", *Journal of Physical Chemistry B*, **109**, 11083 (2005).

[190] H. Wang, K. Fu, R. A. Drezek, N. J. Halas, "Light scattering from spherical plasmonic nanoantennas: effects of nanoscale roughness", *Applied Physics B-Lasers and Optics*, **84**, 191 (2006).

[191] B. N. Khlebtsov, A. Melnikov, N. G. Khlebtsov, "On the extinction multipole plasmons in gold nanorods", *Journal of Quantitative Spectroscopy and Radiative Transfer*, **107**, 306 (2007).

[192] G. Laurent, N. Felidj, J. Aubard, G. Levi, J. R. Krenn, A. Hohenau, G. Schider, A. Leitner, F. R. Aussenegg, "Surface enhanced Raman scattering arising from multipolar plasmon excitation", *J Chem Phys*, **122**, 011102 (2005).

[193] A. V. Whitney, J. W. Elam, S. L. Zou, A. V. Zinovev, P. C. Stair, G. C. Schatz, R. P. Van Duyne, "Localized surface plasmon resonance nanosensor: A high-resolution distance-dependence study using atomic layer deposition", *Journal of Physical Chemistry B*, **109**, 20522 (2005).

[194] A. D. McFarland, R. P. Van Duyne, "Single silver nanoparticles as real-time optical sensors with zeptomole sensitivity", *Nano Letters*, **3**, 1057 (2003).

[195] L. J. Sherry, S. H. Chang, G. C. Schatz, R. P. Van Duyne, B. J. Wiley, Y. N. Xia, "Localized surface plasmon resonance spectroscopy of single silver nanocubes", *Nano Letters*, **5**, 2034 (2005).

[196] E. Prodan, C. Radloff, N. J. Halas, P. Nordlander, "A hybridization model for the plasmon response of complex nanostructures", *Science*, **302**, 419 (2003).

[197] E. Prodan, P. Nordlander, N. J. Halas, "Electronic structure and optical properties of gold nanoshells", *Nano Letters*, **3**, 1411 (2003).

[198] E. Prodan, P. Nordlander, "Structural tunability of the plasmon resonances in metallic nanoshells", *Nano Letters*, **3**, 543 (2003).

[199] P. Nordlander, "The Ring: A Leitmotif in Plasmonics", *Acs Nano*, **3**, 488 (2009).

[200] L. Gunnarsson, T. Rindzevicius, J. Prikulis, B. Kasemo, M. Kall, S. L. Zou, G. C. Schatz, "Confined plasmons in nanofabricated single silver particle pairs: Experimental observations of strong interparticle interactions", *Journal of Physical Chemistry B*, **109**, 1079 (2005).

[201] M. Quinten, A. Leitner, J. R. Krenn, F. R. Aussenegg, "Electromagnetic energy transport via linear chains of silver nanoparticles", *Optics Letters*, **23**, 1331 (1998).

[202] M. L. Brongersma, J. W. Hartman, H. A. Atwater, "Electromagnetic energy transfer and switching in nanoparticle chain arrays below the diffraction limit", *Physical Review B*, **62**, 16356 (2000).

[203] S. A. Maier, P. G. Kik, H. A. Atwater, S. Meltzer, E. Harel, B. E. Koel, A. A. G. Requicha, "Local detection of electromagnetic energy transport below the diffraction limit in metal nanoparticle plasmon waveguides", *Nature Materials*, **2**, 229 (2003).

[204] P. Muhlschlegel, H. J. Eisler, O. J. F. Martin, B. Hecht, D. W. Pohl, "Resonant optical antennas", *Science*, **308**, 1607 (2005).

[205] J. Aizpurua, G. W. Bryant, L. J. Richter, F. J. G. de Abajo, B. K. Kelley, T. Mallouk, "Optical properties of coupled metallic nanorods for field-enhanced spectroscopy", *Physical Review B*, **71**, 235420 (2005).

[206] B. Lamprecht, G. Schider, R. T. Lechner, H. Ditlbacher, J. R. Krenn, A. Leitner, F. R. Aussenegg, "Metal nanoparticle gratings: Influence of dipolar particle interaction on the plasmon resonance", *Physical Review Letters*, **84**, 4721 (2000).

[207] F. J. G. de Abajo, "Colloquium: Light scattering by particle and hole arrays", *Reviews of Modern Physics*, **79**, 1267 (2007).

[208] B. Auguie, W. L. Barnes, "Collective resonances in gold nanoparticle arrays", *Physical Review Letters*, **101**, 143902 (2008).

[209] Y. Z. Chu, E. Schonbrun, T. Yang, K. B. Crozier, "Experimental observation of narrow surface plasmon resonances in gold nanoparticle arrays", *Applied Physics Letters*, **93**, 181108 (2008).

[210] S. L. Zou, N. Janel, G. C. Schatz, "Silver nanoparticle array structures that produce remarkably narrow plasmon lineshapes", *J Chem Phys*, **120**, 10871 (2004).

[211] S. L. Zou, G. C. Schatz, "Narrow plasmonic/photonic extinction and scattering line shapes for one and two dimensional silver nanoparticle arrays", *J Chem Phys*, **121**, 12606 (2004).

[212] V. G. Kravets, F. Schedin, A. N. Grigorenko, "Extremely narrow plasmon resonances based on diffraction coupling of localized plasmons in arrays of metallic nanoparticles", *Physical Review Letters*, **101**, 087403 (2008).

[213] B. Auguie, W. L. Barnes, "Diffractive coupling in gold nanoparticle arrays and the effect of disorder", *Optics Letters*, **34**, 401 (2009).

[214] P. Johansson, "Light scattering from disordered overlayers of metallic nanoparticles", *Physical Review B*, **64**, 165405 (2001).

[215] A. Leitner, Z. S. Zhao, H. Brunner, F. R. Aussenegg, A. Wokaun, "Optical-Properties of a Metal Island Film Close to a Smooth Metal-Surface", *Applied Optics*, **32**, 102 (1993).

[216] K. R. Catchpole, S. Pillai, "Absorption enhancement due to scattering by dipoles into silicon waveguides", *Journal of Applied Physics*, **100**, 044504 (2006).

[217] J. Mertz, "Radiative absorption, fluorescence, and scattering of a classical dipole near a lossless interface: a unified description", *Journal of the Optical Society of America B-Optical Physics*, **17**, 1906 (2000).

[218] F. Leblanc, J. Perrin, J. Schmitt, "Numerical Modeling of the Optical-Properties of Hydrogenated Amorphous-Silicon-Based P-I-N Solar-Cells Deposited on Rough Transparent Conducting Oxide Substrates", *Journal of Applied Physics*, **75**, 1074 (1994).

[219] S. Linden, A. Christ, J. Kuhl, H. Giessen, "Selective suppression of extinction within the plasmon resonance of gold nanoparticles", *Applied Physics B-Lasers and Optics*, **73**, 311 (2001).

[220] K. Kneipp, H. Kneipp, I. Itzkan, R. R. Dasari, M. S. Feld, "Surface-enhanced Raman scattering and biophysics", *Journal of Physics-Condensed Matter*, **14**, R597 (2002).

[221] S. M. Nie, S. R. Emery, "Probing single molecules and single nanoparticles by surface-enhanced Raman scattering", *Science*, **275**, 1102 (1997).

[222] L. R. Hirsch, R. J. Stafford, J. A. Bankson, S. R. Sershen, B. Rivera, R. E. Price, J. D. Hazle, N. J. Halas, J. L. West, "Nanoshell-mediated near-infrared thermal therapy of tumors under magnetic resonance guidance", *Proceedings of the National Academy of Sciences of the United States of America*, **100**, 13549 (2003).

[223] S. Lal, S. E. Clare, N. J. Halas, "Nanoshell-Enabled Photothermal Cancer Therapy: Impending Clinical Impact", *Accounts of Chemical Research*, **41**, 1842 (2008).

[224] M. Westphalen, U. Kreibig, J. Rostalski, H. Luth, D. Meissner, "Metal cluster enhanced organic solar cells", *Solar Energy Materials and Solar Cells*, **61**, 97 (2000).

[225] C. Hagglund, M. Zach, B. Kasemo, "Enhanced charge carrier generation in dye sensitized solar cells by nanoparticle plasmons", *Applied Physics Letters*, **92**, 013113 (2008).

[226] M. D. Yang, Y. K. Liu, J. L. Shen, C. H. Wu, C. A. Lin, W. H. Chang, H. H. Wang, H. I. Yeh, W. H. Chan, W. J. Parak, "Improvement of conversion efficiency for multi-junction solar cells by incorporation of Au nanoclusters", *Optics Express*, **16**, 15754 (2008).

[227] S. P. Sundararaian, N. K. Grady, N. Mirin, N. J. Halas, "Nanoparticle-induced enhancement and suppression of photocurrent in a silicon photodiode", *Nano Letters*, **8**, 624 (2008).

[228] W. Warta, "Defect and impurity diagnostics and process monitoring", *Solar Energy Materials and Solar Cells*, **72**, 389 (2002).

[229] D. Derkacs, W. V. Chen, P. M. Matheu, S. H. Lim, P. K. L. Yu, E. T. Yu, "Nanoparticle-induced light scattering for improved performance of quantum-well solar cells", *Applied Physics Letters*, **93**, 091107 (2008).

[230] G. K. Celler, S. Cristoloveanu, "Frontiers of silicon-on-insulator", *Journal of Applied Physics*, **93**, 4955 (2003).

[231] E. Moulin, J. Sukmanowski, F. X. Royer, H. Stiebig, "*Integration of metallic nanoparticles in thin-film solar cells*", *Proceedings of 21st EC PVSEC*, Dresden, Germany (2006).

[232] N. C. Panoiu, R. M. Osgood, "Enhanced optical absorption for photovoltaics via excitation of waveguide and plasmon-polariton modes", *Optics Letters*, **32**, 2825 (2007).

[233] M. Kirkengen, J. Bergli, Y. M. Galperin, "Direct generation of charge carriers in c-Si solar cells due to embedded nanoparticles", *Journal of Applied Physics*, **102**, 093713 (2007).

[234] C. Rockstuhl, S. Fahr, F. Lederer, "Absorption enhancement in solar cells by localized plasmon polaritons", *Journal of Applied Physics*, **104**, 123102 (2008).

[235] F. Hallermann, C. Rockstuhl, S. Fahr, G. Seifert, S. Wackerow, H. Graener, G. von Plessen, F. Lederer, "On the use of localized plasmon polaritons in solar cells", *Physica Status Solidi a-Applications and Materials Science*, **205**, 2844 (2008).

[236] J. R. Cole, N. J. Halas, "Optimized plasmonic nanoparticle distributions for solar spectrum harvesting", *Applied Physics Letters*, **89**, 153120 (2006).

[237] K. R. Catchpole, A. Polman, "Plasmonic solar cells", *Optics Express*, **16**, 21793 (2008).

[238] K. R. Catchpole, A. Polman, "Design principles for particle plasmon enhanced solar cells", *Applied Physics Letters*, **93**, 191113 (2008).

[239] L. Vincent, P. Soille, "Watersheds in Digital Spaces - an Efficient Algorithm Based on Immersion Simulations", *Ieee Transactions on Pattern Analysis and Machine Intelligence*, **13**, 583 (1991).

[240] S. A. Boden, "*Biomimetic nanostructured surfaces for antireflection in photovoltaics*", *Ph.D. thesis*, University of Southampton, (2009).

[241] P. B. Johnson, R. W. Christy, "Optical-Constants of Noble-Metals", *Physical Review B*, **6**, 4370 (1972).